UNIVERSITÀ DEGLI STUDI DI CATANIA

DOTTORATO DI RICERCA IN FISICA

STEFANO SPATARO

CHARACTERIZATION OF THE HADES SPECTROMETER IN PP COLLISIONS AT 2.2 GEV: ELASTIC SCATTERING AND EXCLUSIVE ETA RECONSTRUCTION

TESI DI DOTTORATO

Coordinatore:

Prof. F. Riggi

Tutor:

Prof. G. BELLIA

Dr. P. FINOCCHIARO

XVIII CICLO 2002-2005

CONTENTS

1 INTRODUCTION

The study of hadron properties inside the nuclear matter, in conditions of high density and high excitation energy, is one of the main interests of the modern nuclear physics.

Figure 1.1 shows a scheme of the nuclear matter properties in nuclear collisions, as a function of the collision energy.

As the incident kinetic energy increases well above the Coulomb barrier, the nuclear shell structure becomes less and less relevant; up to 30 A MeV, collective states of nuclei still play an important role. Beyond the Fermi energy, the scenario evolves toward nuclear matter dynamics.

Within such a scenario we try to understand the nuclear matter behaviour in terms of an equation of state that, connecting variables such as pressure, temperature and density, could provide an explanation of the colliding nuclei as a liquid-gas phase transition.

At even higher energies, above 1 A GeV, a large fraction of the beam energy is transferred into the excitation of nucleon resonances and meson production. This exotic phase of nuclear matter is called hadronic matter. At even higher densities and temperatures, of the order of T = 170 MeV, a new nuclear matter phase characterized by the melting of hadrons into a plasma of quarks and gluons is expected to occur.

The investigation of the nuclear matter phase diagram in such a broad range of temperatures and/or densities offers a unique way to study the strong interaction and its theory, Quantum Chromo Dynamics (QCD), in a region of transition from hadronic to partonic degrees of freedom.
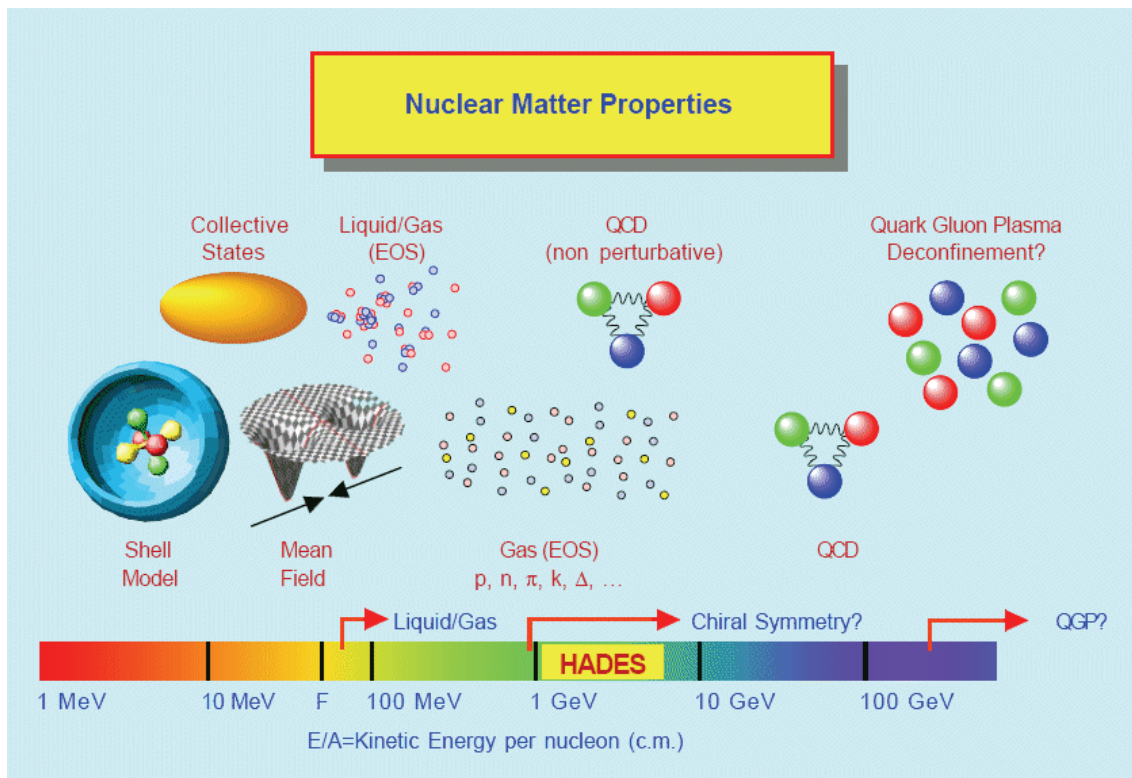
Figure 1.1 - Properties of nuclear matter as a function of the collision energy.

For low values of temperature and density the elementary particles of QCD, quarks and gluons, cannot be detected singularly; they are confined by the strong interaction to stay inside composed particles called *hadrons*. At the moment there is no experimental evidence of free quarks.

Hadrons are divided into two groups, *baryons* and *mesons*. The *baryons* are composed by three quarks, and they include stable particles such as protons and neutrons, but even higher energy nucleonic resonances and a multitude of instable particles. The *mesons* are constituted by a quark-antiquark pair, and they are not stable; in the beginning they were assumed to be the quanta of the strong interaction (Yukawa theory). The lightest of them are the pions, and they include the vector mesons which are very important for the study of nuclear matter properties.

In this context fundamental symmetries, spontaneous symmetry breakdown, and the mass generation mechanism are of particular importance.

One of the most important symmetries of the QCD is the chiral symmetry, which is connected to *helicity* conservation: we define *helicity h* of a particle the projection of its spin σ over the momentum p direction:

$$h = \frac{\sigma \cdot p}{|\sigma| \cdot |p|}$$

(Eq. 1-1)

The QCD Lagrangian exhibits this symmetry in the limit of massless quarks. As a consequence, left and right handed quarks decouple and "handedness" is conserved in strong interaction. But if we move to massive particles, we know it always exists an inertial coordinate system frame where the particle moves toward opposite direction, in this case the helicity changes its sign and so it is not conserved anymore.

In spite of the small current mass of the (u, d) quarks (see Table 1-1), the chiral symmetry is considered to be approximately valid.

The problem arises when considering hadron masses; as an example, if we consider a proton we know it has mass 938 MeV/c^2 and it is composed of a combination of *uud* quark; its mass value cannot be explained by simply summing the bare mass of its constituent quarks, and this discrepancy it is present for all the hadron masses. This means there is another effect which plays an important role in generating mass values.

Quark	electric charge	Mass [MeV/c^2] Bare	Constituent
down	-1/3	4 ÷ 8	≈ 300
up	+2/3	1.5 ÷ 4	≈ 300
strange	-1/3	80 ÷ 130	≈ 450
charm	+2/3	1150 ÷ 1350	
bottom	-1/3	4100 ÷ 4400	
top	+2/3	~ 178.1·10^3	

Table 1-1 – Table of the quark masses. The difference between the values of bare mass and constituent mass is strong for the lightest ones [PDG04].

It is commonly believed that chiral symmetry is spontaneously broken at the ground state. This is demonstrated by the different mass values of chiral partners: if we

consider ρ (770 MeV/c^2, $I^P = 1^-$) and a_1 (1260 MeV/c^2, $I^P = 1^+$), they have exactly the same quantum numbers except for opposite parity. Their different mass values show that the QCD Lagrangian is not invariant under chiral transformation, therefore the chiral symmetry is broken.

Left-handed and right-handed mesons decouple and their Lagrangian is a non-trivial feature of the QCD vacuum, resulting in the appearance of a quark condensate [Koc95]. This implies that hadrons are not only constituted by bare quarks, but also by a cloud of quark-antiquark pairs which are continually created and annihilated within the limit of the indetermination principle.

"Dressing" of quarks by the quark condensate is responsible for the generation of the constituent quark mass and hence hadron masses. In this case we talk about *constituent* quarks, and the calculated values are shown in Table 1-1; we can see the discrepancy between bare and constituent mass values is strong in particular for lighter quarks.

Moreover, the quark constituent masses appear in this picture as dynamical quantities depending on the temperature and/or density of the surrounding nuclear matter.

Several models have been proposed and developed throughout the last years, in order to try to predict the behaviour of hadron masses at higher temperature and density. At high values of baryonic density or temperature a new phase transition is foreseen, where the chiral symmetry is restored and the degeneracy of left and right handed particles vanishes.

The most frequently faced problem concerns the mass of mesons, mainly because their structure is intrinsically simpler than that of baryons (two valence quarks instead of three).

In this context the most relevant mesons have been the vector mesons ρ, ω and ϕ, which are spin 1 states with negative parity. When emitted in a nuclear collision, where high excitation energies and densities are reached, their short life time (few fm/c) is comparable to the life time of the fireball, so they can be used as a probe for the nuclear matter at those extreme conditions.

Obviously the very short lifetimes of these particles exclude any possibility of direct measurements, and therefore any experimental method in order to study these mesons has to be indirect. The best method consists on studying their direct decays in e^+e^- pairs. Despite of their low branching ratios ($\sim 10^{-5}$), dileptons do not undergo the strong interaction with the other hadrons present in the nuclear medium, so they carry the substantially undistorted information about the meson which produced them. Conversely the vector mesons hadronic decays are affected by the final state interaction. Thus, by studying invariant mass distributions of dilepton pairs emitted in nuclear collisions, it is possible to study the properties of vector mesons in the nuclear matter.

There is a variety of theoretical papers showing how different approaches lead to different conclusions about the vector meson properties in nuclear matter: each model tends to predict a different behaviour for each different vector meson. Sometimes a broadening of the resonance, sometimes a shift toward lower or higher energy, sometimes both are obtained (see chapter 2 for details). In this context one should mention that hadronic models are also predicting significant meson mass changes due to strong meson-hadron couplings. There is no established clear connection of this mechanism to the picture based on the chiral symmetry breakdown.

Dielectron e^+e^- invariant mass distributions were measured by the DLS collaboration [Por97] for proton-proton, light and heavy ion reactions at the 1-2 A GeV

energy range of BEVALAC laboratory, and at higher temperatures and densities in Pb+Au collisions at 158 A GeV by CERES experiment at CERN [Dre98].

The available experimental data seem to indicate a shift toward lower mass, namely the dropping mass of vector mesons. As a consequence it is important to measure the vector meson masses as a function of the medium density, but unfortunately both mass and density are difficult to be measured.

Density can, however, be deduced from theoretical transport model calculations assuming given dynamical conditions of the collision, that is, projectile, target, incident energy, impact parameter (this latter can be inferred by measuring the charged particle multiplicity produced in the collisions). Measuring vector meson masses is straightforward in vacuum, but very difficult in medium.

The HADES spectrometer [Had94], built at GSI Darmstadt by a collaboration between 19 institutions from 10 European countries, is a highly selective tool specially suited for the study of the high energy dielectron decay channels in nucleus-nucleus collisions around 1–2 A GeV. At the same time, it can serve as a high performance hadron spectrometer with superior resolution, particle identification, and rate capabilities. Additional important entrance channels are represented by proton-proton, proton-nucleus, pion-nucleon and pion-nucleus collisions.

The HADES experimental program combines systematic studies of dielectron production in elementary reactions with dielectron spectroscopy in heavy ion collisions, with special emphasis on the vector meson properties in nuclear matter.

A first HADES physics run was conducted in 2002 with C+C at 2AGeV [Hol05], to reinvestigate the enhancement measured by the DLS collaboration. But in order to provide absolute measurement of the dielectron reconstruction efficiency, needed for the final interpretation of C+C data, an independent measurement is needed, by means of well known calibration reactions.

The pp→ppη reaction channel, which can be exclusive reconstructed via the hadronic and dilepton decay channels whose branching ratios are known, is ideally suited for this purpose.

A proton-proton run was done on January 2004 at 2.2GeV, with the full coverage of outer chambers in 4 (out of 6) sectors, and so allowing the high resolution particle tracking for the first time. The main aims of this experiment were to collect elastic pairs, in order to calibrate the alignment of the tracking system, and then to measure the pp→ppη reaction channel.

In this work the characterization of the HADES spectrometer will be presented, by analysing experimental data from pp collisions acquired during the January 2004 production run. The analysis is focused in particular on the characterization of the tracking system, of the time of flight system, and in the exclusive reconstruction of the η meson decay channels. The latter can be used as calibration reaction to evaluate the spectrometer acceptance and efficiency for dielectron pairs, in view of heavy ion experiments.

In the second chapter the physical motivations which brought to the construction of the HADES spectrometer will be shown, and in the third chapter a description of the spectrometer will be presented as well as a summary of the experimental runs already done.

In the fourth chapter the analysis framework used for the HADES experiment will be presented, and a description of the simulation procedure used to make a proper comparison with the experimental data. A particular study of the spectrometer acceptance for the η meson reconstruction under different trigger selection will be presented, as performed before the experimental production run by using simulations;

by means of this analysis the data acquisition trigger was optimised to enhance the storage of events which contains η meson decays, thus reducing the number of acquired events coming from background reactions.

The fifth chapter will show a full characterization of the HADES tracking system, in terms of alignment and momentum reconstruction. By using the pp elastic scattering reaction, and thus well known kinematical constraints, is was possible to evaluate the quality of the drift chambers alignment, and the momentum and invariant mass resolution, according to different tracking algorithms. This measurement is mandatory in order to achieve the envisaged momentum and invariant mass resolution required to distinguish the width of the ω meson (about 8 MeV/c^2 at mass of ~ 800 MeV/c^2).

The sixth chapter is focused on time of flight measurements, which are used for particle identification. The HADES time of flight system is based mainly on a START detector and two plastic scintillator stop detectors (TOF and TOFINO); for the January 2004 run the START detector was not used, therefore it was necessary to develop a new procedure for the time calibration and for the reconstruction of the start time of the reaction, to make particle identification possible.

The chapter is divided into two parts. In the first part the time and position calibration procedures will be presented for the whole system; in the second part the developed algorithm for the start time reconstruction will be shown, by using a sample of simulation and experimental data (taken at low beam intensity with a START detector in operation in September 2003) in order to evaluate the resolution and the efficiency of the method.

The seventh chapter will show the procedure used for the exclusive η meson reconstruction, by means of the hadronic (ppη→ppπ$^+$π$^-$π°) and the electromagnetic (ppη→ppe$^+$e$^-$γ) decay channels. In the analysis of these decay channels it is not possible to fully reconstruct the event, because one neutral particle (respectively π° and γ) crosses the spectrometer undetected.

It will be shown how to select η events by searching for the missing particle (π° or γ) through a missing mass analysis technique, improved by a kinematical refit procedure in order to improve the resolution and the signal/background ratio.

Finally, in the eight chapter, the conclusions.

2 MOTIVATIONS OF THE EXPERIMENT

In this chapter the theoretical aspects which led to the realization of the HADES spectrometer will be presented.

The electromagnetic structure of hadrons in vacuum is almost known, and the vector meson dominance model (VDM) can describe very well the experimental data acquired from elementary reactions, even if there are some measurements still missing or with a poor statistics (such as the η Dalitz decay).

But the current knowledge of hadron structure inside the nuclear medium is incomplete; several experiments showed that their data cannot be explained by theoretical calculations which include free from factors, and only a change of the in-medium hadron properties could explain this discrepancy with the theory.

Moreover, several theoretical models using different approaches predict hadron properties modifications, but at the moment the available experimental data cannot help to distinguish between different scenarios, due to their limited resolution and low statistics.

For these reasons the HADES spectrometer was built, with the aim to provide experimental data with high resolution and statistics, in order to try to disentangle the different theoretical predictions.

But in order to understand experimental data from heavy ion collisions, a study of elementary reactions is mandatory, to evaluate the tracking resolution and efficiency, and to fully understand each single possible source of dileptons in the experimental spectra by an exclusive analysis.

2.1 Electromagnetic structure of hadrons

2.1.1 Non relativistic form factor

The study of the electromagnetic structure of hadrons played an important role in elaborating our present knowledge on the nature of matter.

The classical method to study the electromagnetic structure of charged[1] hadrons was used for the first time in the Rutherford experiment, in which the structure of atoms was analysed and the atomic nucleus was discovered. The method consists on analysing the scattering from a charged probe in the electromagnetic field of the object under investigation. For example high energy electron beams are an effective tool for probing the structure of the nucleon.

Let us consider the scattering of a non-relativistic electron with momentum p in the Coulomb field of a finite particle whose charge is uniformly distributed within a sphere of radius a. If an electron moves at distance l larger than a, the probability to be scattered is mostly independent of the structure of the particle. But at smaller distance the electron penetrates into the charged cloud, and it reaches regions where the electric field is lower than the field of a point-like charge. Large impact parameters correspond to small scattering angles θ, and so to small changes in momentum $|q|=p\theta$, small impact parameters correspond to higher momentum transfer q. We can state that the weakening

---

[1] One particle will be defined as "charged" if any of its "charges" characterizing it has a non zero value. We refers not only to electric charge, but also to baryonic number, magnetic moment, strangeness, etc. In this case the particle has an antiparticle counterpart with opposite signs of all "charges".

of the internal electric field, because of the spatial distribution of the charge, drastically reduces the probability of scattering with high momentum transfer.

We can express the differential cross-section for the scattering of an electron by a charged particle, with a specific space structure, in the form:

$$\frac{d\sigma}{dq^2} = \left[\frac{d\sigma}{dq^2}\right]_{point\,like} \cdot \left[F\left(q^2\right)\right]^2 \qquad \textbf{(Eq. 2-1)}$$

The function $F(q^2)$ is called the form factor of the particle. If we compare experimental data with the results of a computation of differential cross section for the scattering of an electron by a point-like particle, $[d\sigma/dq^2]_{pointlike}$, we can evaluate the particle form factor. The form factor provides a characterization of the spatial charge distribution for an extended object, and in the non-relativistic case it is related to the charge density distribution by a Fourier transformation.

In the low momentum transfer limit $q^2 \ll 1/a^2$ the form factor is $F(q^2) \approx 1$; on the contrary, at high momentum transfer values $q^2 \gg 1/a^2$ it drops down rapidly and it becomes lower than unity.

The analysis of the scattering of real particles, such as protons or neutrons, is more complicated because now the spin and the magnetic moment of the scattering particles become important. The magnetic moment of hadrons has also a spatial distribution which is characterised by its own form factor. A description of the electromagnetic structure of protons and neutrons requires two different form factors, one electric and one magnetic.

2.1.2 Relativistic form factor

In relativistic quantum mechanics it is not possible to establish a simple relationship between the form factor of a particle and the spatial distribution of its charge density. Nevertheless form factors continue to carry with themselves the information on the electromagnetic structure of the particle, and they represent a directly measurable feature of this structure.

According to quantum field theory, the electromagnetic interaction between particles occurs by means of the exchange of a virtual photon. A simple case of electromagnetic interaction is the electron-hadron scattering, as shown in the left part of Figure 2.1.

Due to the uncertainty principle the standard relativistic relation between energy, momentum and mass $E^2 = p^2 + m^2$ does not hold for virtual particles. For a "real" particle the quantity $E^2 - p^2$ is equal to its mass (this is said "on mass shell"), while for virtual particles this does not happen ("off mass shell"). Indeed virtual photons have $E^2 - p^2 \neq 0$ (the real photon is a massless particle).

In the relativistic description of the scattering process we can define the 4-momentum transfer q^2 for the electron as the difference of the squares of the variations of energy and momentum:

$$q^2 = \left(\Delta E_e\right)^2 - \left(\Delta p_e\right)^2 \qquad \textbf{(Eq. 2-2)}$$
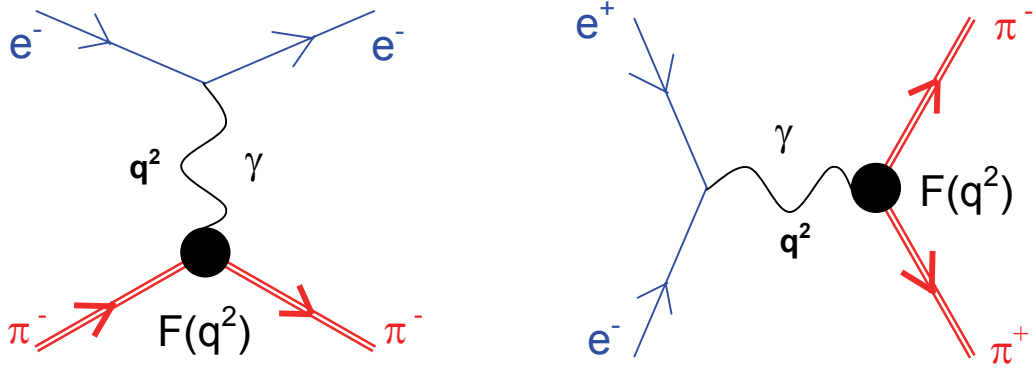
Figure 2.1 – The pion form factor. On the left diagram the $\pi^- e^-$ scattering process is represented as exchange of one virtual photon in the space-like momentum transfer region ($q^2 < 0$). On the right $e^+ e^-$ annihilation by production of a virtual photon in the time-like momentum transfer region. Both processes are affected by the π meson structure $F(q^2)$.

which is the 4-momentum transferred by the virtual photon.

We can analyse the $e^- \pi^-$ scattering process in the centre of mass reference frame; there the electron energy remains the same ($\Delta E_e = 0$), while only its momentum direction changes ($\left| \Delta \vec{p}_e \right| = 2 p_e \cdot \sin(\theta/2)$). In this case:

$$q^2 = \underbrace{\left(\Delta E_e\right)^2}_{0} - \left(\Delta p_e\right)^2 = -4 p_e^2 \sin^2(\theta/2) < 0 \qquad \textbf{(Eq. 2-3)}$$

the squared 4-momentum is negative, and the virtual photon does not transfer energy but only momentum. Such momentum transfer is called "space-like". The larger $|q^2|$ the smaller the space region where the scattering process takes place.

The internal electromagnetic structure of a hadron can be summarized by the form factor $F(q^2)$, which can be directly measured in experiments.

Another way to probe the structure of hadronic particles is by electron-positron annihilation, studied at electron-positron colliders.

On the right side of Figure 2.1 the reaction $e^+ e^- \rightarrow \pi^+ \pi^-$ is represented, which can be reduced to the annihilation of the lepton pair and the emission of a virtual photon, which then creates a pair of π^+ and π^- mesons. In this case, if we analyse the same reaction in the centre of mass reference frame, when the electron and positron with momentum $\vec{p}$ and $-\vec{p}$ and energies $E = \sqrt{p^2 + m_e^2}$ annihilate, the squared 4-momentum of the virtual photon is positive and equal to square s of the total energy of the colliding particles:

$$q^2 = \left(2E\right)^2 - \left(\vec{p} - \vec{p}\right)^2 = \left(2E\right)^2 = s > 0 \qquad \textbf{(Eq. 2-4)}$$

The virtual photon does not transfer momentum but only energy, and it is called "time-like"; by changing the energies of colliding particles it is possible to study different values of the transferred momentum. Not all the positive regions of transferred momentum can be explored; indeed the total energy of the colliding particles must be

higher than the sum of the masses of the two outgoing pions. Only if we have enough available energy we can produce these two particle ($s > (2m_\pi)^2$).

In the case of point-like pions the cross section of the process $[\sigma(e^+e^- \to \pi^+\pi^-)]_{\text{pointlike}}$ can be calculated in the framework of quantum electrodynamics as a function of q^2, and then the electromagnetic structure of the $\pi^\pm$ mesons could be evaluated by:

$$\sigma(e^+e^- \to \pi^+\pi^-) = [\sigma(e^+e^- \to \pi^+\pi^-)]_{po\,int\,like} \cdot |F_\pi(q^2)|^2 \qquad \textbf{(Eq. 2-5)}$$

So the annihilation process offers another way to study the pion form factor $F(q^2)$, but in the time-like region of momentum transfer.

Experiments on the scattering of charged π mesons off electrons, and on e^+e^- $\to \pi^+\pi^-$ annihilation are complementary to understand the pion form factor in the whole physical range of q^2, as well as for other hadrons (see Figure 2.2).
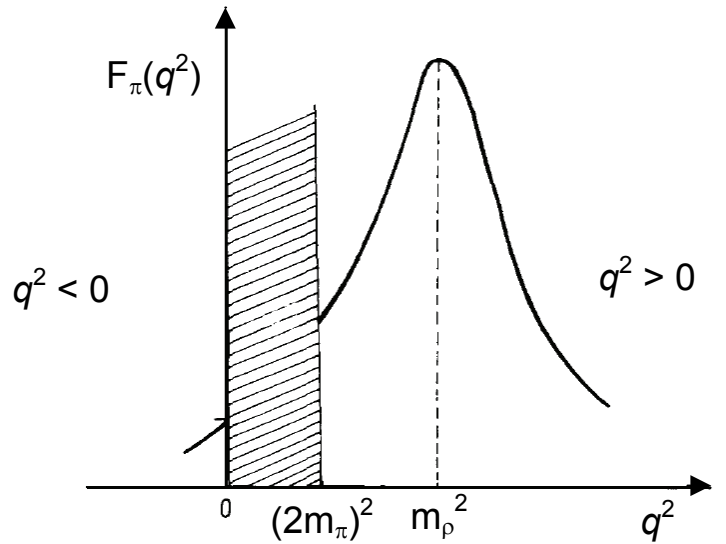
Figure 2.2 – The quantitative behaviour of π form factor in the whole physical accessible range of momentum transfer q^2. The dashed area is a non physical region kinematically prohibited.

2.1.3 Vector Meson Dominance Model

As already mentioned, as q^2 increases in elastic scattering processes the particle from factor decreases: at high momentum transfer the virtual photon is sensitive only to the "inner" part of the hadron. For the time-like regions another effect occurs, the resonance interaction between photons and hadrons. This effect is usually called vector dominance.

Vector mesons are short lived particles which have the same quantum numbers of the photon; they have spin 1 and negative parity: $J^P = 1^-$. The lightest of them are ρ^0 ω and ϕ mesons, whose properties are shown in Table 2-1.

VECTOR MESON	J^{PC}	MASS [MeV/c^2]	WIDTH [MeV/c^2]	MEAN LIFE [fm/c]	MAIN DECAY	BRANCHING RATIO e$^+$e$^-$
ρ	1^{--}	776	150	1.3	$\pi\pi$ (~100%)	$4.7 \cdot 10^{-5}$
ω	1^{--}	783	8.5	23	$\pi^+\pi^-\pi^0$ (89%)	$7.1 \cdot 10^{-5}$
ϕ	1^{--}	1019	4.3	44	K^+K^- (49%)	$3.0 \cdot 10^{-4}$

Table 2-1 – Properties of light vector mesons in the vacuum [PDG04].

According to Vector meson Dominance Model (VDM) a virtual photon can interact with a hadron of interest not only directly but also after a transition to a virtual vector meson state, as shown in Figure 2.3 [Sak69]. The quantum numbers of these particles allow the direct transition.
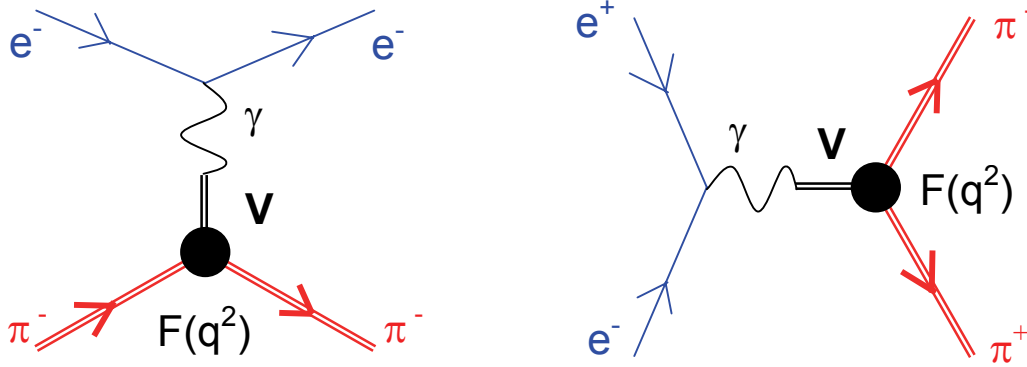
Figure 2.3 – Diagrams for the one photon exchange process in the Vector meson Dominance Model (in the diagram V represents the virtual vector meson).

The concept of this type of interaction between hadrons and photons first arose in *ep* scattering, and it was later confirmed by a number of other experiments. The mechanism becomes important in particular in the cases of time-like photons, when the squared momentum q^2 approaches to the vector meson squared mass value ($q^2 \approx m_\rho^2$). Here the virtual meson reaches "mass shell" and it becomes real, then decays by the channel $\rho^0 \to \pi^+\pi^-$ (over a time of 10^{-23} s). The creation of an intermediate particle results in a strong enhancement of the pion form factor, for transfer momentum values close to the vector meson mass. After the resonance maximum ($q^2 > m_\rho^2$) the form factor starts to decrease.

In Figure 2.4 the experimental pion form factor is shown from $e^+e^- \to \pi^+\pi^-$ reactions; the resonance at ρ mass value is well visible, which confirms the hypothesis of VDM model. Moreover it is possible to see a sharp drop at masses just a bit higher than the pole value; this effect is interpreted as the interference between ρ and ω mesons whose mass values are close to each other.

The pion form factor can be approximated by a Breit-Wigner function:

$$\left|F_\pi\!\left(q^2\right)\right|^2 = \frac{m_\rho^4}{\left(q^2 - m_\rho^2\right)^2 + m_\rho^2 \Gamma_\rho^2}$$

(Eq. 2-6)

where m_ρ and Γ_ρ are respectively the mass and the decay width of ρ meson.
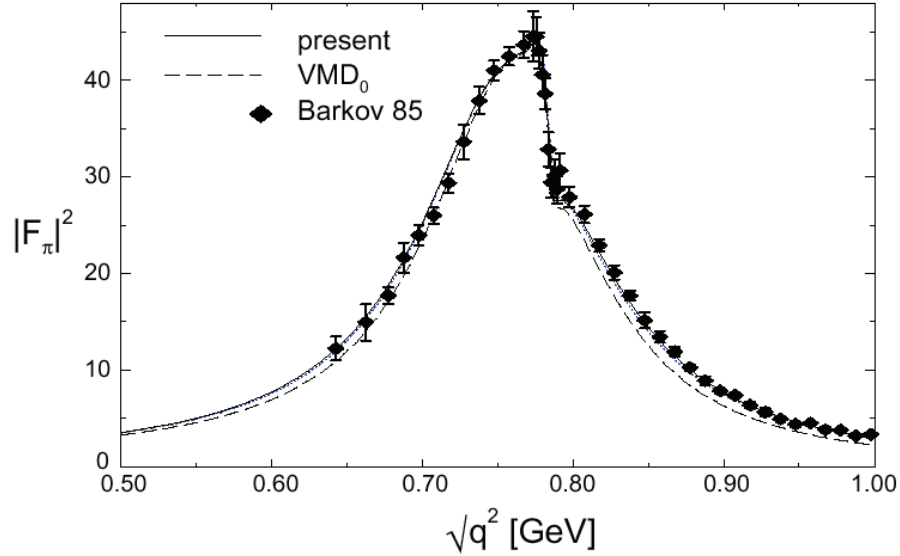
Figure 2.4 – Experimental pion form factor from $e^+e^- \to \pi^+\pi^-$ reactions, which denotes a resonance close to the ρ mass region. The spectrum shows the comparison between experimental data [Bar85] and theoretical calculations by using VDM model and ρ-ω interference [Kli96].

2.1.4 Transition form factor

After the previous discussions on the form factor of charged particles, we will talk about truly "neutral" particles, which have a "zero" value in all their charges (electric, spin, isospin and so on). These particles transform into themselves by a charge conjugation, so they are identical to their antiparticles. This group includes the photon and some mesons, such as $\pi°$, η, η', $\rho°$, ω and ϕ meson.

It follows that neutral particles must have an additional quantum number, which is called charge conjugation parity (C) and it can be positive or negative. The operation of charge conjugation transforms the wave function of the particle into itself (positive C) or it reverses its sign (negative C). This quantum number is conserved in strong and electromagnetic interactions.

The photon has a negative value of C parity, it is the quantum of electromagnetic field and so electric and magnetic fields change their signs under charge conjugation.

Electromagnetic interactions are responsible for the decay of $\pi°$, η and η' mesons into two γ photons. The C parity of these particles is given by the product of the two photon C parities, and so it is positive. Particles which decay into one single photon have a negative C parity, such as vector mesons.

The processes of single photon exchange shown in Figure 2.1 are forbidden for truly neutral mesons, because of the C parity conservation. The amplitude of these processes is always equal to zero, and also their form factor.

However the internal structure of neutral hadrons can manifest itself in phenomena in which the neutral particle is converted into another particle of reversed sign of C parity plus a photon. In this case the charge conjugation parity is conserved, for example in the decay:

$$A \rightarrow B + \gamma \qquad \textbf{(Eq. 2-7)}$$

where A and B are two neutral mesons with charge conjugation parity C_A and C_B; the C parity of the photon is $C_\gamma = -1$, so from C parity conservation we find $C_A = C_B \cdot C_\gamma = -C_B$.

Another process is also possible in which the γ goes off-shell, becomes virtual and it produces a lepton pair:

$$A \rightarrow B + \gamma_v \rightarrow B + l^+ + l^- \qquad \textbf{(Eq. 2-8)}$$

This effect is called internal conversion, where the virtual photon transfers a certain 4-momentum to the lepton pair. The probability of formation of the lepton pair in a conversion decay with an effective mass $m_{l^+l^-}$ is proportional to the probability of emitting a virtual γ with time-like 4-momentum $q^2 = m_{l^+l^-}^2$, and so to the vertex of the transition A→B. In this case the ordinary form factor of neutral hadrons vanishes, but the so called "transition form factor" appears.

We can express the probability of a conversion decay $d\Gamma/dq^2$ in unity interval of q^2 as:

$$\frac{d\Gamma}{dq^2} = \left[\frac{d\Gamma}{dq^2}\right]_{po\text{int}\,like} \cdot \left|F_{AB}\left(q^2\right)\right|^2 \qquad \textbf{(Eq. 2-9)}$$

where $F_{AB}(q^2)$ is the transition form factor. By comparing the measured spectrum of lepton pairs with QED calculations for point like particles, it is possible to estimate the transition form factor in the time-like region of momentum transfer.

The decays $A \rightarrow \gamma + l^+ + l^-$ occupy a special place, because they correspond to the internal conversion of a photon in the decay $A \rightarrow 2\gamma$, which is allowed for pseudoscalar mesons such as $\pi°$ and η. In this case the transition form factor describes the electromagnetic structure of the "vertex" A→γ; the corresponding form factor defines the electromagnetic properties of this hadron.

In Figure 2.5 the diagram of the η Dalitz decay into $\gamma \, \mu^+ \, \mu^-$ is represented: by using vector meson dominance model the virtual photon is coupled to the hadron by the production of a virtual vector meson.

The left plot shows experimental data obtained in $\pi^-p \rightarrow \gamma\mu^+\mu^-n$ reactions [Djh80]; the experimental data can be well described by the calculation within the VDM model (dashed line).

In general the η meson form factor can be approximated by:

$$F_\eta\left(q^2\right)^2 = \left|\left(1 - \frac{q^2}{\Lambda_\eta^2}\right)\right|^{-1} \qquad \textbf{(Eq. 2-10)}$$

where Λ_η is a cut-off parameter, which results from a fit $\Lambda_\eta = 0.72$ GeV/c^2 (continuous line in the plot).
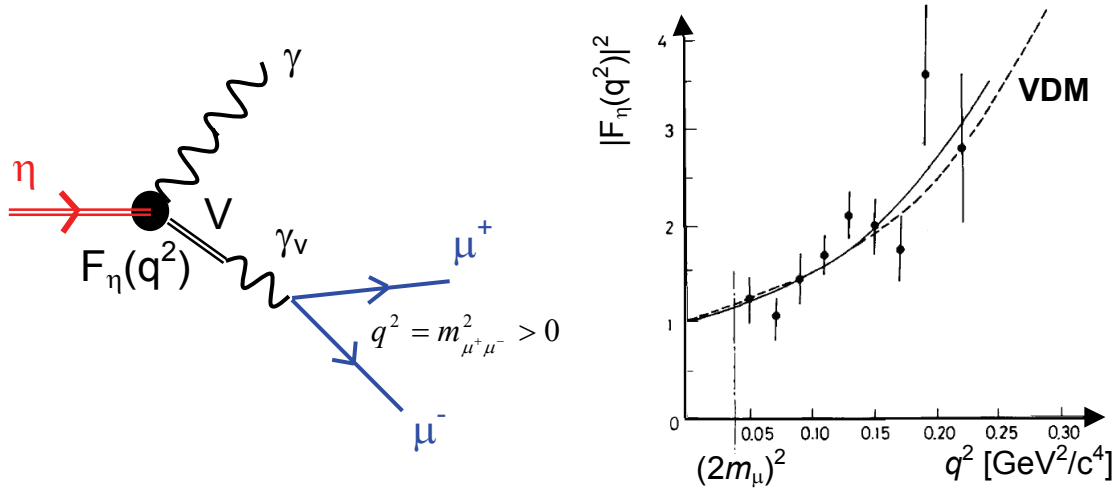
Figure 2.5 – The diagram for Dalitz decay $\eta \rightarrow \gamma \mu^+ \mu^-$ (left side) through vector meson dominance model. On the right side experimental data on the η transition form factor [Djh80]. VDM model can describe the data very well (dashed line).

2.2 Hadrons in nuclear matter

The study of hadron properties inside the nuclear medium, at any density and temperature values, is one of the main goals of the nuclear physics. Indeed new effects, not present in elementary reactions and not yet fully understood, play an important role in determining the hadron structure.

Light vector mesons are good probes to study nuclear matter in extreme conditions; when produced in a heavy ion nuclear collision, their short mean life (Table 2-1) is lower than the mean life of the fireball, so they decay mainly inside the high density region.

In order to study the vector meson production we must consider that their main decay channels are hadronic. Hadrons undergo strong interaction with the other hadrons present inside the nuclear matter; thus the outgoing hadronic particles, produced by meson decays inside the nuclear medium, carry an information which is modified by the final state interaction.

Leptons do not feel the effects of strong interaction from the hadrons in the medium, they leave the reaction region substantially undistorted and carry with themselves the original information of the meson which produced them; so dilepton decay channels are a good tool to investigate hadron properties inside the nuclear matter.

However the study of electromagnetic probes is rather difficult. There are several competing background processes generating dilepton, such as photon conversion effects, Bremsstrahlung and Dalitz decays of Δ, ω, η and π°; these decays produce e^+e^- pairs mainly in the low mass region. Moreover dilepton decay channels are rare probes because of their low branching ratios ($\sim 10^{-5}$), and so their detection requires well suited experimental devices.

In summary, the study of in-medium meson structures is possible by studying dilepton invariant mass spectra in nuclear collisions. Modifications are predicted by the theory, but at the moment several theoretical models exist, which take into account different nuclear effects and often providing misleading predictions, each one different from the others.

In the following paragraphs two scenarios will be presented: one which takes into account the in-medium effects on the hadron spectral function and predicts a broadening of the ρ meson resonance, the other one which predicts a scaling of the hadron masses as a function of the baryonic density (Brown-Rho scaling).

2.2.1 In-medium spectral functions

While considering form factors of vector mesons produced in the nuclear medium, it has to be included also the hadron interaction with the other particles present in the same space region; this interaction changes the meson structure itself.

Hadrons are strongly interacting objects and many body excitations in the medium may carry the same quantum numbers as the hadrons under investigation. In this picture the change of the hadron properties is due to their mutual interactions, and as a consequence of these interactions the hadron becomes very short lived, or melt inside the nuclear medium.

In the ρ spectral function approach we can express the dilepton yield from ρ meson decay, at baryonic density ρ_B and temperature T, such as:

$$\frac{dN_{l^+l^-}}{dM} = -Br\left(q^2\right)\frac{2M}{\pi}\operatorname{Im}D_\rho\left(q,\rho_B,T\right) \qquad \textbf{(Eq. 2-11)}$$

where M is the dilepton invariant mass ($M^2 \equiv q^2$), q is the transferred momentum, $Br(q^2)$ is the branching ratio to dileptons in vacuum, and $\operatorname{Im}D_\rho$ is the imaginary part of the ρ meson propagator, correlated to the interaction with the other hadrons and resonances which are present in the nuclear medium.

We can express the imaginary part of the propagator as:

$$\operatorname{Im}D_\rho^{L,T}\left(q,\rho_B,T\right) = \frac{\operatorname{Im}\Sigma_\rho^{L,T}\left(q,\rho_B,T\right)}{\left|M^2 - \left(m_\rho^{bare}\right)^2 - \Sigma_\rho^{L,T}\left(q,\rho_B,T\right)\right|^2} \qquad \textbf{(Eq. 2-12)}$$

where L,T are the longitudinal and transverse meson polarisations, m_ρ^{bare} is the ρ meson mass in the vacuum, and $\Sigma_\rho^{L,T}$ is a complex meson self-energy which has to be calculated according to which interactions we consider. In analogy with the elementary case, the propagator plays the same role as the π form factor; indeed for the ρ meson in vacuum the self energy can be expressed as $\Sigma_\rho = -im_\rho\Gamma_{\pi\pi}$, and so we obtain the Breit-Wigner formula shown in 2.1.3.

In Figure 2.6 calculations of the propagator imaginary part are shown for different light vector mesons, made by using the spectral function approach [Kli97], for different values of baryonic densities and averaged over longitudinal and transverse part.

If we look into the ρ meson distribution we can see that by increasing ρ_B the main peak remains centred at the same mass value, but the distribution becomes broader and even a second structure appears at lower mass region. In the ω meson case, at higher densities the peak is shifted toward lower mass values, while the width remains substantially unchanged. The distribution for ϕ meson remains unchanged, the position of the peak remains the same, only a small broadening is foreseen.
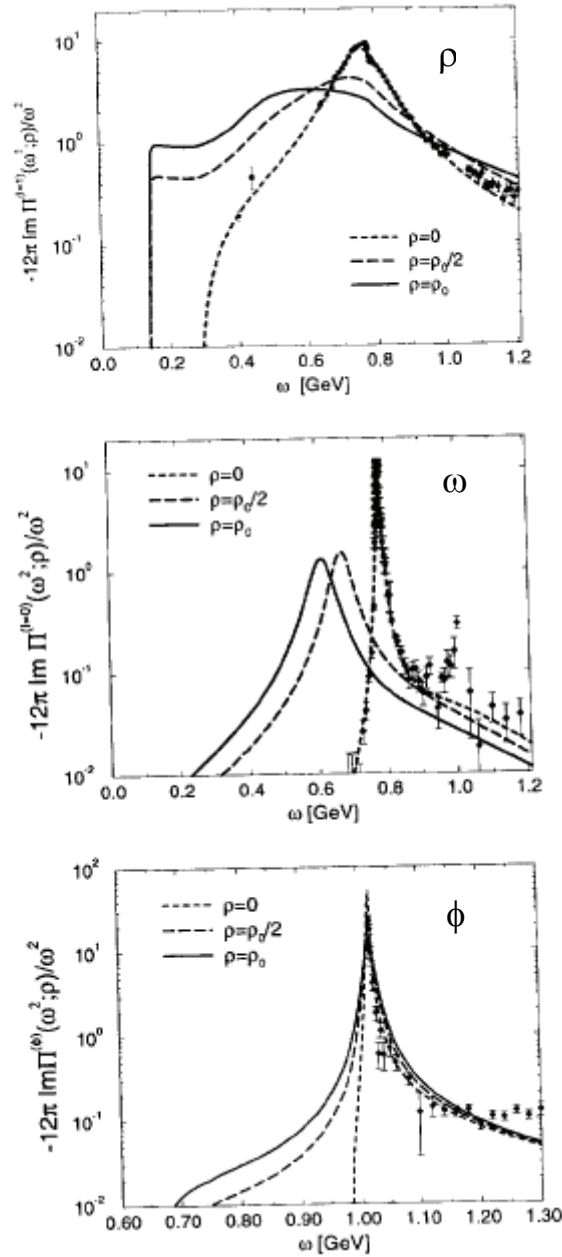
Figure 2.6 – Imaginary part of the vector meson propagator calculated by means of the spectral function approach for different mass value ω and at different baryonic densities, for ρ (upper) ω (central) and ϕ (lower) mesons [Kli97]. We can see that while for the ρ meson a broadening is foreseen, for ω meson the peak results shifted toward lower mass values; the ϕ meson peak is almost unchanged, apart from a small broadening.

2.2.2 Brown-Rho scaling

Another effect which a particle should undergo according to QCD calculations is the so called Brown-Rho scaling.

By definition hadrons are particles constituted by quarks; hadrons constituted by three quarks are called *baryons*, while *mesons* are the ones made of a quark-antiquark pair.

Nucleons are baryons constituted only by quarks up and down, which are supposed to have *bare* mass values below 5 MeV/c^2. If we consider nucleon masses, close to 1 GeV/c^2, they cannot be explained only by the sum of constituent quark masses. Indeed this discrepancy is explained in Quantum Chromo Dynamics by the definition of QCD vacuum, which is dominated by the continuous production and annihilation of quark-antiquark pairs.

We can evaluate the scalar quark condensate $\langle \bar{q} q \rangle$, proportional to the expectation value of the number of virtual pairs produced, which is non vanishing in the vacuum due to a spontaneous breaking of the chiral symmetry[2]:

$$\langle \bar{q} | 0 | q \rangle = \langle \bar{q} q \rangle_0 \approx -(230\, MeV/c)^3 \rightarrow -1.6\, fm^{-3} \qquad \textbf{(Eq. 2-13)}$$

The expectation value [Cas99] means that in vacuum there are about 1.6 virtual $\bar{u} u$ pairs per fm^3, and also for the *d* quarks.

When heating up the vacuum state, or increasing the baryonic density, the scalar quark condensate reduces in magnitude. A full evolution of the quark condensate as a function of density and temperature is not available yet, it can be obtained only in a model dependent way. For example Figure 2.7 shows results of a calculation made inside the Nambu-Jona-Lasinio model [Kli90]. We can see that while the condensate scales almost linearly with the density, by heating the system there is a sudden drop at a critical temperature $T_c \sim 150$ MeV, which coincides with the temperature phase transition from a normal to a quark-gluon plasma phase of hadronic matter, as predicted by QCD lattice calculations.

In this contest hadron mass modifications were proposed as a key observable for the chiral symmetry restoration when temperature or density is increased. Brown and Rho suggested that a decrease of the condensate in nuclear matter can be related to a reduction of hadron masses, and it can be formulated by a scaling law [Bro91]:

$$\frac{M_N^*}{M_N} \approx \frac{m_V^*}{m_V} \approx \left(\frac{\langle \bar{q} q \rangle_\rho}{\langle \bar{q} q \rangle_0} \right)^{1/3} \qquad \textbf{(Eq. 2-14)}$$

where M_N^* and m_V^* are the nucleon and the vector meson masses in nuclear matter. In this case the mass of all the vector mesons should decrease by increasing the baryonic density.

---

[2] The QCD Lagrangian of a massless particle is symmetric with respect to a SU(3) gauge transformation (chiral invariance); this implies that the sign of the projection of the fermion spin on its momentum direction cannot be changed by the dynamics, and so right-handed and left-handed particles should be identical. This does not happen in the vacuum, as can be seen from the different masses of the ρ meson and its chiral partner a$_1$ meson. In an approximated scheme the Lagrangian function can be written as the sum of a chirally symmetric part plus a symmetry violating term ($m \bar{\psi} \psi$).

In summary, significant in-medium mass modifications are predicted from various hadronic models; from the theoretical side there is no connection between the Brown-Rho scaling and the spectral function approach. Only experimental results from dilepton measurements can help to understand in-medium effects on hadron properties, in order to disentangle between these two scenarios.
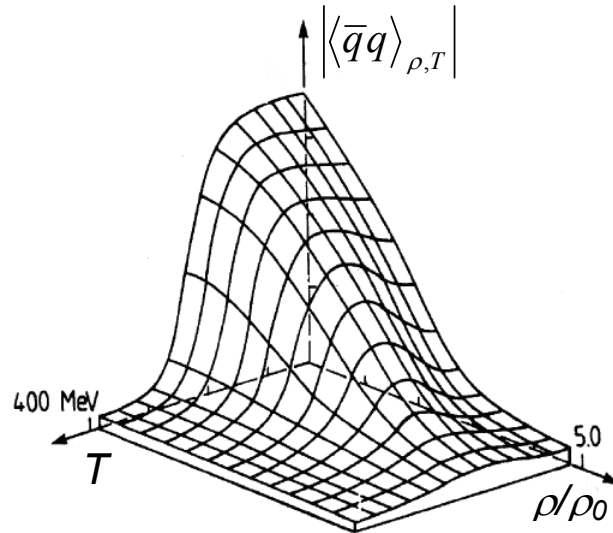

Figure 2.7 – Quark condensate value as a function of the nuclear matter temperature T and density ρ, according to NJL model [Kli90].

2.3   Dilepton pairs from heavy ion reactions

Invariant mass spectra of e^+e^- pairs were measured for proton-proton, light and heavy ion reactions at 1-2 A GeV energy range by the DLS[3] collaboration at BEVALAC. Within the given experimental error bars the extracted e^+e^- production rates in proton-proton reactions could be reproduced very well by theoretical calculations including various hadronic sources, such as *pn* bremsstrahlung, π°, η and ω Dalitz decays, and the direct decays of vector mesons.

For the heavy ion collisions an excess of the dielectron yield was found in the invariant mass range between 200 and 600 MeV/c^2, with respect to theoretical calculations made with BUU transport model, by using hadron spectral functions in the vacuum (Figure 2.8 left plot). The complete dilution of the ω and ϕ meson signal is connected to the low invariant mass resolutions.

This excess can neither be explained by the medium-modified ρ spectral function, nor by a meson mass dropping scenario as predicted by Brown-Rho scaling; this case is usually referred as the "DLS puzzle".

In the region of high temperatures studied in ultra relativistic collisions at CERN, a large dilepton excess below ρ/ω region was observed by the CERES experiment, in collisions Pb+Au at 158 A GeV [Dre98]. The right plot of Figure 2.8 shows the experimental invariant mass distribution in comparison with different theoretical calculations, by using free spectral functions, in-medium spectral functions and dropping mass scenario [Rap00].

---

[3] **D**i-**L**epton **S**pectrometer.

In this case the excess is in agreement with both calculations, even if they lead to different representations; the important difference among the two models is the dielectron yield in the ρ-ω mass region, where the present quality of data cannot distinguish between the two scenarios.

For that purpose a much better mass resolution above the ρ mass pole is required. Nevertheless we must consider that at those high energies the number of open channels is large, therefore it is much difficult to understand which is the exact process that led to this excess, and the results can be misleading.
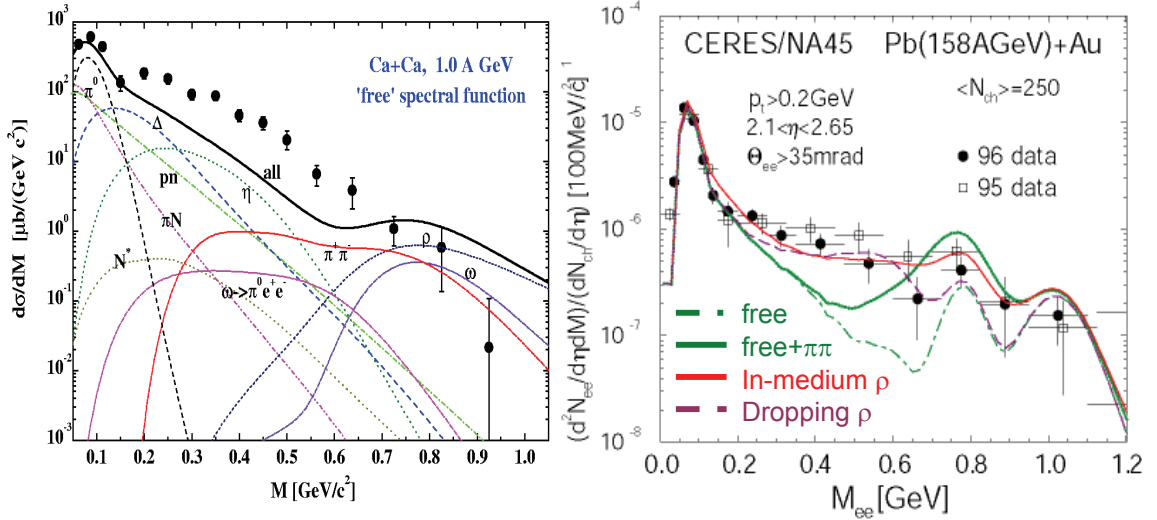

Figure 2.8 – On the left: invariant mass distribution for dielectron pairs in Ca+Ca collisions at 1 A GeV measured by the DLS collaboration [Por97], in comparison to theoretical predictions from BUU transport model by using hadron spectral functions in vacuum [Bra98]. On the right: dielectron invariant mass distribution from Pb+Au collisions at 158 A GeV measured by CERES experiment [Dre98]; theoretical predictions by simulating free spectral function, in-medium spectral function and dropping mass scenario for ρ meson are shown for comparison [Rap00].

2.4 *Dilepton spectroscopy with HADES*

The HADES[4] collaboration was born on 1994 with the main goal to construct a high performance spectrometer for electron/positron pairs at GSI laboratory in Darmstadt (Germany), in order to study adequately the dilepton production in nuclear collisions at an energy range of 1-2 A GeV.

The physical program of HADES is quite wide and it foresees the systematic study of e^+e^- dilepton pairs produced in elementary reactions (πp, pp, pd), such as in hadron induced nuclear collisions (pA, πA), and in heavy ion collisions. With the range of energy available at GSI (protons up to 4.5 GeV, ions of 1-2 A GeV, and the possibility to use pion beams), the main interest is focused on pairs with invariant mass value up to 1 GeV/c^2.

If compared to DLS spectrometer, HADES has a better resolution in invariant mass, which should be around 1% at 800 MeV/c^2 (against the 15% of DLS), in order to distinguish even the ω meson width (8 MeV/c^2), and an acceptance of about 40%

---

[4] Acronym of **H**igh **A**cceptance **D**i-**E**lectron **S**pectrometer.

(against ~5% of DLS), in order to acquire a sufficient statistics of dilepton pairs in a reasonable amount of time. With the high count rates foreseen, a full day of acquisition with HADES could reveal as many dilepton pairs as DLS did during all its beam times.

A large number of acquired pairs should allow to perform an exclusive analysis, such as transverse momentum distribution for different regions of invariant mass, in order to improve our knowledge about the dynamical mechanism which brings to the production of meson vectors.

During November 2002 there was the first production run of HADES; C+C collisions were studied at 2 A GeV beam energy, about 220 millions of events were recorded with the low resolution tracking setup (i.e. a mass resolution of ~10%).

Figure 2.9 shows the preliminary invariant mass distribution corrected for detector and lepton-track reconstruction efficiencies, as compared to a cocktail based on known meson properties in the vacuum filtered with HADES acceptance and momentum resolution. We can see that the excess in the mass range between $200 - 600$ MeV/c^2 is visible.
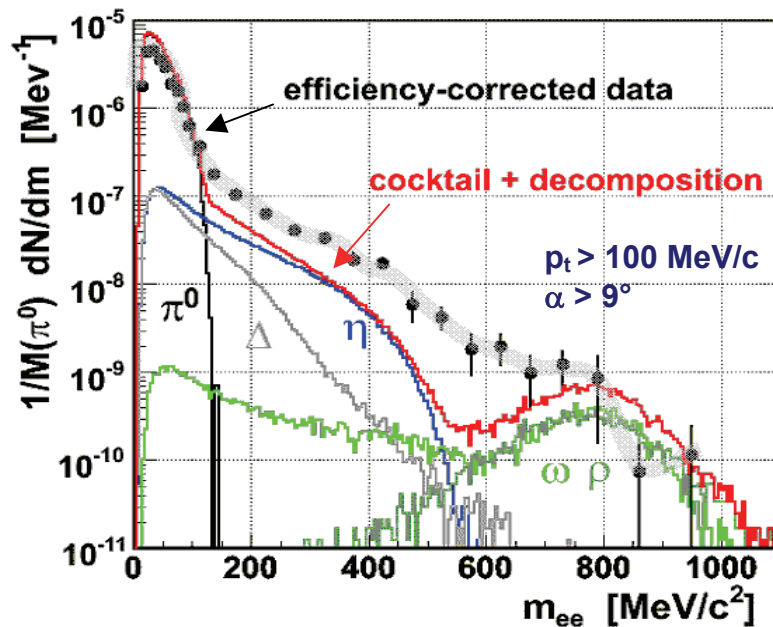
Figure 2.9 – Dilepton pairs invariant mass distribution for C+C at 2 AGeV with HADES experiment [Hol05], compared to a simulated cocktail filtered with the HADES acceptance and mass resolution, considering the known meson properties in vacuum.

But in order to fully understand the invariant mass distribution, the dilepton yield has to be normalized by means of a calibration reaction, and we must completely understand the response of the HADES spectrometer. To fulfil these goals a study of elementary collisions in needed.

2.5   *The HADES pp programme*

Dilepton invariant mass spectra in elementary collisions were explored by several experiments at SPS and BEVALAC energies. Their results showed that the dielectron yield can be quantitatively understood as a sum of freely decaying hadrons

[Ern98][Fäs03][Mos03]. At low invariant masses, below 0.6 GeV/c^2, the spectrum is characterized by *pn* bremsstrahlung, by the Dalitz decay of π^0, η and ω mesons, and of the Δ baryon; moving to higher masses the direct decays of ρ, ω and ϕ mesons dominate the distribution.

The HADES collaboration plans to perform a systematic study of dilepton sources through *pp* and *pn* reactions, where it is possible to fully reconstruct the event by detecting all the particles in the exit channel. All the informations available at energies between 1 and 5 GeV are known only from inclusive measurements, while an exclusive study can provide new hints on the understanding of the dielectron elementary sources. To perform this analysis the HADES physics program foresees several proton runs at different energies, in order to study separately each possible source. In these reactions the electron background from secondary sources can be kept at minimum, and the observed spectra can be compared reliably to simulations.

The first production run was done on January 2004, with pp collisions at 2.2GeV. The main goal of the experiment was to collect data with *pp* elastic scattering, for tracking alignment, and to identify $pp{\rightarrow}pp\eta$ reactions through an exclusive reconstruction of the hadronic and the dielectron decay channel.

In order to technically understand the detector setup the study of elastic proton-proton scattering is foreseen; with this method very strong kinematical conditions can be applied for a detailed study of the drift chamber position and calibration. This measurement is crucial to achieve the envisaged momentum and invariant mass resolution, since optical measurements of the detector locations cannot be performed with a resolution similar to the intrinsic position resolution of the detector. Furthermore the low multiplicity environment is essential to investigate the detector response in a well defined environment. It further allows to study secondary processes induced in the setup.

The study of the η meson is of particular interest for several reasons. In the vicinity of the threshold the production of the η meson was studied extensively and the inclusive cross sections are well known, as shown in Figure 2.10 [Bal01]. The observed electron pair invariant mass distribution for the η Dalitz decay branch can therefore be used to check contributions from other sources (such as Δ Dalitz, combinatorial background, etc.) as well as the lepton trigger efficiency.

In addition, if both protons and both leptons are detected, the reconstruction of this decay mode is kinematically complete without requiring an additional photon detector, and a missing mass cut on the η mass can be applied. This would allow to separate the η Dalitz from all other sources and to map the effective acceptance of the spectrometer. The η production cross section can be measured both through the hadronic ($\eta{\rightarrow}\pi^+\pi^-\pi^0$) and the dielectron ($\eta{\rightarrow}e^+e^-\gamma$) Dalitz decays, whose branching ratios are known. This fact allows to use the $pp{\rightarrow}pp\eta$ channel as a calibration reaction for the dielectron identification of the spectrometer, in order to normalize the dielectron yields in the heavy ions experiments. As a result quantitative numbers for the contribution of combinatorial background can also be obtained.

Moreover two existing measurements of the η Dalitz decay have been published so far, one based on a sample of 80 counts [Jan75], the other based on a sample of 2366 counts corresponding to a hypothetical background free yield of 106 signal pairs [Aga98].

The main source of dileptons at this energy value (2.2 GeV/c) is the Dalitz decay of neutral pions, and an estimate of the yield can be compared to the values measured by other experiments, in order to check the HADES capability.

In order to study Δ^+ Dalitz decay and *pn* bremsstrahlung, we also plan to explore *pp* and *pn* collisions at lower energies (1.25 GeV), thus decreasing the η contribution and highlighting these channels.
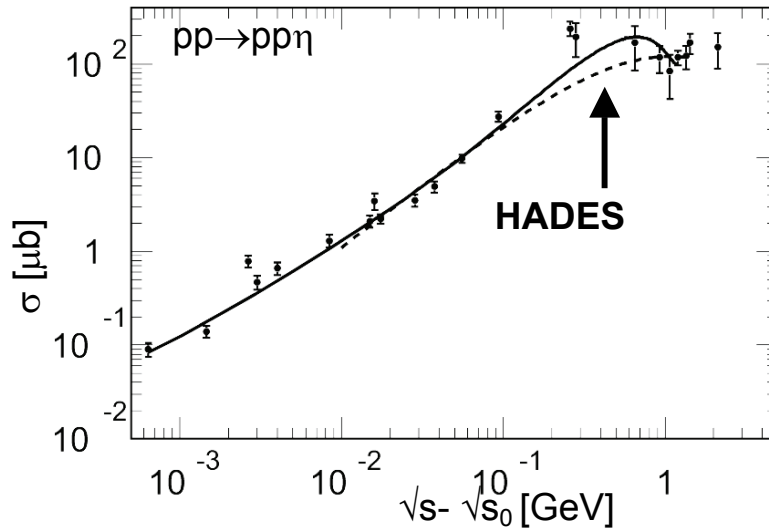

Figure 2.10 - Exclusive cross section for the reaction pp→ppη as a function of the total CM energy above the η production threshold [Bal01].

There is a general agreement that in *pn* collisions an important contribution comes from the bremsstrahlung channel, due to the strong dipole term in these collisions. However, a theoretical description is not easy due to a difficult evaluation of the nucleon form factor in the time-like region. At the moment the quality of the existing data does not allow to make decisions about the theoretical predictions. The *pn* collisions, that can improve our current knowledge, will be explored using a deuteron beam and detecting the spectator via a forward angle detector.

As for the Δ baryon, until now the Dalitz decay has not been experimentally explored, except for the DLS data at energies below the η production threshold $E_{pp} <$ 1.27 GeV [Wil98]; in order to learn more about it, an exclusive study of pp→pΔ$^+$→ppe$^+$e$^-$ will be performed.

At a beam energy of 3.5GeV vector mesons, such as ρ and ω, can be produced with large cross sections, and can be efficiently identified by the HADES spectrometer. This is very important because it will be possible to check the invariant mass resolution and the reconstruction capability of the spectrometer, before any considerations about in-medium effects in heavy ion collisions could be done; moreover, the identification of the ω peak can be used as a reference point to further pA collisions, where in-medium modifications are theoretically predicted.

The analysis of the p+p at 2.2 GeV experiment performed in January 2004 will be presented in this work.

3 THE HADES SPECTROMETER

Figure 3.1 – Back view of the HADES spectrometer.

3.1 Overview

The HADES spectrometer (Figure 3.1) is installed at GSI laboratory (Darmstadt, Germany), and it was designed in order to be best suited for the identification and invariant mass reconstruction of electron-positron pairs, coming from the decay of mesons in p, π and heavy ion induced collisions at SIS synchrotron energies (few GeV per nucleons).

The probability to produce a lepton pair coming from the decay of a vector meson is rather low; indeed the branching ratio of the dilepton channel is about 10^{-5}. As a consequence, in order to accumulate significant statistic in a reasonable amount of time the spectrometer has to fulfil several requirements:

- *Large acceptance*: to maximize the number of detected pairs once they are produced. The HADES acceptance is $\varepsilon_{pair} \approx 40\%$;
- *High count rates*: considering the rarity of the interesting channels it is mandatory to operate with high intensity beams. The main goal is to run experiments with beam intensity around 10^8 particles per second;
- *Electron trigger system*: most of the reactions are characterized by the production of only hadrons, which keep the data acquisition busy with events uninteresting for the physics purpose of the experiment; a fast electron trigger allows to reject on-line these uninteresting events, in order to save disk space and to reduce the amount of raw data by 1-2 orders of magnitude;
- *High identification efficiency for lepton pairs*, and a good discrimination between hadrons and leptons, to perform the analysis in the correct way ;
- *High lepton pair mass resolution*: an invariant mass resolution for dileptons of about 1% is required in order to distinguish the width of ω meson (8 MeV/c^2 for a mass value of about 780 MeV/c^2), and this value calls for a momentum resolution of 1% to 1.5%;
- *High granularity*: the need to measure heavy systems imposes a high granularity, which allows to deal with collisions where there is a large number of outgoing particles (such as in Au + Au) by decreasing the probability to have double hits in the same pad.

The geometry of the spectrometer is divided azimuthally into six identical sectors, each one covering a polar angle region between 18° and 88°, and almost the full azimuthal angle (apart from inefficiency in between neighbour sectors); in this way the acceptance for dilepton pairs corresponds to about 40% [Sch96] in the mid rapidity region.

The spectrometer is divided into several sub-detectors; the detector systems are, from inner to outer:

- **START-VETO** detectors, capable of providing a signal when there is a reaction in the target and the start to time-of-flight measures (for the proton beams it was not possible to use them, as explained in the following chapters).
- A Ring Imaging Cherenkov (**RICH**) threshold detector, placed around the target region; it provides lepton identification, being substantially insensitive to fast hadrons (pions up to about 3 GeV).
- A tracking systems constituted by a superconductive toroidal magnet and a set of four planes of Mini Drift Chambers (**MDC**). The chambers provide the position and the direction of the charged particles which cross them, before and after the region of magnetic field. From the deviation of the trajectories inside the field it is possible to determine the momentum of each particle; the magnet provides the momentum kick necessary to obtain charged particle momenta with a resolution of about 1%.
- A second system of lepton identification placed in the outer part of the spectrometer, called **META** (Multiplicity Electron Trigger Array), formed by:
  - A time-of-flight wall (**TOF**), made by several thin scintillator rods, to distinguish leptons from hadrons by a time measurement. The TOF detector covers a region between 45° and 88° of polar angle, while the region between 18° and 45° is currently covered by a system made by scintillator rods of lower granularity and worse resolution (**TOFINO**); in the near future it is foreseen to replace it with a Resistive Plate Chamber detector system (**RPC**).
  - In the lower polar angle region the higher momentum of particles reduces the effectiveness of the lepton identification by time-of-flight measurements. In

order to improve the lepton/hadron discrimination a detector for electromagnetic showers (**SHOWER**) is used.

- A sophisticate **TRIGGER** system, to reduce the number of uninteresting events acquired, and therefore to decrease the amount of data to be stored.

Figure 3.2 shows a schematic view of the whole spectrometer divided into its sub-detectors. The beam is represented by the green line and it comes from the lower left direction. The spectrometer has a diameter of about 6 meters.

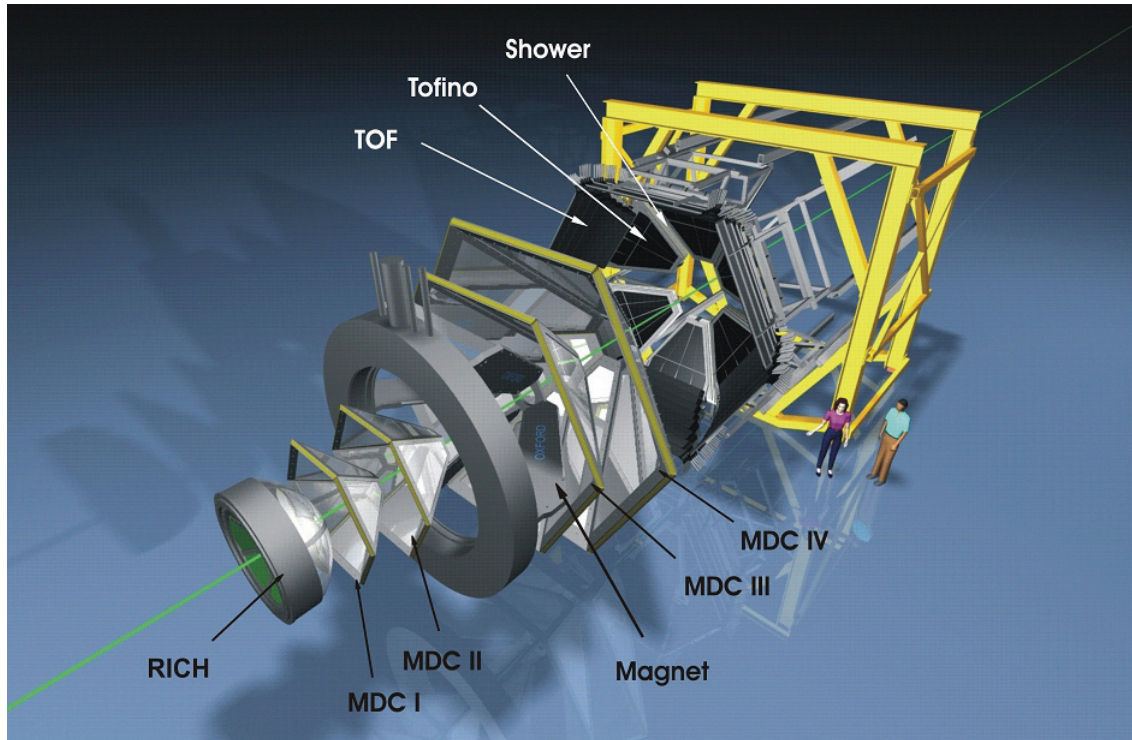The following chapters will explain each sub-detector system with more details.

Figure 3.2 – Schematic view of the HADES spectrometer, with all the sub-detectors in evidence.

3.2 The accelerator

The accelerator machine providing the beam for HADES is located at the GSI Institute in Darmstadt, Germany.

The accelerator complex consists of 4 major structures: a linear accelerator (UNILAC) injecting ions into a 60 meter diameter Synchrotron (SIS). From there the beam can be extracted to the FRagment Separator (FRS), to the Electron Storage Rings (ESR) or the experimental areas (Figure 3.3).

The UNILAC was constructed in 1975 as a Wideroe-Alvarez linear accelerator, and was recently upgraded (in 1999) to become a high current injector for the Sis. The new High Current Injector (HSI) provides an increase in the beam intensities, filling the synchrotron up to its space charge limit for all ions. Two ion sources feed the HSI; after stripping and charge state separation, the beam from the HSI is matched to the Alvarez accelerator, which accelerates the highly space charge dominated ion beams without any significant particle loss, up to a few AMeV.

The SIS is a synchrotron with a circumference of 216 meters, consisting of 24 curvature magnets and 36 magnetic lenses. Before entering the SIS, ions from the UNILAC interact with a carbon foil achieving ionisation states up to 72+ for Uranium. In those cases SIS allows energies up to 1GeV per nucleon, while for light systems (like Neon) it is possible to achieve full ionisation and consequently increase the energy up to 2 GeV per nucleon.

The acceleration takes place in two resonance cavities diametrically opposed, where ions see a potential of 15 kV. The operation frequency ranges from 800KHz to 5.6MHz. The vacuum in the beam line is lower than 10^{-11} Torr. The cycle length is selectable between 1 to 10 seconds, with around 10^8 ions per cycle.
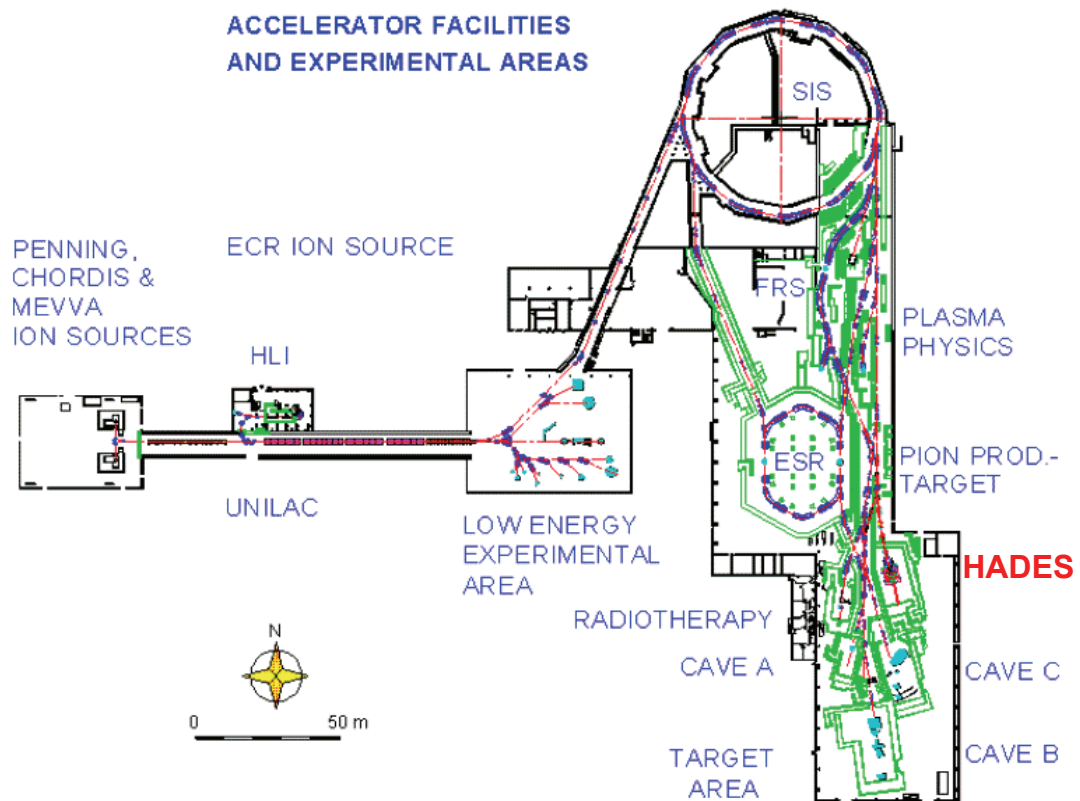
Figure 3.3 – GSI accelerator facility. From the left to the right: the ion sources, the UNILAC, the SIS and the experimental areas.

3.3 START-VETO detectors

A START-VETO system is needed to provide a fast signal when a reaction takes place, and to give the start to time-of-flight measurements.

The system is constituted by two identical detectors in anti-coincidence placed along the beam line, one before (START) and one after (VETO) the target. When a particle of the beam crosses the target without interacting with it, the particle provides a signal in both detectors; in this case the event is discarded. When an interaction occurs inside the target, the particle produces a signal in the START but not in the VETO; in this case the signal is sent to the trigger system, and it starts the time-of-flight measurement of TDCs.

These detectors should be resistant to high radiation damage, considering the high particle intensity of GSI synchrotron (even 10^8 particles per seconds). They should provide fast signals with a high time resolution, and should be thin enough in order not to alter the properties of the beam itself.

For these purposes two different kinds of detectors were used, one for the carbon beams one for the proton ones, according to the different properties of the beams. The proton detector was used only for the commissioning run, because of several problems which showed up during the proton commissioning beam time.

3.3.1 Carbon beams: Diamond detector

For the carbon experiments it was decided to use CVD diamond detectors [Ber98] for their radiation tolerance, their capacity to operate at high count rates and for their fast signal and good time resolution.

The START-VETO system consists of two CVD diamond detectors placed 75cm downstream and 75cm upstream of the target. Each detector (Figure 3.4) has an octagonal shape and is divided into eight strips. The strip width is optimised such that a coincidence of one START detector strip with three VETO detector strips provides a veto efficiency of about 96.5%. The detectors thickness is 100μm, small enough to keep multiple scattering and secondary reactions very low.

By analysing the data of the November 2002 run (C+C at 2.2AGeV), a time resolution of about 92ps [Spa02] was evaluated.
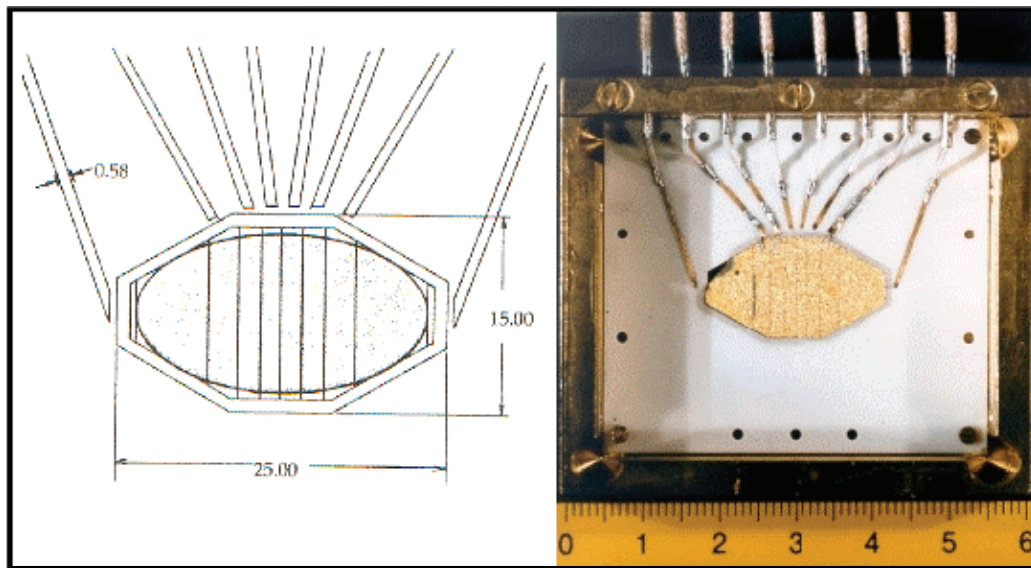
Figure 3.4 The START detector for C+C experiments (on the right) and its technical drawing (on the left). All the distances are expressed in millimetres.

3.3.2 Proton beams: Hodoscopes

The diamond detectors cannot be used under proton beams, because the energy loss inside the START material is so small that it does not produce a useful signal.

Therefore for the proton experiment it was decided to use a pair of hodoscope detectors, made of scintillating rods. Each hodoscope is constituted by 16 rods of Bicron BC408, each one 1cm wide and 12 cm long; each end of the rod is read out by a photomultiplier (see Figure 3.5).

The detectors were placed 2.5 m upstream of the target (START), and 2.7 m downstream (VETO). From the coincidence of left and right signals the START trigger signal was generated, which was put in anti-coincidence with the VETO signal to select only events when a reaction occurred. The START signal was also used to start the time-of-flight measurement in the TDCs.

The hodoscopes were used only during the September 2003 commissioning beam time, and a time resolution of almost 230 ps was estimated. It was found that with the presence of hodoscopes the number of secondaries produced by the interaction of the proton beam with the detectors was too high to have a proper data acquisition: these secondary particles triggered too many spurious events, so for the January 2004 experiment it was decided to not use any start detector.
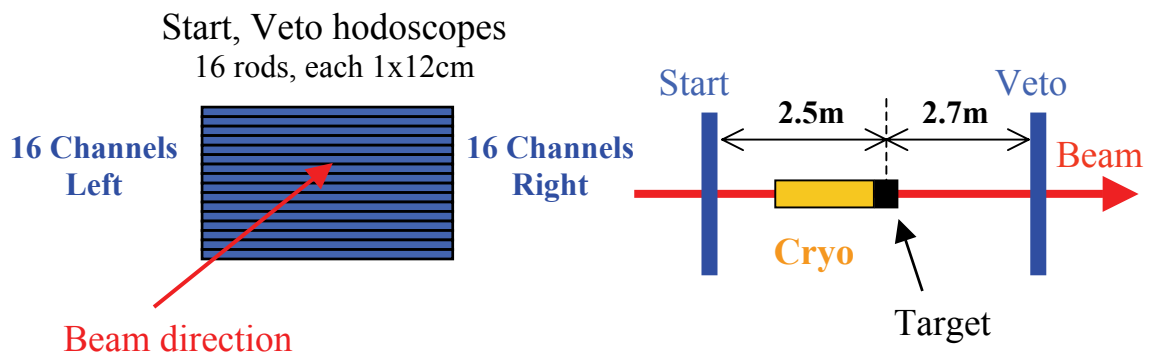

Figure 3.5 – Schematic view of the START-VETO system for p+p experiment.

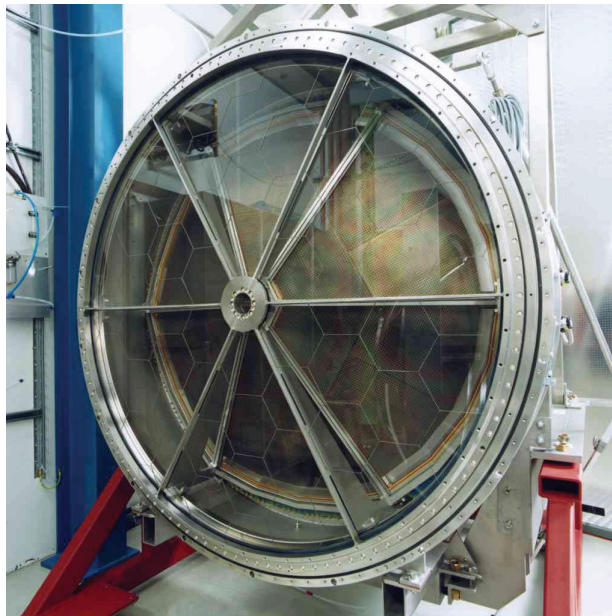## 3.4 The Ring Imaging Cherenkov detector

Figure 3.6 – The RICH detector

The Ring Imaging Cherenkov detector [Zei99] (Figure 3.6) has been built to identify online e$^+$ e$^-$ pairs emitted in nuclear collisions.

Cherenkov detectors are able to identify particles on the basis of their velocity. When a charged particle crosses a dielectric medium it generates a time-dependent electric field around its trajectory, leading to a variable polarization in the particle neighbourhood. If the particle is faster than the speed of light in the medium ($c' = c/n$, where n is the medium refraction index), the produced wavefronts will generate constructive interference, and a cone of light will be emitted around particle trajectory. This principle is called Cherenkov effect [Che37].

The opening angle between the emitted cone of light and the particle direction is given by:

$$\cos\theta_c = \frac{1}{n\beta}, \quad \beta = \sqrt{1 - \frac{1}{\gamma^2}}, \qquad \textbf{(Eq. 3-1)}$$

where θ_c is the opening angle, n the refraction index, β and γ respectively the velocity and the Lorentz factor of the particle.

In order to produce Cherenkov effect the main requirement is that the particle must exceed the speed of light in the medium. In the energy range of the experiment (1-2 AGeV), electrons by meson decays are very fast and they travel close to the speed of light (β ~ 1), while most hadrons have much lower velocity. By choosing a dielectric medium with an appropriate refraction index, the Cherenkov effect becomes a good tools to discriminate leptons from hadrons.
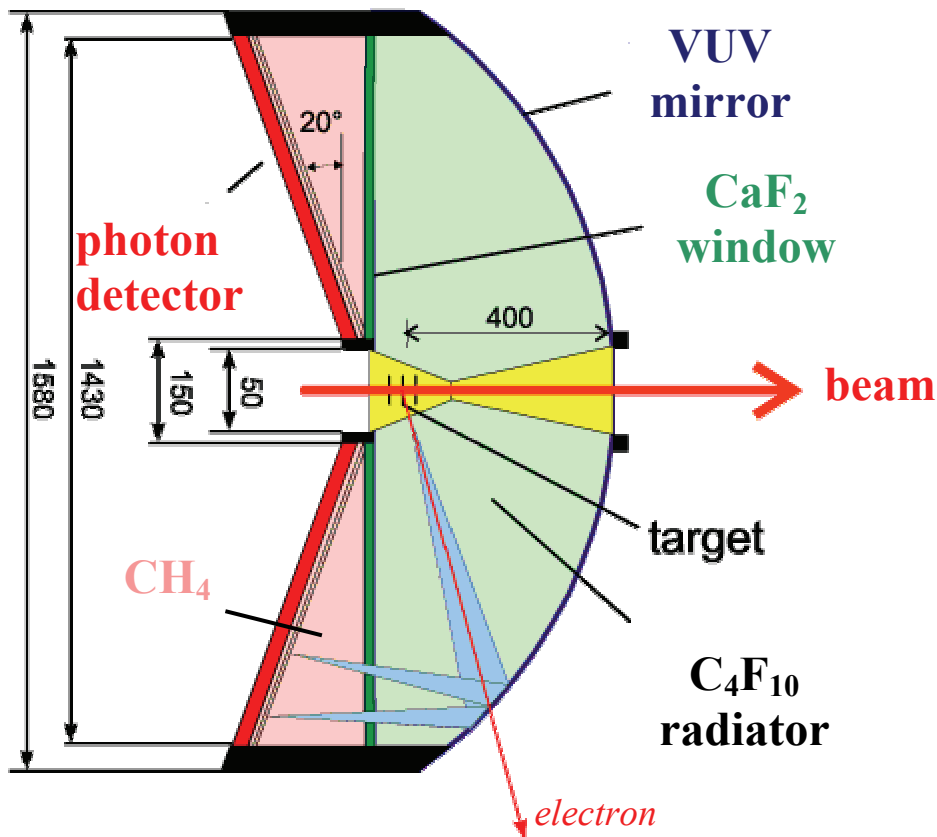

Figure 3.7 – Schematic view of the RICH detector and its components.

HADES's RICH (Figure 3.7) consists of a gaseous radiator of C_4F_{10} placed around the interaction region, and outside the magnetic field; its refraction index is

1.00151 and the corresponding Cherenkov threshold is $\gamma_{th} \sim 18.2$. While electrons need an energy of only 9 MeV to produce Cherenkov light, much below the energies we want to study, the energy thresholds for protons and pions are respectively 17 GeV and 2.5 GeV, far from the range of energies which are involved in the collisions.

The cones of light have an opening angle of about $\theta_c \sim 3.18°$; the photons are mostly produced at ultra-violet frequencies, so the radiator has to be transparent to those wavelengths. Light is reflected to a photon detector by a special spherical mirror, which must have good properties at VUV frequencies and large radiation length, to minimize multiple scattering and production of secondary photons.

The ceramic carbon mirror (SIGRADUR G) is spherical, has a diameter of 145 cm and a curvature of 871mm; its radiation length is $X_0 = 25$ cm and its thickness 2 mm. Due to its large size, the mirror is segmented into 18 wedges, three per each HADES sector; it is covered by a layer of Al and a layer of MgF_2, to reduce oxidation effects. The average reflectivity on the frequency range of interest is about 80%.

Photons reflected by the mirror cross a window of CaF_2, which separates the radiator from the photon detector and has a high transmission in the UV range of interest ($T \sim 70\%$).
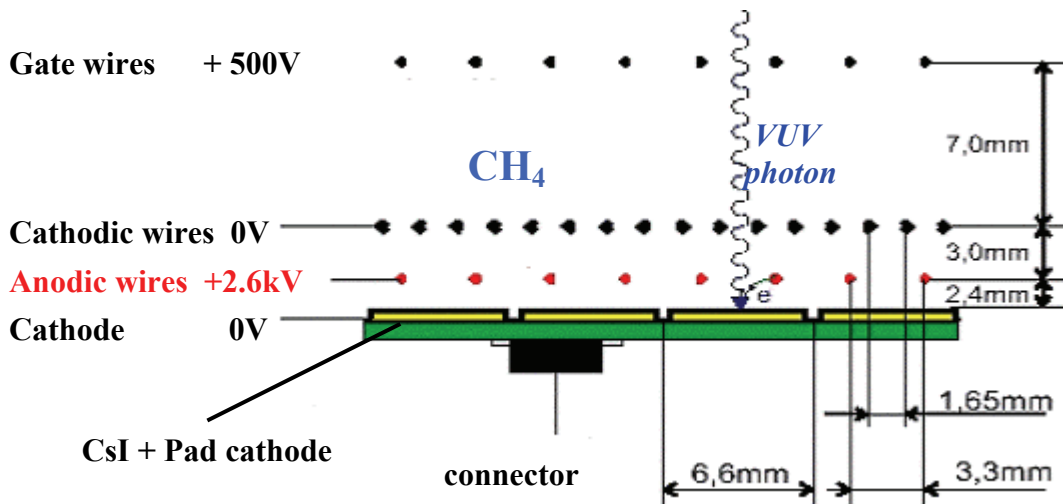

Figure 3.8 – Schematic view of the photon detector, constituted by multi-wire proportional chambers (MWPC), coupled to cathodic pads covered by CsI (for the photo-conversion).

The photon detector (Figure 3.8) covers the whole reflection plane of the mirror, and it is able to detect single photons providing an information about position. The detection/acquisition system must be very fast, in order to provide a logic signal for the 2nd level trigger, and to make the data acquisition start under the condition that a lepton pair is present inside the event. It is constituted by six Multi Wire Proportional Chambers (MWPC) which follow the hexagonal geometry of the spectrometer; they are filled with pure methane (CH_4), and each one is coupled to a cathodic plane, coated with a layer of CsI.

When a photon reaches a pad plane, there is a certain probability that a photo-electron is ejected, given by the quantum efficiency of the CsI layer.

The emitted photoelectron drifts from the cathodic plane toward the anodic wires, and it generates an avalanche; the produced ions drift back to the cathodic plane and induce a mirror charge on the cathode, which is connected to a preamplifier that senses the pulse height of the charge deposited on it.

The photon detector is tilted with respect to the beam direction, in order to be shielded from the large number of particles which are emitted during the reactions. The shape of each pad is variable in order to get rid of the different eccentricity of the rings at different polar angles.
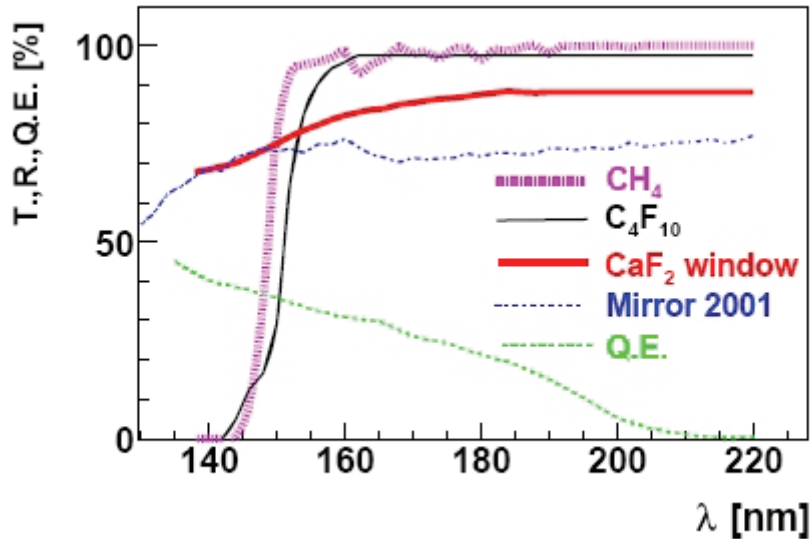

Figure 3.9 – Optical parameters of the different RICH detector components. The different curves show: the transmission of the radiator gas (C_4F_{10}), of the CaF_2 window and of the detector gas CH_4, the mirror reflectivity measured in 2001 (Mirror 2001) and the CsI photocathode quantum efficiency (Q.E.).

Figure 3.9 shows the optical response of all the RICH detector components as a function of the photon wavelength. The single lepton efficiency is limited at the longer wavelengths by the CsI quantum efficiency.

All the signals coming from the photocathodes are handled by special algorithms in order to identify a ring shape, and thus to find lepton candidates.

3.5   The tracking system

In order to achieve an invariant mass resolution of 1% in the ω meson region, it is mandatory to reconstruct tracks with a resolution in momentum of the order of 1% for electrons with momenta larger than 100 MeV/c. For this purpose HADES has a magnetic spectrometer, consisting of a superconductive toroidal magnet and 24 multi-wire drift chambers in six sectors.

The Iron-Less Superconductive Electromagnet [Bre99] (ILSE) consists of 6 superconducting coils, producing an inhomogeneous magnetic field which reaches a maximum value of 3.2 T inside the coils, and a maximum field of 0.7 T within the acceptance region; at maximum field value the momentum kick ranges between 40 and 120 MeV/c. In the region where RICH and time-of-flight detectors are placed the field is below $5 \cdot 10^{-3}$ T, so it does not harm their measurements.
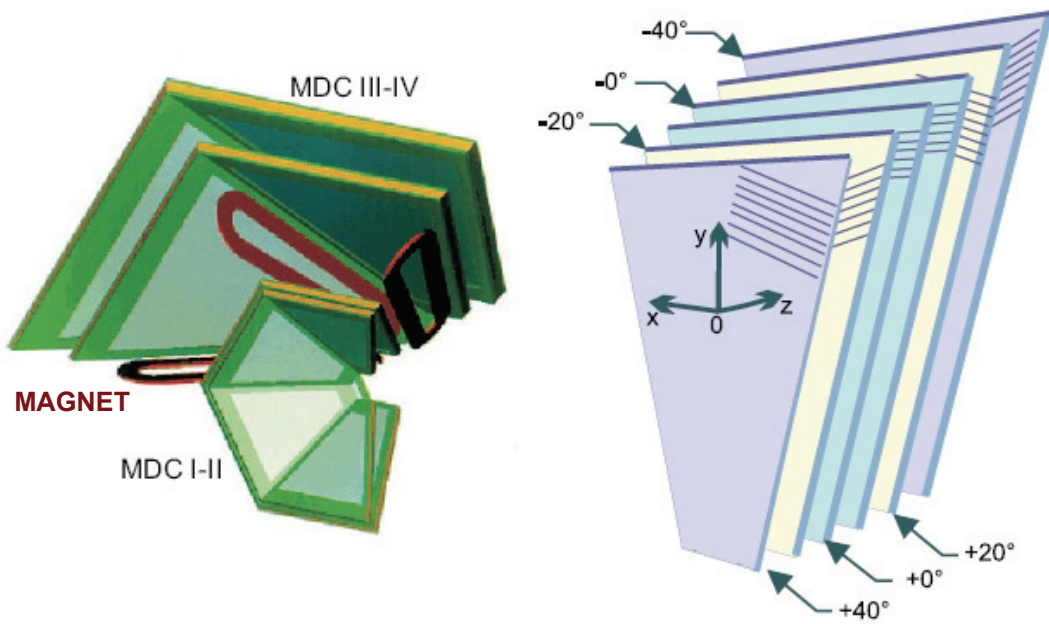
Figure 3.10 – Left side: sketch of MDC tracking system; MDC I-II are placed in the region between the target and the magnetic field, while MDC III-IV stay in the outer region. Right side: orientation of the 6 anodic wire layers inside each chamber plane.

The tracking is performed by a set of four Multi-wire Drift Chambers (MDCs) planes [Mün04], two of them placed in the region between the target and the magnet, and the other two in the outer region; each plane is divided into six sectors according to the hexagonal geometry of the spectrometer, and the chamber frames fall in the shadow region defined by the magnet's coils, in order not to further reduce the acceptance (see Figure 3.10 – left side). By measuring the deflection of the particle trajectory before and after the magnetic field it is possible to evaluate the particle momentum.

Each chamber is constituted by six layers of anodic wires; each plane is tilted of a different angular value (from the inner layer to the outer: +40° –20° +0° -0° +20° -40°) in order to have a better resolution on the polar angle with respect to the azimuthal one (see Figure 3.10 – right side).

The space between anodic and cathodic wires defines a drift cell (Figure 3.11 – left side); each particle, while crossing these cells, ionises the gas (a mixture of helium-isobutane 60:40) producing electrons and positive ions along its trajectory. The electronic cloud will induce a signal into anodic wires, after a time proportional to the distance from the wire; the signal provides the STOP to a time measurement on both wire edges, while the START is provided by the reaction trigger opportunely delayed.

For each hit wire the corresponding drift times are converted into the minimal distance of the particle trajectory from the wire; by combining the information of the six layers it is possible to have not only the *hit* position in local coordinates, but also the particle direction.

The right side of Figure 3.11 shows an example of event seen by one MDC chamber; the lines represent the anodic wires which were hit, while the circles are the recognized hits.

The high granularity (total of 26300 cells in all the chambers) and the good time resolution (few nanoseconds) allow to operate at high count rates, and to obtain a position resolution figure between 100 and 130 μm.

By correlating *hits* belonging to different chambers of the same sector, before and after the magnetic field region, the full *track* of the particle is reconstructed, and the particle momentum can be calculated by using different tracking algorithms (see next chapter).
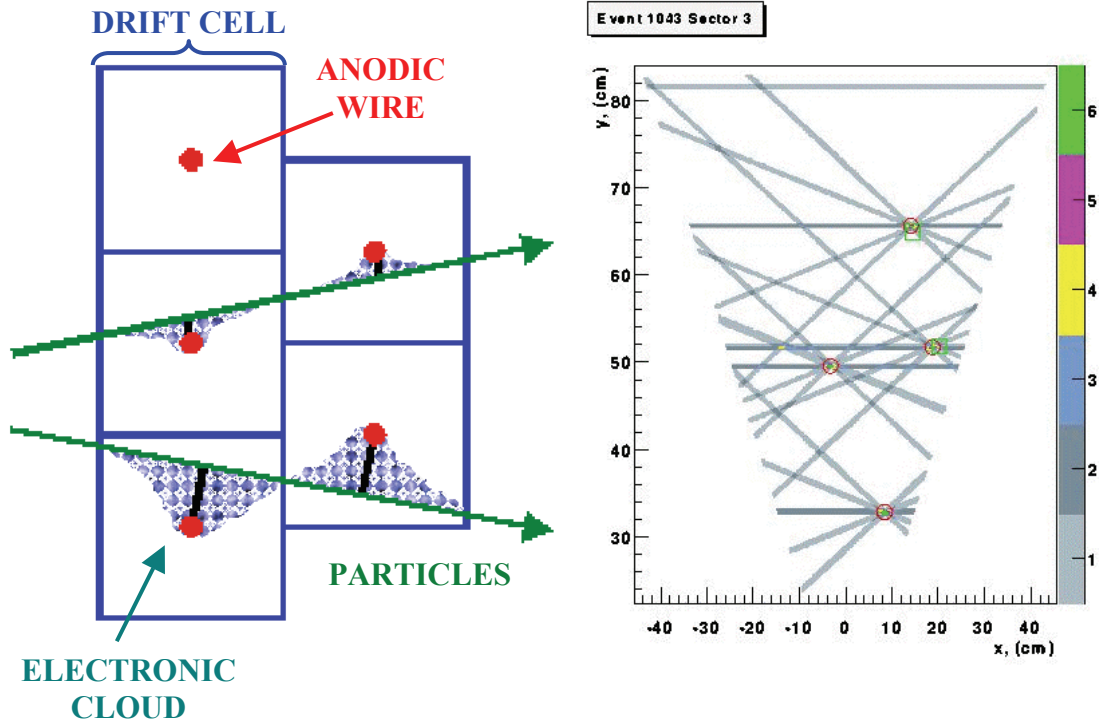
Figure 3.11 – Left side: scheme of trajectory reconstruction inside drift cells. Right side: example of MDC event; lines represent the anodic wires which produced a signal, while circles correspond to reconstructed hits by the tracking software.

3.6   META detectors

3.6.1   The TOF detector

The time-of-flight (TOF) wall [Ago02], shown in Figure 3.12, is meant to three main purposes:

- Fast determination of the charged particle multiplicity of the event, in order to select central collisions and to provide a first level trigger to the data readout electronics.
- Fast tracking, by determining the impact position of each hitting particle, in order to allow a fast second level trigger decision about the event.
- Measurement of the time-of-flight of each hitting particle in order to separate electrons and positrons from more massive particles, like protons and pions, and to perform particle identification.
- Measurement of the energy loss of the particle, which can also be used for particle identification.

The TOF wall is based on a scintillator rod element structure. Each rod, being read out at its ends by photomultipliers (PMT), when hit by a particle provides two

signals, each one further split into two, that are suitably handled and then converted into numbers. By combining this information one can extract time-of-flight, hit position and deposited energy.
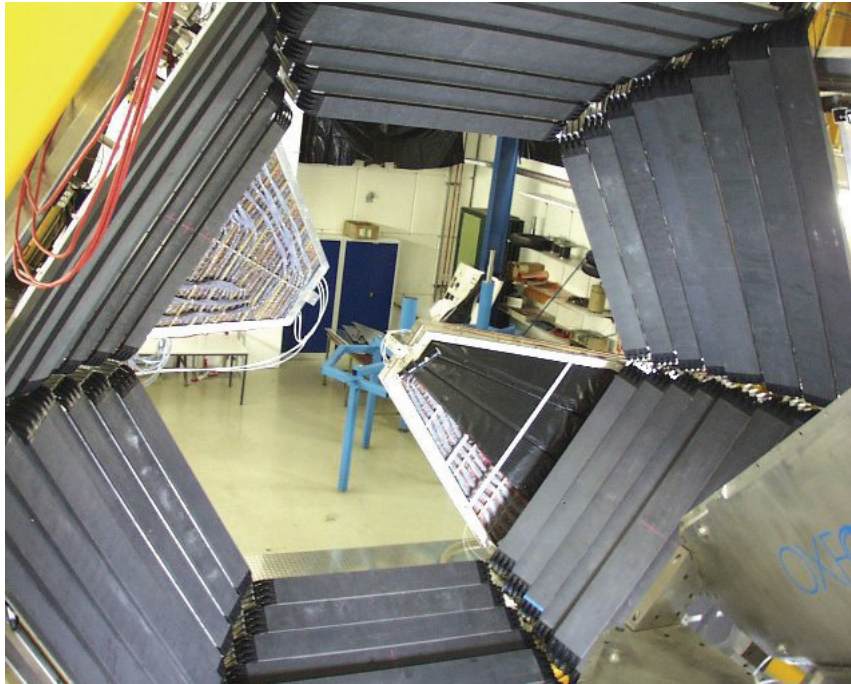

Figure 3.12 – The TOF detector.

The TOF detector follows the hexagonal geometry of the whole spectrometer, and it covers the polar angle region between 44° and 88°. It is divided into six sectors, each sector is divided into eight modules and each module, enclosed in a special carbon-fibre case, is composed by a set of eight scintillator rods (a total of 384 rods).

The rod length increases while ranging from smaller to larger polar angles. The cross-section is square, 20×20 mm^2 for the innermost 192 rods (32 per sector), 30×30 mm^2 for the outermost 192. This geometry allows to have a finer granularity in the forward angle region, where the multiplicity of produced charged particles is higher, to reduce the probability that two particles emitted in the same collision hit the same rod, giving rise to a wrong physical information.

Each rod is made of BC408 plastic scintillator from Bicron, mainly due to its good attenuation length (3.8 m in bulk) combined with high scintillation efficiency (about 10^4 photon/MeV) and speed (2.1 ns decay time). The overall length is 200 mm for the 30×30 mm^2 cross-section, and 100 mm for the 20×20 mm^2 one. Each rod end has been glued to a light guide, bent of 65°-67° with respect to the rod itself, and coupled to a photomultiplier by means of a thin silicon disc of high optical quality. The rods, along with light guides, have been wrapped one by one in aluminised mylar sheets, in order to optimise the optical properties of their surfaces.

All the sectors are equipped with 9133B photomultipliers from Electron Tube Limited; each one provides two signals, one from the last dynode for the amplitude measurement, one from the anode for timing[1]. Timing is measured by an electronic chain which includes a constant fraction discriminator (CFD), followed by a logic

---

[1] Before September 2003 run one sector was equipped with FEU115 photomultipliers of Russian production, which provided only the timing signal.

active delay (LAD) and then by a time to digital converter (TDC). The amplitude signal measurement is performed by an electronic chain made of a shaper and an amplitude to digital converter. Figure 3.13 shows the electronic chain flowchart of one channel.

The signal from the discriminator is split into two paths and it reaches also the 1st level trigger electronic chain; by performing an analog sum of all the digital signals it is possible to evaluate the hit multiplicity of the collision, and so to select its centrality. The multiplicity signal is combined with the one from START detector (if present), to provide the START to the time-of-flight measurement.
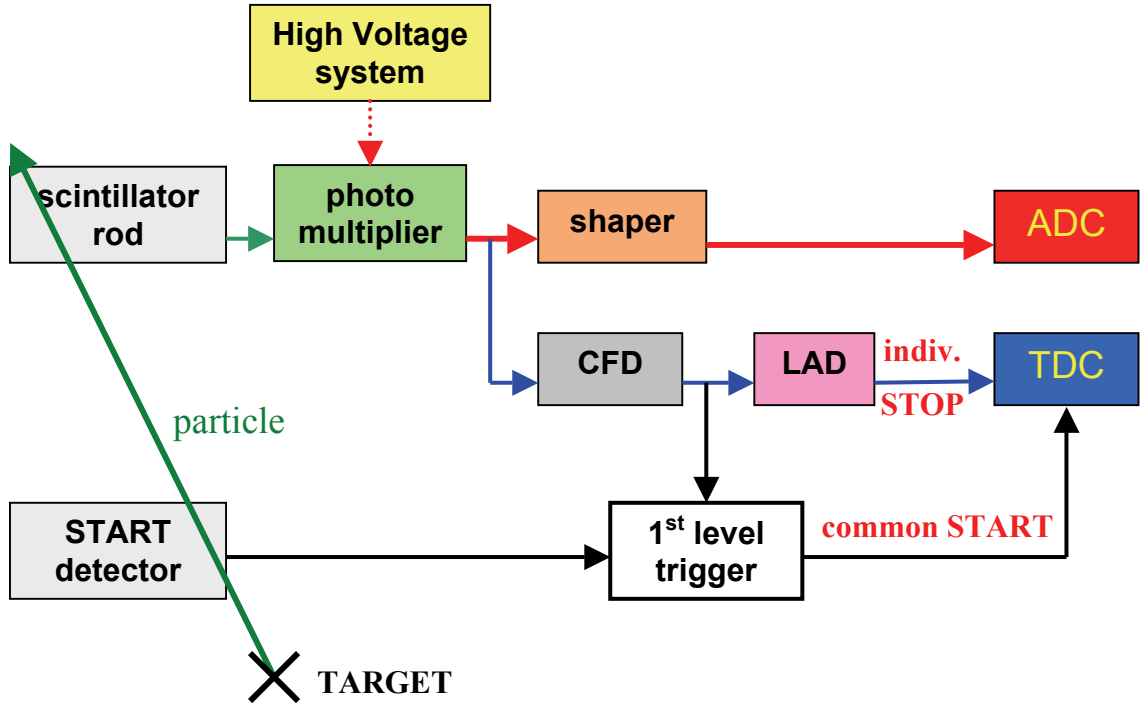
Figure 3.13 – Schematic view of TOF electronic chain.

The time of flight *t* of a particle with momentum *p* and mass *m* is given by the relation:

$$t = \frac{L}{\beta c} = \frac{L}{c}\sqrt{1+\left(\frac{mc}{p}\right)^2}$$

(Eq. 3-2)

where *L* is the path length of the trajectory and *c* is the speed of light. The identification, for particles with the same momentum and different masses m_1 and m_2, is based on their different time of flight:

$$\delta t_{12} = \frac{L}{c}\left[\sqrt{1+\left(\frac{m_1 c}{p}\right)^2} - \sqrt{1+\left(\frac{m_2 c}{p}\right)^2}\right]$$

(Eq. 3-3)

If σ is the standard deviation, we can separate particle species at 95% confidence level when $\delta t_{12} \geq 4\sigma$. By obtaining the δt_{12} distributions for cases of p/e and π/e discrimination, and calculating the value of hadron contribution into the $\delta t \leq 2\sigma$

region, the number of fake electrons was estimated as a function of timing resolution (see Figure 3.14) for Au+Au collisions at 1 AGeV.

In the C+C run of November 2002, by analysing experimental data, it was estimated that TOF detector achieved the design performance, showing a time resolution below 150 ps, and a corresponding spatial resolution of about 2 cm.
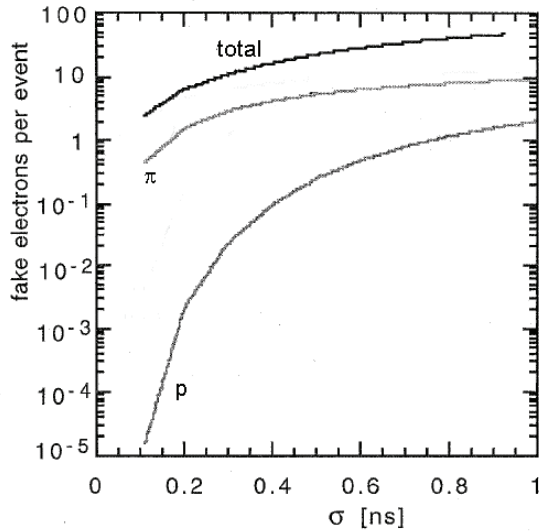
Figure 3.14 – Expected number of fake electrons per event in Au+Au collisions at 1 AGeV. The separate contributions from protons and pions are shown.

3.6.2 The TOFINO detector

For time-of-flight measurements the region of polar angle below 45° is currently covered by a low granularity system called TOFINO (Figure 3.15).
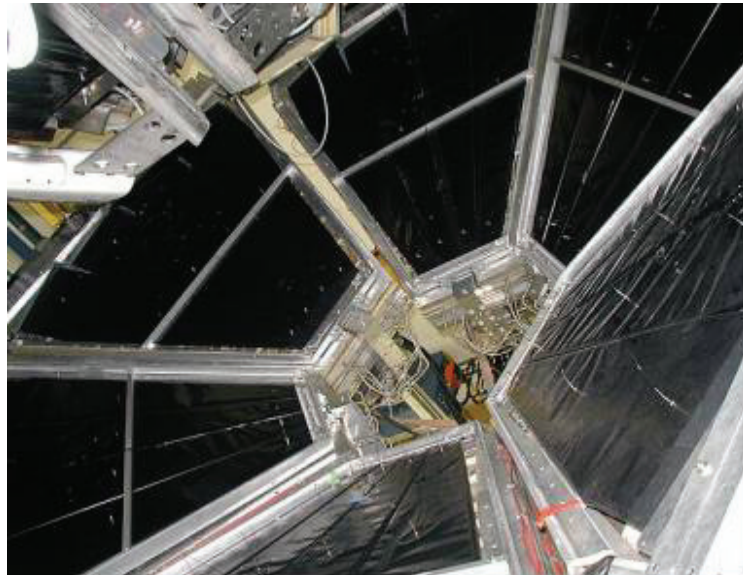
Figure 3.15 – The TOFINO detector.

It is divided into six sectors, and each sector is made by four BC408 scintillator pads , arranged radially with respect to the beam axis.

The basic principle is the same of TOF detector: a particle which hits a rod loses energy, and the energy is converted into a light signal. The signal reaches the pad edge

and is converted into an electronic signal by a photomultiplier. In this case only one edge is coupled to a photomultiplier, so there is no information about the hit position. The achieved time resolution is about 500 ps.

The replacement of the TOFINO detector by a Resistive Plate Chamber (RPC) wall [Alv04] is foreseen in the near future. The new detector will provide the granularity needed to deal with the higher particle multiplicities expected in the heavier ion collisions, thus decreasing the probability of double hits in each pad.

3.6.3 The Pre-Shower detector

At low polar angles ($\theta < 45°$) the separation of electrons from protons by time-of-flight measurements is more difficult, due to higher hadron momenta. In particular in this angular region the contamination of high momentum pions mistakingly recognized as electron becomes not negligible. For this reason an additional electron/hadron separation method was chosen: an electromagnetic shower measurement in the Pre-Shower detector.
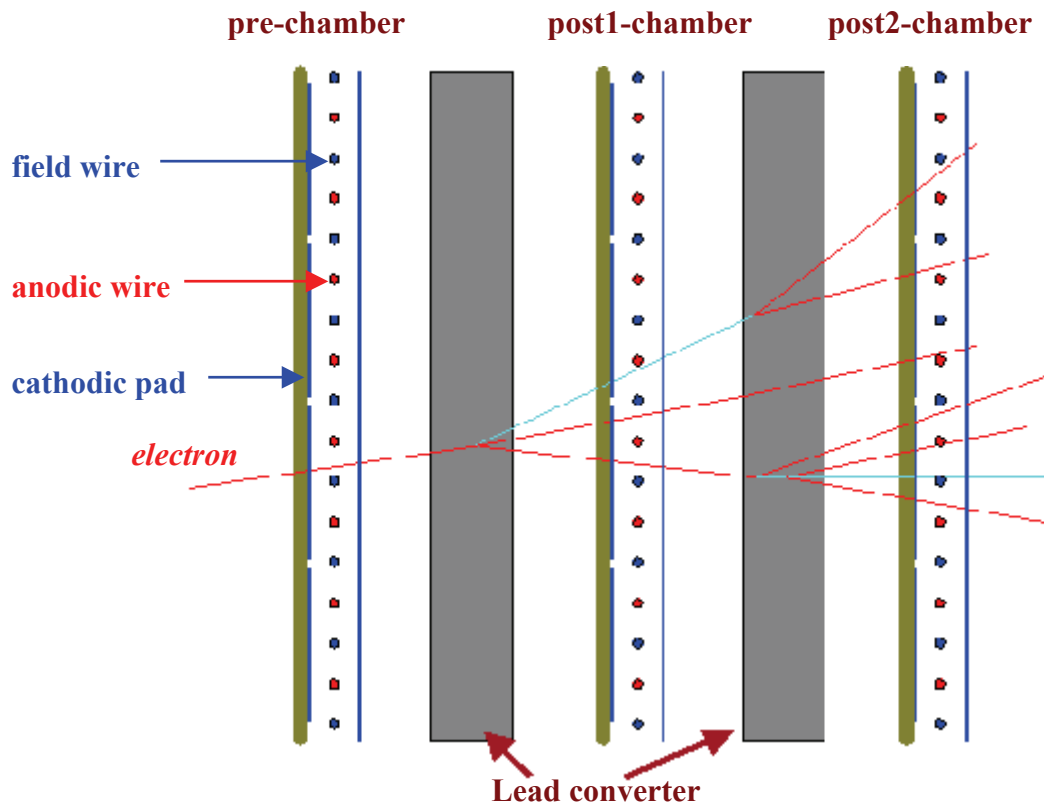
Figure 3.16 – Scheme of Pre-Shower detector, with an example of electromagnetic shower.

The Pre-Shower detector [Bal04] consists of a stack of three trapezoidal wire chambers (pre-chamber, post1-chamber, post2-chamber), separated by two lead converter plates. Each cathode plane is subdivided into individual pads where the induced charge signal is taken from. A charged particle passing through the gas chambers produces an ionisation avalanche, with electrons drifting towards the closest anode wire; the cloud motion induces a positive charge on the nearby cathode pads, connected to charge-sensitive preamplifiers. The integrated charge is proportional to the

avalanche charge, and an integration over several pads around the pad with the highest charge value (local maximum) has to be performed, in order to obtain the complete charge of the electromagnetic shower. By comparing the integrated charge of the same track in different layers it is possible to distinguish electromagnetic showers from hadronic tracks.

The wire chambers are filled with an isobuthane-based gas and they are operated in the self-quenching streamer mode (SQS); in this way the avalanche charge does not depend on the particle energy loss but it is only proportional to the number of particles crossing the chambers[2].

3.7 *The Trigger system*

The main aim of the HADES spectrometer is to measure dileptons coming from rare vector meson decays, which have very low branching ratios (10^{-5} - 10^{-6}). To perform this kind of study high intensity beams are needed, and even a good on-line selection trigger which allows to acquire only interesting events and reject the others.

The beam intensity for HADES operation is about 10^8 particles per second, which are reduced to 10^6 collision events per second because of the 1% interaction length target. The number of events is still too high to be recorded, therefore a three level trigger was designed capable of selecting events containing lepton pairs, that can be stored to disk at a suitable rate.

While the first two levels are operational and working, the 3rd level trigger is still under development.

Figure 3.17 shows an overview of the whole trigger system.

3.7.1 *1st level trigger*

The first level trigger (LVL1) consists on a fast hardware selection of central collisions, by measuring the hit multiplicity in META system.

In heavy ion collisions higher nuclear densities are reached by central collisions, where the number of emitted particles is rather high. By putting a lower threshold on the particle multiplicity it is possible to perform a selection on impact parameter, and so on the centrality of collisions. It was estimated that this kind of selection, linked to the START-VETO anti-coincidence, reduces the number of triggered events of about a factor 10.

In elementary reactions, such as proton-proton collisions, it is possible to apply multiplicity selections in TOF and TOFINO separately and sectorwise, in order to select only interesting decay channels.

3.7.2 *2nd level trigger*

The second level trigger (LVL2) [Tra00] is based on the search for lepton candidates in the event. To perform this kind of selection only the RICH, TOF and SHOWER information is used, keeping the rest of the data in intermediate First-In-First-Out (FIFO) memories until a decision is taken.

---

[2] In the studied collisions protons are emitted even with not minimum ionising energies, so with higher energy losses and they could be misidentified as electrons. The SQS mode and a selection on time-of-flight using TOFINO information allow to strongly reduce their contamination.

The lvl2 trigger analysis can be divided in two steps. On the first step the information from detectors is sent to Image Processing Units (IPUs), ad hoc processors which search for electron signatures in their respective detectors. These are ring images in RICH pad planes, clusters with an electromagnetic shower signature in Shower, and hits with the appropriate time-of-flight in the TOF detector. In the second step the Matching Unit (MU) correlates in angle the position of these candidates in RICH and META detectors, taking into account the trajectory bending due to the magnetic field.

This trigger system currently enables a data reduction by a factor 10 [Toi03]. If the selection is done on candidate pairs of opposite charge, with a minimum opening angle of 20°, the reduction factor should go up to 100, reducing the acquisition rate to 10^3 events per second.

3.7.3 3rd level trigger

The third level trigger (LVL3) performs a consistency check of the electron candidates determined by the second level trigger, by evaluating the hit pattern of the wires from MDC modules. It gains another reduction factor of 10 that brings the final event rate to the order of 100 Hz.
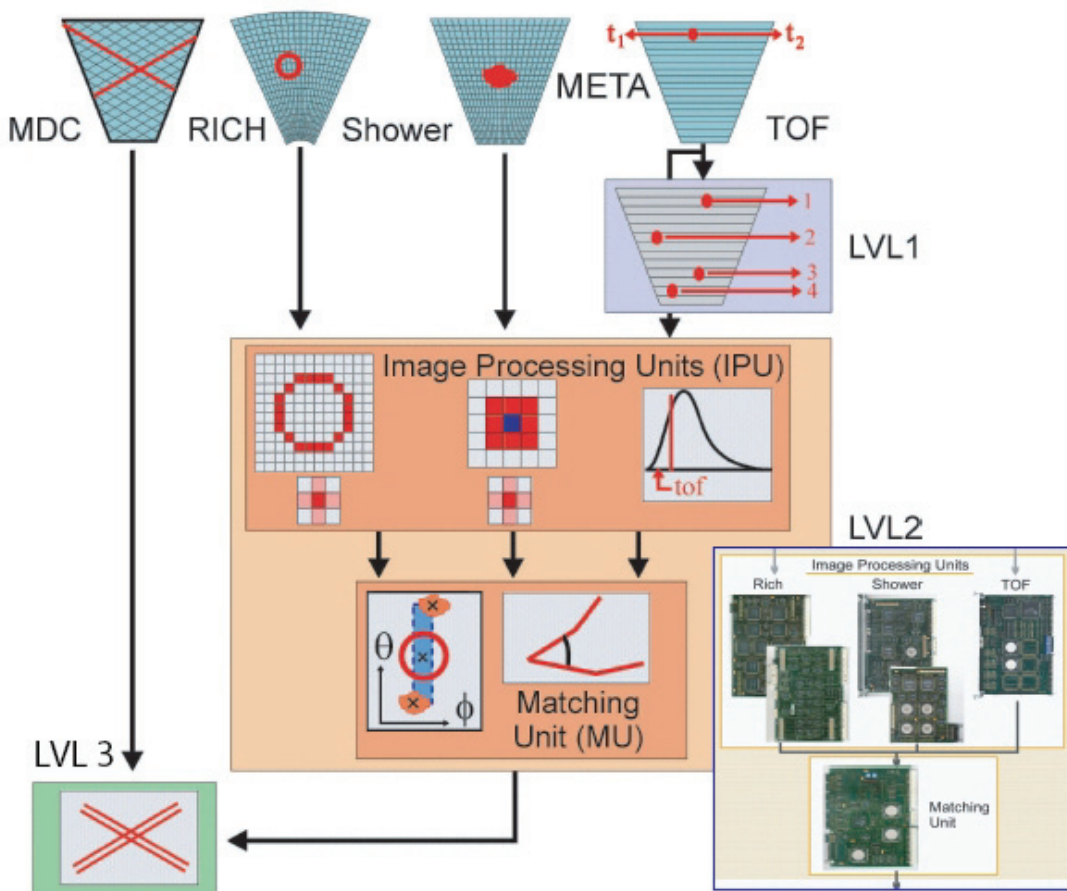

Figure 3.17 – Overview of the HADES trigger system.

3.8   Experimental runs

The physical activity of the HADES spectrometer started on November 2001, with a commissioning beam time on C+C collisions. After that first run other beam time followed, with a massive data acquisition in different kinds of experiments.

The measurements already performed can be summarized by the following table.

- **November 2001**: commissioning run
  Target = 5% interaction length
  - C+C 2 AGeV LVL1 triggered events (Mult.>3) :   **45 Mevents**
  - C+C 1 AGeV LVL1 trigger   :   **7.3 Mevents**
  full coverage with inner MDC chambers ($\Delta p/p \sim 10\%$ at 0.7 GeV/c)

- **November 2002**: C+C 2 AGeV, production runs
  Target= 2 x 2.5% interaction length
  - 56% LVL1 trigger + 44% LVL2 trigger   **220 Mevents**
  6 outer drift chambers (MDC) in 4 sectors

- **September 2003**: p+p commissioning run (1 GeV, 2 GeV)
  Target: beam pipe of liquid H_2, 5 cm length
  full coverage with outer MDC III (4 MDC IV)

- **January 2004**: p+p 2GeV production run (2.2. GeV)
  Target: 5 cm LH2   **400 Mevents**

- **August 2004**: C+C 1AGeV production run
  Target: 3 x 1.5% interaction length
  - 56% LVL1 trigger + 44% LVL2 trigger   **650 Mevents**

- **September 2005**: Ar+KCl 1.76AGeV production run
  Target: **850 Mevents**

Further informations on the experimental runs analysed in this work, September 2003 and January 2004, will be given in the next chapter.

4 EVENT RECONSTRUCTION AND ANALYSIS

In this chapter an overview of the analysis framework used for the HADES experiment will be presented, describing how simulation is performed and how data are structured.

The pp reaction cross sections used to generate simulation events will be shown, and a study for the optimisation of the 1st level trigger, in order to select preferentially events with an η decay channel and discard uninteresting events, which was later adopted for the January 2004 experiment.

At the end the main features will be shown of the data sample used for the analysis performed in this thesis.

4.1 Simulation framework

Simulations are an integral part of the experimental programs associated with nuclear collision experiments at particle accelerators. Such studies are required both during the initial detector design phase and afterwards, in order to understand the properties of the experimental setup. Thus information like acceptance and efficiency can be estimated for each subdetector to several particle species, in a wide range of energy. Moreover, by using theoretical models for the particle production in the collisions under study, one can also evaluate the reaction dependent acceptance of whole detector system, as well as gain insight into the processes of interest. This way relevant experiments may be optimised and the experimental data may be interpreted. Simulation data can also be used to develop procedures and algorithms, to check their validity and their response in terms of resolution, efficiency and overall performance.

In the HADES experiment the simulation framework was designed to reproduce the behaviour of each subdetectors, in order to have in the final stage a data structure which is similar to what we get in experiment. After this stage, the simulated data can be used as input for the same analysis used for experimental data, in order to reproduce the same kind of results with exactly the same procedures.

The simulation framework is divided into three steps:

1. **Event generation**, which simulates the reaction channels of interest by providing particle momenta in the outgoing channels;
2. **Monte Carlo tracking**, which propagates the emitted particles through the spectrometer, simulating the detector geometry, the interaction with all the present materials and the magnetic field;
3. **Digitizers**, which convert all the hit informations from the various sub detectors into TDC and ADC channel values, as in experimental data.

In the following paragraphs these three steps will be presented.

4.1.1 Event generation

By "event generation" we denote the Monte Carlo procedure which simulates physical reactions occurring in nuclear collisions.

For proton experiments the Pluto++ code was used [Kag00].

Pluto is a software package for Monte Carlo simulations of hadronic interactions written in C++. Empirical models of resonance production, hadronic and electromagnetic decays are implemented, motivated by the physics program of HADES. Empirical angular distribution parameterisations for many processes are utilized as well, such as resonance excitation in hadronic interactions, and nucleon-nucleon elastic scattering.

The code comprises a self-contained framework for stand alone principle simulations, including a data base of elementary particles and properties with support for additional usert data, as well as utilities for the implementation of elementary detector setup and acceptance cuts.

The user can also set cross sections, branching ratios and decay modes, in order to not depend on the transport code.

The output file consists of a table which contains, for each event, the information about all the generated particles in terms of momentum vectors, particle identities and generator reactions, in order to identify in the later stages of analysis which process produced each particle.

It is possible to set single reactions (such as η production and Dalitz decay or *pp* elastic scattering) or a full cocktail with a set of known processes.

After the events are generated, they have to be tracked inside the HADES spectrometer.

4.1.2 Monte Carlo tracking

The software used to simulate the HADES spectrometer response is HGEANT, a package based on CERN software GEANT 3.21 [Gea3], which is used to define and represent the detector geometry, volumes and materials, and to track particles through these volumes, to generate detector hits based on a realistic modelling of the physical processes occurring along the tracks.

The GEANT program simulates the passage of elementary particles through the matter. It is possible to describe the experimental setup by a structure of geometrical volumes and the corresponding materials. The HADES spectrometer was described according to its technical drawings, in order to fully emulate its structure.

The particles coming from the event generator are transported through the various regions of the setup, taking into account geometrical volume boundaries and physical effects according to the nature of particles themselves, their interaction with matter and the magnetic field. This allows to have a realistic detector acceptance, and to simulate most of the possible sources of background and fake hits, such as secondaries or interaction of the particles with some detector frames.

For the *pp* collision simulation the same setup of the experimental data was used, in terms of target definition, number of present MDC chambers and magnetic field scaling. The START detector was not included in the setup, and all the time of flight measurements have a common start generated by the reaction.

The target, from where the generated primary events are propagated, is defined as a cylinder along the *z* axis, 50 mm long with 2 mm diameter, centred at the (0,0,0) position in the laboratory coordinate system. This definition does not take into account the possibility of shifted or tilted beam direction, as it will be shown in chapter 5.

In Figure 4.1 there is an example on how particles are tracked inside the spectrometer, in case of a p→ppη→ppe$^+$e$^-$γ reaction when all the charged particles fall within the HADES acceptance. All the physical interactions related to the passage of a particle into the matter, such as the Lorentz force inside the magnetic field, the

Cherenkov effect on the RICH radiator or the electromagnetic shower in the lead converter of Shower detector, are taken into account.

After processing Pluto events by means of HGEANT, for each subdetector we have the position of the particles which hit it (including secondaries), the time when each hit occurred, its momentum and deposited energy. All this information must be converted into the digital response the detectors provide.
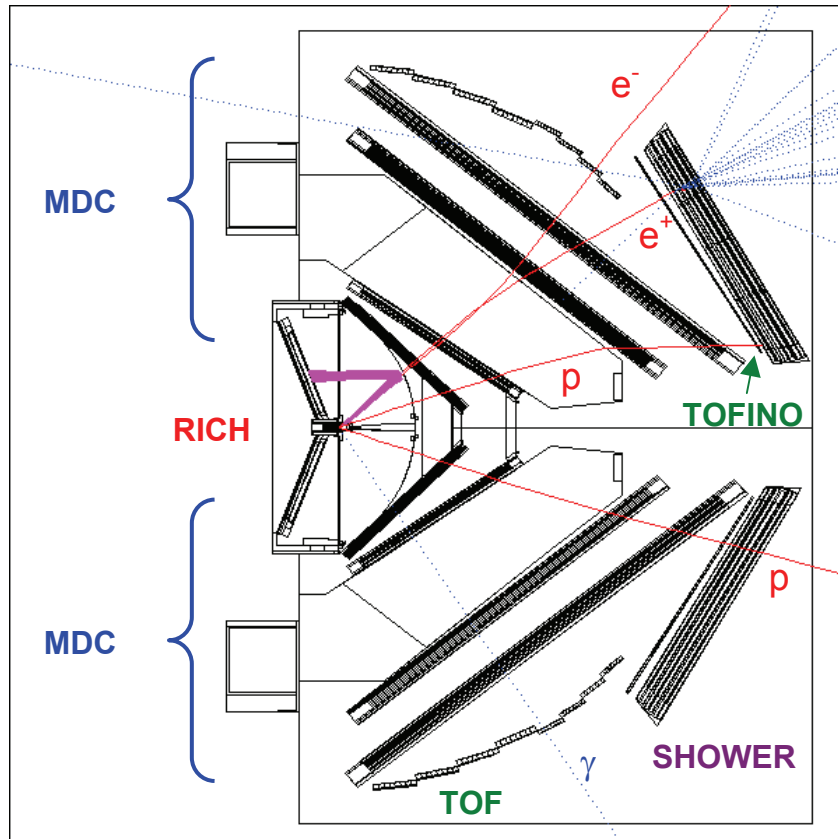

Figure 4.1 – Example on how a pp→ppη→ppe$^+$e$^-$γ event is tracked by HGEANT inside the spectrometer. The two protons are emitted at low polar angles, and they both hit the TOFINO detector. Electrons and positrons are emitted at close angles, and they produce a cone of light in RICH detector (in violet); later on the two particles are bent toward different directions by the magnetic field: at last the electron hits the TOF detector, the positron hits TOFINO and produces an electromagnetic shower in the SHOWER detector. The photon does not interact with the detectors and crosses the spectrometer without producing any useful signal.

4.1.3 Hit digitization

The hit information provided by HGEANT is in general different from the signal recorded in the experimental data. For this reason the hit position must be converted into something similar to what is obtained in experimental runs, the digital values of TDC and ADC components.

This job is called "hit digitization" and it is done by software packages called "digitizers". They consist of algorithms which simulate the electronic response of each detector, by taking into account resolution smearing, electronic noise, and most of the effects which play a role in the analog to digital conversion procedure. All the digitizer

parameters were optimised in order to provide the same raw distributions as the experimental data.

After the simulated hits are converted into detector digital signals, all the analysis procedures which are used for the experimental data can be applied on them, in order to get results which can be compared to what is obtained from real data.
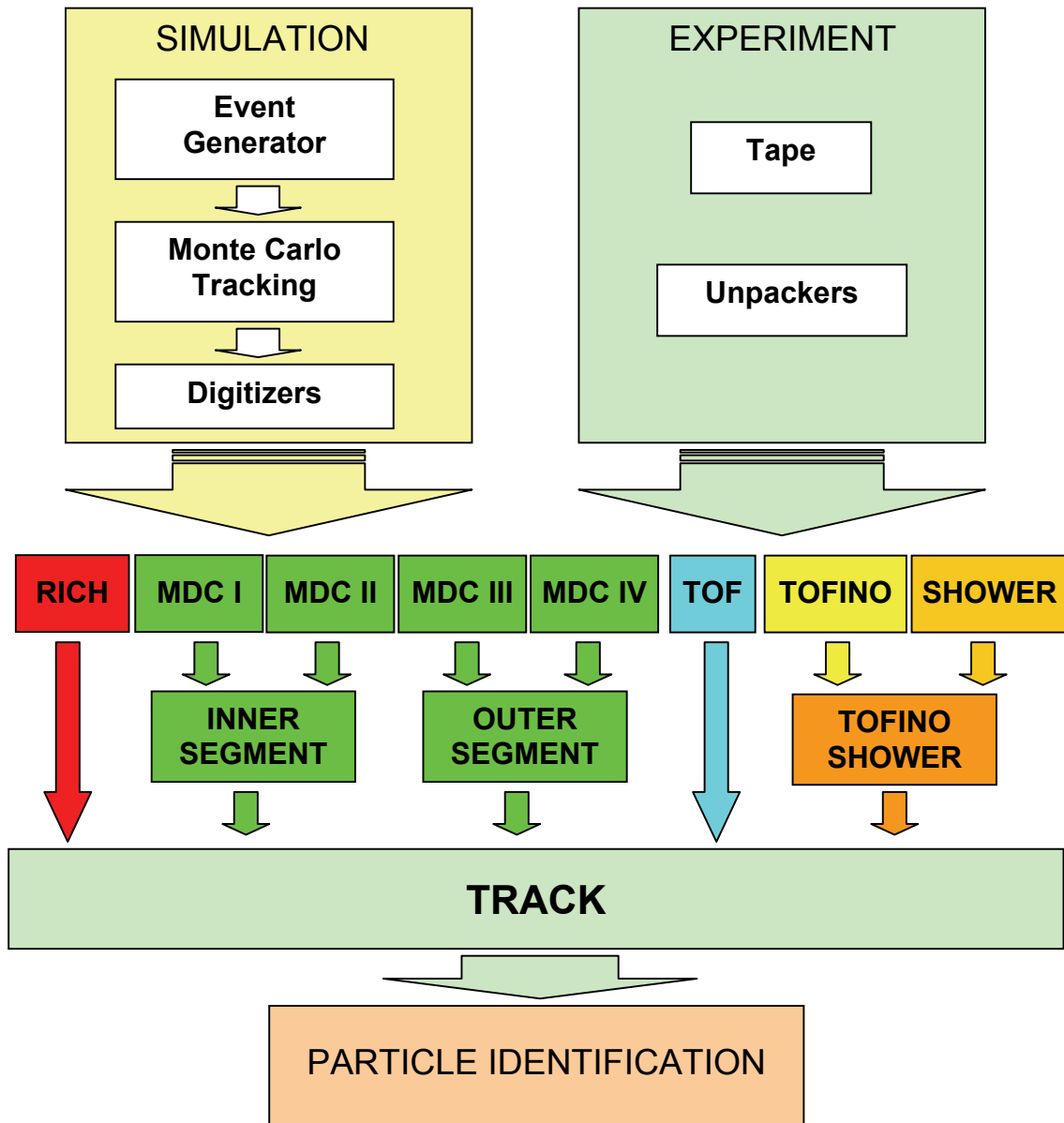
Figure 4.2 – Scheme of the data structure of the HADES analysis framework.

4.2   Event reconstruction

The main task of the HADES analysis framework is the event reconstruction, thus the application of various algorithms to transform the data which are acquired by digital modules into a physical information which can be used in the physical analysis.

The reconstruction proceeds in steps, each algorithm reads the output of a previous algorithm and takes it to a higher level of computation. In this sense we can speak of several *data levels*, which correspond to different levels of computation.

Figure 4.2 shows a scheme of the analysis framework which is used for the HADES experiment.

A physical event is an interaction between a particle of the beam and the target; during an experiment, when the event is acquired it is stored as a series of binary data words, each one containing the numbers as converted by digital modules.

The first analysis level consists of sorting the data inside the event, in order to associate each binary number to the correct detector which produced it. This job is done by the *unpackers*, software packages which read the compact raw data and expand them into a complex data structure that is a logical representation of the whole spectrometer. At the end of this step we have all the numbers, separately for each sub detector, expressed in channel units as produced by the TDC and ADC converters. This is the so called *raw* data level. The unpacking procedure is used only on the experimental data, simulation digitizers provide directly the *raw* level of data without intermediate steps.

The *raw* data are converted into physical numbers by means of several calibration steps (such as energy loss in TOF system, drift times for MDC modules, etc.), different for each sub detectors, to form the so called *cal* level. Following the full calibration procedure, the data are represented as a collection of *hits*, data objects containing the physical information provided by a each sub detector in physical units.

RICH and TOF data do not need further improvements. TOFINO and SHOWER hits are merged together to form a unique object, containing the time of flight of the particle provided by TOFINO, and the position and charge measurement from the SHOWER detector. Hit positions from MDC module pairs are merged together to form *segments*, as shown in Figure 4.2; the combined information of modules before the magnetic field region provides the inner segment, and the same happens for outer modules. Each segment mainly contains information on the angular trajectory of a particle. Further details will be provided in chapter 5.

The hit information provided by all the subdetectors are finally merged into a unique object, called *track*. The track is the basic object used by physical analysis, and it is constituted by all the physical information we can get from a particle, such as trajectory, momentum, time of flight, and so on.

From these informations the particle identification can be performed. By means of an angular correlation with the RICH detector, a proper time of flight selection and by detecting an electromagnetic shower in the SHOWER detector, the lepton identification is performed. Hadrons are in general identified by a combined measurement of velocity and momentum (see chapters 6 and 7).

After the particle is identified, the analysis can be properly.

4.3 PP cross section

As previously stated, in Pluto simulations the branching ratios and decay channels are set by the user, according to values known from experiments or from theoretical calculations.

For *pp* simulations a full cocktail was generated according to most of the known physical processes. The main goal of the simulation was to produce realistic distributions as compared to experimental data for elastic scattering, η exclusive reconstruction and dilepton inclusive invariant mass spectra.

They are summarized in Table 4-1, where the primary decay channels are indicated with the used values of cross section and branching ratio. The reaction channels analysed in this work are indicated in red, and they are the *pp* elastic scattering and the η production.

In the Pluto simulation the $pp \to d\pi^+$ reaction was not included, because the outgoing particles are emitted almost totally out of the HADES acceptance.

The two pion production cross section is described via the excitation of baryonic resonances, such as $\Delta(1232)$ and N(1440), and their subsequent decay into two pions according to branching ratios and decay widths given by [Tei96].

	Branching ratio	Cross section [mb]
pp→pp (elastic)	0.422734	18.0
pp→nΔ^{++}	0.253640	10.8
pp→pΔ^+	0.084547	3.6
pp→pN(1440)	0.065759	2.8
pp→pp$\pi°$	0.003523	0.15
pp→pnπ^+	0.023485	1.0
pp→p$\Delta^+\pi°$	0.011273	0.48
pp→n$\Delta^{++}\pi°$	0.046970	2.0
pp→pN(1440)$\pi°$	0.055425	2.36
pp→pp$\pi°\pi°\pi°$	0.003523	0.15
pp→pp$\pi^+\pi^-\pi°$	0.007750	0.33
pp→pn$\pi^+\pi^+\pi^-$	0.014091	0.6
pp→pN(1535) (inclusive)	0.007280	0.31

Table 4-1 – PP cross section table for Pluto simulation, primary decay channels.

Table 4-2 shows the branching ratios of baryonic resonance decays, except for N(1535).

For three pion decays we assumed only phase space production, and cross sections were extrapolated.

The N(1535) cross section value includes all the decay processes shown in Table 4-3. It is known that the N(1535) resonance couples to the η meson; in our simulation only decay channels with the η meson production were included. Moreover, there were additional processes which foresaw the possibility of producing one or two pions in the final state. This feature of the code was included to check some theoretical models which predict these decay channels, but it does not affect the main analysis of the $pp \to pp\eta$ channel.

In the simulation code all the mesons decay according to the vector meson dominance model; their branching ratios are reported in Table 4-4. The channels analysed in this work are highlighted in red; the cross section values of the η decay channels are referred to pp→ppη reactions. No cross section values for $\pi°$ were reported because they are produced in many reaction channels and each one should be checked separately.

All the events simulated by the Pluto code were tracked through the spectrometer by HGEANT, by using the same detector setup of the *pp* experimental runs. After the hit digitization an analysis on the particle multiplicity in η-producing reactions was performed, in order to optimise the first level trigger for the data acquisition.

	Branching ratio	Cross section [mb]
$\Delta^{++} \rightarrow p\pi^+$	1.0	10.8
$\Delta^+ \rightarrow p\pi^\circ$	0.666	2.4
$\Delta^+ \rightarrow n\pi^+$	0.333	1.2
$\Delta^+ \rightarrow pe^+e^-$	$4.1 \cdot 10^{-5}$	0.000144
$N(1440) \rightarrow p\pi^\circ$	0.278	0.78288
$N(1440) \rightarrow n\pi^+$	0.559	1.56548
$N(1440) \rightarrow \Delta^{++}\pi^-$	0.161	0.45164

Table 4-2 – Branching ratios for baryonic decay channels, except for N(1535).

	Branching ratio	Cross section [mb]
$pp \rightarrow pp\eta$	0.624	0.19344
$pp \rightarrow pp\eta\pi^\circ$	0.152	0.04712
$pp \rightarrow pp\eta\pi^+$	0.152	0.04712
$pp \rightarrow pp\eta\pi^+\pi^-$	0.036	0.01116
$pp \rightarrow pp\eta\pi^\circ\pi^\circ$	0.036	0.01116

Table 4-3 – Cross section values of the N(1535) inclusive reactions, with the final production of a η meson.

	Branching ratio	Cross section [mb]
$\pi^\circ \rightarrow \gamma\gamma$	0.988	
$\pi^\circ \rightarrow \gamma e^+e^-$	0.012	
$\eta \rightarrow \gamma\gamma$	0.394	0.076215
$\eta \rightarrow \pi^\circ\pi^\circ\pi^\circ$	0.325	0.062868
$\eta \rightarrow \pi^+\pi^-\pi^\circ$	0.226	0.043717
$\eta \rightarrow \pi^+\pi^-\gamma$	0.047	0.009053
$\eta \rightarrow e^+e^-\gamma$	0.006	0.001161
$\eta \rightarrow \mu^+\mu^-\gamma$	$3.1 \cdot 10^{-4}$	0.000060
$\eta \rightarrow e^+e^-$	$7.7 \cdot 10^{-5}$	0.000015
$\eta \rightarrow \mu^+\mu^-$	$7.7 \cdot 10^{-5}$	0.000015

Table 4-4 – Decay channels of mesons. The η cross section values are referred to $pp \rightarrow pN(1535) \rightarrow pp\eta$ channel.

4.4   First level trigger optimisation

The main goals of January 2004 proton experiment were (i) to collect data on the *pp* elastic scattering and (ii) on the η decay channels like ppη→ppπ$^+$π$^-$π° (hadronic decay) and ppη→ppe$^+$e$^-$γ (electromagnetic Dalitz decay).

A simulation data study was performed before the production beam time, to evaluate a suitable 1st level capable of enhancing these reactions and of suppressing most of the uninteresting processes.

The first level trigger operates with digital signals coming from the constant fraction discriminators (CFD) of TOF and TOFINO detectors. Each CFD module has 16 channels; moreover it has an additional analog output that provides a square signal whose amplitude is proportional to the number of fired channels (50mV/channel on a 50Ω load). A few steps of fan-in and analog sum allow to produce a signal whose amplitude is proportional to the global TOF multiplicity, plus 6 signals providing the same information sectorwise.

A similar procedure for TOFINO, with some electronic trick in order to take into account that it has only one photomultiplier per pad instead of the two per rod employed by TOF, allows to generate the same multiplicity signals.

Finally the multiplicity signals from the six TOF sectors and the six TOFINO sectors are summed, to produce a global TOF+TOFINO multiplicity signal, whose amplitude is proportional to the total number of hits in the two combined detectors..

A discriminator threshold decides about the minimum trigger multiplicity, by firing only if the final sum is above a threshold level adjusted experimentally after a few quick iterations of data acquisition and online analysis. The signals used are 40-80 ns long, thus the required multiplicity has to build-up within this time. Very slow protons or secondaries will not contribute, if they arrive too late.

We can easily see that the multiplicity signal does not correspond exactly to the particle multiplicity in META, because it can be affected by electronic noise from a single photomultiplier, noise that will not be reconstructed as a TOF hit because the signal on the other end is missing. If only one end of a TOF rod fires, it will contribute as a half particle; thus, if two different single ends fire somewhere in TOF, they will wrongly increase the multiplicity by one unit. This is however a rather rare event.

Moreover, it is possible to combine signals coming from different detectors and different sectors in order to impose more restrictive selections, such as that two opposite sectors have fired.

All these hardware options of the 1st level trigger were implemented in the simulation code, in order to fully emulate the features of the data acquisition system in the production of simulated events.

For the *pp* elastic scattering the main feature used to select this kind of reaction is the coplanarity of the two outgoing protons.

Elastic scattering is a two body reaction and both the outgoing particles must lay on the same reaction plane (see chapter 5 for details about the elastic channel). Thus to select this reaction we need at least two hits in META detectors, and we can impose a condition on two opposite sectors hit in the same event (M2opp). Via simulation it was checked that this criterion does not appreciably reduce the number of acquired elastic collision events, and then it was applied for the real data taking.

The selection of η decays required a more complicated study in simulation, because there exist many background processes which have four charged particles in the final state, so the physical properties of the η decays must be studied.

In order to perform this analysis, simulation events were produced with only the interesting η decay channels: 500,000 events for the hadronic decay channel (pp→pN(1535)→ppη→ppπ⁺π⁻π°), and 500,000 events for the η Dalitz decay (pp→pN(1535)→ppη→ppe⁺e⁻γ).

Moreover, 6 million events were produced with the full cocktail, by including all the reactions; in this way several 1st level trigger selections can be applied on both data samples, and the reduction factors on η mesons and on the total number of acquired events can be evaluated.

The first condition in order to do an exclusive study of η decay channels is a selection on events with at least four charged particles in the META system. This condition is mandatory and cannot be avoided, because we need at least four tracks to reconstruct the events (the missing π° or γ can be extrapolated by a missing 4-momentum analysis, as it will be shown in chapter 7); in order to perform a more restrictive selection additional input from the simulation data can be very helpful.

In our simulation the events with a fully reconstructed η decay channel, i.e. with all the four outgoing charged particles reconstructed up to the *track* level, were selected; analysing these data it is possible to check the emission angles and to identify each different particle.

In Figure 4.3 the polar angle distribution is shown for all the particles in the exit channel of η hadronic (left side) and Dalitz (right side) decays. In the plot the primary protons (*p*, in blue) are separated from the ones coming from the decay of N(1535) resonance (p_{N*}, in black). We can see that the proton distribution from N(1535) decay is peaked at smaller polar angles than the primary protons. The different distribution for π⁺ and π⁻ is related to the HADES acceptance, different for positive and negative particles, mainly due to the magnetic field which bends positive charged particles toward lower θ, negative charged particles toward higher θ. This effect becomes less relevant in the case of lepton pairs, for kinematic reasons[1].

While pions and leptons cover almost the whole HADES acceptance, protons are focused on polar angles below 40°, in the region covered by the TOFINO system. So an additional condition of at least two hits in TOFINO can be applied, and the related event reduction evaluated.

In analogy to the elastic scattering channel, we can argue that the two outgoing protons hit opposite sectors and the related selection could be applied. Figure 4.4 shows the difference in azimuthal angles between the two outgoing protons, separately for the hadronic and the Dalitz decay channel. We can see that the distributions are peaked at 180° for both the decays, thus the most of the η events will have two opposite sectors hit; moreover we expect a symmetry in azimuthal angle between the primary proton and the N(1535) resonance, so we can assume that if the second proton does not hit the opposite sector probably another particle from the resonance decay will hit it. The condition on opposite sectors, and the consequent event reduction, has to be evaluated.

If the two protons go to the TOFINO system, an additional condition is to check whether there are two particles which hit two opposite TOFINO sectors.

In order to check whether the η decay channel can be reconstructed in an exclusive way, it was evaluated in simulation whether the four charged particles in the exit channel can be reconstructed by the tracking software up to the *track* level; in this way the particle must produce a useful signal in all the detectors (except for RICH), so the method includes both the spectrometer acceptance and tracking reconstruction efficiency.

---

[1] Electrons and positrons from Dalitz decay are mostly emitted at higher polar angles with respect to pions from η hadronic decay, thus positrons are less affected by the 18° θ cut.
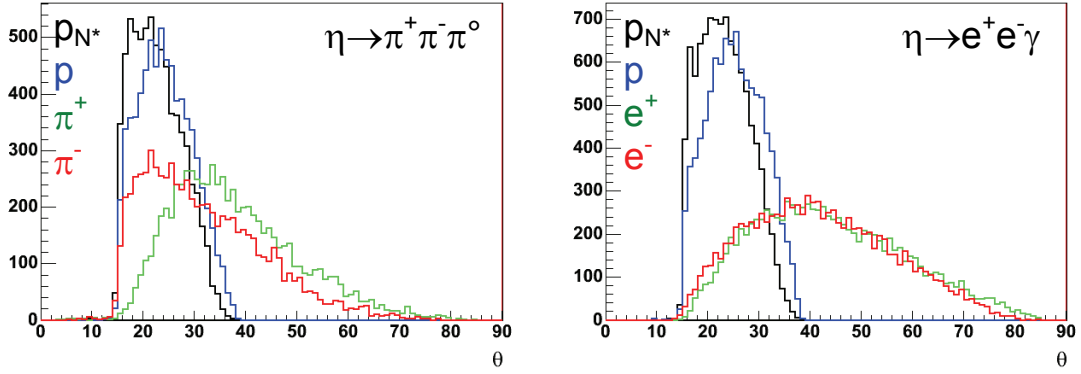
Figure 4.3 – Polar angular distribution for final state particles coming from η meson decays, hadronic (on the left) and electromagnetic (on the right).
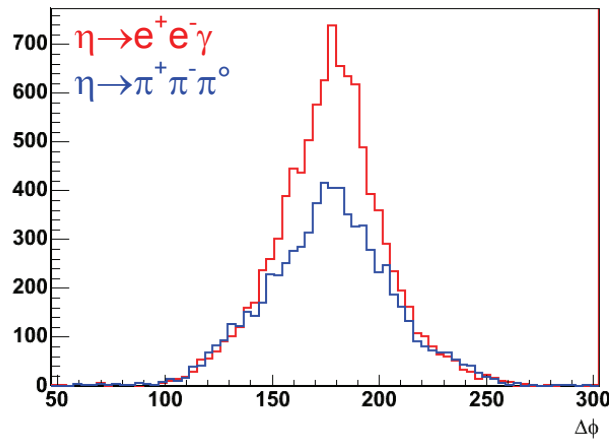

Figure 4.4 – Difference in azimuthal angles between the two outgoing protons, separately for hadronic (blue) and Dalitz (red) decays.

Table 4-5 shows a summary of the number of η mesons reconstructed by the whole HADES under several different first level trigger selections, separately for hadronic and Dalitz decays. The reported value of acceptance/efficiency ε consists of the number of reconstructed events divided by the total number of simulated η meson decays.

The first thing which comes out is that the acceptance for the electromagnetic channel is a little higher than the hadronic one; this effect mainly depends on the different phase space between outgoing pions and leptons.

If we compare the number of surviving η mesons with respect to the minimum bias condition (META≥4), we do not observe a strong reduction. While the condition on TOFINO multiplicity leaves intact the number of signal events, the opposite sector conditions decrease the number of counts (94% and 90% event reduction relative to the META≥4 condition respectively for hadronic and Dalitz decays). We can conclude that all the selections can be applied without losing too many useful events. The condition on TOFINO opposite sectors further reduces the number of acquired signal events (88% and 86% for hadronic and Dalitz decays).

Table 4-6 shows the event reduction values calculated in the full *pp* cocktail. We can see that each condition reduces the number of acquired events quite a bit, as compared to the relative η signal reduction shown in Table 4-5.

A condition on opposite sectors, linked to TOFINO multiplicity, can be exploited for a considerable event reduction (71.31% with respect to META$\geq$4 minimum bias selection) with a moderate signal reduction (94% and 90% with respect to META$\geq$4 condition for hadronic and Dalitz decays).

The selection on TOFINO opposite sectors strongly reduces the number of uninteresting events (47.40%). In principle it could be applied, but it was decided to not use it during data acquisition in order to prevent a possible bias on $\pi°$ production, used as a cross check, where protons can also hit TOF detector.

In conclusion, the official 1st level trigger used for January 2004 acquisition was based on (i) at least multiplicity four in META detectors, (ii) at least multiplicity two in TOFINO detectors, and (iii) a condition on opposite META sectors hit in the same event. This special trigger was called M4smart.

	$\eta \rightarrow \pi^+\pi^-\pi°$		$\eta \rightarrow e^+e^-\gamma$	
	events	ε [%]	events	ε [%]
Total Events	500,000	100.00	500,000	100.00
META$\geq$1	7,131	1.43	10,056	2.01
META$\geq$4	6,697	1.34	8,814	1.76
META$\geq$4 TOFINO$\geq$2	6,697	1.34	8,814	1.76
META$\geq$4 TOFINO$\geq$2 OSEC$_{META}$	6,294	1.26	7,960	1.59
META$\geq$4 TOFINO$\geq$2 OSEC$_{TOFINO}$	5,906	1.18	7,597	1.52

Table 4-5 – Event reduction for η decay channels under different 1st level trigger selections.

	cocktail	events/M4 [%]
Total Events	6,000,000	
META$\geq$1	2,873,378	
META$\geq$4	599,055	100.00
META$\geq$4 TOFINO$\geq$2	533,952	89.13
META$\geq$4 TOFINO$\geq$2 OSEC$_{META}$	427,210	71.31
META$\geq$4 TOFINO$\geq$2 OSEC$_{TOFINO}$	283,924	47.40

Table 4-6 - Event reduction for the full pp cocktail under different 1st level trigger selections. The third column shows the event reduction in percentage with respect to META$\geq$4 trigger (minimum bias).

4.5 Proton experiment setup

Two acquisition run were performed by using proton beams. On September 2003 there was the commissioning run, with the first tests of the outer tracking system and of the new liquid hydrogen target. The two experimental setup will be presented in the following paragraphs.

4.5.1 September 2003 commissioning run

In September 2003 we installed for the first time a liquid hydrogen target for proton and pion experiments. The target was constituted by a cylindrical chamber 5 cm long, filled with liquid hydrogen with about $2 \cdot 10^{23}$ protons/cm^2.

Several data sets were stored by using proton beams of 1 and 2 GeV kinetic energy, and exploiting a combination of full-target and empty-target measurements in order to estimate the background coming from secondary interactions.

Moreover, for the first time the magnetic field intensity was raised to 92% of the maximum value, against the 72% of *C+C* experiments; larger trajectory deviations follow from a higher intensity field, and therefore a better momentum resolution in particular for high momentum particles.

In the meantime two additional outer chambers were installed and operational, and for the first time we could use the full high resolution tracking system for 4 (out of the forthcoming 6) sectors. Unfortunately a few MDC readout motherboards were destroyed by an electronic malfunctioning. Apart from this problem, the overall stability and performance of the MDC tracking system was satisfactory.

A system of START-VETO detectors was used to select reactions which occurred in the target region, as explained in paragraph 3.3.2.

Four sectors of the RICH detector were upgraded with new carbon mirrors featuring an increased reflectivity of 85% at $\lambda = 150$ nm (as compared to 75% of the remaining two old ones made from glass). However, during the test experiment the RICH experienced high voltage stability problems at beam intensity well below 10^7 protons/s. They could be uniquely related to a large charged particle background resulting from the interaction of the beam with the START detector and other materials in front of the RICH. The optimisation of the target area via installation of a vacuum pipe, the removal of the START detector and a better beam tuning, strongly reduced the background and allowed a stable production run in January 2004.

4.5.2 January 2004 production run

During the January 2004 experiment we used a proton beam at 2.2 GeV kinetic energy, with an intensity around 10^7 particles per second.

During the beam time the detector setup remained unchanged from the September 2003; the only difference was in the missing START detector as already explained.

Figure 4.5 shows the scheme of the experimental detector setup of the HADES spectrometer during the January 2004 run. All the operational subdetectors are indicated with full colour, the missing ones by white boxes (only two MDC chambers were missing, now they are going to be installed quite soon), while subdetectors with a somewhat anomalous behaviour are represented by dashed boxes.

Concerning the MDC tracking system, 22 drift chamber modules out of a total of 24 (as foreseen in the forthcoming complete configuration) were installed and operational; due to some troubles with large currents in MDC modules, a few wire layers were not used. Most of the problems occurred in MDC1 sector 1, where two out of six layers were switched off; in MDC1 sector 3 and MDC3 sector 3, where for each of them one layer was not used. The lack of some layers, combined with some sparse broken motherboards, reduced the momentum resolution of those sectors, as will be shown in the next chapter. While for the inner segment reconstruction in sector 1 there were in total 10 available wire layers (4×MDC1 + 6×MDC2), for sector 3 the missing

MDC4 chamber and the switched-off layer made the outer segment reconstructed from only 5 wire layers (5×MDC3), and it caused several problems to the drift time fits and to the track reconstruction. The tracking characterization will be presented in chapter 5.

The data acquisition was performed by using different 1st level trigger settings, to select *pp* elastic scattering and η hadronic decay. For the η electromagnetic decay we also used a 2nd level trigger to enhance events with electron pairs. Both data sets are important for a detailed understanding of the high resolution tracking and of the HADES acceptance for electron pairs.
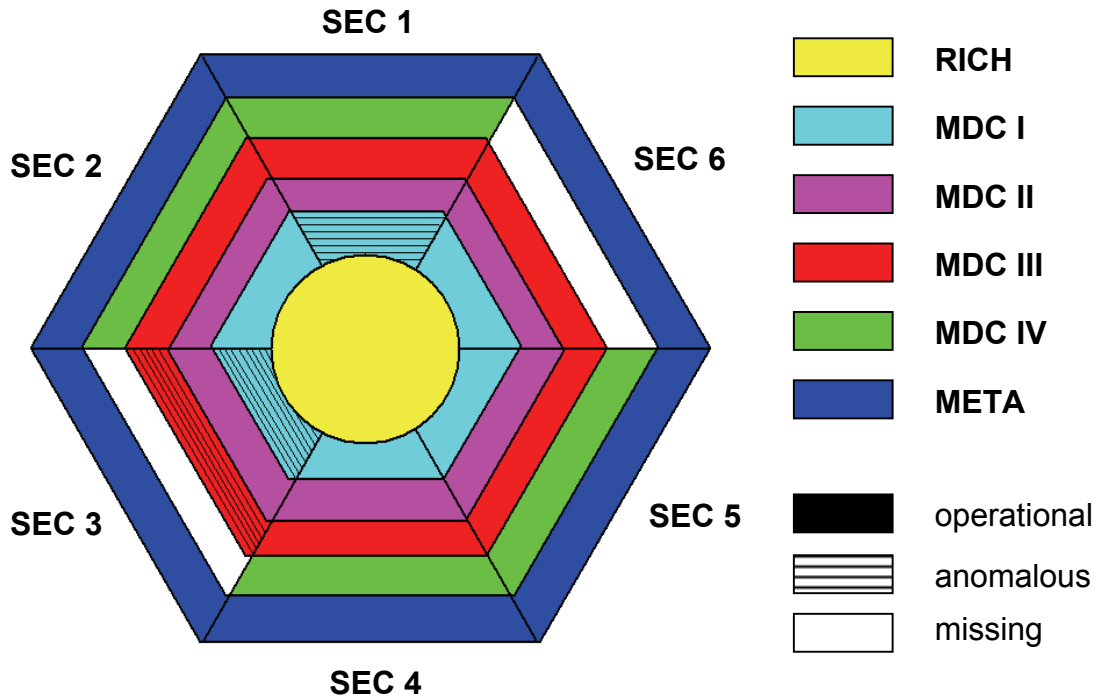

Figure 4.5 – Scheme of the HADES experimental setup during the January 2004 production run.

4.6 January 2004 experimental data set

During the January 2004 experiment almost 500 million events were recorded, including a few test runs, no-field and field data.

The interesting pool is constituted by field data which were used for the exclusive analysis, but first some considerations about the 2nd level trigger are needed.

4.6.1 The HADES 2nd level trigger

All the data which pass the 1st level trigger decision are sent to the matching unit board, which decides whether the event has to be accepted or discarded. This decision is taken separately by two different systems which operate independently: the downscaling box and the 2nd level trigger itself.

The 2nd level trigger selects events which contain a lepton pair, according to the information from Image Processing Unit processors (IPU); all these events are stored into the data file. We call them LVL2 events.
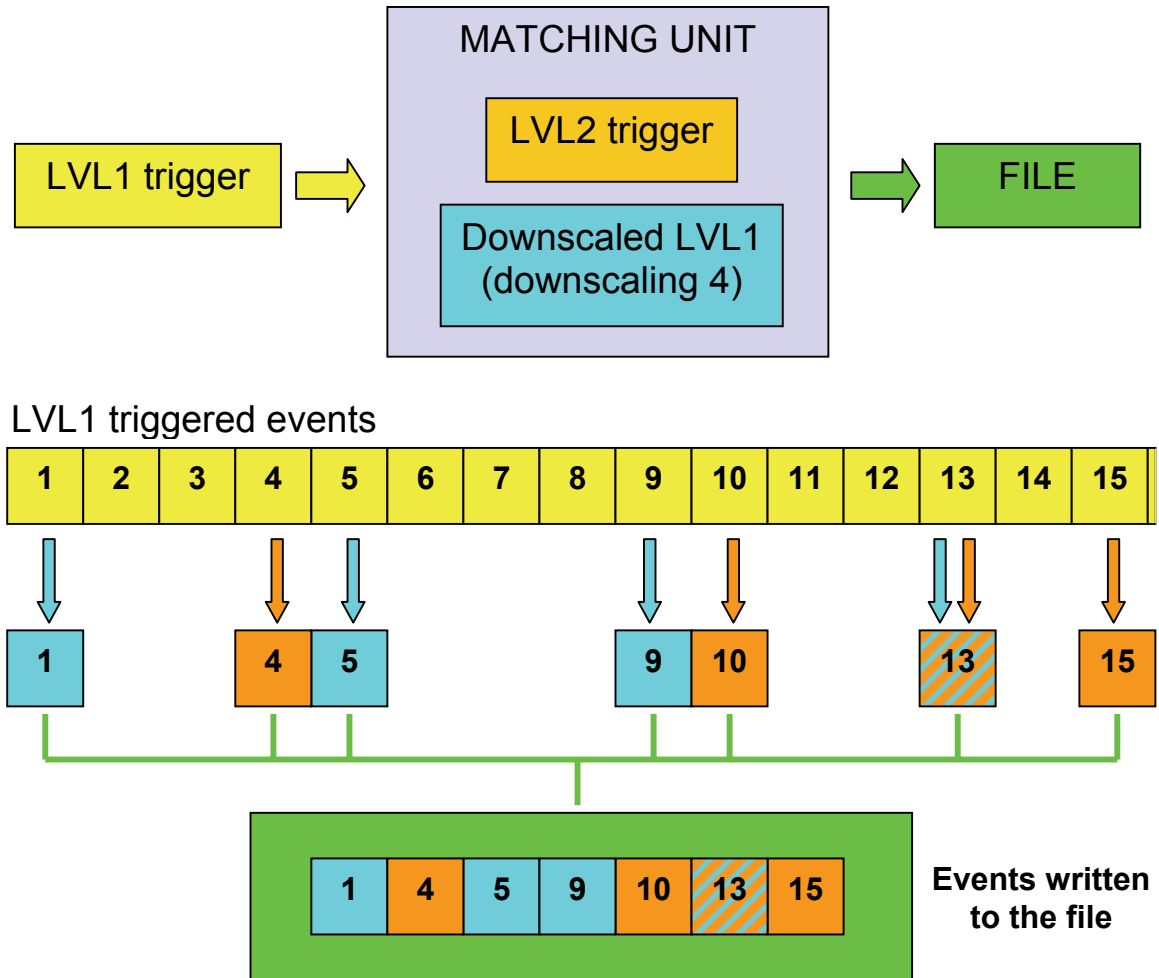
Figure 4.6 – Scheme of the event selection used for data acquisition.

However, we do not want to acquire only events with lepton pairs, but also events which contain only hadrons; if we recorded all the 1st level triggered events without any further scaling, the stored data would be dominated by hadronic reactions.

The downscaling box purpose is to select and scale down events in a statistical fashion, regardless of whether they contain lepton pairs or not, for hadronic analysis and normalization factors; in this case we talk about *downscaled* events. It is possible to program via software a *downscaling* factor, which tells the downscaling box the number of events to be discarded between two accepted events. The information about the type of event trigger is also stored inside the data stream in a part called *event header*.

As an example we can look at Figure 4.6, which represents a scheme of the event selection used for data acquisition. A first selection of events is done by the 1st level trigger (yellow boxes), and they are sent to the matching unit, where the downscaling factor is set to 4. This means that one event out of four is stored (1, 5, 9, 13, …), regardless of the 2nd level trigger decision. It is flagged as *downscaled* in the event header and the related downscaling factor is stored as well. All the events with a recognized lepton pair are stored as well, and flagged as *LVL2*. This means that an event can be at the same time downscaled (LVL1) and with a positive 2nd level trigger decision (LVL2), like for instance the event number 13 in the example.

If we want to have the total number of 1st level triggered events, we must multiply the number of downscaled events (4) by the downscaling factor (4); in this

case we obtain 16 triggered events, against 7 which are effectively stored to file. This means that in our example we found 4 lepton pair candidates by storing only 7 events, instead of 16. In this particular case we are roughly saving half of the disk space, and half of the time needed for the data acquisition.

Indeed the 2nd level trigger has an efficiency below 100%, therefore in evaluating the number of dilepton events in the data sample this correction has to be taken into account.

4.6.2 Experimental data set

The first part of the experiment was focused on the alignment and detector checkout and repairs; data were first taken with cosmic rays, and afterwards with beam but with the magnetic field switched off, for straight track alignment.

The second part was the real production run, based on the acquisition with magnetic field and mainly with the M4smart 1st level trigger decision, optimised for the η meson reconstruction.

About 310 million events were analysed, with different trigger types, as shown in Figure 4.7. 263 million events were acquired with "M4smart" trigger (multiplicity ≥4 in META, multiplicity ≥2 in TOFINO, and opposite META sectors), and they were used for exclusive η meson reconstruction (chapter 7), while about 33 millions had the trigger "M2opp" (2 META hits and opposite sectors) and were mainly analysed for elastic scattering (chapter 6).

Other minor 1st level trigger events are present in the data sample. "M1" and "M2" are respectively multiplicity 1 or 2 in META detector, while "Clock" are pulser runs. "SMASH" events were triggered by a small hodoscope detector, placed at forward angles ($\theta \sim 10°$) as a reference point for elastic scattering reactions.

The most interesting part of the data is constituted by M4smart events; several downscaling factors were used during the beam time, and the corresponding numbers of events are reported in Figure 4.8.
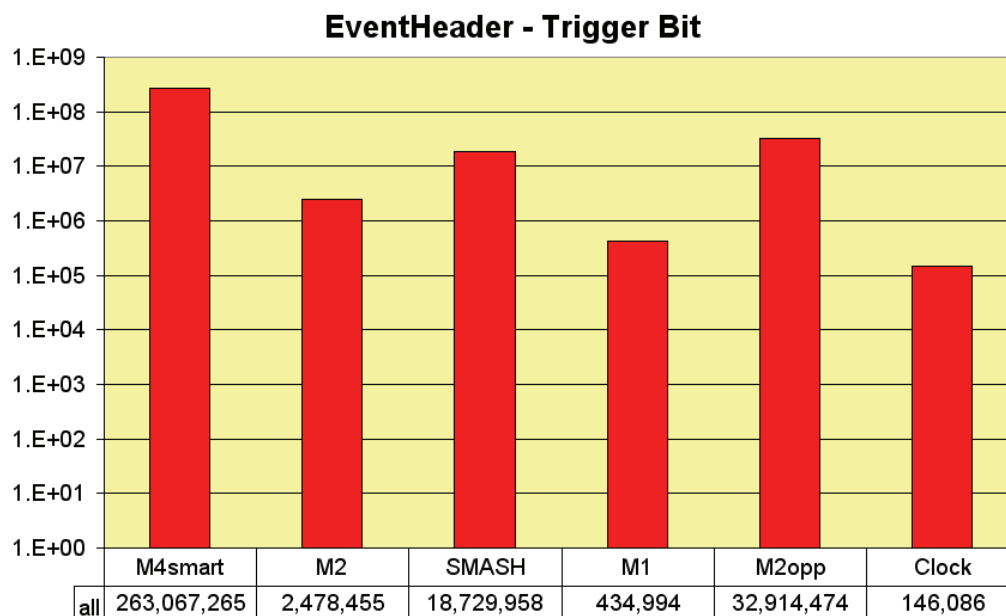

EventHeader - Trigger Bit

	M4smart	M2	SMASH	M1	M2opp	Clock
all	263,067,265	2,478,455	18,729,958	434,994	32,914,474	146,086

Figure 4.7 – Number of analysed events by different 1st level trigger selections.

EventHeader - Downscaling

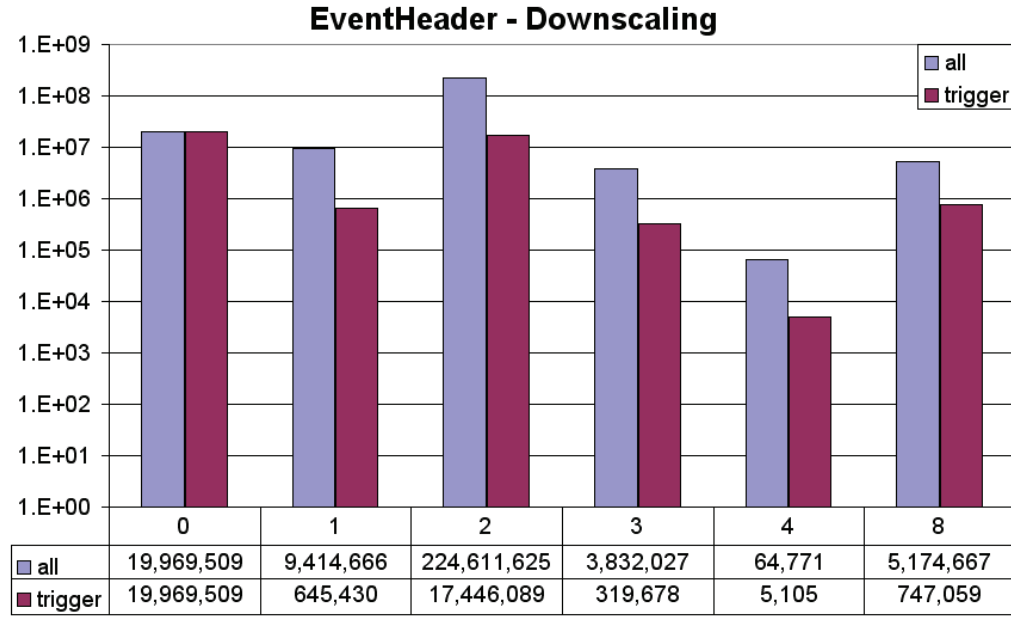|	0	1	2	3	4	8
all	19,969,509	9,414,666	224,611,625	3,832,027	64,771	5,174,667
trigger	19,969,509	645,430	17,446,089	319,678	5,105	747,059

Figure 4.8 – Number of M4smart events according to different downscaling factors, separately for all the events (blue) and all the LVL2 triggered ones (violet). Downscaling equal to zero represents events triggered by 2nd level but not from downscaling machine.

In the plot the contributions from all the M4smart events (*all*), and from LVL2 triggered ones (*trigger*) are shown separately.

The downscaling factor "zero" represents events which were never selected by the downscaling box but had a positive 2nd level trigger decision. We can see that most of the statistics was acquired with downscaling 2 (224 millions of events); in the last part of the beam time it was decided to use a higher downscaling factor, up to 8.

In order to evaluate to how many 1st level triggered events the data sample corresponds, we must consider only the downscaled events, which are about 243 millions. If we multiply the number of downscaled events by their corresponding downscaling factor, by adding these numbers we get the total number of events which passed the M4smart 1st level trigger selection, which is 512 millions.

By dividing these two numbers we can calculate that the average downscaling factor for the whole data sample is about 2.2. The total number of LVL2 events is 39 millions.

4.6.3 Simulation data sample

In simulation no downscaling and no 2nd level trigger decisions were applied. The only selection on the stored events was done at the 1st level trigger level, by the emulation code which was developed according to the hardware system, as shown in paragraph 4.4.

Only two LVL1 triggers were adopted; for the exclusive η reconstruction about 155 million events were simulated with M4smart trigger, while for the elastic analysis 10 millions of M2opp events were generated.

5 TRACKING AND ALIGNMENT

During the first *pp* production run the HADES spectrometer was equipped for the first time with an almost complete outer tracking system (four MDC chambers in four sectors, three chambers in the remaining two sectors).

One of the main goals of this experiment was to collect data with pp elastic scattering, in order to perform a full characterization of the tracking system, to check and improve the alignment of the chambers, and in particular to evaluate the momentum reconstruction resolution.

As it will be shown in chapter 7 a high momentum resolution is mandatory to perform an exclusive η identification, and this calls for precise MDC calibration and detector alignment. For this purpose several alignment procedures had to be developed, and tracking algorithms which reconstruct momentum by using also the information coming from the outer chambers.

In this chapter the current status of HADES tracking will be presented, as evaluated using the January 2004 experimental data.
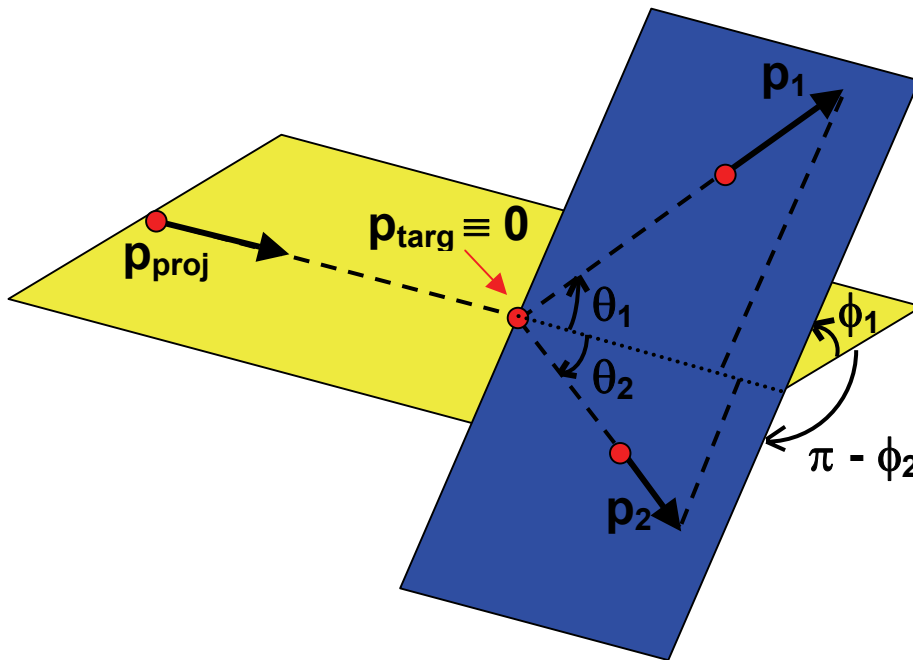

Figure 5.1 – Scheme of a two-body collision in the laboratory frame.

5.1 Elastic kinematics

The *pp* elastic channel is a wonderful tool to study the detector alignment and its tracking capability. Indeed in elastic scattering the kinematics of the reaction is fixed, as well as the relationship between the angular variables of proton pairs. We will show how the information on the polar angle allows to calculate the particle momentum, and therefore, by comparison with the initial conditions, to evaluate the momentum reconstruction resolution.

Figure 5.1 shows a scheme of a two-body collision, like pp elastic scattering, in the laboratory frame. In the figure we have a projectile with momentum p_{proj} hitting the

target particle which is at rest ($p_{\text{targ}} \equiv 0$). After the collision the two outgoing particles will be emitted in the same reaction plane (the blue one), with emission polar angles θ_1 and θ_2 and with momenta p_1 and p_2; the two particles are identical so it is not possible to distinguish projectile and target after the collision.

The first kinematical constraint comes from the fact the two particle trajectories must lay on the same reaction plane, and it imposes the condition on azimuthal angles (ϕ_1 and ϕ_2):

$$\left|\phi_1 - \phi_2\right| = 180° \qquad \textbf{(Eq. 5-1)}$$

Furthermore, considering that the two particles have the same rest mass, a relativistic calculation shows that the relationship between their polar angles (θ_1 and θ_2) is given by:

$$\tan\theta_1 \cdot \tan\theta_2 = \frac{1}{\gamma_{CM}^2} \qquad \textbf{(Eq. 5-2)}$$

where γ_{CM} is the γ Lorentz factor calculated in the centre of mass frame [see Appendix A].

In the elastic scattering there is a direct relationship between emission angle and particle momentum; by means of some more calculations [Appendix A] we can obtain:

$$p(\theta) = \frac{p_{proj}}{\cos\theta + \gamma_{CM}^2 \sin\theta \tan\theta} \qquad \textbf{(Eq. 5-3)}$$

From the last equation, if we are able to measure correctly the θ polar angle, we can predict the theoretical momentum the particle should have, and to compare this value with the one given by tracking algorithms. This way we can estimate the momentum resolution of the tracking system.

But the main purpose of the HADES spectrometer is to plot invariant mass spectra of dilepton pairs, so we are interested much more in invariant mass resolution rather than momentum.

In relativistic notation, we can express the four-momentum p_i of a particle as:

$$p_i = \left(E_i, \vec{p}_i\right); \quad E_i = \sqrt{p_i^2 + m^2} \qquad \textbf{(Eq. 5-4)}$$

where E_i is the total energy of the particle, $\vec{p}_i$ its momentum vector and m its rest mass. If we have a system made of two particles, the invariant mass M will be given by:

$$M = \sqrt{\left(E_1 + E_2\right)^2 - \left(\vec{p}_1 + \vec{p}_2\right)^2} \qquad \textbf{(Eq. 5-5)}$$

By selecting a proton elastic pair and measuring their emission angles in the laboratory frame, we can evaluate their momenta and therefore the invariant mass. By

comparing the obtained value with the known initial state we can estimate the spectrometer resolution in terms of invariant mass.

Table 5-1 shows a summary of the kinematical properties of proton elastic scattering pairs, for the two energies which were used in January 2004 experiment.

No field data were taken at a proton incident kinetic energy of 2 GeV, to perform alignment using straight tracks, while the field data were taken at 2.2 GeV.

	No field	Field
Momentum (proj) [MeV/c]	2784	3000
Total energy (proj) [MeV]	2938	3143
Kinetic energy (proj) [MeV]	2000	2205
Invariant mass [MeV/c^2]	2697	2768
γ_{CM}	1.4372	1.4747
$1/\gamma^2_{CM}$	0.4841	0.4598

Table 5-1 – Summary of the kinematical properties of proton elastic scattering.

5.2 Alignment strategy

Each MDC chamber provides information about the position and the trajectory direction of the particle which hit it, in the chamber coordinate frame[1], by fitting time signals coming from different wire layers.

The particle trajectory before and after the magnetic field is reconstructed by spatial correlation of different chambers belonging to the same sector, and then the particle momentum is evaluated. The position information of the single MDC is then converted into the laboratory coordinate system, and it is important to know the absolute position of each chamber with high precision to obtain high precision in the trajectory reconstruction.

We have developed alignment procedures based on photometric measurements and cosmic-ray data for the inner chambers, and on straight tracks reconstruction in runs without magnetic field for the outer ones.

Photometry is a photo-camera based method to survey objects in three dimensions. For this purpose a 8 Megapixel mirror reflex camera with a special 20 mm USM wide-angle-lens was used, to take high resolution pictures of large areas from short distances.

First the camera has to be calibrated, by photographing from all sides a special array of dots whose positions are fixed and known. Subsequently same special markers are glued on the chambers, in detector reference positions. The software can make a fit to the marker pattern and then calculates the centre of gravity in sub-pixel precision. By

---

[1] The chamber coordinate frame is defined by the middle plane of each chamber (*xy* plane) and its central point (origin).

means of this procedure we can to calculate the position and rotation parameters of each chamber.

For the January 2004 experimental run the photometric method was used for the inner chambers. First, photos were taken on MDC II chambers and the magnet support structure and then, after moving plane I to its measuring position, the same was done for MDC I. Afterwards the two projections were merged as shown in Figure 5.2. By comparing results to technical drawings a maximum mean deviation of 0.38 mm was found.
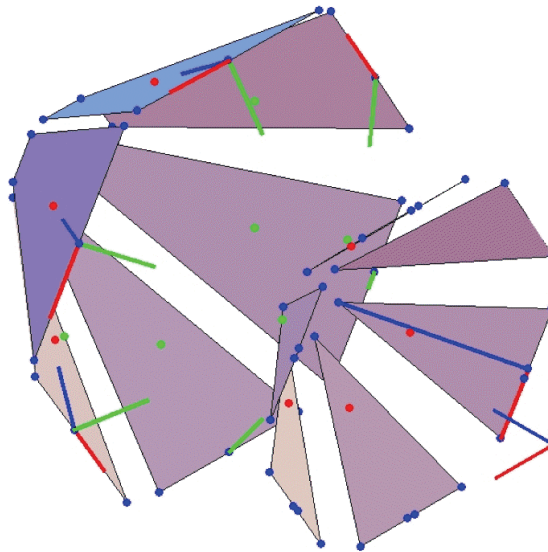

Figure 5.2 – Optical survey data (blue points) for MDC I and II. The local chamber coordinate systems are plotted in red-green-blue for the *x y* and *z* axes. The red points marking the physical centre points of the chambers on the aluminium frame, the green points the physical centres on the middle plane as used for the hits.

After performing the photometric procedure the relative positions of magnet structure and MDC II are known, and the positions of MDC I chambers with respect to each other. But for the experiment MDC I was moved toward its nominal position, and its relative alignment with respect to MDC II had to be calculated.

This was done by measuring cosmic rays, which at sea level are mostly high energy muons. We used an opposite TOF/TOFINO sector trigger for taking cosmics with a mean data rate of about 80 Hz.

A sketch of reconstructed cosmic rays by inner chambers is shown in Figure 5.3, for the sector pair 1-4. The ray hits four chambers; we start from the optical survey alignment, and the position and orientation of MDC I is varied until the distances between measured points and projected ones is minimized for all the sector combinations. After the minimization procedure most of the sector residuals are around or below 100 μm.

The last part of the procedure consists on outer chambers alignment. For them no photometric measurement was done in January 2004, so a procedure using straight tracks from no magnetic field runs was adopted.

Since we have an alignment of inner chambers, we can use straight tracks from these runs to align the outer chambers. The procedure consists of projecting the hits of inner chambers toward outer ones, and to minimize the residuals of the hit points by

shifting and rotating each outer chamber. Figure 5.4 shows a scheme of the used procedure.

The alignment obtained after all these steps can be checked by analysing the elastic scattering, as will be shown in the next paragraphs. In this case the misalignment with respect to different sectors and to the beam axis can be studied, and it is possible to estimate the angular reconstruction.
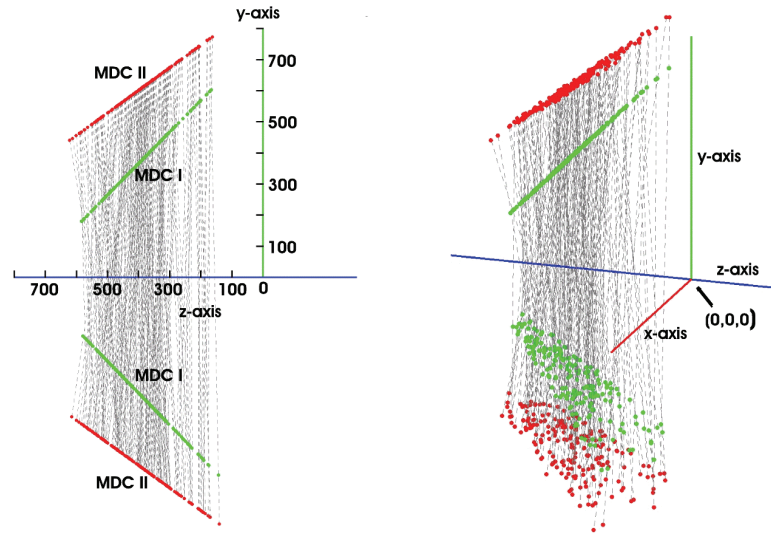

Figure 5.3 – Reconstructed cosmic rays with 4 hits in the inner chambers (MDC I and II) for the sector combination 1-4. On the left a side view (the scale is in mm), on the right a 3-D view.
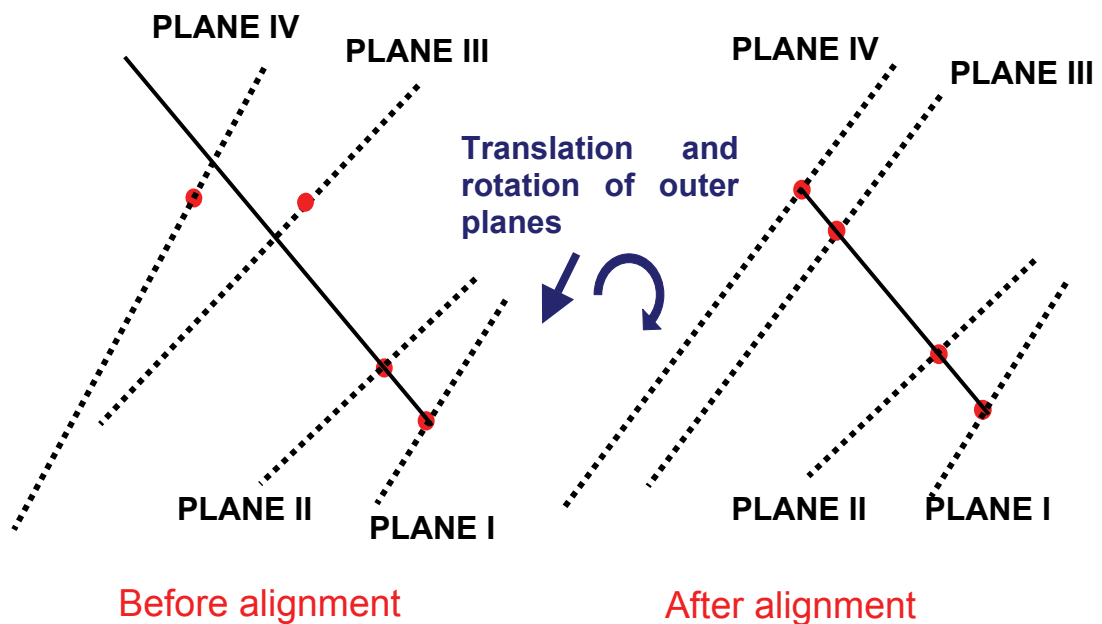
Figure 5.4 – Scheme of the outer modules alignment. The hits on the inner modules are projected onto the outer chambers, and the distance between the projected hit point and the measured one is minimized.

5.3   Tracking algorithms

The momentum of a particle which crosses the spectrometer can be reconstructed by measuring its deflection before and after the magnetic field region.

For this purpose several tracking algorithms were developed and used. "Kickplane" is a low resolution algorithm which uses the information coming from the inner MDC modules and the META system, while "Spline" and "Runge-Kutta" perform high resolution momentum reconstruction using the full tracking setup.

In the following paragraphs a description of the tracking algorithms will be given.

5.3.1   Kickplane

By measuring the trajectory deflection of a charged particle inside a magnetic field region, it is possible to reconstruct its momentum value. Indeed a charged particle which crosses a uniform magnetic field region undergoes the Lorentz force, its kinetic energy remains unaltered but it experiences a deviation from the original trajectory, as a function of its momentum.

The trajectory in the region before the magnetic field is well determined by the inner MDC chambers. Before the installation of the outer tracking system, and in particular for the November 2002 experimental run, the only information in the region after the magnetic field came from TOF and Shower hit positions. In order to reconstruct the track after the magnet, at least another point in the space is needed.

The main idea for the momentum reconstruction with this setup is to use a virtual deviation plane, called "*kick plane*" [San00]. It consists on the assumption that the trajectory deflection in the field region happens abruptly on a well defined surface, called kick plane, in which the particle momentum undergoes a transversal deviation P_T determined by the path integral of the track in the field, and not by the original momentum, as shown in Figure 5.5.

In this way the momentum P of a particle with charge Z can be calculated, in a first approximation, by knowing the momentum kick P_T and the deviation angle $\Delta\theta$, by the formula:

$$\frac{P}{Z} = \frac{P_T(\theta, \phi)}{2\sin\left(\dfrac{\Delta\theta}{2}\right)}$$

(Eq. 5-6)

By projecting the track measured by the inner MDC chambers onto the kick plane we can determine the position upon this surface. From the kick plane position we can evaluate P_T, which is parameterised by knowing the magnetic field intensity in each point of the space (measured in the past by a special magnetic probe) and by simulation studies. From hit positions in TOF or Shower detectors we can calculate angular deviations, and at last momentum values.

For a better approximation the momentum deviation depends also on the particle path length inside the magnetic field region (the longer the particle path inside the field, the larger the deviation), which is proportional to the momentum kick $P_T = 2P\sin\frac{\Delta\theta}{2}$; to take into account the effect on low momenta, another parameter is needed.
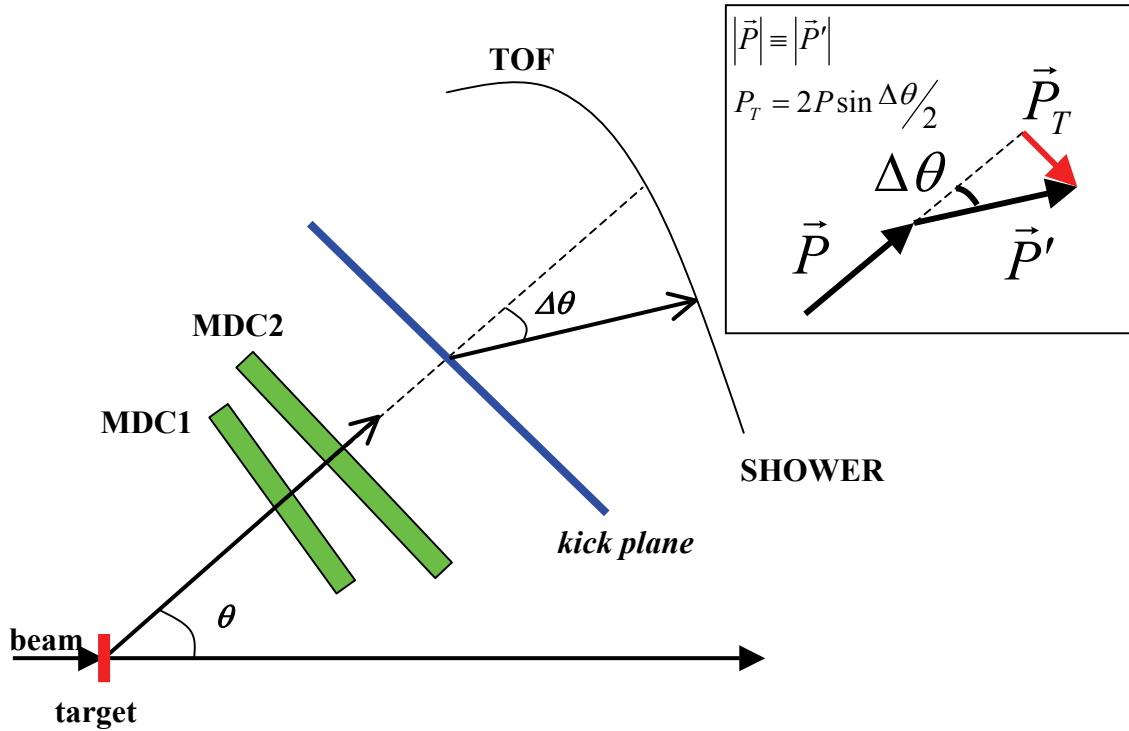
Figure 5.5 – Schematic view of the *kick plane* algorithm. It is based on the assumption that particle deviation in the magnetic field region happens abruptly in a well determined surface, called kick plane.

After these corrections, the correct momentum formula becomes:

$$\frac{P}{Z} = \frac{A(\theta,\phi)}{2\sin\left(\dfrac{\Delta\theta}{2}\right)} + B(\theta,\phi) \cdot 2\sin\left(\frac{\Delta\theta}{2}\right) + C(\theta,\phi) \qquad \textbf{(Eq. 5-7)}$$

The main limitation of this algorithm is that the track evaluation in the outer region depends on the position resolution of META system, which is around 2-3 cm (much worse than the hundreds of micron of MDC chambers). The momentum resolution estimated in simulation for C+C reactions is about 10%, which is similar to what showed by DLS [Por97].

For the p+p experiment the outer MDC setup was present and momentum reconstruction was performed by using different high-resolution methods. For this reason the kickplane algorithm analysis will not be shown in this work.

Nevertheless the kickplane algorithm is still used for tracking in 3MDC sectors; for these sectors only one hit position after the magnetic field is not enough to determine the particle trajectory. An additional point is given by the hit projection into kickplane as in the low resolution case; by combining the information of the outer chamber and kickplane point it is possible to evaluate the trajectory outside the field and then to recalculate the momentum.

5.3.2 Spline tracking

The Spline algorithm is a high resolution tracking method which uses the hit positions in all the MDC chambers, and its trajectory reconstruction is based on interpolation by spline functions.

The equations of motion of a particle inside the magnetic field, considering (x, y, z) the coordinates in the laboratory system of the HADES experiment, are the following:

$$\frac{d^2 x}{dt^2} = \ddot{x} = \frac{1}{m}\left(\dot{y}B_z - \dot{z}B_y\right)$$ **(Eq. 5-8)**

$$\frac{d^2 y}{dt^2} = \ddot{y} = \frac{1}{m}\left(\dot{z}B_x - \dot{x}B_z\right)$$ **(Eq. 5-9)**

$$\frac{d^2 z}{dt^2} = \ddot{z} = \frac{1}{m}\left(\dot{x}B_y - \dot{y}B_x\right)$$ **(Eq. 5-10)**

where B is the magnetic field and m is the mass of the particle.

The particle momentum can be written accorded to the expression:

$$P = m\sqrt{\left(\frac{dx}{dt}\right)^2 + \left(\frac{dy}{dt}\right)^2 + \left(\frac{dz}{dt}\right)^2} = m\dot{z}\sqrt{1 + \left(\frac{dx}{dz}\right)^2 + \left(\frac{dy}{dz}\right)^2}$$ **(Eq. 5-11)**

If we consider $\dot{y} = dy/dt = dy/dz \cdot \dot{z}$, we can have the equation:

$$\frac{d^2 y}{dz^2} = \frac{d}{dz}\left(\frac{dy}{dz}\right) = \frac{d}{dz}\left(\frac{\dot{y}}{\dot{z}}\right) = \frac{d}{dt}\left(\frac{\dot{y}}{\dot{z}}\right)\frac{1}{\dot{z}} = \frac{\ddot{y}\dot{z} - \dot{y}\ddot{z}}{\dot{z}^3}$$ **(Eq. 5-12)**

From this relation, by substituting $\ddot{y}$ and $\ddot{z}$ with what obtained from equations 5-9 and 5-10, after several mathematical passage we obtain:

$$\underbrace{\sqrt{1 + \left(\frac{dx}{dz}\right)^2 + \left(\frac{dy}{dz}\right)^2}\left(-B_z\frac{dx}{dz} - B_y\frac{dy}{dz}\frac{dx}{dz} + B_x\left[1 + \left(\frac{dy}{dz}\right)^2\right]\right)}_{A(z)} = P\frac{d^2 y}{dz^2}$$ **(Eq. 5-13)**

which is a differential equation that can be expressed in the form:

$$\frac{d^2 Y}{dz^2} = A(z)$$ **(Eq. 5-14)**

Coming back to the particle trajectory evaluation, the Spline algorithm reconstructs them by interpolating the hit points given by MDC chambers, two before the field and two after it[2].

---

[2] In sectors with only one MDC plane in the outer region, the algorithm evaluates the hit point in the kickplane surface and reconstructs a segment passing through this point and the MDC hit. By the intersection of this segment and the "virtual" plane of the missing chamber, the second point in the outer region is calculated.
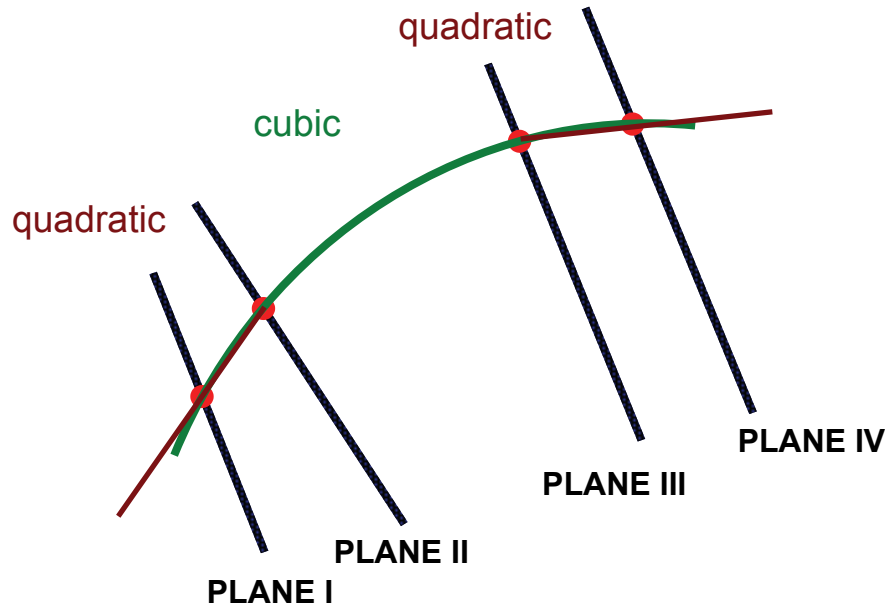
Figure 5.6 – The Spline algorithm: the trajectory of a particle is approximated by a cubic spline in the region inside the magnetic field, and by a quadratic spline in the outer region.

It assumes a cubic spline model in the field region, while the trajectory outside the field is approximated by a quadratic function, as shown in Figure 5.6.

The particle trajectory in the space is therefore determined by two spline fits, one for the x and another for the y coordinate.

After we have interpolated the particle trajectory, so x and y as a function of z, we can divide this trajectory into several steps (in general 50 steps are used) and calculate the left side of equation 5-13 for each step of the discretization. Instead to use this numerical form for $A(z)$, we evaluate it analytically by means of another cubic spline fit.

After we have an analytical form for $A(z)$, this is put it into equation 5-14, and by integrating it twice we obtain the calculated value Y_i for each point in the trajectory. In this case $Y(z)/P$ will be a good representation of the trajectory.

After we have calculated in this way the particle trajectory, we need to reconstruct its momentum. For this purpose we minimize the distance F (squared) between the calculated solution of equation 5-14 and what was obtained by the spline fit of the four MDC hit points:

$$F \equiv \left(\frac{Y_i}{P} + c_1 + c_2 (z_i - z_0) - y_i \right)^2 \qquad \textbf{(Eq. 5-15)}$$

where c_1 and c_2 are the two integration constants.

At the end, by a least square fitting of the F quantity we can calculate the particle momentum P, as well as the two integration constants c_1 and c_2, by simply imposing that the derivative of F respect to the three constants is zero and by solving the linear equation system.

As shown here the Spline algorithm is based on approximations and interpolations of particle trajectories, so the momentum value it provides does not take fully into account the physical interaction of the particle inside the magnetic field. This

means that this estimation can be improved, as it will be shown in the next paragraph. Nevertheless this algorithm has the advantage to be fast, because it does not require complicated or long calculations.

5.3.3 Runge-Kutta tracking

The Runge-Kutta algorithm is used to improve the high resolution tracking. By a minimizing procedure it adjusts the particle trajectory according to the equation of motion, obtaining better values of momenta and angles.

A charged particle moving in a magnetic field has to satisfy the following equation of motion, which describes the action of Lorentz force on a moving charged particle:

$$\frac{d^2\vec{x}}{ds^2} = \left(\frac{kq}{P}\right) \cdot \frac{d\vec{x}}{ds} \times \vec{B}(\vec{x}(s)) \qquad \textbf{(Eq. 5-16)}$$

where s is the path length, k is a constant which is proportional to the speed of light, q is the charge of the particle in units of e, P is the absolute value of the momentum and $\vec{B}$ is the intensity of static magnetic field.

A track is then completely determined by five initial (boundary) values called track parameters, which in our case are direction angles (θ and ϕ), positions (r and z^3) and momenta. A track model is a set of cross positions in each detector surface for the track defined by certain track parameters. We will denote the track parameters as p and the track model as $f(p)$.

The track model can be formulated either as a full trajectory from an analytical or numerical solution of the equation of motion (5-16), or as a functional relation $f(p)$ which relates the impact points on specific chambers to some initial parameters p.

In the Runge-Kutta algorithm the track parameters p are estimated by minimizing the least squares function:

$$Q(p) = (m - f(p))^T W (m - f(p)) \qquad \textbf{(Eq. 5-17)}$$

where m is the measurement vector, f is the track model (i.e. estimated hit vector from a given track parameter p), and W the weight matrix. The $Q(p)$ at minimum satisfies the χ^2 distributions.

In our simple case we assume the errors are uncorrelated with respect to different track parameters, so W is of the form $W_{ij} = \delta_{ij}/\sigma_j^2$, where σ_j are the errors propagated by the track fitting.

In the presence of an inhomogeneous magnetic field, as the one of HADES spectrometer, an appropriate track tracing algorithm is needed to allow a particle to be driven efficiently through a given detector setup. In our case the fourth order Runge-Kutta method of Nystrom was used for this purpose [Pre02].

---

[3] In our case the track hit position is determined by the minimum approach distance between the track and the beam axis (r coordinate), and their minimum approach point projected into beam axis (z coordinate).

In order to minimize the χ^2 value $Q(p)$, we need a functional dependence of track interceptions on each detector surface for a given set of track parameter. In practice we need to differentiate Q with respect to the track parameter p and to find a zero value for the equation below:

$$\frac{\partial Q}{\partial p} = -2(m - f(p))^T W \frac{\partial f}{\partial p} \equiv 0 \qquad \textbf{(Eq. 5-18)}$$

The partial derivative of $f(p)$ with respect to p can be computed by numerical differentiation:

$$\frac{\partial f_i}{\partial p_k} = \frac{f_i(p_0 + \Delta_k p) - f_i(p_0)}{\Delta p_k} \qquad \textbf{(Eq. 5-19)}$$

where $\Delta_k p = (0,...,\Delta p_k,...,0)$. Consequently, the equation of motion has to be solved six times: one initial trajectory $f_i(p_0)$, five variational trajectories $f_i(p_0 + \Delta_k p)$.

We need an initial trajectory (zero trajectory) to start our computation; this track model is defined by the track parameters coming from MDC angles and positions, and Spline momentum. From these track parameters we evaluate the corresponding track model (trajectory) and calculate its intersection points with the MDC planes.

This information is put into equation 5-18. In order to solve it one applies Newton's method and obtains a recursive relation between the track parameters and the ones from the previous recursive step.

In a self consistent way new track parameter values are found with a χ^2 smaller than in the previous step, and they are put again into the equation .

When the χ^2 converges ($|Q(p_i) - Q(p_{i-1}) < \varepsilon|$, usually $\varepsilon < 0.001$ is enough), the fit procedure stops and give the final track parameters. So the Runge Kutta algorithm not only improves the momentum value but also the angular variables, as it will be shown in experimental data.

5.4 No-Field runs

In the following paragraphs it will be shown the analysis of angular information from the inner and outer MDC chambers, obtained in no-field runs by means of the elastic scattering channel.

In particular no-field runs are the only ones where it is possible to study the behaviour of the outer chambers, because in this case the outer polar angle information is not distorted by the bending of the magnetic field.

The elastic selection is performed by taking combinations of two fitted segments in the same event which hit opposite sectors, and belonging to the same kind of modules (therefore combining inner segments with only inner segments, outer segments with only outer segments). An additional condition was put at the 1st level trigger bit, selecting only events with multiplicity two in META and opposite sectors.

First the vertex reconstruction will be explored, which allows to estimate the position of the beam line. Then, a study on azimuthal and polar angles will be shown.
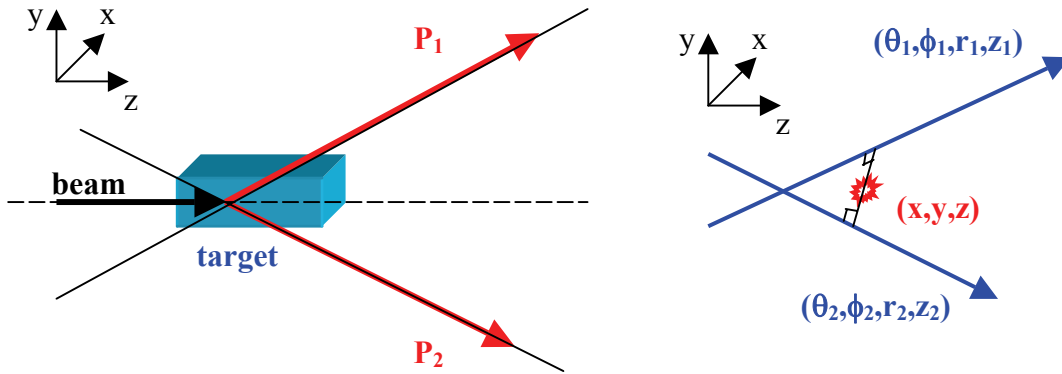
5.4.1 Vertex reconstruction

Figure 5.7 – Target reconstruction for a segment pair. The vertex is defined as the point of closest approach of the two straight lines.

A relevant information about a nuclear collision is the point in the target where it took place. Assuming that the interaction between projectile and target is point like, we can define the interaction vertex as the point of closest approach of all primary tracks in the event.

By knowing the vertex position we are able to select only reactions which occurred inside the target region, we can check if there are other particle sources and where they are placed, and also evaluate the beam quality (Figure 5.7).

In our case we use fitted track segments belonging to opposite sectors, and we analyse separately inner and outer chambers. If we assume both tracks are coming from the same interaction point, we can calculate the vertex point.

A line in the space is defined by four parameters[4], which in our case are the polar and azimuthal angles θ and ϕ, and the two position parameters r and z. Each pair of MDC chambers (inner and outer) reconstructs the trajectory of the particle which hit them, a straight line if we can neglect the residual magnetic field in the chamber region, and it provides the parameters which are needed to geometrically define the line.

Let's define a line in the space as:

$$\vec{P}_i = \vec{r}_i + \vec{\alpha}_i \cdot t \qquad \text{(Eq. 5-20)}$$

where $\vec{r}_i$ is the position vector for the line i, $\vec{\alpha}_i$ its direction vector and t is a free parameter.

The distance of a point $\vec{x}$ from the line will be given by:

$$d_i = (\vec{r}_i - \vec{x}) \times \vec{\alpha}_i \qquad \text{(Eq. 5-21)}$$

---

[4] A line in the space (not parallel to the *z* axis) can be expressed in the reduced form as:

$$\begin{cases} x = hz + x_1 \\ y = kz + y_1 \end{cases}$$

where h, k, x_1 and y_1 are opportune coefficients. In this case the point $(x_1, y_1, 0)$ is the intersection point between the line and the plane *xy*.

We can than build a χ^2 function as the sum of the squares of the distances between the vertex point $\vec{x}$ and the two track lines:

$$\chi^2 = \sum_{i=1}^{2} \frac{d_i^2}{\sigma_i} = \sum_{i=1}^{2} \frac{\left((\vec{r}_i - \vec{x}) \times \vec{\alpha}_i \right)}{\sigma_i}$$

<div align="right">**(Eq. 5-22)**</div>

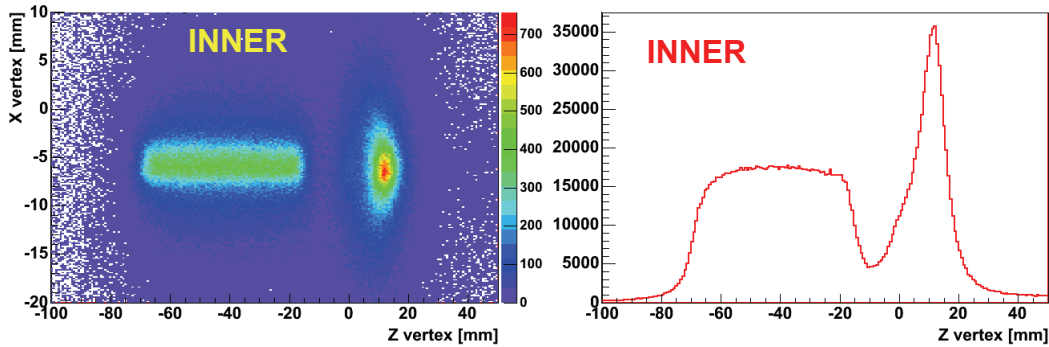where σ_i is the position error given by the error propagation from MDC time fits.

Figure 5.8 - Vertex reconstruction plots for inner MDC chambers. Left side: *x* vs *z* plot for vertex coordinates in the laboratory frame. Right side: *z* distribution. Apart from the target shape it is possible to see a prominent peak downstream, coming from the interaction of the beam with material of the beam pipe.

The vertex position is then calculated by minimizing this χ^2 function, and the obtained χ^2 will be a measure of the minimum distance of the two tracks.

The left side of Figure 5.8 shows a two-dimensional plot of the reconstructed vertex (*z* vs *x*) for the inner MDC chambers, in the laboratory coordinate system.

In the laboratory coordinate system the *z* axis corresponds to the beam line, larger values of *z* are in the downstream direction, while negative ones are upstream. The beam is thus supposed to stay on *x*=0, *y*=0.

The target shape is correctly reconstructed and its 5 cm length is well visible, as shown in the right side of Figure 5.8, but it is possible to see a second structure at about 3 cm from the target in the downstream direction.

The reason of this second peak comes from the beam focusing in the early days of the January 2004 experiment, when the no-field measurement was being performed. Indeed if we check the *x* distribution we can see it is not centred on the zero, but it has a displacement of about 6 mm; the beam direction was shifted with respect to the centre of the beam pipe, and it hit a piece of material placed downstream. This effect is due to the fact the beam pipe becomes slightly narrower after the end point of the target; by checking technical drawings of the target region it was found that a shift of 6 mm is enough to let the beam hit even this metal structure, and so to produce the secondary peak whose position in *z* is in agreement with the drawings.

 In the field-data, after the beam was better aligned and focused, this structure becomes negligible.

As we want to select elastic pairs, we have to remove all the tracks coming from this second peak. This is done by selecting only pairs coming from the target region, applying a cut on the *z* vertex coordinate of -80 mm < z < -20 mm.

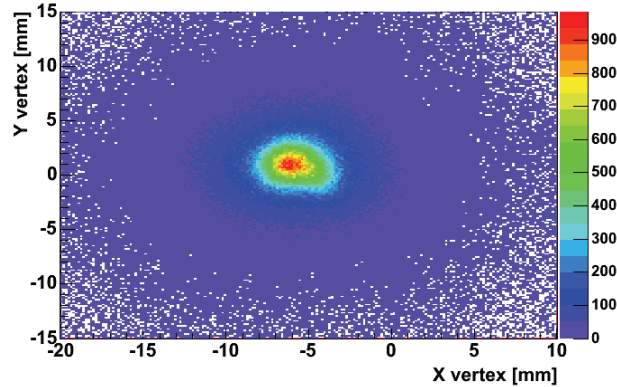**Figure 5.9** – Vertex plot for *y* vs *x* after the *z* selection (−80 mm < *z* < -10 mm). The estimated vertex reconstruction resolution is of about 2mm for both the coordinates.

Figure 5.9 shows the *y* vs *x* distribution after the *z* selection. By fitting in a range close to the peak the *x* and *y* one-dimensional distributions with gaussian functions, we obtain the position of the beam and its spread[5] in *x* and *y* coordinates:

- X_{inner} = -5.8 ± 2.0 mm
- Y_{inner} = 0.8 ± 1.9 mm

The same procedure can be repeated for the outer MDC chambers.
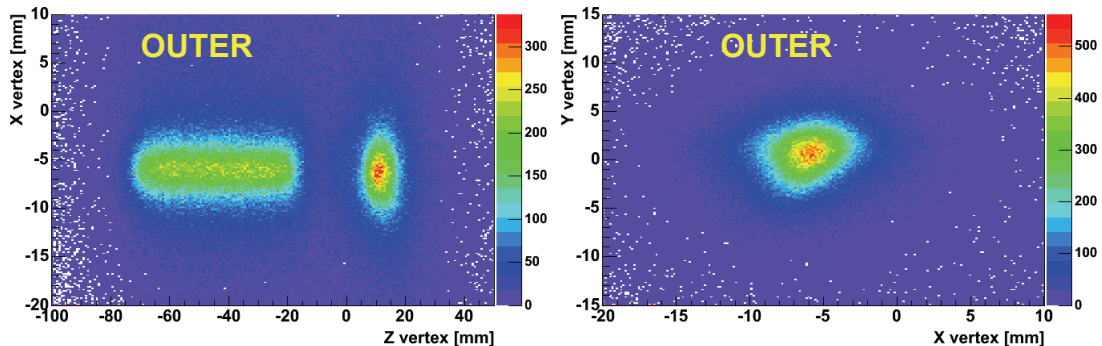
Figure 5.10 – Vertex plots for outer MDC chambers (left side: *x* vs *z* - right side: *y* vs *x* after the −80 mm < *z* < -10 mm selection). We can see that the *x* and *y* widths are larger than the corresponding ones from the inner modules, because of their larger distance from the target region, and therefore their reconstruction power turns out to be less effective.

The vertex plots for the outer MDC chambers are shown in Figure 5.10. Even for the outer chamber pairs the second peak is prominent, and then the same *z* selection was applied.

We can see that the *x* and *y* distributions are broader than the inner chamber ones, as it is evident from the results of gaussian fits near the peak:

---

[5] The sigma of the gaussian fit is the quadratic sum of the beam width plus the vertex reconstruction resolution. Considering that the MDC chambers have a position resolution of ∼ 100 μm, the corresponding vertex precision can be considered as negligible.

- $X_{outer} = -6.0 \pm 2.4$ mm
- $Y_{outer} = 0.6 \pm 2.5$ mm

This because the outer chambers are farther than the inner ones from the target region: the error on hit positions, after being propagated back to the target region, becomes larger than the error obtained using the inner ones.

As we can see, the centres of vertices positions are consistent with what evaluated by the inner modules.

5.4.2 Azimuthal angle

After selecting track pairs coming from the target region, that is after removing the right hand side peak, we can evaluate angles by using elastic pairs.

The first considerations come from azimuthal angles. Coplanarity of the two elastic protons is expressed by the equation:
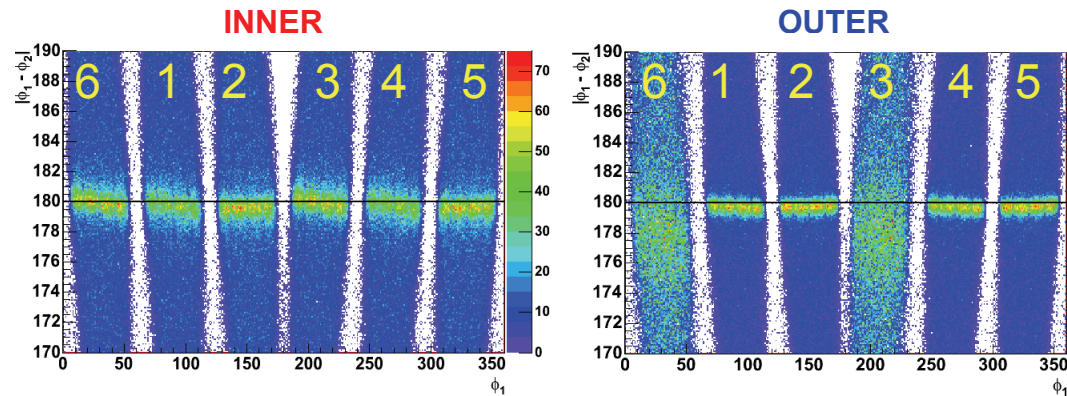
Figure 5.11 – Difference in azimuthal angles between two tracks hitting opposite sectors, for inner chambers (left side) and outer chambers (right side). For outer chambers the counts on 3MDC sectors are multiplied by a normalization factor in order to compare their distributions to other sectors.

$$\left|\phi_1 - \phi_2\right| = 180° \tag{Eq. 5-1}$$

we can plot this difference to check the azimuthal angle resolution of the alignment.

Figure 5.11 shows the difference in azimuthal angle of opposite sector pairs as a function of the azimuthal angle ϕ of one of the two tracks, separately for inner (left plot) and outer (right plot) segments.

In the laboratory notation, the first sector is placed between 60° and 120°, the second one between 120° and 180° and so on, while the sixth stays between 0° and 60°. In the right plot we can see the loss in angular resolution for the sectors equipped with only 3 MDC chambers (the 3rd and the 6th sectors). These sectors were missing the outermost module and then the lower resolution kickplane information was used for the angular reconstruction.

Even if no particle identification was performed, by simply using tracks in opposite sectors we are able to find the elastically scattered protons. Indeed the peak at 180° is well defined and prominent (apart from the sectors with 3 MDC modules).

By comparing inner and outer chambers (only for sectors with 4 MDC modules), the outer ones have a better resolution than the inner ones, contrary to what was shown in paragraph 5.4.1 for the vertex reconstruction. This means that the particle direction is better reconstructed by the outer planes, mainly because it is calculated on a longer distance and then the spreads are reduced with respect to the inner chambers. By checking the behaviour of the 180° peak as a function of the azimuthal angle, some small systematic deviations are present: for some sectors the distribution looks a bit tilted, instead of being a perfectly horizontal line. The alignment procedure worked quite well, but some improvements can still be done.

The main reason of the small systematic deviations is the beam position not centred along the *z* axis but a bit shifted, as shown in Figure 5.9 and Figure 5.10; this fact introduces a low order effect on the direction reconstruction in the laboratory coordinate system. Moreover at the moment the hypothesis of a tilted beam direction with respect to the *z* axis is under study, and it could explain these systematic deviations and the angular resolution values worse than expected[6].
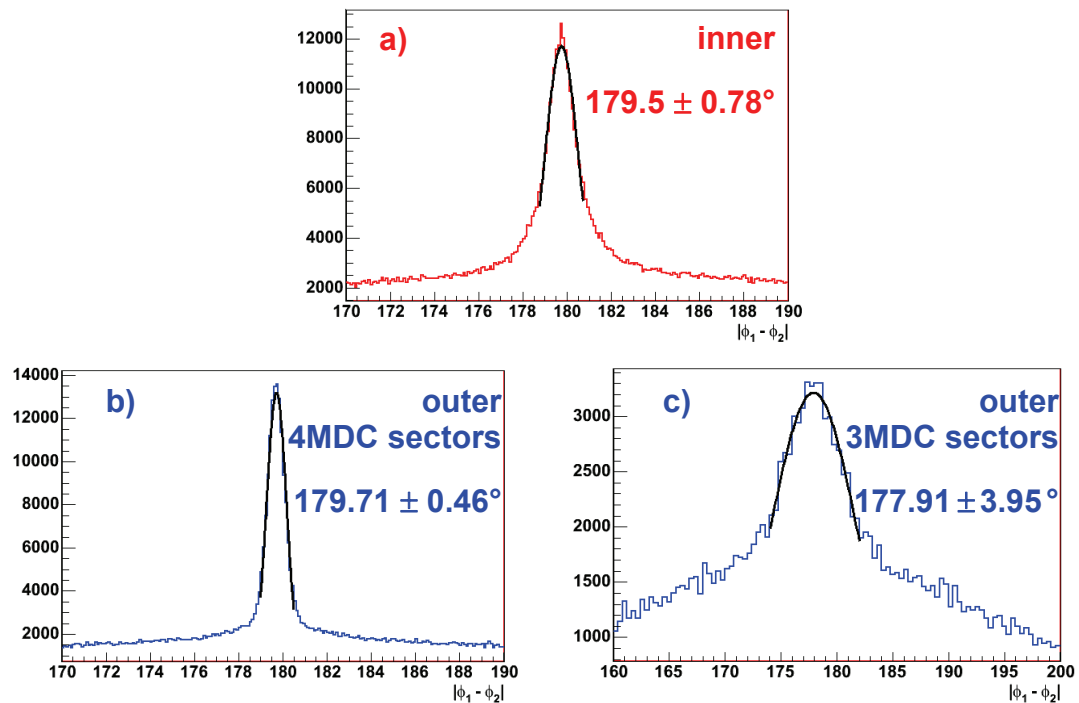
Figure 5.12 – Coplanarity plots for different chambers: a) inner MDC modules; b) outer MDC modules, 4MDC sectors; c) outer MDC modules, 3MDC sectors. The gaussian fit near the peak provides an estimate of the single segment azimuthal angular resolution.

Looking to the outer chambers– of the 3MDC sectors, the bump width is much broader and not centred in the correct 180° position. This is due to the poor resolution of one chamber segment reconstruction, which does not allow to obtain high resolution tracking and alignment.

The plots of Figure 5.12 show differences in ϕ for inner and outer segments, the latter separately for 4MDC and 3MDC sectors.

---

[6] The alignment procedure calculates absolute positions in the laboratory coordinate system. But a possible inclination of the beam alters the reconstructed angular variables as well as the momenta.

Assuming the same azimuthal resolution for both the opposite sectors chambers ($\sigma_{\phi_1} = \sigma_{\phi 2}$), we can evaluate the average single chamber ϕ resolution by the relation:

$$\sigma_{|\phi_1 - \phi_2|} = \sqrt{\sigma_{\phi_1}^2 + \sigma_{\phi_2}^2} \equiv \sqrt{2}\sigma_\phi \qquad \textbf{(Eq. 5-23)}$$

If we divide by $\sqrt{2}$ the fit widths shown in Figure 5.12, we obtain the following resolution values:

$$\sigma_\phi^{inner} = 0.6°$$

$$\sigma_\phi^{outer\,4MDC} = 0.3°$$

$$\sigma_\phi^{outer3\,3MDC} = 2.8°$$

5.4.3 Polar angle

An analysis similar to what was done for the azimuthal angle ϕ can be applied also for the polar angle θ. In this case the useful relation is:

$$\tan\theta_1 \cdot \tan\theta_2 = \frac{1}{\gamma_{CM}^2} \qquad \text{(Eq. 5-2)}$$

where for 2 GeV collisions (no-field run) the reaction kinematics states that $1/\gamma_{CM}^2 = 0.4841$.

Figure 5.13 and Figure 5.14 show sectorwise distributions for θ_1 vs $\tan\theta_1 \cdot \tan\theta_2$, respectively for inner and outer modules.

The plots are very useful in order to establish the quality of the alignment, because they are strongly dependent on it.

In the outer chambers we can see the poor resolution of 3MDC sectors, but even in this configuration the peak is visible and close to the kinematical prediction.

In Figure 5.15 there are the $\tan\theta_1 \cdot \tan\theta_2$ plots for different chambers. The peaks were fitted with gaussian functions, and the obtained centroids stay in the position expected by the kinematical calculation. Once again we see that the 3MDC-sector geometry needs an improvement, but apart from this consideration the numbers clearly show the high quality of the alignment achieved by means of the described procedure.

At the moment new alignment procedures are under study, which could achieve even better results. In particular it is under study how to use the additional information coming the from proton-proton elastic scattering. None of these procedures was tested on the January 2004 data yet.
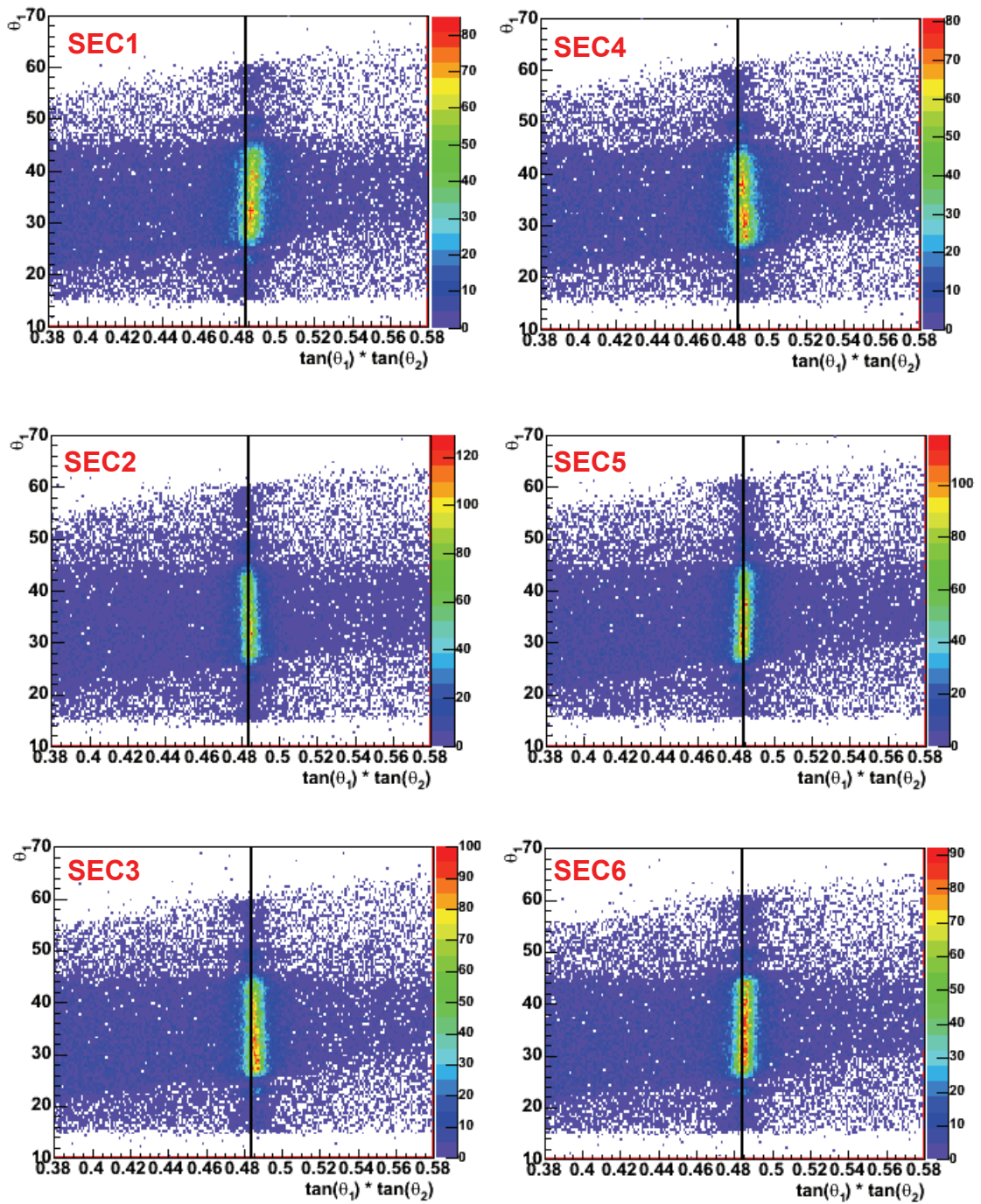
Figure 5.13 – 2D plots for θ_1 vs $\tan\theta_1 \cdot \tan\theta_2$ (inner chambers), sectorwise; the black line represents the expected value from the reaction kinematics. The chambers show quite a good alignment, and no systematic deviations are present.
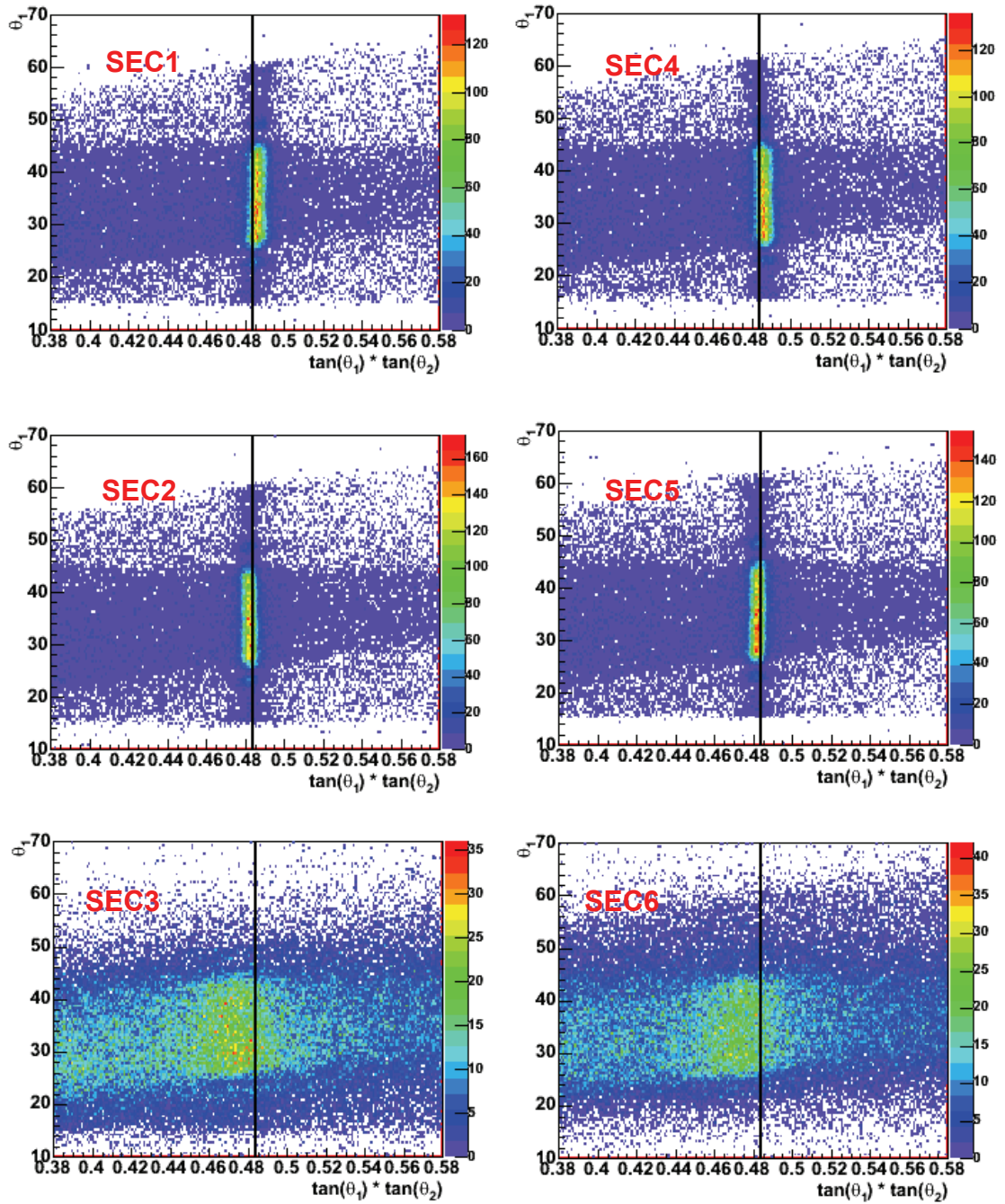
Figure 5.14 – θ_1 vs $\tan\theta_1 \cdot \tan\theta_2$ plots for the outer chambers, sectorwise; the black line is the expected value from the reaction kinematics. Also these chambers show a good alignment, apart for 3MDC sectors.
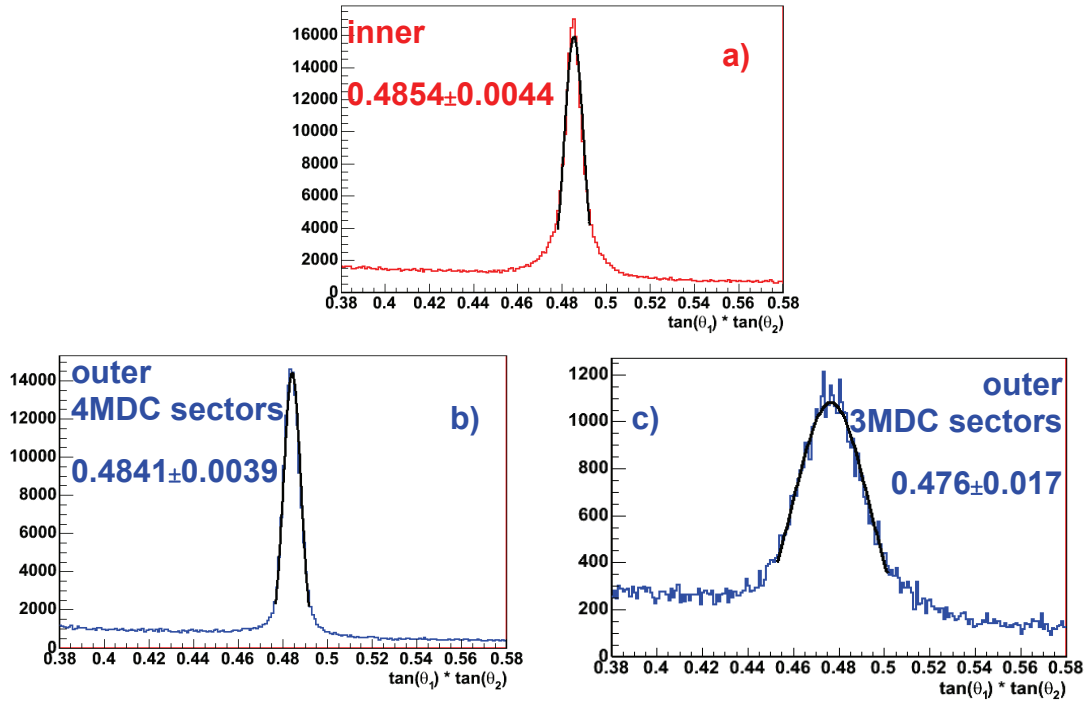
Figure 5.15 - $\tan(\theta_1)\cdot\tan(\theta_2)$ distributions for different chambers: a) inner MDC modules; b) outer MDC modules, 4MDC sectors; c) outer MDC modules, 3MDC sectors. The peaks were fitted with gaussian functions, and the fit values are reported in the plots.

5.5   *Field data – Spline Tracking*

While the no-field data were used only for calibration and alignment purposes, most data were acquired with magnetic field, in order to use the deflection to reconstruct the particle momenta.

But during the magnetic field ramp-up the beam focusing was changed and improved, and it has to be checked again; the same alignment analysis has to be redone, in order to highlight possible effects of the magnetic field on the angular resolution.

Because of the magnetic deflection, the information from the outer segments cannot be used for alignment purposes, therefore only the analysis for the inner one will be shown.

Momentum reconstruction will be studied, and its resolution will be evaluated, by using spline tracking algorithm.

The analysis of Runge Kutta algorithm and the comparison with spline will be shown in the paragraph 5.6.

5.5.1   *Vertex reconstruction*

The same procedure of paragraph 5.4.1 was applied for field data.

This time we do not use the segment information from MDCs, but we use the full tracks reconstructed by spline algorithm. A full track is made by the correlation of an inner segment, an outer segment and a META hit, and it carries along the value of the reconstructed momentum.

In Spline case angular and position parameters are given by the inner MDC segment. All the plots that will be shown were made using these variables.

But this time we can use an additional information, which was not present in the files without magnetic field, while trying to select our proton elastic pair. From the trajectory deviation inside the magnetic field the tracking algorithm can evaluate the charge polarity of the particle; thus we can select positive charged particles hitting opposite sectors, in order to select our protons.
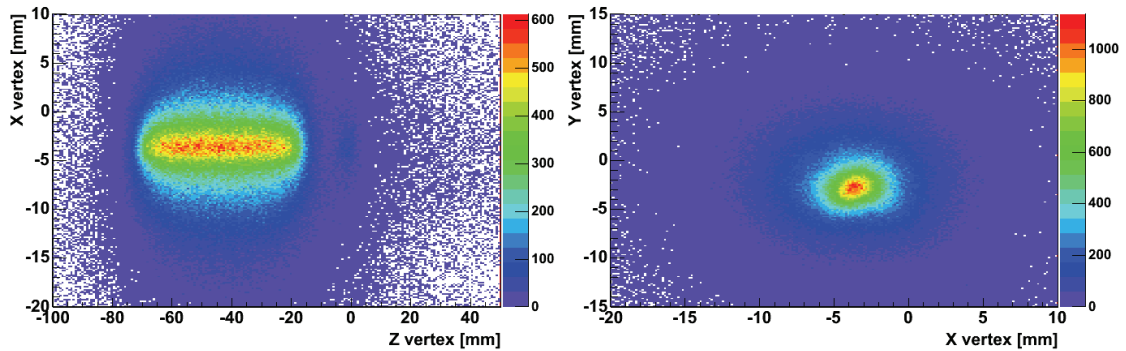
Figure 5.16 – Vertex plots for opposite sector tracks (left side: *x* vs *z* - right side: *y* vs *x*). With the new beam focusing, the second peak is now negligible and the cut on *z* is not needed anymore.

Figure 5.16 shows vertex plots for field data, after the beam focusing. As it is shown in the *y* versus *x* plot (right side), the beam spot was shifted a few millimetres in both *x* and *y* directions; in particular it results better centred in the *x* position. The main result of this improved focusing is that now the second peak (left plot) is reduced with respect to the no-field runs, because the number of particles hitting the beam pipe narrowing was strongly reduced.

In this case the selection on the *z* vertex coordinate is not needed anymore, because this contribution became negligible.

One dimensional distributions for *x* and *y* were fitted once again with gaussian functions. The results are:

- X_{spline} = -3.6 ± 2.5 mm
- Y_{spline} = -2.7 ± 2.5 mm

The widths are broader than those obtained in no-field data, but we have to consider that a low fringing field is still present near the MDC chambers, in particular for those planes closer to the coils. This low field influences the track reconstruction, and can give rise to a decrease in the resolution.

5.5.2 Azimuthal angle

The same analysis of 5.4.2 was performed for field data.

Figure 5.17 shows coplanarity distributions as a function of the azimuthal angle for one particle of the pair (left side). We can see that the distribution is well centred at 180° as expected, and no strong systematic behaviour can be seen from the plot. However the worse resolution does not allow to perform a fine check of the alignment.
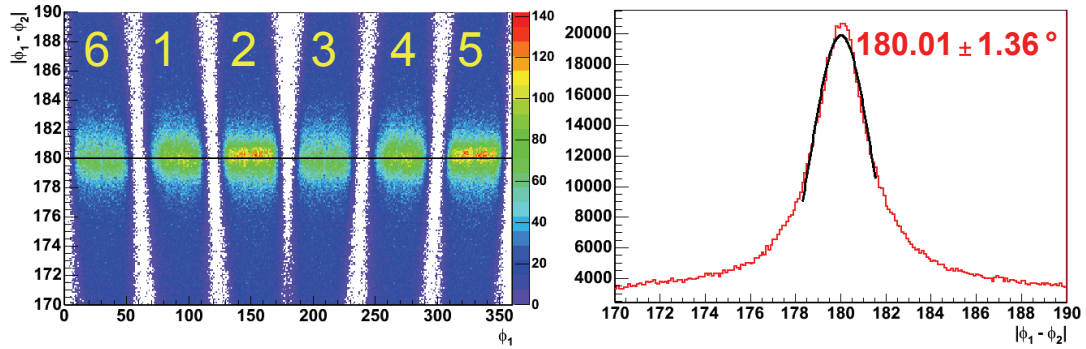
Figure 5.17 – Azimuthal plots for Spline tracking. On the left-hand side $|\phi_1 - \phi_2|$ vs ϕ_1; on the right-hand side a single $|\phi_1 - \phi_2|$ distribution with the results of a gaussian fit.

In the one-dimensional spectrum on the right-hand plot, the main peak is closer to 180° than before (mainly due to the beam closer to the z axis), but the width of the gaussian fit is about twice as large. We can compute the angular resolution by means of the same procedure, obtaining a value of $\sigma_\phi = 0.96°$ (in no-field data it was 0.6° for the inner MDC chambers).

5.5.3 Polar angle

In the field data the kinetic energy of the incoming proton was 2.2 GeV, thus the polar angle kinematical constant was $1/\gamma_{CM}^2 = 0.4598$.

Figure 5.18 shows the one-dimensional distribution for $\tan\theta_1 \cdot \tan\theta_2$, integrated over all the sectors. We can see that the peak is in the expected position. The width of a gaussian fit shows also in this case a worsening, consistent with what was found for the azimuthal angle resolution.
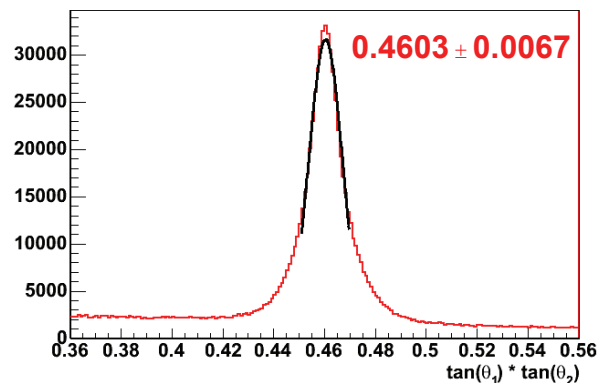
Figure 5.18 – Distribution for $\tan\theta_1 \cdot \tan\theta_2$ integrated over all the sectors.

In Figure 5.19 θ_1 versus $\tan\theta_1 \cdot \tan\theta_2$ plots are shown sectorwise. The distributions are well centred around the kinematical value, but some systematic deviations from the vertical line are visible, in particular in the low polar angle regions. Nevertheless the achieved alignment is quite good and it can be fruitfully used with field data, as will be shown in the following chapters.
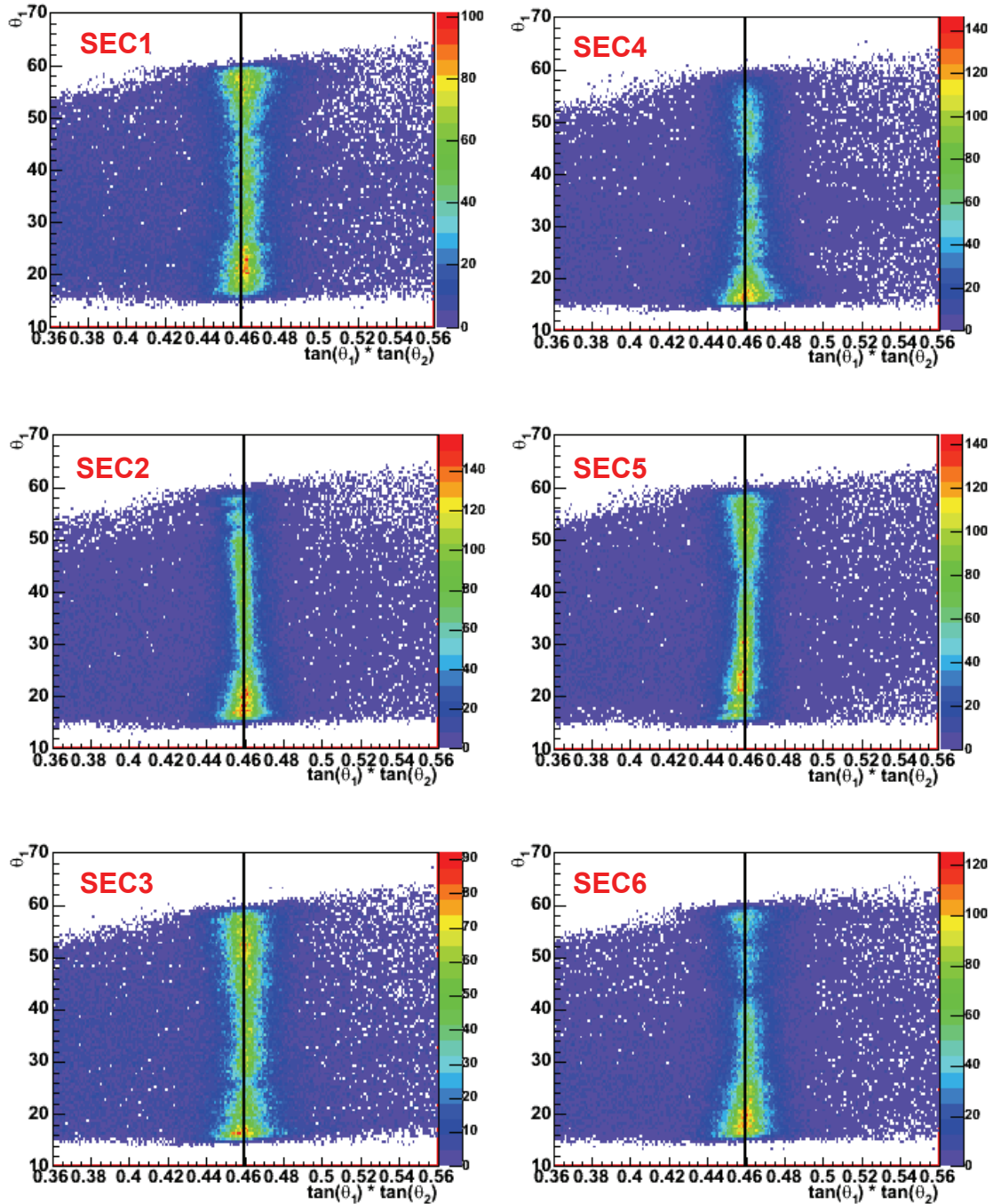
Figure 5.19 – 2D plots for θ_1 vs $\tan\theta_1 \cdot \tan\theta_2$ for positive charged spline tracks, sector by sector; the black line represents the expected kinematical value. The distributions are well centred around the expected position. Nevertheless some small deviations are still visible.

5.5.4 Elastic selection

By combining the angular information about polar and azimuthal angles we can choose pairs close to the expected peak positions, in order to select only elastic pairs and take out most of the background.
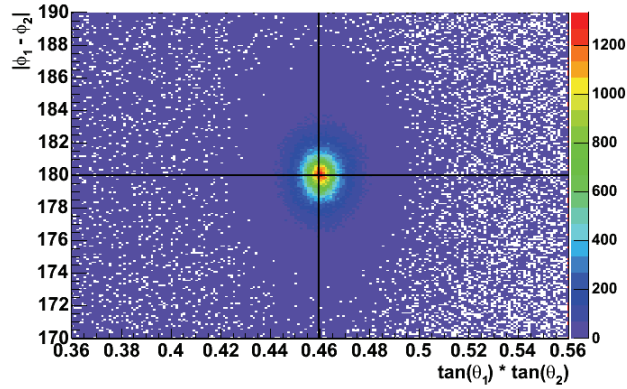
Figure 5.20 − $|\phi_1\text{-}\phi_2|$ vs $\tan\theta_1\cdot\tan\theta_2$ plot. Elastic pairs are placed in the region of the main peak. The black lines show the kinematical prediction

In Figure 5.20 we can see how the use of a suitable topological constraint can help to identify pairs coming from the elastic scattering.

First of all we can define two variables given by:

$$\Phi \equiv |\phi_1 - \phi_2|, \qquad \Theta \equiv \tan\theta_1 \cdot \tan\theta_2 \qquad\qquad \textbf{(Eq. 5-24)}$$

So we can construct a χ^2 function as:

$$\chi^2 = \frac{(\Phi - \Phi_0)^2}{\sigma_\Phi^2} + \frac{(\Theta - \Theta_0)^2}{\sigma_\Theta^2} \qquad\qquad \textbf{(Eq. 5-25)}$$

where Φ_0 and σ_Φ are centroid and sigma of the gaussian fit over azimuthal difference distributions (Figure 5.17), while Θ_0 and σ_Θ are the fit results obtained by the product of polar angle tangents. In this case elastic pairs should stay at the peak positions, and their χ^2 value should be minimal.

On the left plot of Figure 5.21 the χ distribution is shown. The main peak corresponds to elastic pairs so that we can select them by introducing an upper threshold, in order to strongly decrease the background contribution coming from other processes (which is almost constant). A selection on pairs with $\chi < 3$ was applied, in order to have most of the elastic pairs with low background contamination. The right plot of Figure 5.21 shows how this cut selected pairs on the main peak (the black dots correspond to pairs rejected by the cut).

By applying the shown topological angular selection for positive charged pairs, we are able to select elastic pairs and to evaluate their momentum reconstruction.
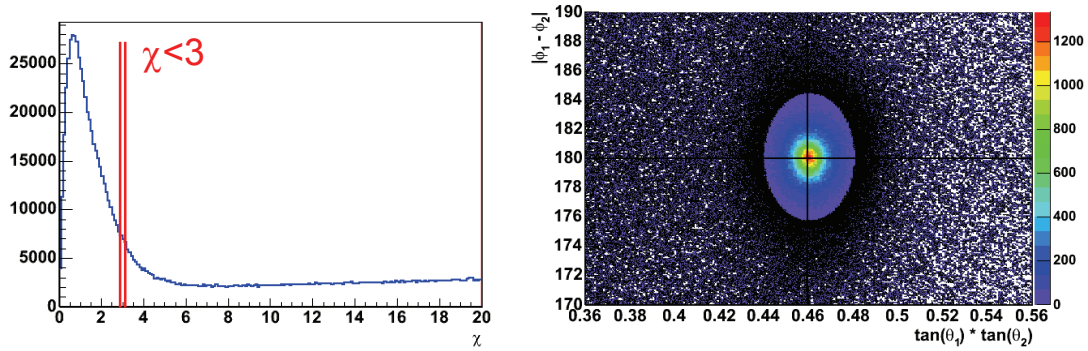
Figure 5.21 – χ distribution for positive charged pairs (left-hand side). By selecting pairs with χ<3 it is possible to separate elastic pairs from the background. On the right-hand side the topological spectrum is shown after this cut; the black dots correspond to rejected pairs.

5.5.5 *Momentum reconstruction*

Assuming that a track is a proton coming from an elastic collision, from its polar angle θ it is possible to calculate the "theoretical" value of momentum, and to compare it with the results of the tracking algorithm.

Indeed the relation that correlates momenta to polar angles (for elastic scattering) is given by the formula:

$$p(\theta) = \frac{p_{proj}}{\cos\theta + \gamma_{CM}^2 \sin\theta \tan\theta} \qquad \text{(Eq. 5-3)}$$

where p_{proj} is the momentum of the incoming proton (projectile).

After selecting elastic pairs from spline tracking, by means of the χ cut, we can plot the ratio between the kinematical prediction $p(\theta)$ and the spline value of momentum p for one of the two protons, as shown in Figure 5.22. The used momentum values are in absolute units, no renormalization was applied.

We see that all the peaks are centred around 1 even for the 3MDC sectors, showing that the momentum provided by the algorithm is correct as well as the alignment.

We can do a gaussian fit[7] over the peak, in order to estimate the position of the peak and the momentum resolution of the algorithm. The results of the fit are shown in Table 5-4.

The obtained momentum resolution values also depend on the polar angle resolution, that was used to estimate the theoretical value.

Sector	1	2	3	4	5	6
p/p(θ)	0.958	0.978	0.942	0.963	0.948	0.947
σ[%]	9.3	5.8	16.2	4.9	4.8	7.5

Table 5-2 – Centroids and momentum resolution fit values for Spline algorithm.

---

[7] In reality the momentum p does not follow a gaussian distribution, while the quantity $1/p$ presents this shape, because of the particular geometry of the HADES magnetic field. But we are interested in the momentum resolution, so the fit was done over the momentum distribution.
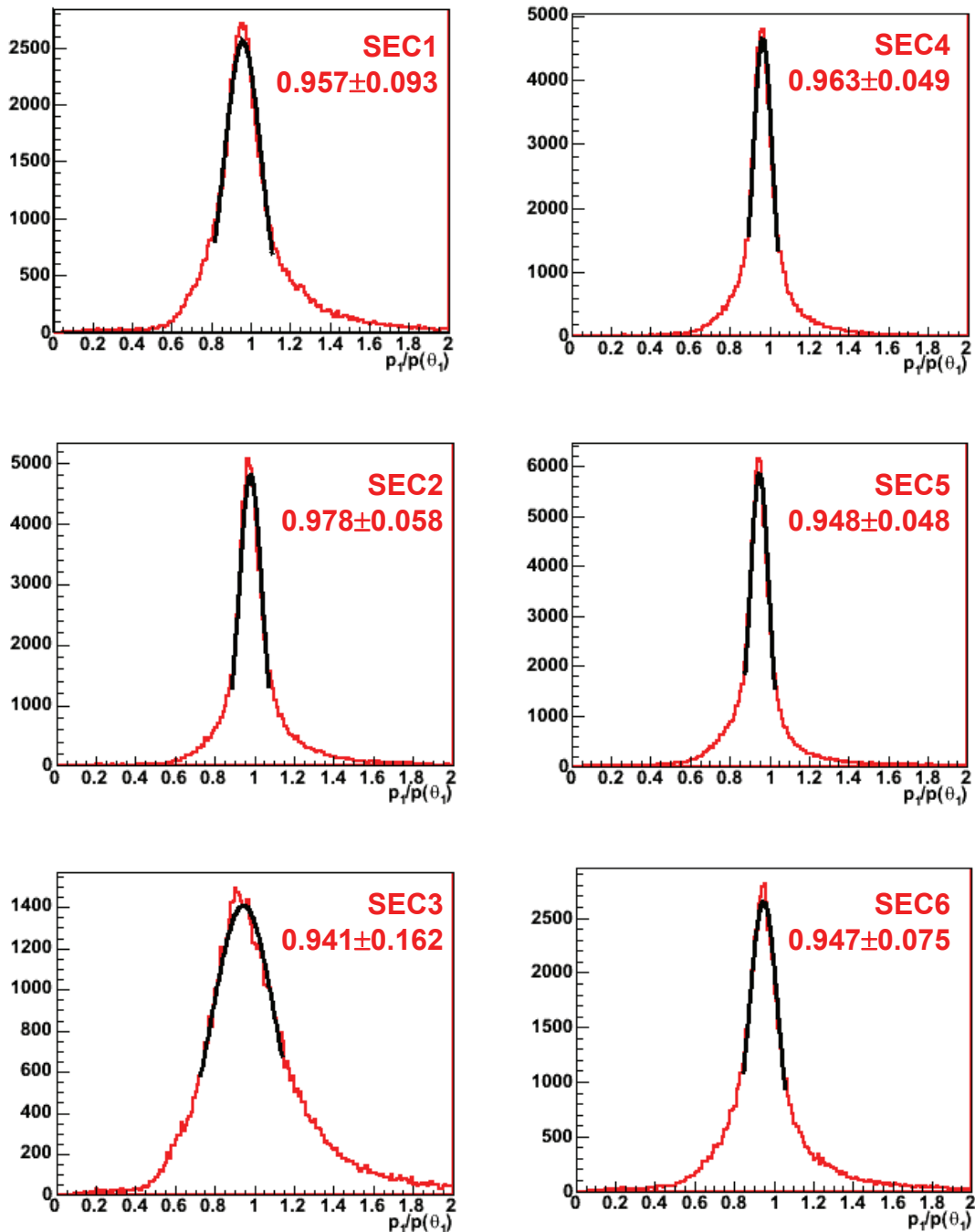
Figure 5.22 – Ratios between reconstructed momentum from spline and kinematical prediction, by using the polar angle θ. The reported values are the results of a gaussian fit in the peak region.

Three MDC sectors show a resolution close to 5% (sectors 2, 4, 5). Sector 1 shows a broader distribution because of two wire layers which were switched off on the inner planes (less cells available for fitting, and thus worse resolution).

Concerning the sectors with only 3 MDC present, namely sector 3 and sector 6, we have to consider that only one MDC chamber was available for the reconstruction of the outer segment. Sector 3 has a bad resolution (16%), but for this sector only five wire layers were working properly, and some cathodes had reduced voltage. For this chamber the drift time fit was not possible for most of the tracks (we need at least 5

points to reasonably fit a line in the space), thus the resolution is mainly what comes from the cell size. Sector 6 shows a resolution (7.5%) which is even better than the sector 1, and below the 10% expected from the low-resolution kickplane algorithm. This tells us that the spline reconstruction can perform quite well even in a 3MDC sector.

In order to check possible systematic deviations we can look at resolution plots as a function of the polar angle, as shown in Figure 5.23.

It is evident that at low polar angles, which correspond to higher momentum values, a systematic deviation is present in all the sectors. This effect is connected to the assumed position of the chambers in the laboratory frame after the software alignment, which is close to the real value but still needs a second order improvement.
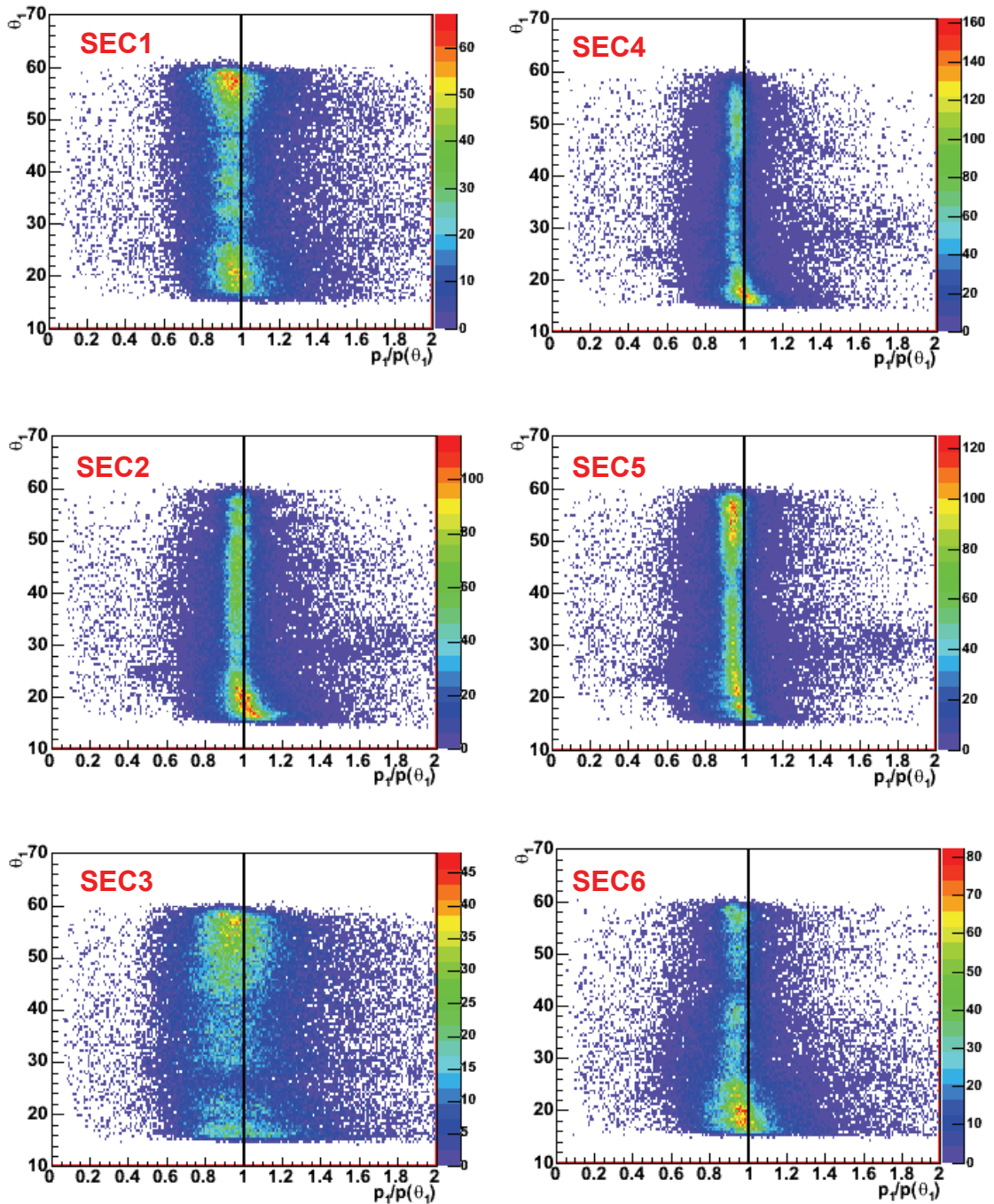
Figure 5.23 – Ratios between kinematical and reconstructed momentum for spline tracking, as a function of polar angles.

Moreover all the peaks show a global systematic shift toward lower values of reconstructed momentum, the distribution centroids are placed at around 95% of the theoretical prediction. So the Spline algorithm underestimates momenta of a factor 5%; this systematic deviation is not present in simulation and it can be correlated to a global misalignment of the chambers respect to the magnetic field. This effect however is recovered by the Runge Kutta algorithm, and it does not harm the physical analysis.
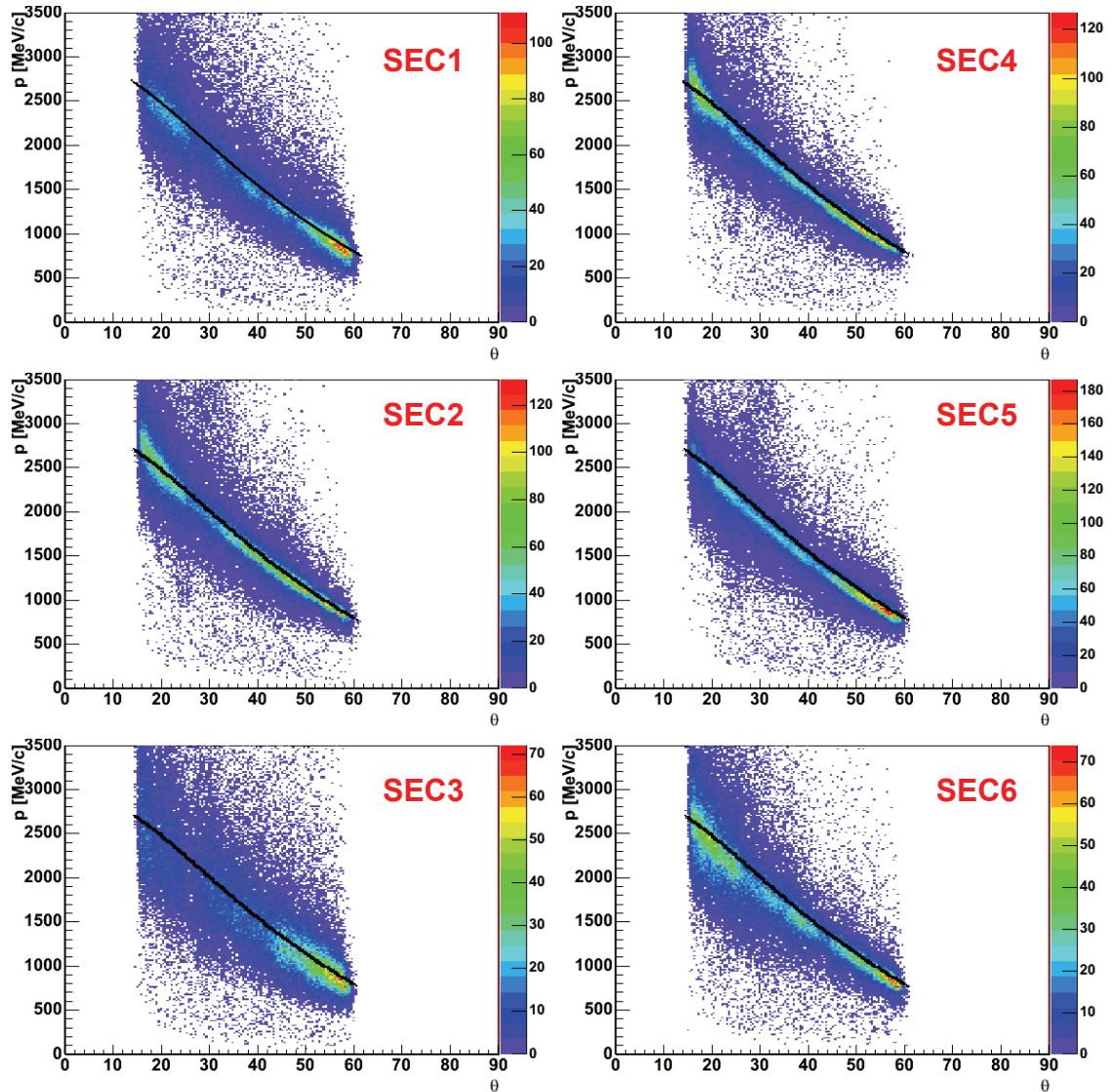

Figure 5.24 – Momentum versus polar angle plots for one particle of elastic pairs. The black lines represent the expected behaviour.

Figure 5.24 shows the measured momentum versus the polar angle of one proton of elastic pairs, sector by sector. The black lines represent the kinematical prediction.

We can see how momenta and polar angles are correlated, and how in the lower angle region the spread in momentum becomes larger, due to high momentum values which are difficult to reconstruct because of their small deviations. The HADES acceptance for elastic pairs is well visible in these plots (between 16°-60° in polar angle, between 800-2700 MeV/c in momentum).

When evaluating the resolution we have to consider that the minimum momentum value of the detected protons is about 800 MeV/c, while in general HADES

is best suited to detect leptons which possess lower momenta. So we can consider these values as a sort of upper limit to the actual momentum resolution for leptons.

In Figure 5.25 plots distributions of momentum of one elastic proton versus momentum of the other one are shown for different sector pairs, compared to theoretical prediction. It appears in the central region of the plot, at momentum values around 1600 MeV/c, there is a discrepancy between the theoretical and the measured value in more or less all the sectors, discrepancy that vanishes at the edge of the plot.
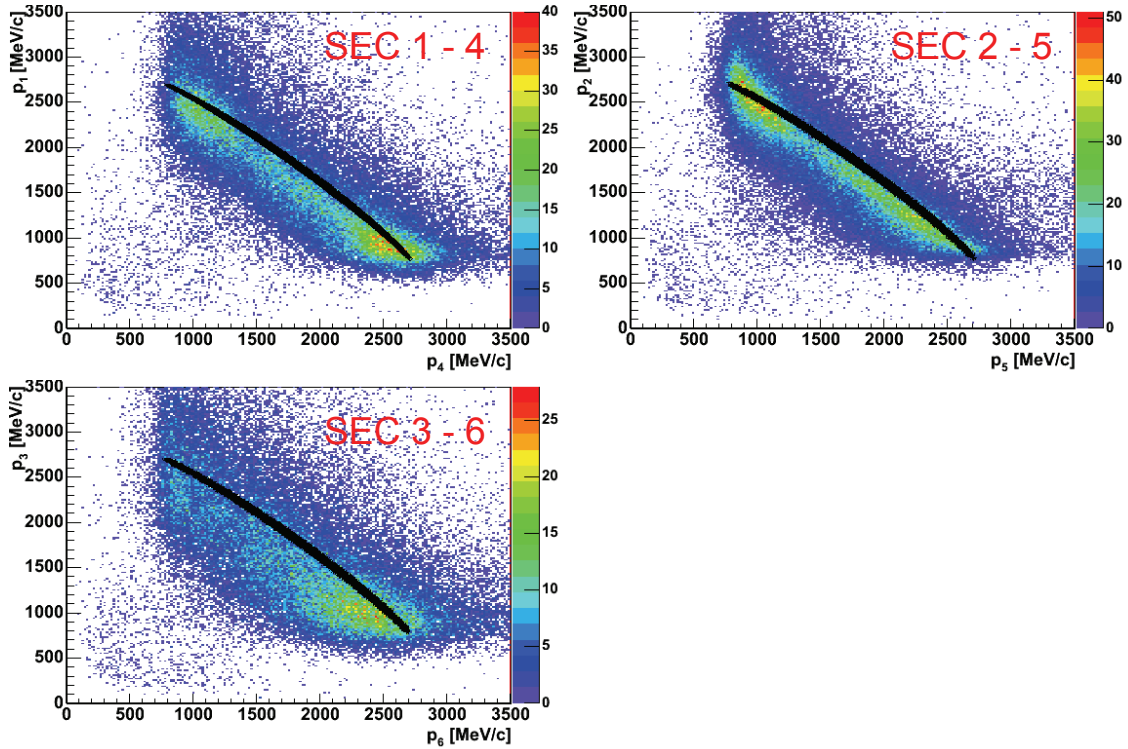
Figure 5.25 – Momentum of one elastic proton versus momentum of the other one for elastic pairs, shown for different sector combinations. The black region corresponds to the kinematical prediction.

We are interested in the evaluation of the invariant mass resolution. From the measured momenta and polar angles we can calculate the total energy E_i and the value of the pair invariant mass (the actual invariant mass value is known from the initial conditions):

$$M = \sqrt{\left(E_1 + E_2\right)^2 - \left(\vec{p}_1 + \vec{p}_2\right)^2}$$
(Eq. 5-5)

In Figure 5.26 invariant mass distributions are presented for different sector pairs. The peaks are centred at values about 2.5% lower than the nominal positions, as we should expect from the Spline systematic deviation in reconstructed momentum, while the best resolution value we can obtain is 2.9% in the sector pair 2-5. The plots as a function of polar angles show the same systematic behaviour of single track resolution plots.

Indeed in the "central" region of polar angles (around 40°, which corresponds to a momentum value of ~ 1600 MeV/c), the obtained invariant mass is underestimated with respect to the expected kinematical value. Something similar is present even in the plots

of Figure 5.25: there is an agreement at the edges of acceptance, while in the central region the experimental values are lower.

The spline algorithm calculates the momentum by interpolation, so it does not take into account the physics of the particle interaction with the magnetic field. Its momentum reconstruction can be improved by the Runge Kutta tracking, as it is going to be shown below.
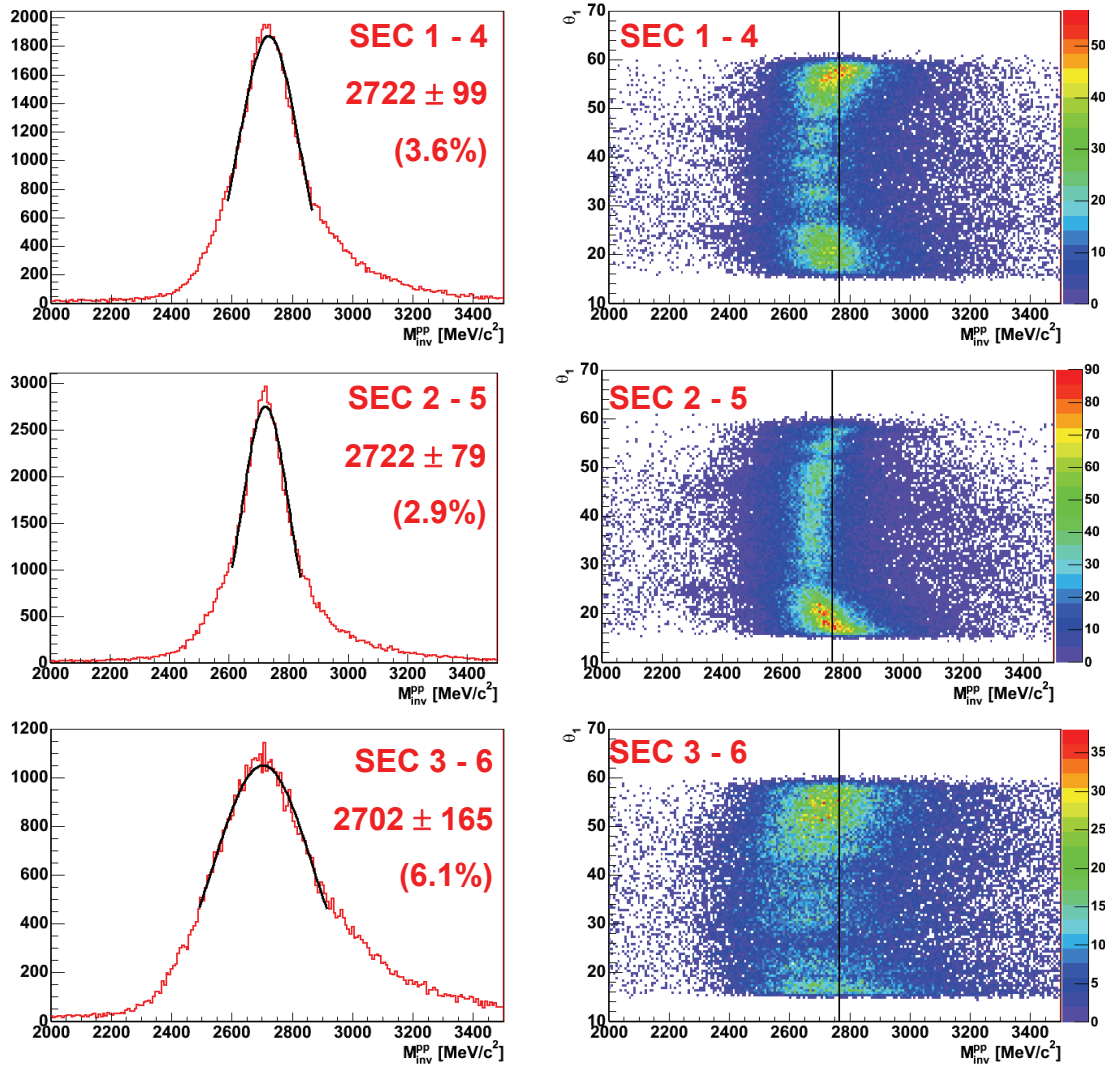

Figure 5.26 – Missing mass distributions on the left, and as a function of the polar angle of one proton on the right, for different sector pairs. The kinematical value of proton-proton invariant mass is 2768 MeV/c^2, and it is indicated by the black lines.

5.6 Field Data – Runge Kutta Tracking

Runge Kutta algorithm takes position and angular variables from the inner MDC segment, momentum values from the spline algorithm, and it does a kinematical refit of the tracks, providing a new set of parameters (θ, ϕ, r, z and p). The quality of these new values, different from the ones used by Spline tracking, will be studied in the next paragraphs and their improvement will be estimated as compared to the previous values.

5.6.1 Vertex reconstruction

Figure 5.27 shows vertex plots for the Runge Kutta algorithm, by using polar angles and hit positions recalculated by the tracking code.

In order to highlight the differences with the values obtained from the segment, Figure 5.28 shows comparison of one dimensional distributions for vertex coordinates between old and new values.

While the *z* coordinate remains almost unchanged, a considerable improvement can be seen in *x* and *y* distributions. In this case the peak positions remain unchanged, while the distributions become narrower, with widths close to the values obtained from no-field data.
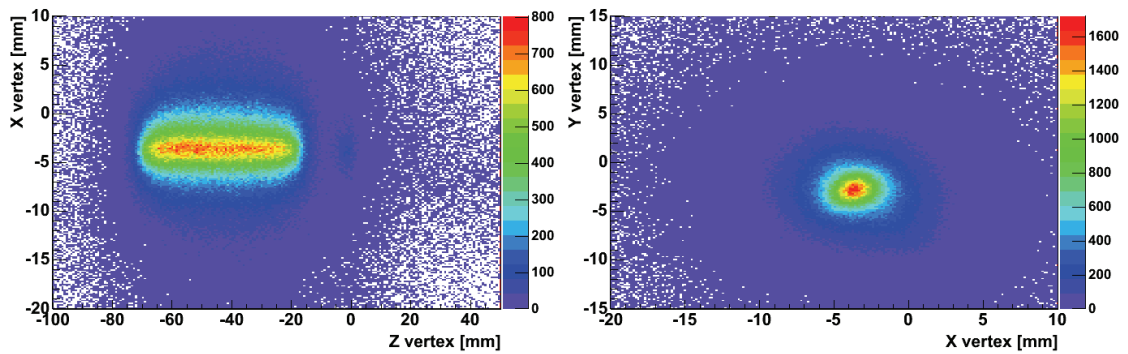
Figure 5.27 – Vertex plots for Runge Kutta algorithm.
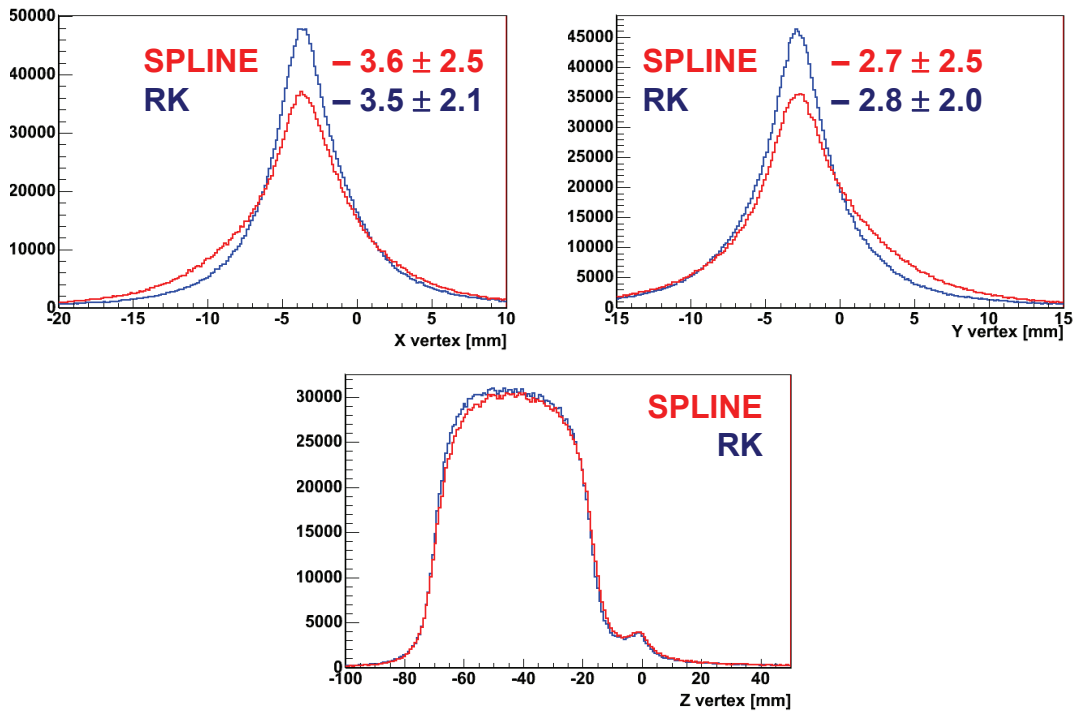
Figure 5.28 – Comparison of vertex coordinate distributions between Spline and Runge Kutta algorithms. While the *z* coordinate remains substantially unchanged, *x* and *y* are corrected toward the peak position. The distribution widths for Runge Kutta are in agreement with the results from the no-field data.

We can argue that Runge Kutta algorithm applies a strong correction on the track variables, and the improvement is visible at the level of vertex reconstruction. In the following paragraphs some results on the angular distributions will be shown.

5.6.2 Azimuthal angle

In order to highlight the improvement achieved by employing the Runge Kutta algorithm, we can look at the distribution of the difference between the segment value of azimuthal angle ϕ and the new one recalculated by Runge Kutta tracking.

Looking at Figure 5.29, which shows the ϕ difference between Runge Kutta and MDC segment, we observe that the azimuthal angle was modified mostly in the lower polar angle region (right plot), where momentum resolution distributions for Spline showed some irregularities; the differences as a function of azimuthal angle are not strong. It seems that the Runge Kutta algorithm can correct the wrong alignment, by moving the track parameters to the "correct" position; we have to stress that the Runge Kutta tracking code does not make use of the elastic scattering information but only of the particle equation of motion inside a magnetic field. Therefore the algorithm is substantially independent of the physical process under study.

Coplanarity distributions after the adjustment are shown in Figure 5.30. On the left-hand plot we can see that some small systematic deviations are still present. Nevertheless, by looking at the one dimensional spectrum (right-hand plot), the angular resolution is improved by about a factor 2, and this value is in agreement with the one found in the no-field data (0.78° for inner MDC segments)

We can thus conclude that the Runge Kutta recalculation of the azimuthal angles, and the consequent correction of the initial segment values, gets rid of possible alignment problems and of the presence of a low fringing field inside the inner MDC chambers.
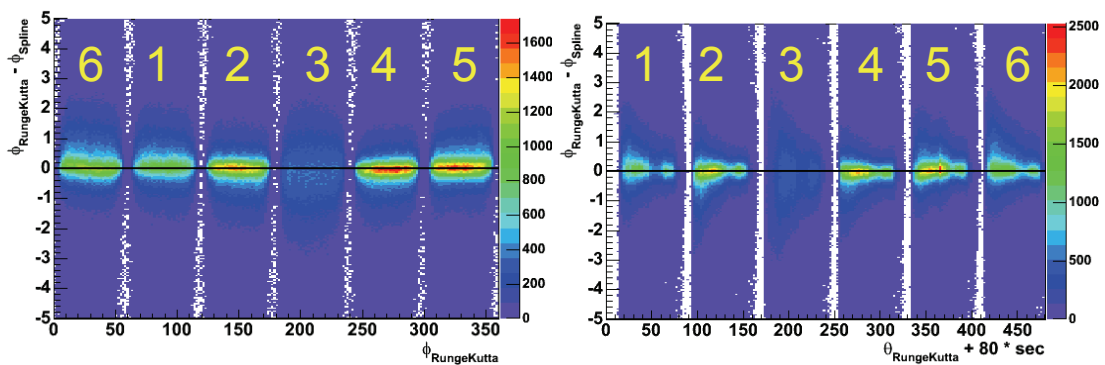

Figure 5.29 – Differences between the azimuthal values obtained by spline tracks (MDC segment values) and the recalculated Runge Kutta ones, as a function of ϕ (left) and θ (right).
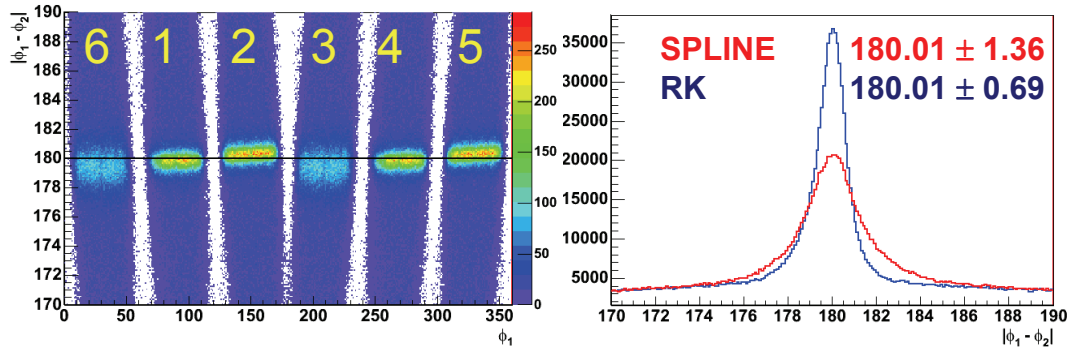
Figure 5.30 – Coplanarity plots for azimuthal angles obtained by Runge Kutta tracking. On the left the distribution as a function of the ϕ value of one proton; on the right the comparison between the $|\phi_1 - \phi_2|$ peaks as obtained by means of Spline and after the correction via Runge Kutta. The improvement is quite relevant.

5.6.3 Polar angle

The same analysis can be done for the θ polar angle. In Figure 5.31 it is possible to see polar angle deviations plotted as a function of ϕ and θ.
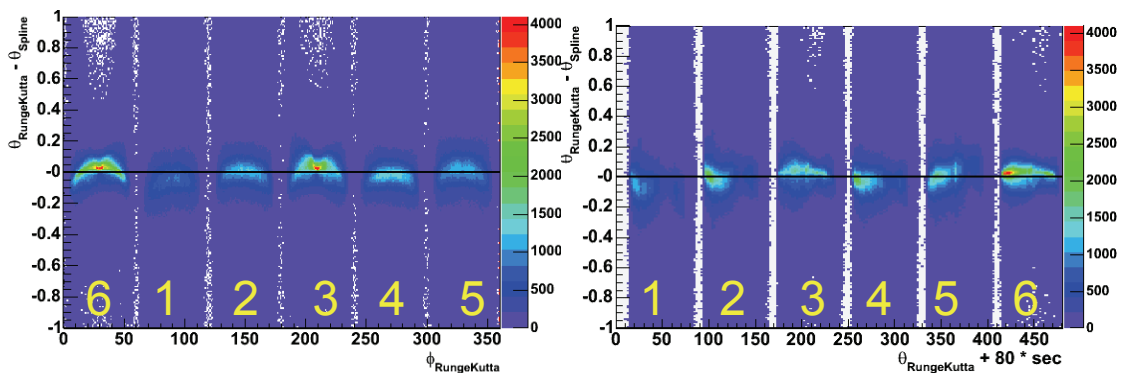

Figure 5.31 - Difference between polar angles obtained by spline tracks and the recalculated Runge Kutta values, as a function of ϕ and θ. We can see that the changes occur mostly at the left-right edges of the chambers.
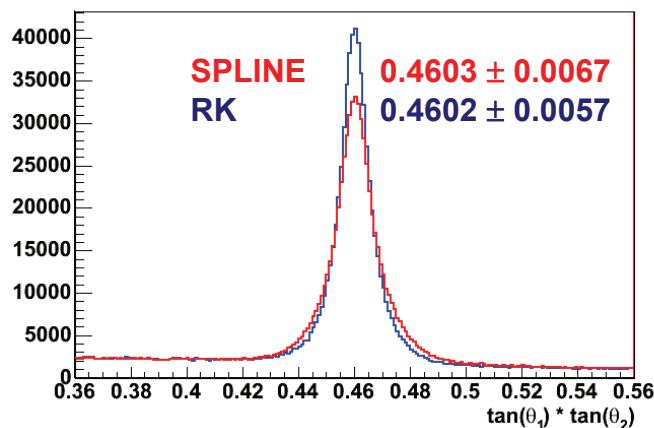

Figure 5.32 – Comparison between $\tan\theta_1 \cdot \tan\theta_2$ distributions for spline and Runge-Kutta algorithms. Also in this case an improvement is visible, but not so strong as for the azimuthal angles.
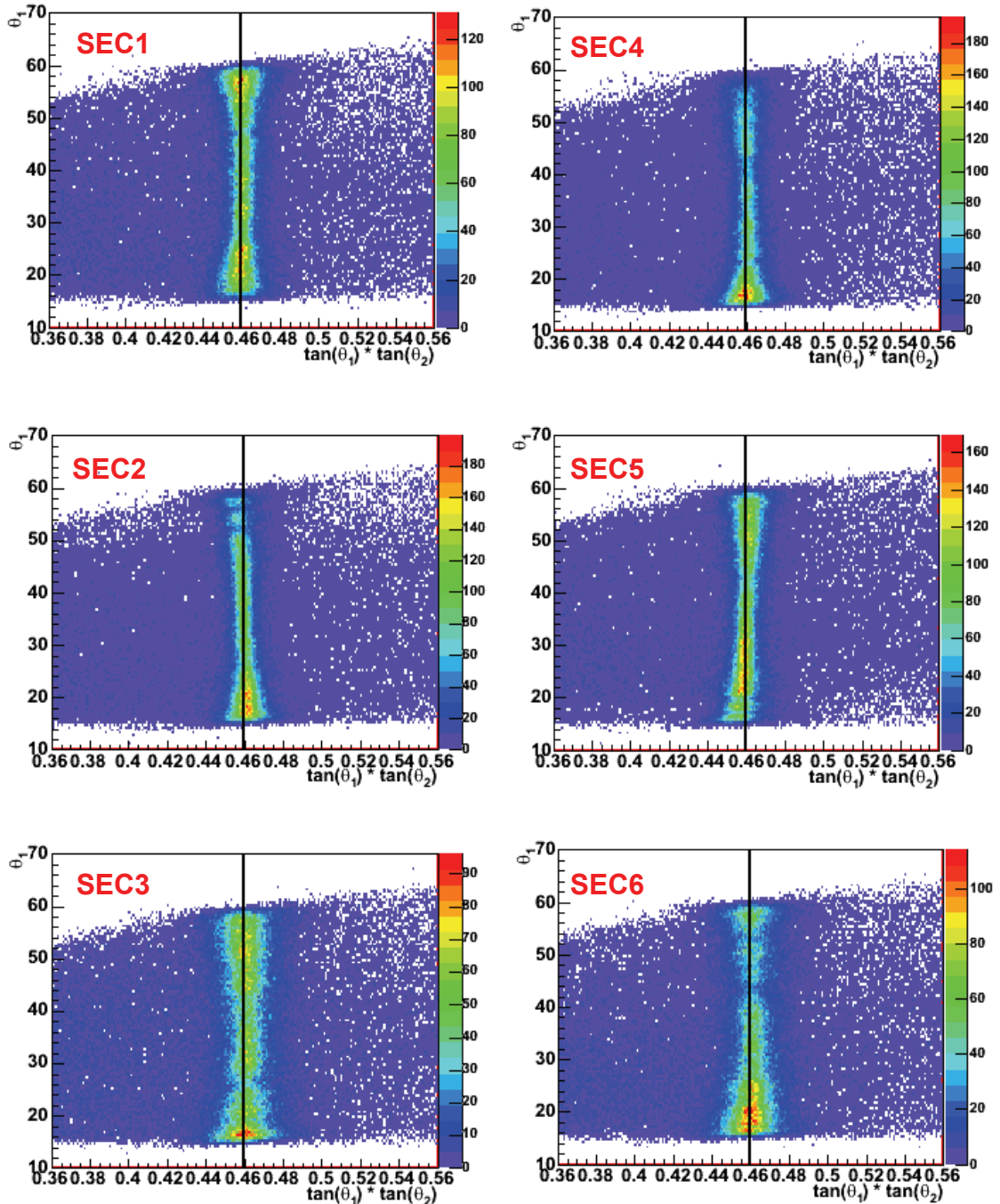
Figure 5.33 - Plots for θ_1 versus $\tan\theta_1 \cdot \tan\theta_2$ by using Runge Kutta recalculated polar angles. As expected the distributions show an improvement with respect to the MDC inner segment values (Figure 5.19), and they are better centred around the kinematical prediction (black lines).

By looking at the distribution as a function of the azimuthal angle, while at the chamber centres the ϕ value is almost good, the reconstructed value at the edges is lower than what obtained via the segment. This implies that the MDC tracking has some problem in the side regions of the chambers. This could be due to alignment problems, but we must also consider that the edges of the MDC modules are closer to the magnet coils, and there the magnetic field is stronger than in the central regions, therefore the particle trajectory is likely to be affected by the fringing field. Conversely,

the Runge Kutta tracking can recover this effect, taking into account the field effect close to the chambers.

By checking the deviations as a function of the polar angle θ, the patterns show that the adjustments were made for each sector in a different way.

In Figure 5.32 the distribution of the new $\tan\theta_1 \cdot \tan\theta_2$ value is shown, in comparison to the Spline one. The position of the peak remains almost unchanged, while the width is reduced to lower values, even though still higher than the no-field case.

By checking the tangents product as a function of θ (Figure 5.33), the distribution is well centred around the kinematical prediction, while the width shows a small improvement with respect to the previous values, which can be checked by simply looking at the scale of the *z* axis (the sample of analysed pairs is the same used for spline analysis).

The obtained resolution is about 1.2%, to be compared with 1.5% from spline and with 0.9% obtained from the inner segment with no-field data.

5.6.4 *Elastic scattering selection*

By using the Runge Kutta angular values we are able to construct a χ^2 function such as 5-25, but this time using the values obtained from fits over the Runge Kutta variables.

The χ distribution is shown in Figure 5.34, and it is similar to what obtained using the Spline tracking.

For consistency reasons the same cut was applied to perform the topological selection on the elastic pairs: a selection on $\chi < 3$ was therefore imposed.

The right side of Figure 5.34 shows the topological distribution after the selection. We can see that the peak is narrower than the Spline one, thus in this case we are cutting away much more background coming from other processes.

After applying the χ selection, we can study the elastic collisions and evaluate the momentum reconstruction resolution as already done before for Spline.
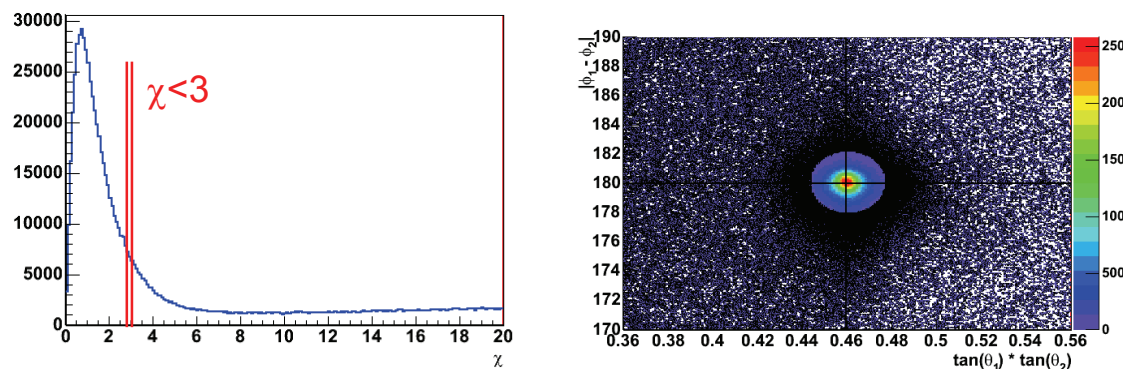

Figure 5.34 - χ distribution for elastic pairs using Runge Kutta tracking (left side). On the right side the elastic scattering topological spectrum is shown after selecting events with $\chi < 3$; the black dots correspond to rejected pairs.

5.6.5 Momentum reconstruction

By comparing the Runge Kutta momentum value with the theoretical one, calculated using the reconstructed polar angle θ, we can evaluate the momentum resolution of the algorithm.

In Figure 5.35 the ratio between experimental values and theoretical ones is plotted as a function of the polar angle θ.

The distributions thus obtained are much better centred to the correct value as compared to spline tracking, and they show a lower spread. By looking at the lower polar angle values some deviations are still present, but they are decreased by the Runge Kutta angular adjustment. We can argue that the alignment needs an improvement, but nevertheless the Runge Kutta tracking algorithm is able to recover the errors caused by a slightly wrong position determination in the laboratory coordinate system.

The obtained resolution plots are shown in Figure 5.36 for the two different tracking methods, and in Table 5-3 the fit values are reported in comparison to what obtained by using Spline algorithm.

Four MDC sectors (1, 2, 4, 5) show an improvement after the recalculation, in terms of peak position and width. Sector 6 is unchanged while in sector 3 the resolution worsens by one percent. We can state at the current stage that the Runge Kutta tracking does not improve the measurement when only 3 MDC planes are used, because of the lower number of points usable for the reconstruction (Runge Kutta tracking does not use kickplane points).

Sector		1	2	3	4	5	6
Spline	$p/p(\theta)$	0.958	0.978	0.942	0.963	0.948	0.947
	$\sigma[\%]$	9.3	5.8	16.2	4.9	4.8	7.5
RK	$p/p(\theta)$	0.992	0.992	0.958	0.989	0.946	0.948
	$\sigma[\%]$	6.0	4.6	17.1	4.4	4.1	7.1

Table 5-3 – Comparison between centroids and momentum resolution values obtained from the fit for Spline and Runge Kutta algorithms.

By checking the 4MDC sectors the improvement in terms of resolution is strong. All the resolution values in these sectors decrease and even the peak position is better centred to the value "one" (1). The improvement is much stronger for sector 1, which showed a worse Spline resolution with respect to the others, mainly connected to the reduced number of operational wire layers. Even in this case Runge Kutta tracking can recover the loss in resolution connected to the lack of wires, by combining the values we can get from all the wire layers which are present in the same sector (inner and outer).

The sector which presents the best momentum reconstruction is number 2, with a resolution of 4.0%, compared to the 4.8% from the spline algorithm.

If we check the plots of Figure 5.37 the difference between reconstructed and theoretical momentum values is reduced with respect to the Spline plots (Figure 5.24), and strong systematic deviations are not visible.

Even looking at Figure 5.38, which shows the momentum of elastic protons versus momentum of the corresponding other proton for different sector pairs, we can see the discrepancy at the centre of the distribution is not evident anymore, while there

is a good agreement between the theoretical prediction of momentum and the reconstructed value.

The last thing to be checked is the invariant mass resolution we can achieve. Figure 5.39 shows the invariant mass plots for different sector pairs, as compared to the distributions using spline.
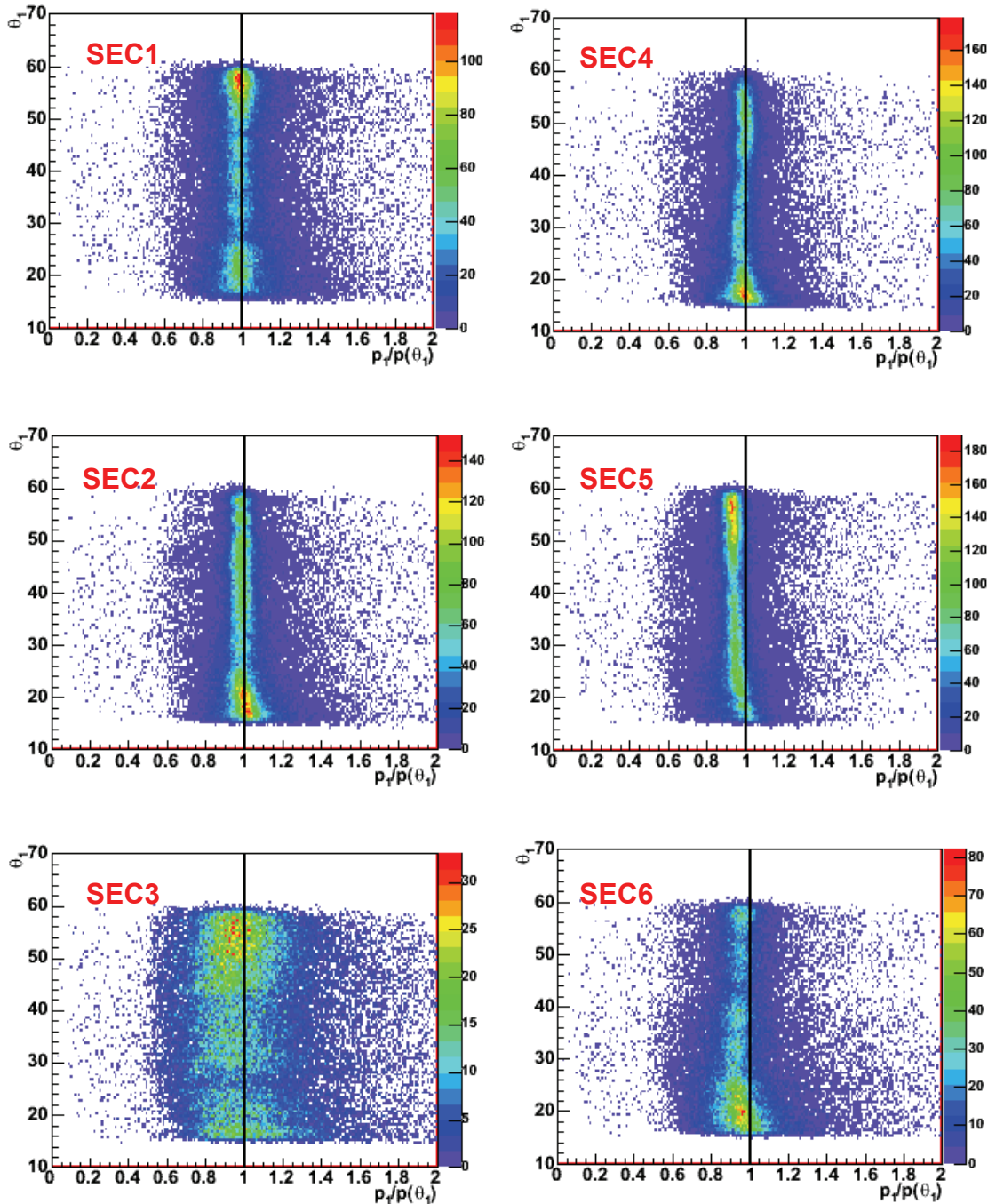

Figure 5.35– Ratios between reconstructed and kinematical momentum for Runge Kutta tracking algorithm, as a function of polar angle. The improvement with respect to spline distributions (Figure 5.23) is well visible.

The improvement in resolution is well visible, in particular in the region of central polar angles (right plots), where the discrepancy present in spline is reduced and the distribution is moved toward the theoretical value.

The best invariant mass resolution value is 2.3% at 2.7 GeV/c^2, for 2-5 sector pair. For 3MDC sectors the resolution stays at 6%, but we have to underline that this large value is mainly connected to the poor resolution in sector 3, due to the lack of wire layers.
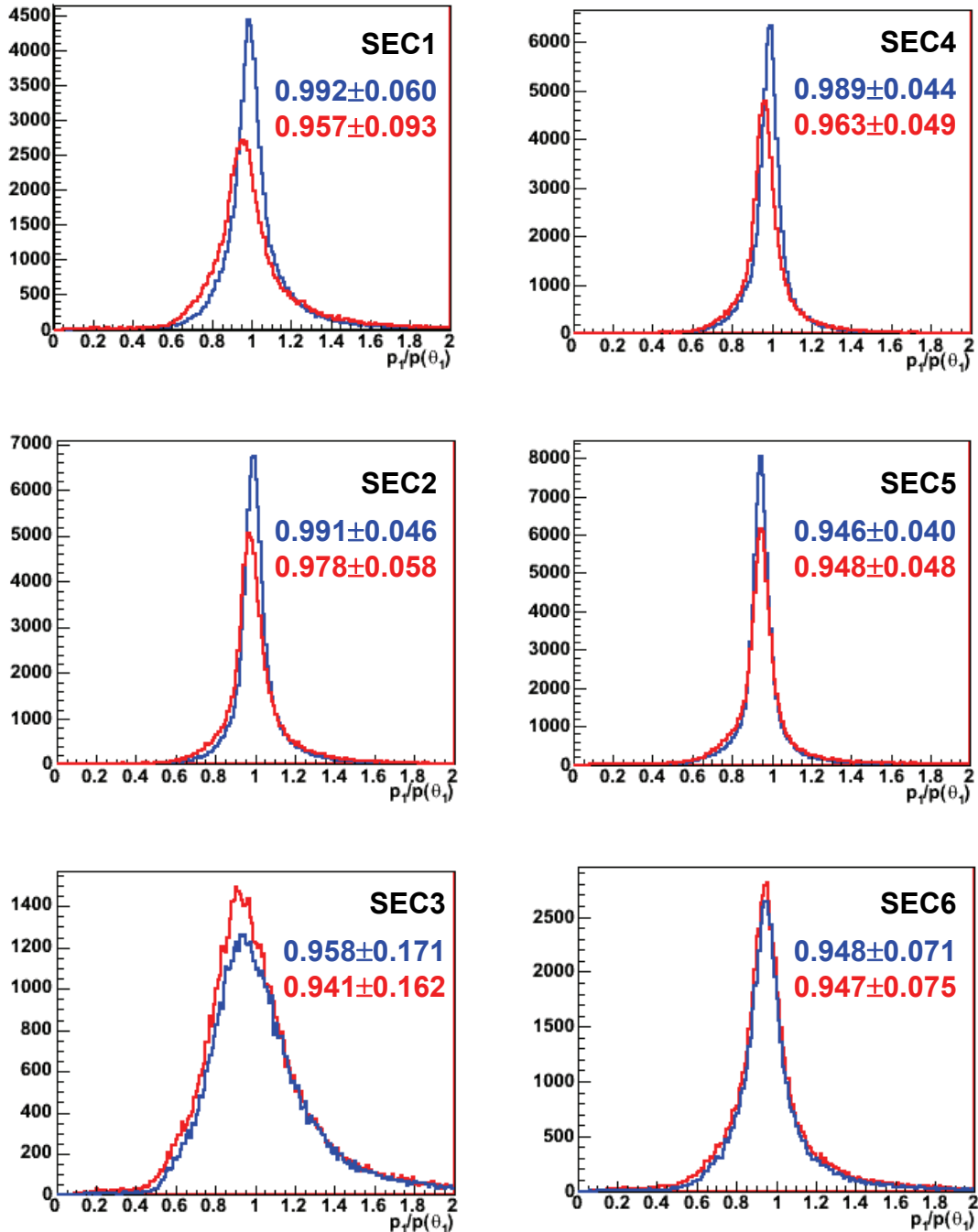

Figure 5.36– Ratio between reconstructed momentum and kinematical prediction from polar angle θ, obtained by using Runge Kutta (in blue) and Spline (in red) tracking algorithms.
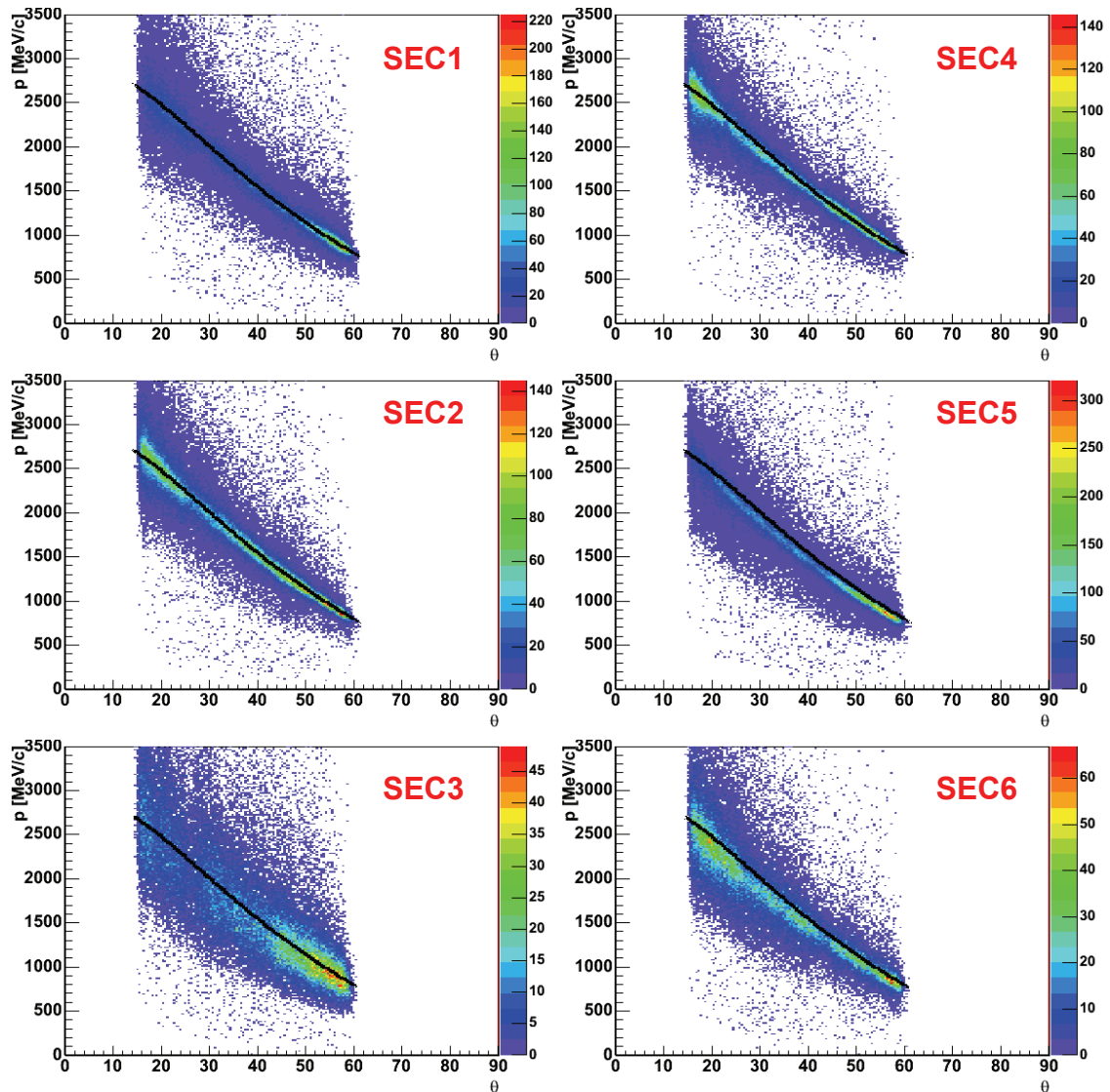
Figure 5.37 – Momentum versus polar angle distributions for different sectors, by using Runge Kutta algorithm. The black lines represent theoretical predictions.

5.7   *Momentum resolution summary*

All the momentum resolution values obtained for the Spline and Runge Kutta algorithms are reported in Table 5-4, together with the values from the simulation analysis, by using exactly the same procedure to select protons from elastic scattering.

Table 5-5 shows the obtained values for the invariant mass resolution of elastic pairs.

The discrepancy between simulation and experimental values is currently under study. The simulation takes into account the number of working layers for each MDC chamber as present during data acquisition, and this feature can be seen in the differences between resolution values for different sectors, which follow the same behaviour as the experimental data. Conversely in simulation the geometry of the various sub-detectors is perfectly known, therefore the effects of misalignments are not present.

Nevertheless the current simulation setup differs from the experiment. First of all in simulation the beam is centred at (0,0) position, while it was found in the vertex

reconstruction analysis that during the experiment the beam was shifted and even moved during the days. This shift imposes a global movement of the "real" coordinate system with respect to the "laboratory" one, which is calculated by means of the alignment procedure.

While this effect is secondary, there are hints that the beam was not running parallel to the beam line, but rather it was a bit tilted with respect to the *z* axis. All the reconstructed angular variables could be affected by this problem, and in particular the expectation value of the momentum calculated from the polar angle. In this case by correcting the geometry definition it will be possible to have better resolution values. What we can state at the moment is that the obtained values are an upper limit of the HADES momentum resolution.

Moreover the effect of the drift times measured by the MDCs without the START detector, and of a possible internal misalignment of some wire layers, are at the moment under study with respect to the implications on loss of resolution.

However, by analysing the elastic scattering process, for the first time it was possible to characterize the experimental angular angle and momentum resolution of the HADES tracking system, in order to understand possible problems and to find out strategies to solve them. This was one of the main goals of the January 2004 experiment.

The second goal was the exclusive η reconstruction, and in chapter 7 we will show that this is possible with the current setup and tracking resolution.
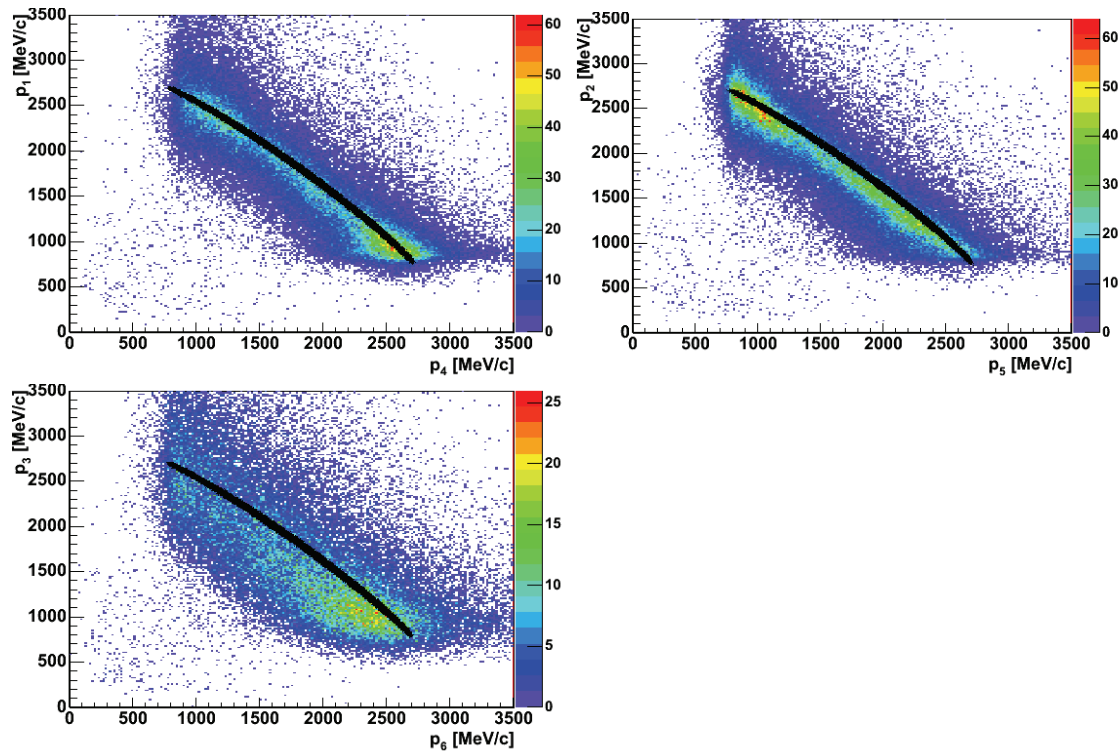

Figure 5.38 − Distributions of momentum of one elastic proton versus momentum of the other proton for elastic pairs, for different sector combinations. The black line is the kinematical prediction.
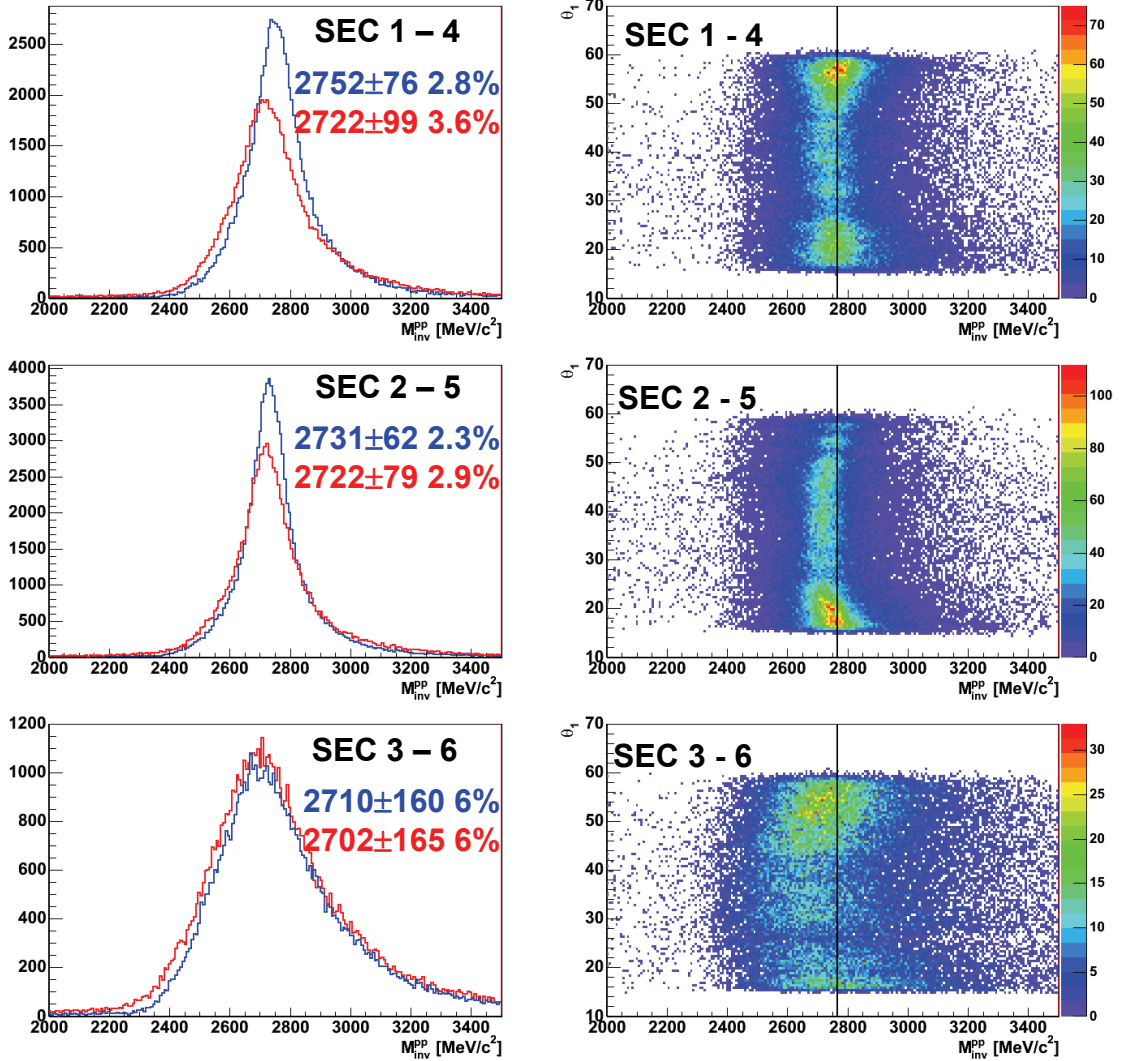
Figure 5.39 – On the left the missing mass distribution for the Runge Kutta tracking (in blue) as compared to the Spline (in red). On the right the RK mass distribution as a function of the polar angle of one proton. The kinematical value of the proton-proton invariant mass is 2768 MeV/c^2, and it is indicated by the black lines.

Sector			1	2	3	4	5	6
Spline	SIM	p/p(θ)	0.995	0.996	0.990	0.992	0.987	0.995
		σ[%]	2.1	1.9	3.4	2.0	1.8	2.4
	EXP	p/p(θ)	0.958	0.978	0.942	0.963	0.948	0.947
		σ[%]	9.3	5.8	16.2	4.9	4.8	7.5
RK	SIM	p/p(θ)	0.998	0.999	0.995	0.997	0.996	0.996
		σ[%]	1.4	1.2	2.7	1.4	1.6	2.0
	EXP	p/p(θ)	0.992	0.992	0.958	0.989	0.946	0.948
		σ[%]	6.0	4.6	17.1	4.4	4.1	7.1

Table 5-4- Values of momentum resolution for Spline and Runge Kutta tracking algorithms, for simulation and experimental data.

Sector pair			1-4	2-5	3-6
Spline	SIM	Mass [MeV/c^2]	2760	2758	2759
		σ [MeV/c^2]	21	20	31
		σ_M/M [%]	0.77	0.73	1.11
	EXP	Mass [MeV/c^2]	2722	2722	2702
		σ [MeV/c^2]	99	79	165
		σ_M/M [%]	3.6	2.9	6.1
RK	SIM	Mass [MeV/c^2]	2764	2764	2763
		σ [MeV/c^2]	16	15	27
		σ_M/M [%]	0.6	0.6	1.0
	EXP	Mass [MeV/c^2]	2752	2731	2710
		σ [MeV/c^2]	76	62	160
		σ_M/M [%]	2.8	2.3	5.9

Table 5-5 - Values of invariant mass resolution for Spline and Runge Kutta tracking algorithms, for simulation and experimental data.

6 TIME OF FLIGHT MEASUREMENTS

In the framework of the HADES spectrometer a time of flight system has been adopted, in order to efficiently select rare events with dilepton pairs produced in nuclear and elementary collisions, in combination with RICH and Shower subdetectors.

Moreover the time of flight (tof) measurement allows to perform also the hadron identification, in combination with the momentum information provided by the tracking system, and to separate protons from pions with good efficiency and purity [Tlu04]. Indeed hadron identification is mandatory in order to perform exclusive analysis of decay channels in elementary collisions, where the identification of all the outgoing charged particles is needed.

The time of flight system is constituted by three detectors which are START, placed along the beam, TOF and TOFINO placed after the magnetic field region, respectively at higher (44°-88°) and lower (18°-45°) polar angles.

The master trigger signal is generated by the 1st level trigger, which correlates the multiplicity information from META to the combined information from START and VETO detectors; this logical signal is sent to TDCs to start the tof measurement, while the individual STOPs are provided by TOF and TOFINO detectors.

In order to achieve a good timing, a calibration procedure is foreseen that will be presented in the next paragraphs. It involves time calibration for the three subdetectors and position calibration for the TOF system; the resolution values obtained in p+p experimental runs will be also shown.

In January 2004 the START detector was not used, so it was necessary to implement a new calibration procedure for the tof walls, and an algorithm to reconstruct the start time of the reactions. Resolution and efficiency values of the method will be shown and compared for simulation and experimental data.

6.1 Calibration parameters

6.1.1 START hodoscope

The time of flight (*tof*) values provided by TDCs can be considered in general as the difference between arrival times of the stop signals t_{STOP} (generated by TOF or TOFINO detector elements), and the start signal t_{START} generated by the 1st level trigger:

$$tof = t_{STOP} - t_{START}$$

(Eq. 6-1)

The START detector in the p+p experiment (hodoscope) was constituted by 16 small scintillator rods (strips); each one was connected at both ends to a photomultiplier with its own electronic chain. This means that the signals from each strip reach the 1st level trigger system with its own delay time, due to cable lengths and electronics.

If we assume that a particle hit the START strip i at the instant t_0, the signal reaches the trigger system at the instant t_{START}^i, given by:

$$t^i_{START} = t_0 + t^i_{offset} \qquad \textbf{(Eq. 6-2)}$$

there t^i_{offset} is the time offset of the strip number i.

Each of these offsets has to be calculated in order for the START system to provide its signals with a timing which does not depend on the hit strip. After the START calibration procedure, these offsets will be subtracted strip-wise from the time provided by META detectors.
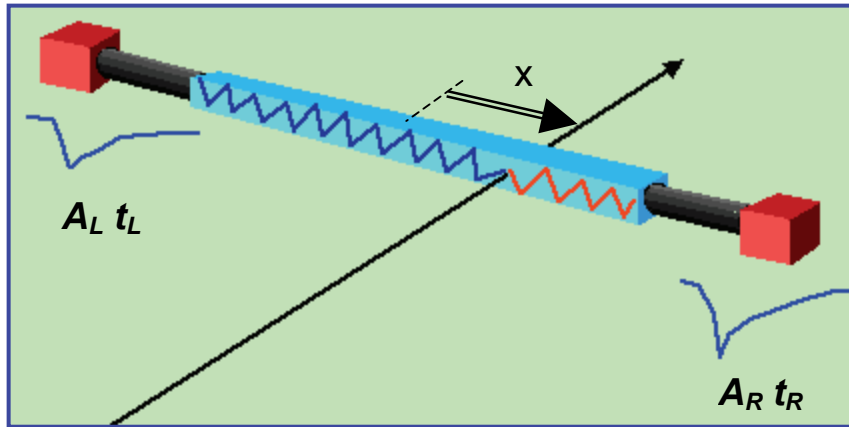
6.1.2 TOF wall

Figure 6.1 – Scheme of a TOF scintillator rod and of its coordinate system.

Figure 6.1 shows the scheme of a TOF rod hit by a particle. The particle generates a light signal proportional in intensity to the released energy, and this signal will reach the rod ends after a time t_R for the right end, t_L for the left one. We can express these two times by the equations:

$$t_R(x) = tof + \frac{1}{Vg}\left(\frac{L}{2} + x\right) + D_R \qquad \textbf{(Eq. 6-3)}$$

$$t_L(x) = tof + \frac{1}{Vg}\left(\frac{L}{2} - x\right) + D_L \qquad \textbf{(Eq. 6-4)}$$

where *tof* is the particle time of flight (assuming the START signal has been already corrected), x is its distance from the rod centre, L and Vg are respectively the rod length and the group velocity of the light signal, $D_{L,R}$ are the offsets connected to discriminators, electronic chains and cable length for left and right channels.

From the previous equations we can calculate not only the particle *tof*, but even its hit position in the rod x:

$$tof = \frac{1}{2}(t_R + t_L) + t_{offset} \qquad \textbf{(Eq. 6-5)}$$

$$x = \frac{1}{2}(t_R - t_L) \cdot Vg + x_{offset}$$ **(Eq. 6-6)**

where t_{offset} and x_{offset} are respectively time and position offsets, given by:

$$t_{offset} = -\frac{1}{2}\left(\frac{L}{Vg} + D_R + D_L\right)$$ **(Eq. 6-7)**

$$x_{offset} = -\frac{Vg}{2}(D_R - D_L)$$ **(Eq. 6-8)**

The group velocity is known from measurements done by using a laser system, thus TOF calibration consists in calculating for each rod the values of position and time offsets[1].

The amplitude information was not used in proton experiment; further information on ADC calibration can be found in [Spa02]. For a detailed explanation of the complete calibration procedure for the TOF system see the reference [Ago02].

6.1.3 TOFINO wall
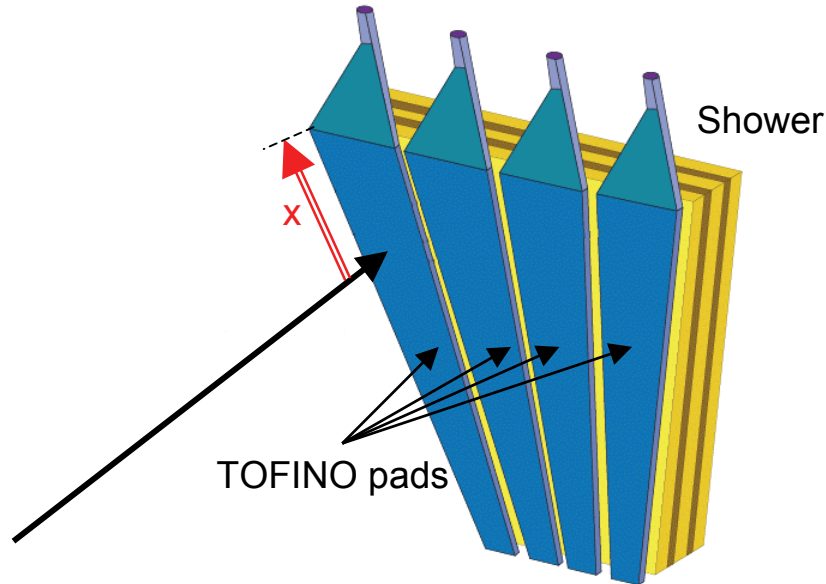
Figure 6.2 – Scheme of TOFINO detector. The position information is given by Shower pads.

---

[1] In effect the signal from a TDC is expressed in channel values t^c [0,4095]. In order to convert these values into nanoseconds they have to be recalculated as:

$$t_{L.R} = k_{L,R}t_{L,R}^c + O_{L,R}$$

where k are the nanosecond/channel slopes which depend only on the TDCs, and could be even measured on the bench, while O are the time offsets that can be included into the global offsets t_{offset} and x_{offset}.

The operating principle of TOFINO wall is similar to the TOF, but in this case the light signal is collected only at one edge of the scintillator pad.

Figure 6.2 shows a scheme of the TOFINO principle; when a particle hits one pad it produces a light signal, which crosses the scintillator material and reaches the PMT edge after a time t given by:

$$t = tof + \frac{x}{Vg} + t_{offset} \qquad \textbf{(Eq. 6-9)}$$

where x is the hit distance from the PMT edge, Vg is the group velocity of the light in the scintillator and t_{offset} is the time offset.

Using only TOFINO it is not possible to have the position information of the hit, but we can obtain this information by correlation with the Shower system, which is segmented into several pads and provides positions with a resolution given by the pad size (2-5 cm). Thus for TOFINO calibration only time offsets must be calculated.

6.2 TOF position calibration

The information of the particle hits in TOF rods is important both for on-line and off-line analysis.

During the data acquisition the 2nd level trigger correlates the positions of hits in RICH and TOF detectors, in order to select events which contain candidate leptons; in order to assign the correct tof to reconstructed tracks, the TOF correlation with the tracking system is needed, and by knowing the exact point in space where the particle hits the META detector we can calculate the track path length. Moreover the META hit position is used by the kickplane algorithm (5.3.1) to reconstruct momenta for sectors without outer MDC chambers (as was done for the November 2002 experiment analysis).

The TOF position calibration is performed through correlation with MDC segments, by analysing straight tracks in no-field data[2]. The procedure is the following.

Let us assume that a particle emitted from the target crosses MDC chambers and TOF wall, creating a useful signal in both detectors. By projecting the segment reconstructed by the drift chambers on the TOF system, we can calculate the position of the projected point, and its distance from the hit measured by the scintillator rod.

Figure 6.3 outlines the procedure. If we consider the plane that crosses the hit rod perpendicular to the beam direction, the position of the projected hit along the rod direction x_{MDC} will be given by:

$$x_{MDC} = \frac{Y_{TOF}}{\tan(\Phi_{MDC})} \qquad \textbf{(Eq. 6-10)}$$

where Φ_{MDC} is the azimuthal angle measured by MDC segment, while Y_{TOF} is the y position of the rod in the laboratory coordinate system, which is fixed by the detector geometry. The procedure can be used for both inner and outer drift chambers, and we expect to obtain the same results.

---

[2] Position calibration can be also done using field data by means of the same procedure, but in this case the ϕ bending from the magnetic field decreases the resolution of the obtained position.
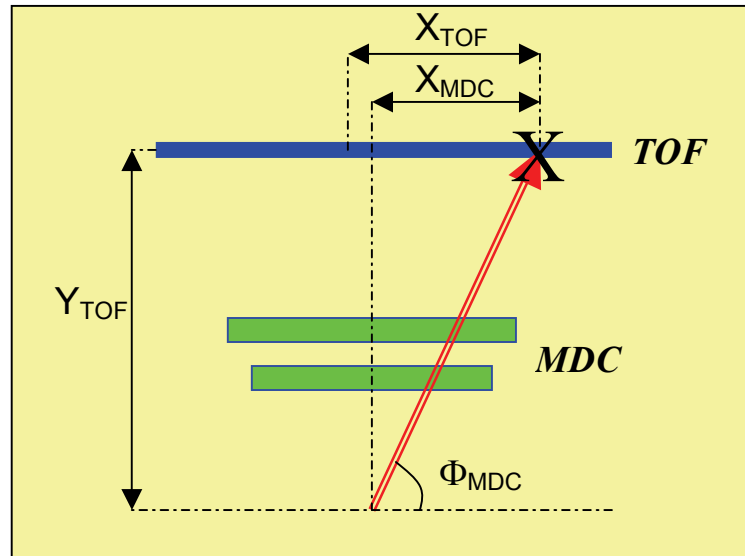
Figure 6.3 – Scheme of TOF position calibration procedure by using MDC correlation.

We can consider the position errors for the projected hit almost negligible, because of MDC resolution (below 1 mm) which is much lower with respect to the TOF one (about 2.5 cm). From the width of the residuals after the calibration we can also evaluate the TOF position resolution.

For the position calibration only inner segments were used, and then the results were compared to what obtained using the outer chambers.

In Figure 6.4 the residuals for January 2004 data are plotted as a function of TOF rod number (one sector is made of 64 rods), for inner and outer chambers, after the position calibration procedure.

The calibration by using the inner segment is consistent also with the outer segment, but here the 3MDC sectors show systematic shifts of few centimetres with respect to the zero value. This is not connected to the TOF position measurement but to the poor angular resolution of segment reconstruction by using only one MDC chamber, as shown in chapter 5; the shift is consistent with the one found by analysing the elastic scattering reaction channel.
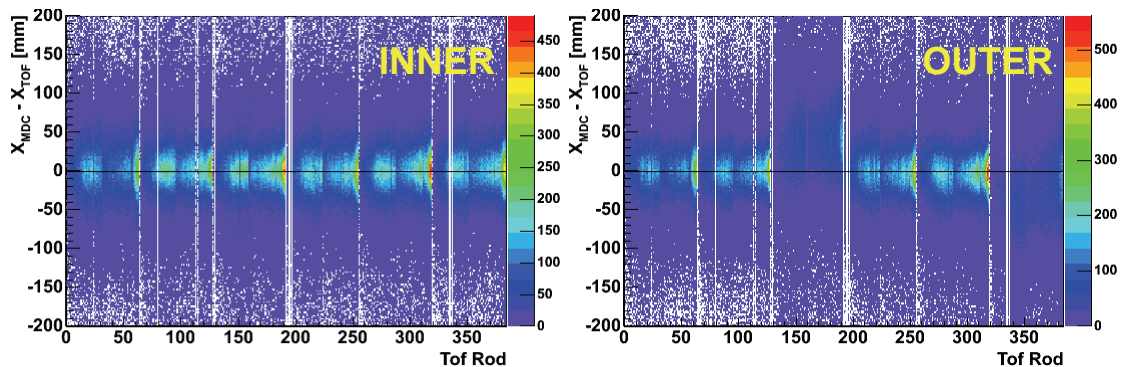

Figure 6.4 – Differences between projected hits (x_{MDC}) and TOF ones (x_{TOF}) as a function of the TOF rod number, by using inner (left) and outer (right) segment. Apart from the 3MDC sectors (number 3 and 6), the distributions are comparable.
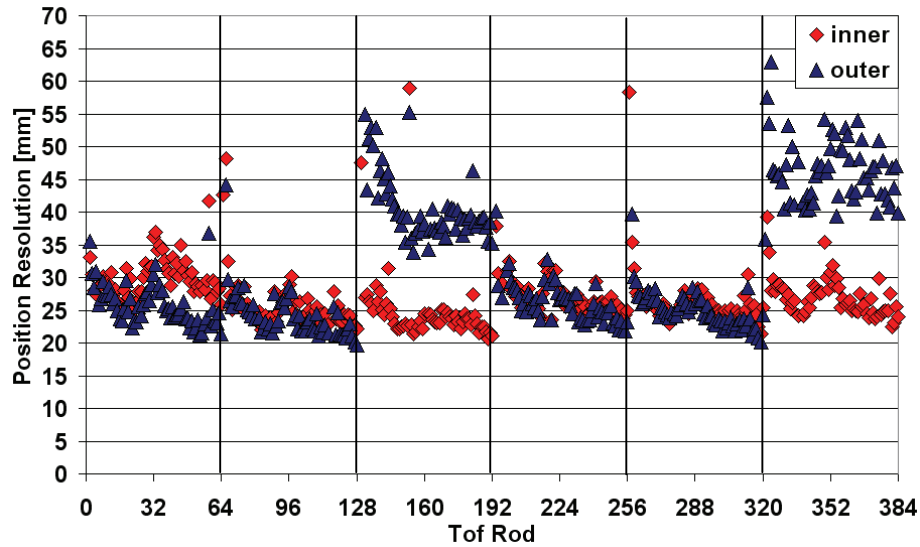
Figure 6.5 – TOF position resolution as a function of the rod number, obtained by residual widths for inner and outer segments.

The difference between the TOF position and the projected one (Figure 6.4) was fitted by a gaussian function for each rod; position offsets are given by the centroids of the distributions, while widths are an estimation of the rod position resolution.

Figure 6.5 shows the obtained width values as a function of the rod number, calculated separately for inner and outer chambers; the two distributions agree for most of the rods. The 3MDC sectors (number 3 [128-192] and number 6 [320-384]) cannot be compared as already mentioned. In the 1st sector [0-64] the inner chamber widths are systematically larger than the outer ones; this is due to the low number of working wire layers in MDC plane I, which decreases the quality of the angular reconstruction.

The average position resolution for thinner and thicker TOF rods, shown in Table 6-1, is about 2.5 cm. We can convert this value into intrinsic time resolution by dividing it by the group velocity values; using this rough calculation we can estimate a time resolution between 150 ps and 160 ps.

	INNER MDC	OUTER MDC[3]
2x2 CM^2 rods	24.6 ± 1.5 mm	23.5 ± 1.7 mm
3x3 CM^2 rods	26.7 ± 2.6 mm	26.3 ± 2.4 mm

Table 6-1 - Position resolution values for TOF rods.

Group velocities were calculated using a laser system on November 2001, and the obtained average values, which were used in the analysis, were 164 mm/ns for 3x3 cm^2 rods, and 162 mm/ns for 2x2 cm^2 rods.

A cross check of these number can be done after the position offset calculation. After the position calibration, from the formula:

$$x = \frac{1}{2}\left(t_R - t_L\right) \cdot Vg + x_{offset} \qquad \text{(Eq. 6-6)}$$

---

[3] In the evaluation of the average value sectors 3 and 6 were not taken into account, because of the 3MDC sectors problem.

if we use the position corrected by the offset (therefore $x_{offset} \equiv 0$), we can write the group velocity as:

$$Vg = x \cdot \frac{2}{t_R - t_L}$$

<div align="right">**(Eq. 6-11)**</div>

If we use the known position of the projected hit as x (x_{MDC}), we can plot $x \cdot 2/(t_R - t_L)$ as a function of the tof rod number, as shown in Figure 6.1.
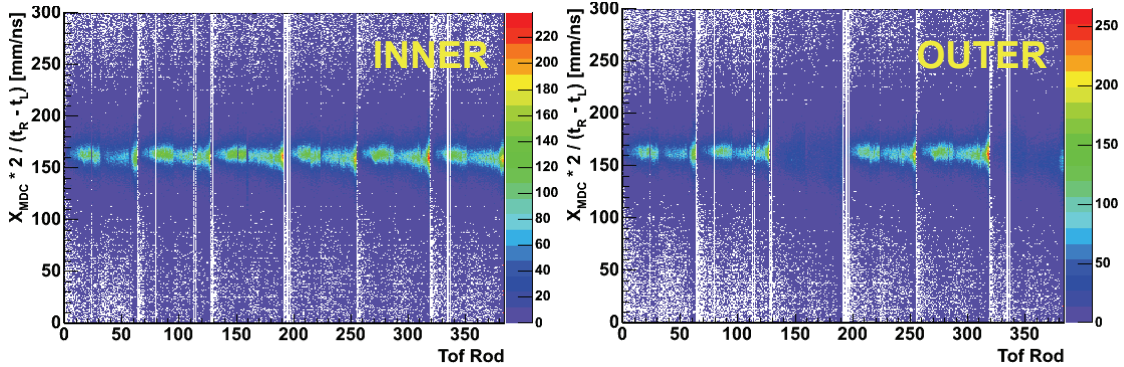

Figure 6.6 – Group velocity evaluation as a function of rod number, using inner (left) and outer (right) segment. No systematic deviations are visible (apart from 3MDC sectors - outer chambers).

The distributions do not show systematic deviations, and they are similar for both inner and outer modules (apart from outer chambers of 3MDC sectors). The average values are shown in Table 6-2; the obtained values are comparable for inner and outer segments, and to the ones evaluated in November 2001.

	INNER MDC	OUTER MDC[3]
2x2 CM^2 rods	160.5 ± 1.1 mm/ns	161.8 ± 0.9 mm/ns
3x3 CM^2 rods	163.7 ± 1.0 mm/ns	163.9 ± 1.0 mm/ns

Table 6-2 - Average group velocity values for TOF rods.

6.3   Time calibration with START detector (September 2003)

The following procedure is used for all the experiments where a START detector is present.

The main idea for time calibration is to use particles which have a well known time of flight. By minimizing the difference between their experimental tof and the predicted one, it is possible to evaluate time offsets for all the time of flight subdetectors.

Electrons (and positrons) can be used to perform the time calibration: in the energy range studied by the HADES spectrometer the emitted leptons travel at velocity close to the speed of light; their time of flight does not depend on their momenta but only on the travelled distance between the emission point and the TOF/TOFINO walls.

We can write the electron tof as:

$$tof = \frac{len}{\beta c} \equiv \frac{len}{c}$$

(Eq. 6-12)

where *len* is the travelled path length, *β* is the electron velocity (*β* ≡ 1), and *c* is the speed of light. If we assume a path length of 2100 mm (the average distance of META systems from the target), the electron time of flight will be about 7 ns.

Electrons and positrons are selected by angular correlation of the track with the RICH detector, which is hadron blind; the path length is given by the META hit position in the laboratory coordinate system (for nofield data) or by the tracking algorithm (for field data); the time of flight is given by TOF and TOFINO walls.

By combining all these data, the time calibration is performed by choosing lepton candidates and calculating their tof normalized to the path length of 2100 mm (by assumption):

$$\overline{tof} = tof \cdot \frac{2100}{len}$$

(Eq. 6-13)

where *tof* is the experimental value and $\overline{tof}$ is the normalized one. In this way $\overline{tof}$ does not depend on the travelled distance and we can tune time offsets by setting it at 7 ns.

In the following paragraphs the procedure will be explained step by step, and the resolution values will be presented, obtained by analysing field runs for September 2003 data.

6.3.1 START calibration

The start detector for September 2003 was constituted by sixteen scintillator strips of size 1x1x12 cm^3. Each one has its electronic chains thus one time offset for each channel has to be calculated.

However from the beam profile (see left side of Figure 6.7) we can see that the beam particles do not hit all the strips, therefore the procedure can be used only for the central ones which have the higher number of counts.
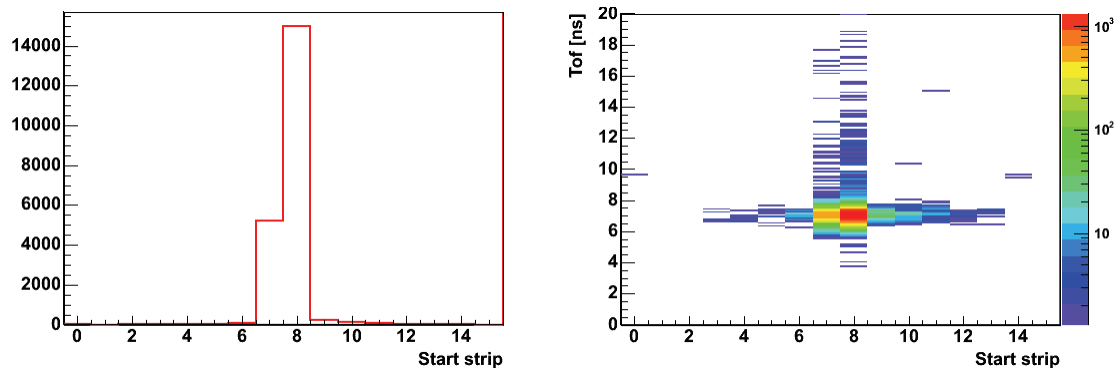

Figure 6.7 – Hit distribution in START strips (on the left), which corresponds to the beam profile. On the right the normalized tof distribution for lepton tracks as a function of the strip number, after the calibration procedure.

The initial time offsets for all the strips are set to zero. In order to calibrate the START we select lepton tracks which hit only one particular TOF rod (in order not to depend on TOF time offsets), and then we calculate their normalized time of flight values. For each different strip we construct tof distributions and fit the peak by a gaussian function.

If the strips are calibrated all the peaks should stay at the position 7 ns; before the calibration this does not happen, so from the difference between peak centroids and the 7 ns assumption we can calculate the time offsets strip by strip[4].

Figure 6.7 shows the distribution of normalized time of flight as a function of the strip number, after calibration.

After this procedure all the tof values will be corrected by:

$$t^i_{START} = t_0 + t^i_{offset}$$ **(Eq. 6-2)**

in order not to depend on the START strips in the later stages of the analysis.

6.3.2 TOF time calibration

After the START detector is calibrated, we can evaluate the time offsets for TOF detector.

We select lepton tracks which hit TOF rods, we calculate their normalized tof and fill histograms with the time of flight distributions rod by rod. Each distribution is fitted by a gaussian function, and the difference between centroids and the assumed value of 7 ns gives the time offsets.

The left plot of Figure 6.8 shows the two dimensional spectrum of normalized tof as a function of the rod number after the time calibration. We can see that all the time distributions are correctly located at 7 ns.

Figure 6.8 shows the normalized tof distribution integrated over the whole TOF. By fitting the peak with a gaussian function the obtained centroid stays at 7 ns, and the sigma of the fit gives us an estimate of the average time resolution of TOF detector.
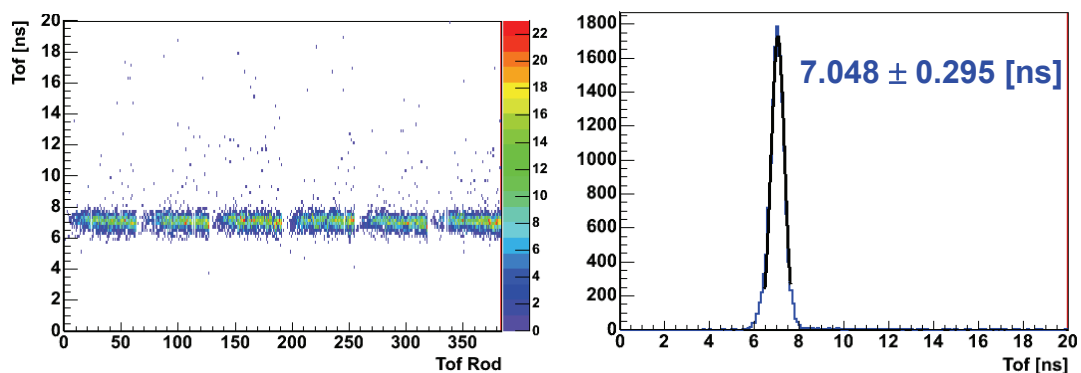

Figure 6.8 – TOF time of flight distributions for leptons, as a function of the rod number (left) and integrated over all the rods (right). The obtained resolution value (295 ps) is the quadratic sum of TOF and START time resolutions.

---

[4] In general, after all the strip offsets are calculated in this way, by convention we add a constant value to all the offsets, in order to put the offset of the most frequently hit strip to zero. The time of flight peak will be adjusted to 7 ns in a second step after TOF and TOFINO calibration.

The obtained resolution value of 295 ps is larger than what expected from position calibration. Indeed the tof measurement is given by:

$$tof = t_{STOP} - t_{START}$$ (Eq. 6-1)

so the tof resolution depends also on the START detector resolution, according to:

$$\sigma_{tof} = \sqrt{\sigma_{STOP}^2 + \sigma_{START}^2}$$ **(Eq. 6-14)**

In order to obtain a value independent of the START detector we can use dilepton pairs.

If we have two leptons emitted in the same event, we can calculate the difference between their normalized time of flight values t_i. If we consider that for both particles the t_{START} is the same, the difference can be simply expressed as:

$$\Delta tof = t_2 - t_1$$ **(Eq. 6-15)**

and the resolution of the time difference is correlated to the single TOF resolution by:

$$\sigma_{\Delta tof} = \sqrt{\sigma_{t_2}^2 + \sigma_{t_1}^2} \equiv \sqrt{2} \cdot \sigma_{TOF}$$ **(Eq. 6-16)**

by assuming $\sigma_{t_1} \equiv \sigma_{t_2} \equiv \sigma_{TOF}$.

From the tracking system we can have the information about the charge polarity of the particle which crosses our spectrometer, that is the direction of the trajectory deviation inside the magnetic field. We can select events which contain lepton pairs of opposite charge, and plot their difference in time of flight (Figure 6.9).

From the fit over the tof difference we obtain a width of 252 ps. By dividing this number by $\sqrt{2}$ we obtain a TOF time resolution of 178 ps, which is the typical value for rods after the calibration.
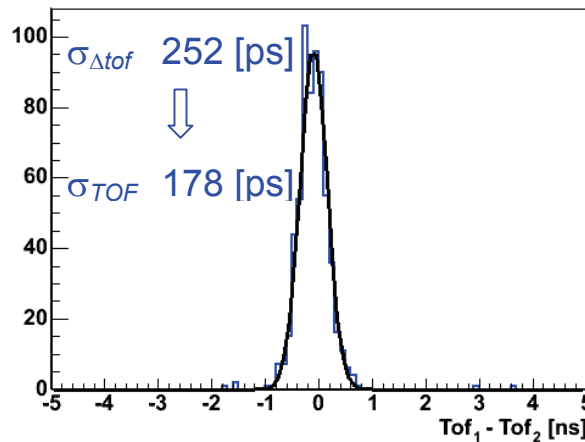

Figure 6.9 – Time of flight difference for dileptons hitting the TOF system.

After we get the intrinsic TOF time resolution, we can derive the value for the START detector. By combining equation 6-14 and the obtained σ_{tof} of 295 ps, we obtain a START time resolution of about 235 ps.

6.3.3 TOFINO time calibration

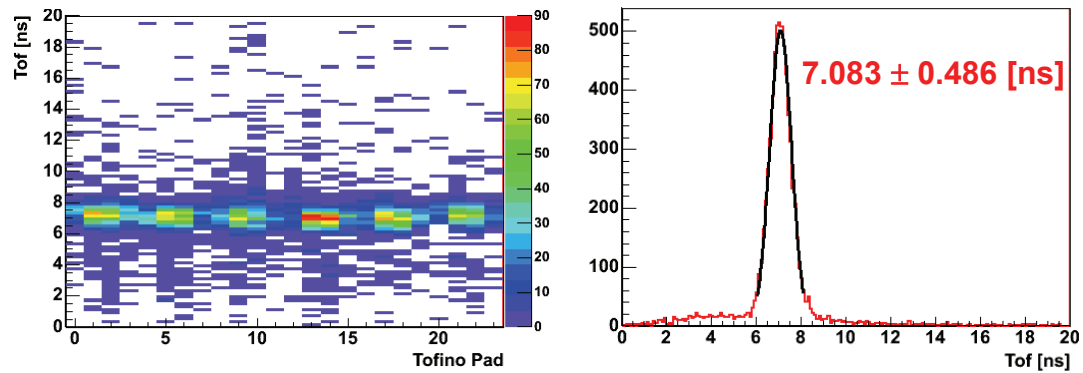The procedure performed for TOFINO calibration is the same that was used for TOF system.

Figure 6.10 - TOFINO time of flight distributions for leptons, as a function of pad number (left) and integrated over all the pads (right), after TOFINO time calibration.

In Figure 6.10 the distributions of TOFINO time of flight values (normalized) are plotted after the calibration, as a function of the TOFINO pad number on the left (one sector is made of four pads) and for the whole system on the right.

The obtained resolution value from the fit (486 ps) includes the effect of START detector; by the squared subtraction of this value minus the START resolution, as for TOF detector, we can evaluate an intrinsic TOFINO time resolution of 425 ps.

In the analysed data sample there are not so many dilepton pairs hitting the TOFINO region, as shown in Figure 6.11.
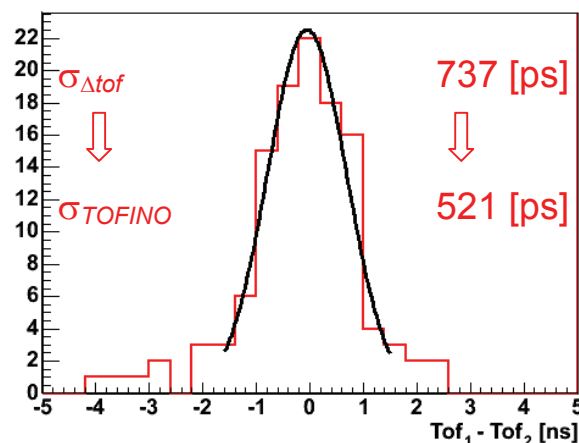

Figure 6.11 – Time of flight difference for dileptons detected in TOFINO system. The small number of counts in the distribution does not allow to provide reasonable fit values.

The peak was fitted by a gaussian function, but the width estimate has large errors due to the limited statistics, so the only affordable value of intrinsic time resolution is 425 ps calculated by means of single lepton analysis.
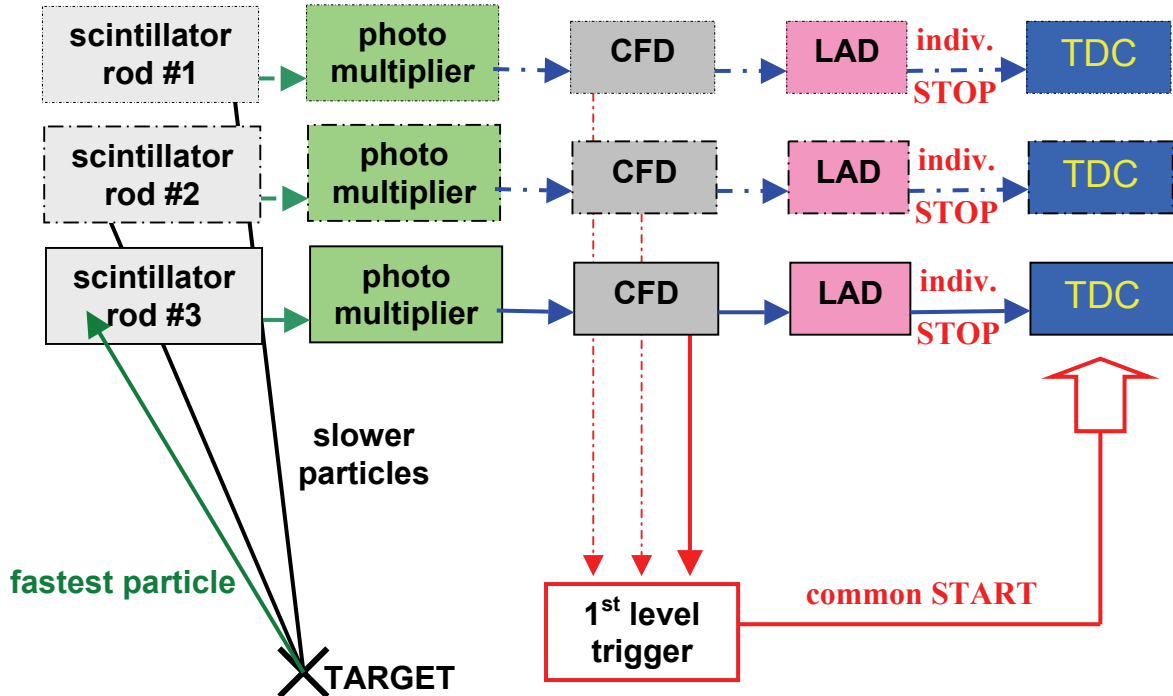

Figure 6.12 – Principle of tof measurement without START detector. The fastest particle which hits a META pad starts the time of flight measurement.

6.4 *Time calibration without START detector (January 2004)*

In the January 2004 experiment the START detector was not used as time reference, because of the high number of secondaries it produced when crossed by the beam. This means that there was no common start time for tracks in the same event, but in general the data acquisition was started by the fastest particle which crossed the TOF/TOFINO walls and produced a signal above discriminator thresholds (see Figure 6.12).

Let us assume that in a nuclear collision a particle is emitted from the target, crosses the spectrometer and produces a light signal in the scintillator rods. The time between the instant when the reaction occurred and when the particle hit the TOF detector is called time of flight (*tof*). The light travels towards each photomultiplier, and is converted into an electronic signal that reaches the TDC after a time τ given by:

$$\tau = tof + \frac{x}{Vg} + offset \qquad\qquad \textbf{(Eq. 6-17)}$$

where *offset* is the time offset of the electronic chain (due to electronics, delay modules, cable length, etc).

TDCs measure the time between a START and a STOP signal. If the acquisition is started from the *"0"* particle, the measured time $\underline{t}^i$ of the ith particle will be expressed as:

$$\underline{t}_i = \tau_i - \tau_0 = tof_i - tof_0 + \frac{x_i}{Vg_i} - \frac{x_0}{Vg_0} + offset_i - offset_0 \qquad \textbf{(Eq. 6-18)}$$

where *offset*$_i$ are the offsets due to the STOP chain, while *offset*$_0$ is connected to the START chain and the 1$^{\text{st}}$ level trigger.

By knowing hit point positions, group velocities and offsets, we can see our measured time does not correspond to the "real" time of flight, but instead to the difference in time with respect to the fastest electronic signal.

In the case of TOF rods we obtain a measured time t_{TOF} given by:

$$t_{TOF} = \frac{1}{2}\left(\underline{t}_R + \underline{t}_L\right) = tof_{TOF} - tof_0 + offset_{TOF} - offset_0 \qquad \textbf{(Eq. 6-19)}$$

while for TOFINO we must correct the measured time by the *x* distance between the hit point and the PMT obtained by means of the SHOWER detector. Generally we obtain:

$$t_{TOFINO} = t_{TOFINO} - \frac{x_{TOFINO}}{Vg_{TOFINO}} = tof_{TOFINO} - tof_0 + offset_{TOFINO} - offset_0 \quad \textbf{(Eq. 6-20)}$$

assuming t_{TOFINO} contains also the distance correction.

The TOF position information is substantially unaffected by this different kind of measurement, because it is based on left/right time difference and it does not depend on the particle which started the acquisition (no dependence on *offset*$_0$).

The time calibration is more complicated because we cannot use single lepton time as we usually do in experiments with START detector; in this case we miss the information on the time of flight of the particle which started the acquisition (we know only the time difference with respect to it).

We can divide the time calibration procedure in two steps; first we calculate the time offsets of TOF/TOFINO pads, and then the start time of the reaction event by event.

In order to calculate time offsets we need to use well known time differences. We can take pairs of identified particles, whose theoretical time of flight can be estimated from momentum and mass values, calculate their experimental difference in time and compare this value to the theoretical one. In this way we can tune time offsets in order to have coherent tof values for all the pads of TOF and TOFINO walls.

To perform this kind of calibration we can use alternatively dilepton pairs or pp elastic pairs.

It is possible to use the RICH information to select pairs of leptons in the same event, as shown in 6.3.2. Their theoretical time of flight is well known (high energy leptons travel close to the speed of light), but their production rate is much lower than that of hadronic processes.

Proton-proton pairs can be easily identified by selecting positive charged tracks (from the trajectory deviation inside the magnetic field) and making a selection on their angular variables, as shown in the previous chapter; the elastic channel cross section is quite high, but elastic protons cover a limited region of the polar angle (below 60°), so

they do not hit all the TOF rods; moreover the theoretical time of flight of the protons has to be calculated from momentum, and it depends also on the tracking resolution.

For these reasons dilepton pairs were chosen as a more suitable tool for the time calibration.

6.4.1 Calibration with dileptons

Electrons and positrons with energies above few MeV travel at velocities close to the speed of light. This means that they should have the same velocity, so they should cover the same path length in the same time.

If we consider a pair of leptons emitted in the same collision, their time of flight normalized to the same path length (t_1 - t_2) (calculated by means of the tracking algorithms) should be centred at zero:

$$0 \equiv t_1 - t_2 = \underbrace{tof_1 - tof_2}_{0} + offset_1 - offset_2 \qquad \textbf{(Eq. 6-21)}$$

where now the offsets are only due to the STOP chain.

By means of the angular correlation between RICH and MDCs we select dilepton pairs; the tracking algorithms are able to estimate the track path length, and the sign of the charge by trajectory deviation in the magnetic field region. From all these informations we can tune the offsets of a pad with respect to the offset of another pad.

By considering that this calibration consists on calculating only relative offsets (the global one has to be calculated event by event and it will be explained in 6.5), we must calibrate TOF and TOFINO systems separately. The adopted procedure is the following:
1. Calibration of TOFINO pads with respect to one TOF rod (sectorwise);
2. Calibration of TOF rods with respect to TOFINO pads (sectorwise);
3. Calibration of offsets between different sectors.

A first analysis was run with the full statistics of January 2004 using the September 2003 parameters; in between the two experiments no cables and no electronic modules were changed, so the September offsets should be close to the good ones, but they need to be refined in order to achieve the correct time resolution.

The following paragraphs will explain the calibration steps and the obtained results, using Runge Kutta as tracking algorithm. Following this calibration procedure the time difference of dileptons was calculated to obtain an estimate of the time of flight resolution.

6.4.2 TOFINO offsets

The first step consists of calibrating TOFINO pad offsets with respect to other pads in the same sector.

The best way to perform this calibration consists on choosing pairs of lepton tracks in the same event, of opposite charge, where one particle hits a TOF rod and the other one a TOFINO pad of the same sector. If we select this kind of pairs, with the TOF particle hitting always the same chosen rod (one for each sector), we can calculate the difference in time between the two particles (normalized to the same path length), and adjust the TOFINO offsets, pad by pad, relatively to the chosen TOF rod, by setting this difference to zero.

In this case we are calculating the TOFINO offsets with respect to the selected TOF rod. We use only one rod, different for each sector, in order for our offset determination not to be influenced by superposition of different TOF rods.

After this offset calculation, Figure 6.13 shows the difference in time (normalized to a path length of 2100 mm) between TOF-TOFINO lepton pairs in the same event belonging to the same sector versus TOFINO pad number (4 pads correspond to one sector). Only one chosen TOF rod was hit, different for each sector.
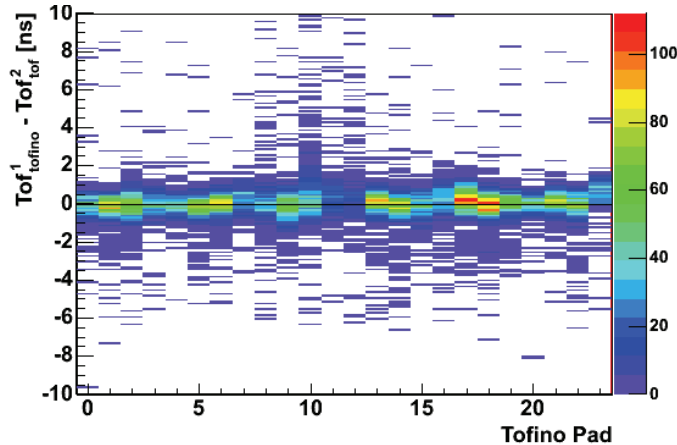
Figure 6.13 – Time difference of dilepton pairs (TOF-TOFINO) versus TOFINO pad number, after TOFINO offsets tuning.

After the TOFINO calibration all the time distributions peak around the same position. This that means TOFINO pads on the same sector are well calibrated with respect to each other, but if we compare pads belonging to different sectors, the time difference will depend on the offsets of TOF rods used for this calibration.

Therefore, after TOFINO calibration, we need to tune TOF offsets as well.

6.4.3 TOF offsets

The same kind of procedure was adopted for TOF rods. After selecting pairs of leptons in the same event, in the same sector and hitting both TOF and TOFINO systems, we can calculate the time difference of the two tracks, this time using as TOFINO values the times corrected by the previous paragraph procedure. In this case we do not use one single TOFINO pad for each sector, because we assume pad offsets are well tuned by the first step of the calibration.

Figure 6.14 shows the time difference for TOF-TOFINO lepton pairs as a function of the TOF rod number, after the correction of TOF offsets.

The time differences are well centred around the zero, but we can see a second structure in the low polar angle region (higher rod number for each sector). The secondary peak is displaced of about -2 ns with respect to the expected position.

This peak is present in all the days of beam, and it is not connected to an offset movement due to some effects of electronics. By analysing files from simulation it was found the same behaviour, and it was understood its origin.

In all the pairs with the 2nd peak, the positron hit a TOFINO pad and its real time of flight corresponds to a value of about 5 ns, so below the correct value of 7 ns of a particle travelling at the speed of light. This can happen when more than one particle hit the same TOFINO pad; in this case one of the two particles will have a wrong time (in general smaller than the correct value).

This effect is secondary so it can be neglected, and it does not harm the time calibration. For the affected rods the fitted time peak is the primary one.
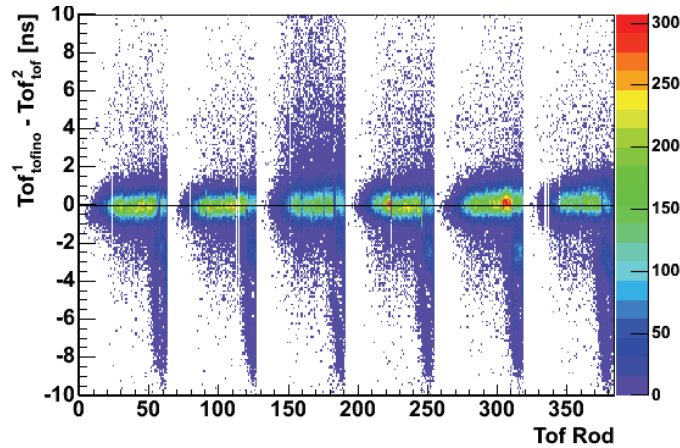

Figure 6.14 – Distribution of dilepton pairs (TOF-TOFINO) time differences versus TOF rod number, after tuning the TOF offsets.

6.4.4 Inter sectorial calibration

After the first two steps of the calibration procedure all the pads of each sectors are well tuned with respect to each other in the same sector. The final step consists of aligning in time all the sectors, thus calculating a global offset for each sector with respect to a well determined one (the reference sector).

We choose dilepton pairs hitting two neighbour sectors, using only TOF system because of its better time resolution, and we impose their time differences to be zero; in this way the offsets are calculated with respect to the previous sector, and of course the sum of all their values is close to zero.

Figure 6.15 shows the final plot after this procedure. It was decided to leave the 6th sector unchanged (number #5 in the plot), and to calculate the other sector offsets with respect to it.
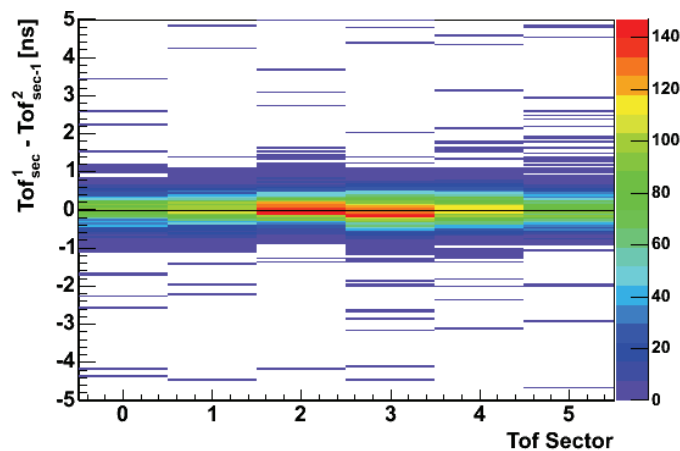

Figure 6.15- Time difference of dilepton pairs belonging to neighbour sector, after the last step of time calibration.

6.4.5 Time resolution

After the calibration is concluded it is possible to evaluate the time resolution obtained, using dilepton pairs as before.

If we consider a pair of leptons we can plot their difference in time of flight $\Delta tof = t_1 - t_2$, and fit the distribution by a gaussian function. In this case the peak should be centred around zero, while the sigma of the gaussian is an estimate of the time resolution, given by:

$$\sigma_{\Delta tof} = \sqrt{\sigma_{t_1}^2 + \sigma_{t_2}^2}$$

(**Eq. 6-22**)

where σ_{t_1} and σ_{t_2} are the resolution values of single time of flight measurement.

If we choose pairs belonging to the same system, we can easily estimate the intrinsic time resolution of TOF and TOFINO detectors by the formulas:

$$\sigma_{TOF} = \frac{\sigma_{TOF-TOF}}{\sqrt{2}}$$

(**Eq. 6-23**)

$$\sigma_{TOFINO} = \frac{\sigma_{TOFINO-TOFINO}}{\sqrt{2}}$$

(**Eq. 6-24**)

In Figure 6.16 we can see the time difference distribution between leptons which both hit the TOF detector. The width of the distribution is 309 ps, which corresponds to a TOF intrinsic time resolution of about 219 ps. This value is higher than the one obtained for September 2003 (178 ps) but the difference is not so much, and considering the different and much complicated procedure which was used to obtain the offset calibration, using different measurements with different systems, it is not possible to further reduce this number with this method for the January 2004 experiment.

Figure 6.17 shows the same distribution for TOFINO-TOFINO pairs. In this case the obtained width value for time difference fit is 704 ps, which corresponds to a TOFINO intrinsic time resolution of about 498 ps. If we compare this number with the one obtained in September 2003 (425 ps), also for TOFINO we are close to the values obtained by the "usual" single track procedure.
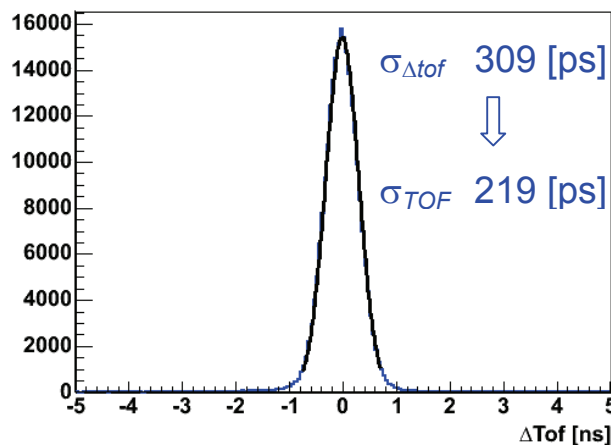

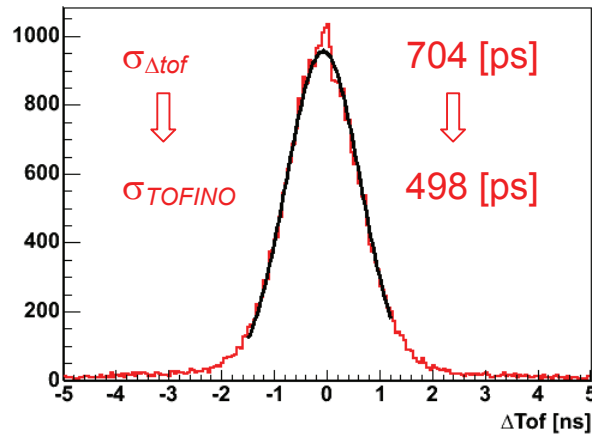**Figure 6.16** - Time difference distribution for lepton pairs which both hit TOF detector.

Figure 6.17 - Time difference distribution for lepton pairs which both hit TOFINO detector.

The January 2004 experiment was the first HADES experiment without START detector; the described procedure was developed for this occasion and never tested before. The obtained resolution values are close to those computed by using data with START detector, and this means that the procedure is under control and it provides good results that can be used for the analysis.

After the single pad time offsets are calculated, the start time of the reaction is needed.

6.5 Start time reconstruction

As previously stated, in a run where the START detector is not present the TOF/TOFINO systems do not measure the particle time of flight, but its difference in time with respect to the particle which triggered the data acquisition. In this case we need to reconstruct the start time of the reaction event by event, in order to have the correct time of flight for all the particles.

To perform this kind of job an algorithm was developed that will be explained in the next paragraph. The capability and the resolution of the method were first explored by studying simulation data, and then checked by means of the experimental data collected during the September 2003 beam time, when the hodoscope detector was present.

Finally, the capability of this algorithm for the January 2004 data will be shown.

6.5.1 The algorithm

From the considerations of the previous chapters, the time of flight (*tof*) of a particle is given by the sum of its experimental time (*t*) measured by the TOF/TOFINO wall plus the time-of-flight (tof_0) of the particle which started the acquisition:

$$tof = t + tof_0 \qquad\qquad \textbf{(Eq. 6-25)}$$

In order to avoid the dependence on the fastest particle, we can simply consider the time difference of any two particles produced in the same event; from the previous equation we can easily obtain the relation:

$$tof_1 = tof_2 + t_1 - t_2 \qquad\qquad \textbf{(Eq. 6-26)}$$

It follows that if we want to know the time of flight value of all the particles inside an event we need to know first the tof of a single particle, and then we can recalculate the tof of all the others.

Let us assume we have a particle whose momentum (*p*) and track length (*len*) are measured by the tracking algorithm; we can calculate the theoretical time of flight of the particle by the formula:

$$tof = \frac{len}{c}\frac{1}{\beta} = \frac{len}{c}\frac{\sqrt{p^2 + m^2}}{p} \qquad\qquad \textbf{(Eq. 6-27)}$$

where *c* is the speed of light and *m* is the mass of the particle. If we can identify one particle inside the event we can assume its mass, we can calculate its theoretical time of flight, and from this value we can recalculate the tof of all the other particles in the same event.

The strongest particle identification algorithm of the HADES spectrometer consists on the simultaneous measurement of momentum and β of the particle, but of course it cannot be used before the start time is reconstructed. Nevertheless there are other methods, independent of the time measurement, that can be adopted.

The first one is the lepton identification by RICH detector. If we select tracks which are correlated to rings in the RICH detector, we can assume they are electrons or positrons.

On a second step, we can select negatively charged tracks (from the trajectory deviation inside the magnetic field) which are not correlated to the RICH detector, and therefore that were not identified as electrons; in this case we can assume these tracks are negative pions.

For all the events where these two kinds of identification are not possible, i.e. events with only positive charged tracks, we cannot make any assumption on the identity of the particles (they can be both protons or pions): this method is not usable for them.

But it is important to stress the reactions of interest are the decay channels of η mesons, that is $pp{\rightarrow}pp\pi^+\pi^-\pi^0$ (hadronic) and $pp{\rightarrow}ppe^+e^-\gamma$ (electromagnetic); events with only positive tracks are not interesting for this analysis, or we are able to use other kinds of identification (such as the elastic channel selection described in the previous chapter).

By identifying a particle in the event, which does not need to be the fastest one, we can assume its mass and then calculate its theoretical time of flight as previously explained. The difference between the experimental value ($t_{\exp}$) and the theoretical one (t_{theo}) allows us to finally calculate the start time of the reaction, by means of the formula:

$$tof_0 = t_{theo} - t_{\exp} \qquad\qquad \textbf{(Eq. 6-28)}$$

and we can add this value to the measured time of the other particles inside the same event, to obtain the corrected time of flight as in equation 6-25.

To summarize the procedure Figure 6.18 and Figure 6.19 show the flowcharts of the algorithms used for the start time reconstruction and the particle identification.

The algorithm was tested with simulation data, where the particle tof is known. After checking that it provided a good response, it was used with the experimental data

of the September 2003 run, where the START detector was present and thus a good time of flight reference was available as well.

At last it was used in January 2004, showing its capability to make particle identification possible even without the START detector, thus allowing to run the experiment at a much higher rate and in a cleaner environment. All these steps will be described in the next paragraphs.
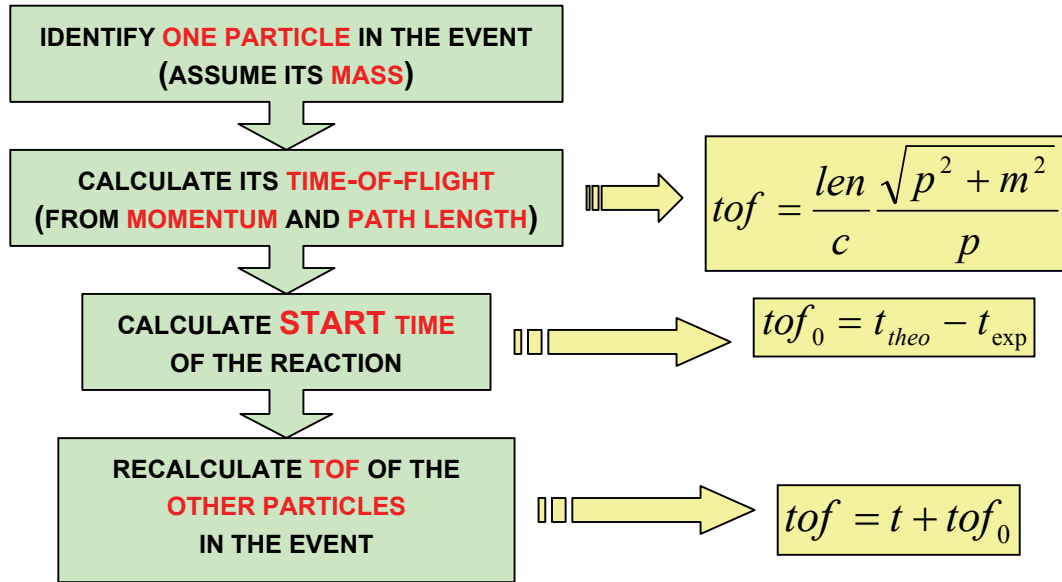

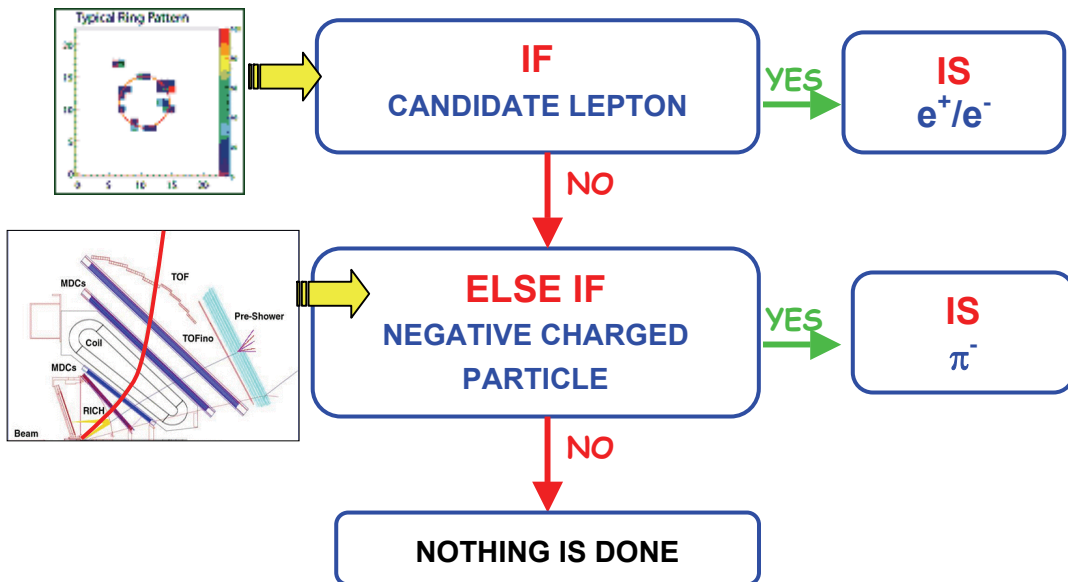**Figure 6.18** – Flowchart of the algorithm used for start time reconstruction.

Figure 6.19 – Schematic view of the particle identification method used for the start time reconstruction.

6.5.2 Simulation

Figure 6.20 shows the two dimensional plot of the product momentum times polarity versus β for simulation data. All the particles fall into well defined regions of

the plot, and by applying an appropriate selection they can be identified. We want to apply the same identification procedure also for the January 2004 experiment, when the START detector was not present, therefore we need the start time reconstruction.

In this simulation the START detector was not included, all the particles have the same start time without any spread of resolution; the only resolution effects are included into the TOF and TOFINO measured values. This means that we can apply the start time reconstruction algorithm to simulated data, and compare the original time of flight value to the reconstructed one, in order to evaluate resolution and efficiency of the method.
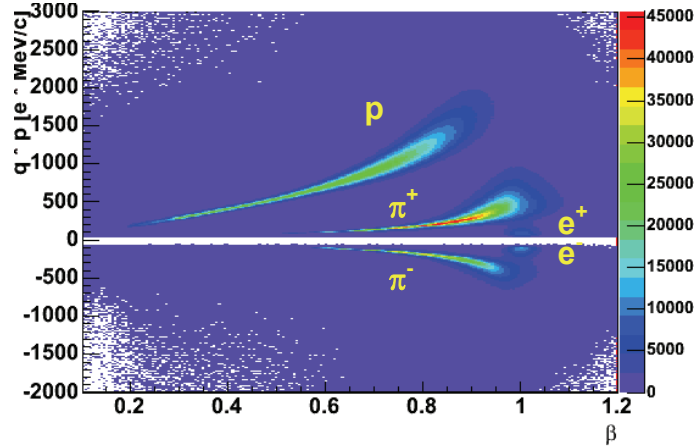

Figure 6.20 – Momentum times polarity versus β spectra for simulation data, by using original tof values. All the particles fall into well defined regions of the plot.

If we consider a particle whose tof was reconstructed, we can express this value tof_{rec} by the formula:

$$tof_{rec} = tof_{exp} + \underbrace{start}_{tof_{rec}^0 - tof_{exp}^0} = tof_{exp} + tof_{rec}^0 - tof_{exp}^0 \qquad \textbf{(Eq. 6-29)}$$

where tof_{exp} is its measured time of flight, *start* is the calculated start time, tof_{rec}^0 and tof_{exp}^0 are respectively the reconstructed tof and the measured one for the particle which we are identifying.

By plotting the difference between reconstructed tof and measured one $tof_{rec} - tof_{exp}$ we can estimate the resolution of the so calculated start time.

Figure 6.21 shows the time difference distributions, only for identified particles in lepton identification case, as a function of momentum times polarity (to distinguish between electrons and positrons), separately for TOF and TOFINO systems.

The distributions are well centred around zero value as expected, but for some tracks the algorithm failed; in simulation we can check the real ID of the track and understand what went wrong.

In the TOF system the noise is negligible and it comes mainly from fake tracks or misidentified pions. In TOFINO system the main sources of errors come from positive charged tracks; in the region of positive differences the bump comes from TOFINO multiple hits: when more than one particle hit the same TOFINO pad, the time measurement is affected and it can produce wrong tof values (even below 6 ns); in the

region of negative differences we can clearly see the region of protons correlated by chance to RICH hits (most protons go to lower polar angles).
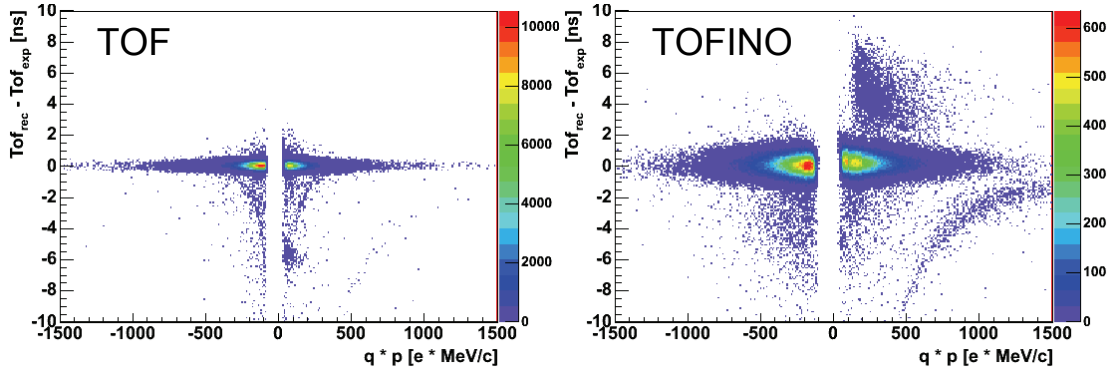

Figure 6.21 – Distributions of differences between reconstructed and measured values of tof for simulation, in cases when an electron/positron is identified (TOF wall on the left side, TOFINO on the right).

Figure 6.22 shows the one dimensional distributions of time differences for identified tracks, in the cases of lepton ID. By fitting the peaks with a gaussian function, from the width we can estimate the start time resolution, which is 162 ps for TOF system and 489 ps for TOFINO; these numbers are substantially the time resolution values of the two detectors, because the time of flight of the electrons at these energies does not depend on momentum ($\beta \sim 1$).
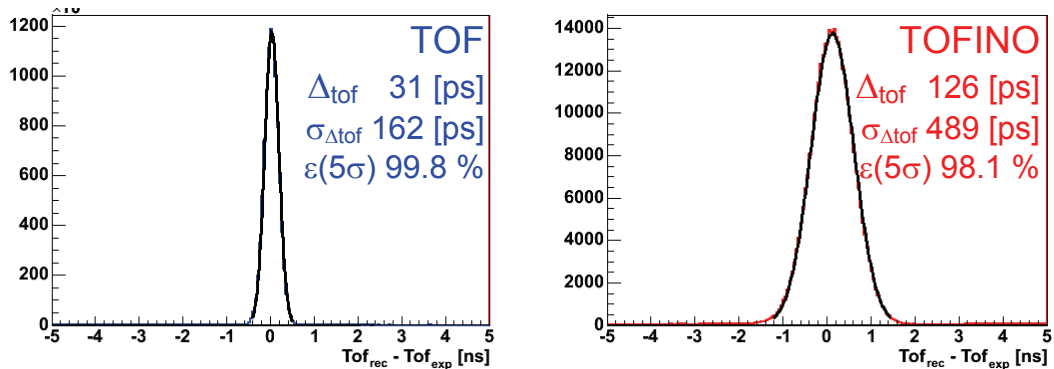

Figure 6.22 – Difference between reconstructed time of flight and measured one, for identified tracks using lepton ID in simulation data (TOF on the left, TOFINO on the right). The reported numbers are the fit values and the efficiency in a 5 σ window.

In order to evaluate the efficiency of the start time so reconstructed, that is to understand how many times the time recalculation fails, we can check the ratio ε between the number of tracks with a time difference within 5 σ and the total number of reconstructed tracks. In the regions far from the main peak all the contributions should come from tracks with a wrong start time value. The obtained values are reported in Figure 6.22, and are 99.8 % for the TOF detector and 98.1 % for TOFINO. The efficiency loss is almost negligible.

Figure 6.23 shows the momentum times polarity versus β plots for all the particles, in events where the start time was reconstructed by lepton identification (z is in logarithmic scale); on the left the time used was the original one, while on the right we can see the reconstructed velocity values.
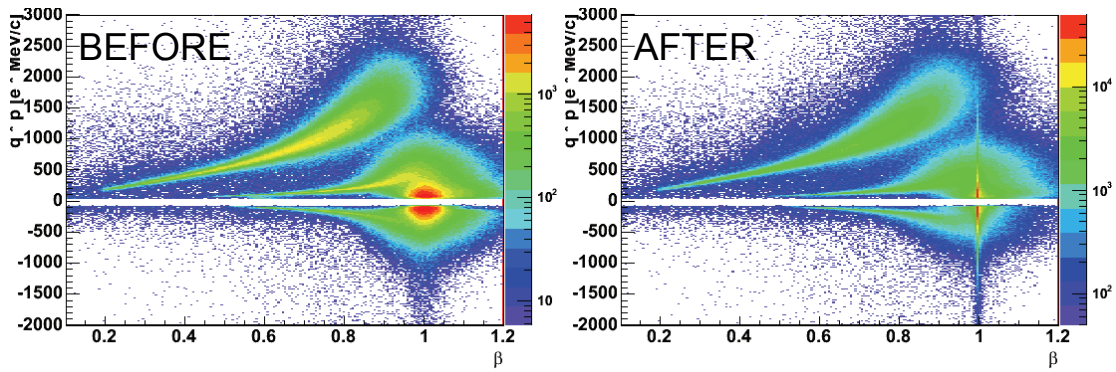
Figure 6.23 – Momentum times polarity versus β spectra before (left) and after (right) start time reconstruction, by identifying an electron/positron in the event (simulation).

In the plot of reconstructed tracks the vertical line is constituted by identified tracks, which have β≡1 by the algorithm assumption. About all the other particles, we can see pions and protons are well separated and located in the correct positions, so the particle identification can be still done using momentum versus β method even with reconstructed values.

The same analysis can be done for events where a negative pions is identified.

Figure 6.24 shows the time difference distributions as a function of momentum values. Apart from the main peak centred at zero, we can see there are some deviations for positive difference values. The problem comes from electrons which are not seen by the RICH detector and are then misidentified as pions; in this case the reconstructed tof is larger than the real one (which is almost 7 ns), and it follows a well defined line as it is possible to see in the low momentum region.

By looking at one dimensional distributions (Figure 6.25) the resolution values are a bit higher (192 ps for TOF, 506 ps for TOFINO) with respect to the case of lepton identification, because momentum plays an important role in the start time evaluation, and then the overall measurement is affected by its resolution. Moreover while the TOFINO efficiency remains stable at 98.5 %, the TOF one feels the effect of lepton misidentification and it is reduced to 85.1 %.

If we look into the momentum versus β plots shown in Figure 6.26, even when the start time is reconstructed from an identified negative pion the proton and the pion regions are well defined and separated, and particle identification can be done. In the plot after the start time reconstruction, the red line corresponds to the identified pions, whose time of flight is calculated as a function of momentum and so its distribution follows a well defined narrow line.

Another way to check the quality of the start time reconstruction is by looking at the mass values M of the particles, which are connected to their momentum p and velocity β by the formula:

$$M = \frac{p}{\beta}\sqrt{1 - \beta^2}$$

(Eq. 6-30)

Figure 6.27 shows the mass distribution (multiplied by charge) of single particles before and after the start time reconstruction, separately for lepton and pion identification. In the spectra all the tracks which were used to reconstruct the start time are not plotted, because they have an imposed mass value (only one bin of the

histograms) and they cannot be compared to the measured one (which is smeared by detector resolution).

The positions of the mass peaks are centred at the correct values of the corresponding particle (i.e. at pion and proton masses), while the widths are a bit broader because of the loss of resolution from the algorithm.

However we can see in simulation that the start time is reconstructed in the proper way, and the recalculated time of flight values can be used for particle identification.

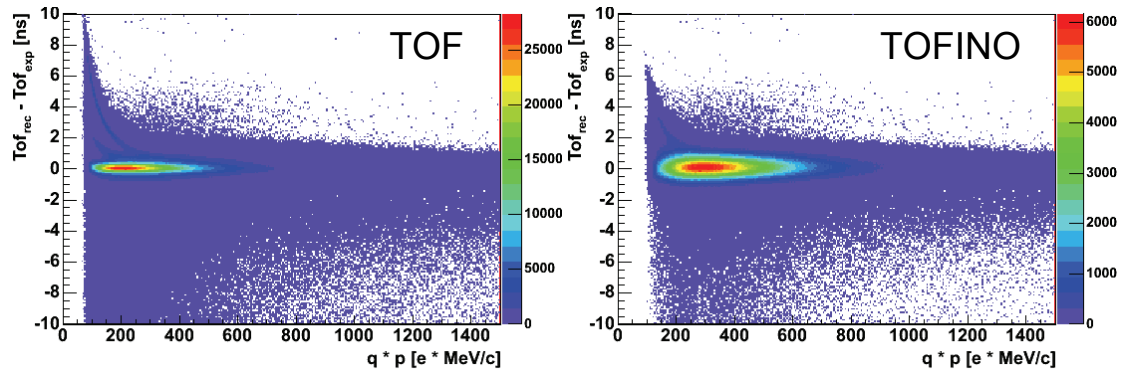In the following paragraph the same analysis will be done for experimental data.

Figure 6.24 – Distributions of differences between reconstructed and measured values of tof (simulation), in cases when a negative pion is identified (TOF wall on the left side, TOFINO on the right).
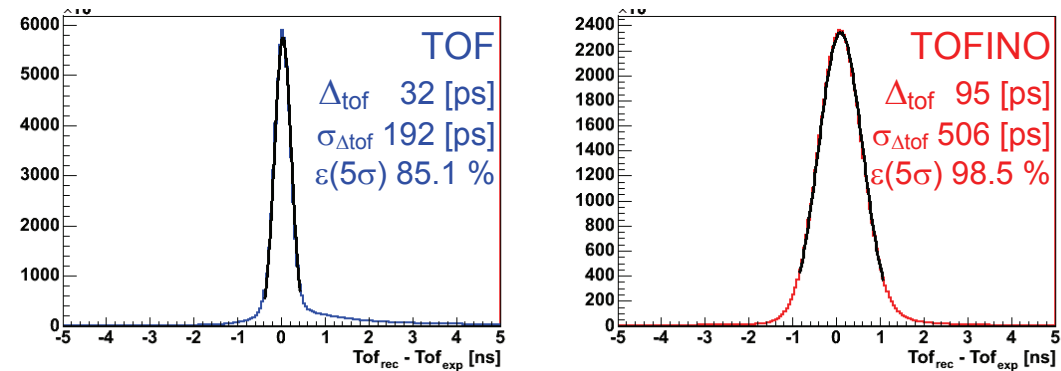

Figure 6.25 – Plots of differences between reconstructed tof and measured one for identified negative pions in simulation, for TOF (left) and TOFINO (right) systems. The TOF distribution has a tail at positive values, connected to electron misidentification.
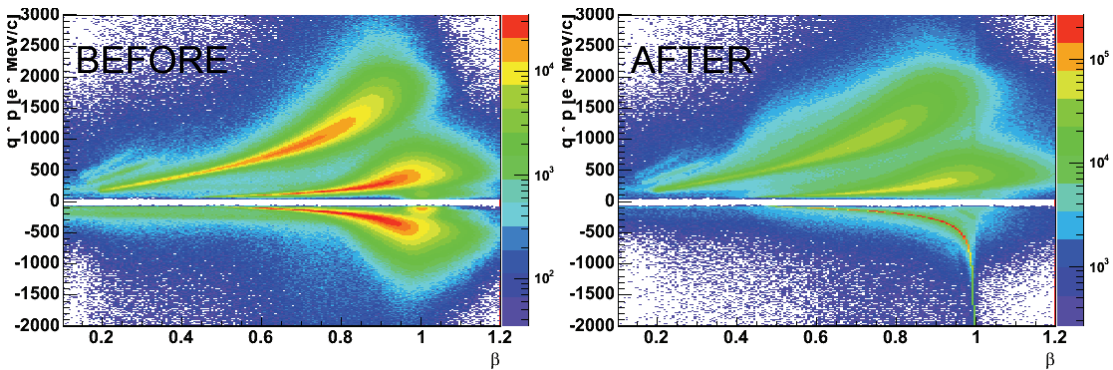

Figure 6.26 – Momentum times polarity versus β spectra before (left) and after (right) start time reconstruction, by identifying a negative pion (simulation).
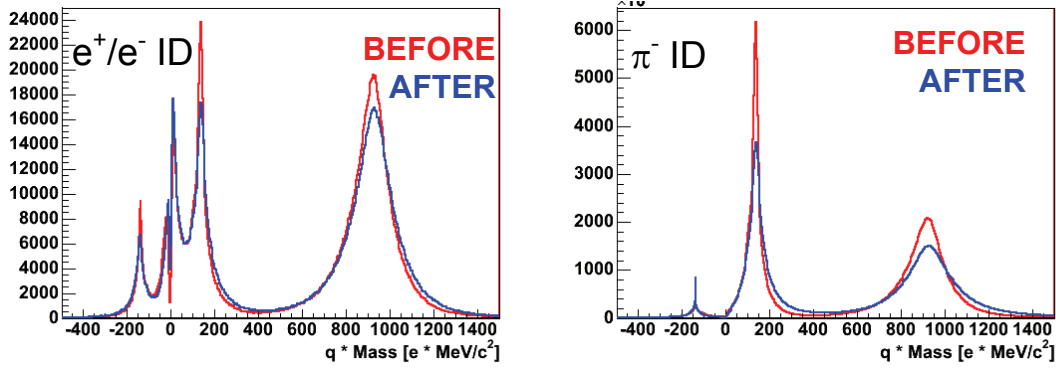
Figure 6.27 – Comparison between single particle mass distributions before and after start time reconstruction (simulation). All the identified tracks are removed from the sample (see the text).

6.5.3 September 2003 data

In September 2003 the START detector was present because the test experiment was operated at lower beam intensity. This means that the measured time of flight can be used as a reference to evaluate the start time reconstruction method for real data.

The time calibration was performed as explained in paragraph 6.3, and the TOF/TOFINO time resolution values are almost the same as found in simulation. But in this case there was also the START detector, then all the time measurements t_{exp} are affected also by its resolution of about 235 ps. We should expect broader time resolution values according to this effect.

Indeed if we consider the relations:

$$start = tof_{rec} - tof_{exp} \, , \, tof_{exp} = t_{exp}^{STOP} - t_{exp}^{START} \qquad \textbf{(Eq. 6-31) (Eq. 6-32)}$$

by propagating the errors we find that the resolution values σ are correlated by this formula:

$$\sigma_{start}^2 = \sigma_{rec}^2 + \sigma_{exp}^2 = \sigma_{rec}^2 + \sigma_{STOP}^2 + \sigma_{START}^2 \qquad \textbf{(Eq. 6-33)}$$

where t_{exp}^{STOP} and t_{exp}^{START} are times of the stop (TOF/TOFINO walls) and start (hodoscope) signals in TDCs, and as σ resolution values we indicate: *start* for the reconstructed start time, *rec* for the method (i.e. resolution of the time reconstruction from momentum), *STOP* for TOF/TOFINO detectors and *START* for the hodoscope.

Figure 6.28 shows the time differences as a function of momenta in the case of lepton identification. The analysed sample was smaller than in simulation data, but all the noise sources are still visible also here.

By looking at Figure 6.29 the resolution values obtained from the gaussian fits (316 ps for TOF, 517 ps for TOFINO), and in particular for TOF detector, are larger than simulation values (162 ps for TOF, 489 ps for TOFINO). In order to compare the experimental values to the simulation ones, by means of a quadratic subtraction of the hodoscope resolution we obtain 211 ps for TOF and 472 ps for TOFINO, which are closer to the expected values. The obtained values of the method efficiency (5σ cut) is 98.9 % for TOF, 98.1 % for TOFINO.
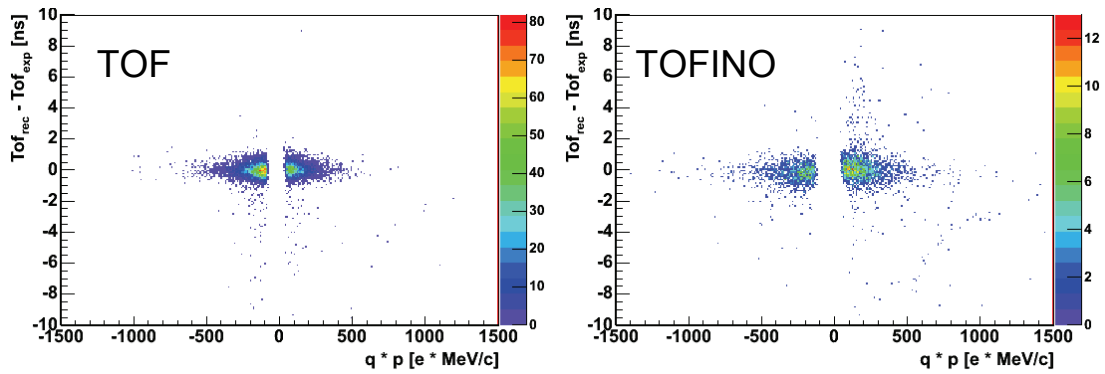
Figure 6.28 – Distributions of differences between reconstructed and measured values of tof (September 2003 data), in the case when a lepton is identified (TOF on the left, TOFINO on the right).
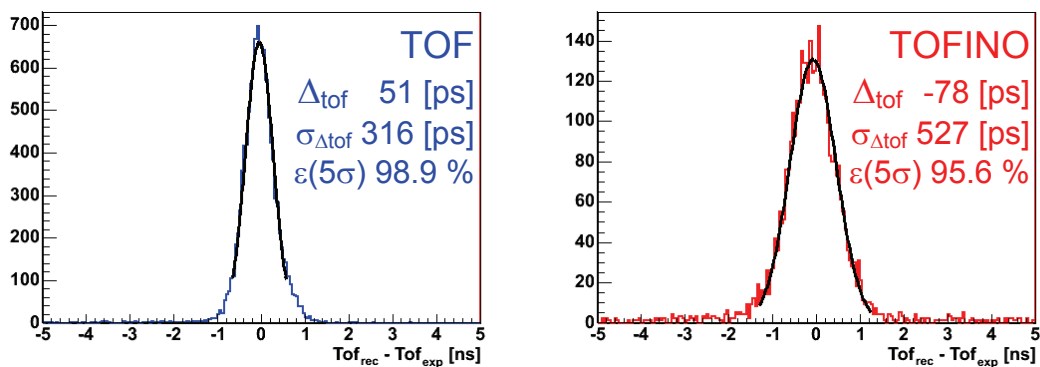

Figure 6.29 – Difference between reconstructed time of flight and measured one for identified tracks using lepton ID (September 2003 data), for TOF (left) and TOFINO (right) systems.
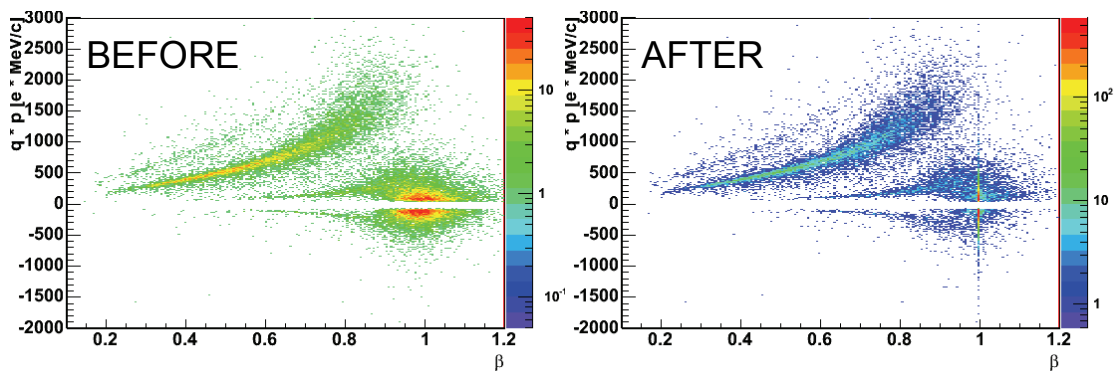

Figure 6.30 – Momentum times polarity versus β spectra before (left) and after (right) start time reconstruction, by identifying an electron/positron (September 2003 data).

Figure 6.30 shows the momentum versus β spectra before and after the time reconstruction and, apart from the identified leptons, the shapes of proton and pion distributions and their good separation are maintained.

The same analysis can be done for identified negative pion cases.

Figure 6.31 and Figure 6.32 show the time difference distributions, respectively as a function of momentum and integrated over all the tracks. Even in this case the contamination from misidentified leptons is present. If we check the resolution values

we have 347 ps for TOF and 527 ps for TOFINO detectors; by subtracting the START resolution value we obtain 255 ps for TOF and 472 ps for TOFINO.

We must consider that in the experimental data the momentum resolution is larger than in simulation, and of course this effect is visible in the obtained reconstructed start time resolution.

In TOF plot the tail from misidentified electrons is less pronounced than in simulation, and then the experimental efficiency value is higher (90.1 % for TOF, 97.2 % for TOFINO).
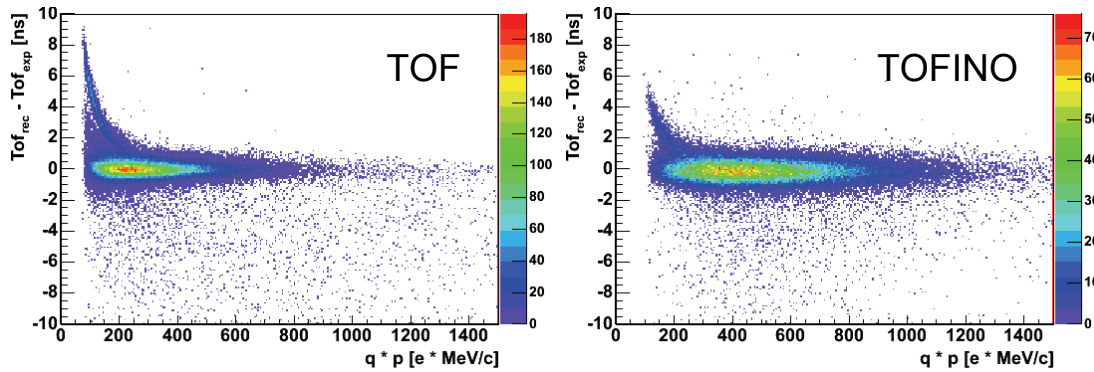

Figure 6.31 – Distributions of differences between reconstructed and measured values of tof in cases of pion identification, for September 2003 data (TOF wall on the left side, TOFINO on the right).
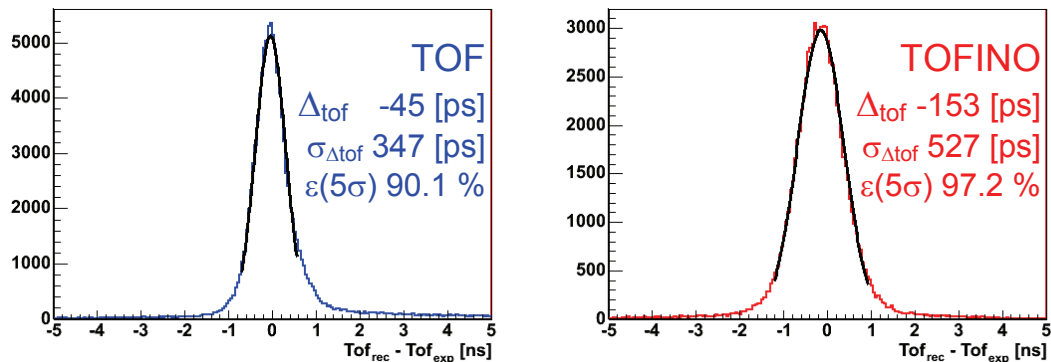

Figure 6.32 – Plots of differences between reconstructed tof and measured one of the identified negative pions (September 2003 data), for TOF (left) and TOFINO (right) systems.
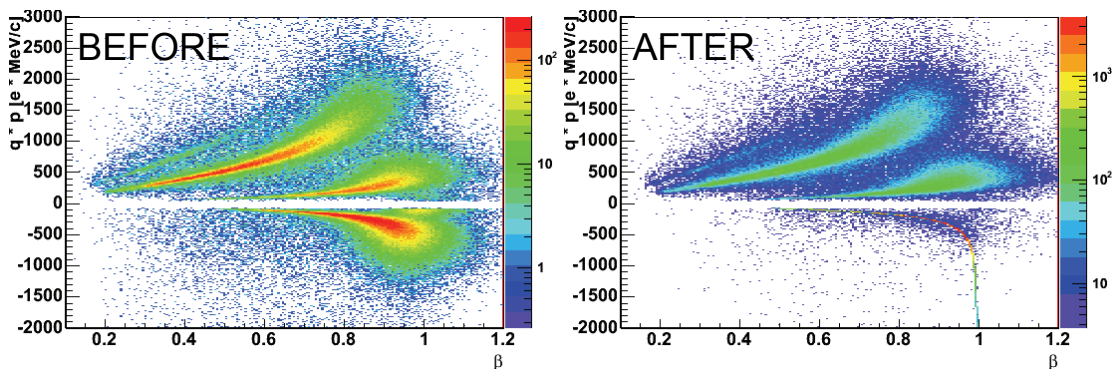

Figure 6.33 – Momentum times polarity versus β spectra before (left) and after (right) the start time reconstruction, by identifying a negative pion (September 2003 data).
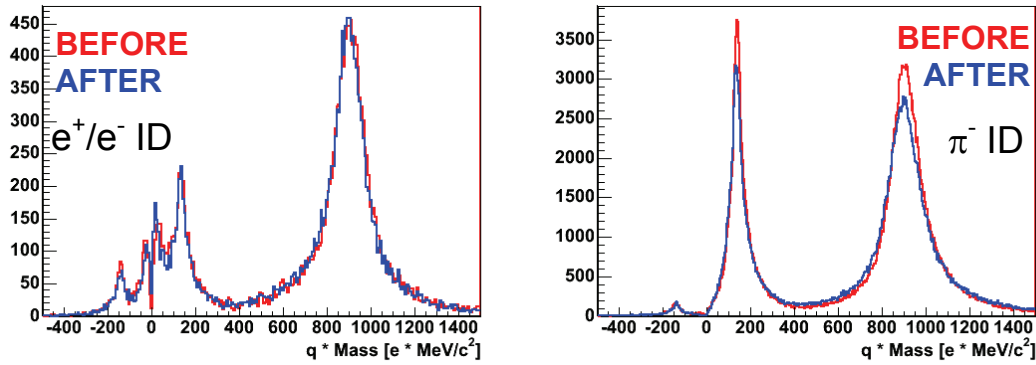
Figure 6.34 – Comparison between single particle mass distributions before and after the start time reconstruction (September 2003 data).

In Figure 6.33 momentum versus β plots are shown before and after the start time reconstruction, and in Figure 6.34 we can see the comparison between mass distributions in the two identification cases. Even from these plots we can state that the reconstruction worked properly and hadron identification is possible.
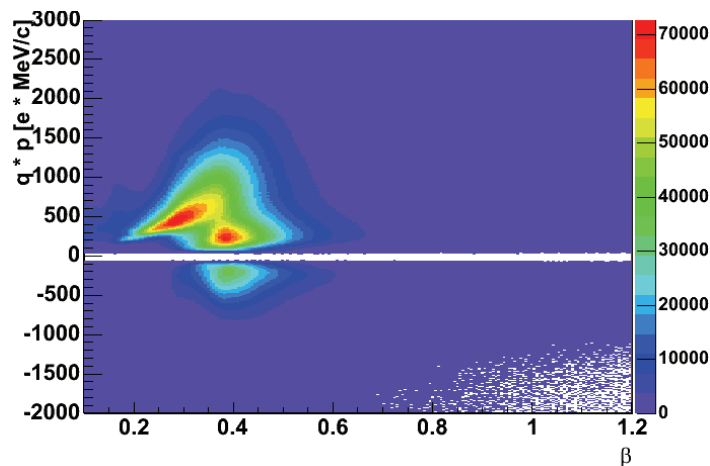
6.5.4 January 2004 data

Figure 6.35 – Momentum versus β plot for January 2004 data, by taking the measured value of time of flight. In this case protons and pions are not separated and particle identification cannot be performed in this way.

During the January 2004 acquisition run the START detector was not present in the spectrometer setup, then the time measurement was started by the particle which produced the first signal to the 1st level trigger system. Figure 6.35 shows the momentum versus β spectrum using the time of flight values measured in this way. As expected we cannot separate in the proper way protons from pions, and it is not possible to see lepton structures as it happens with START measurements.

The following pictures show the difference between the same two dimensional distributions before and after the start time reconstruction, made by selecting events where lepton (Figure 6.36) or pion identification (Figure 6.37) was applied.

We can see that the reconstruction algorithm works quite well even when the START detector is actually not present. Proton and pion distributions are well

separated (the plots are in logarithmic scale) and a graphical selection is possible to identify the two kinds of particle.

At last, by checking single mass distributions (Figure 6.38) before and after the start time reconstruction, the reconstructed mass peaks are placed at the correct position

Figure 6.36 – Plots of momentum versus β for January 2004 data, before and after start time reconstruction from lepton identification.
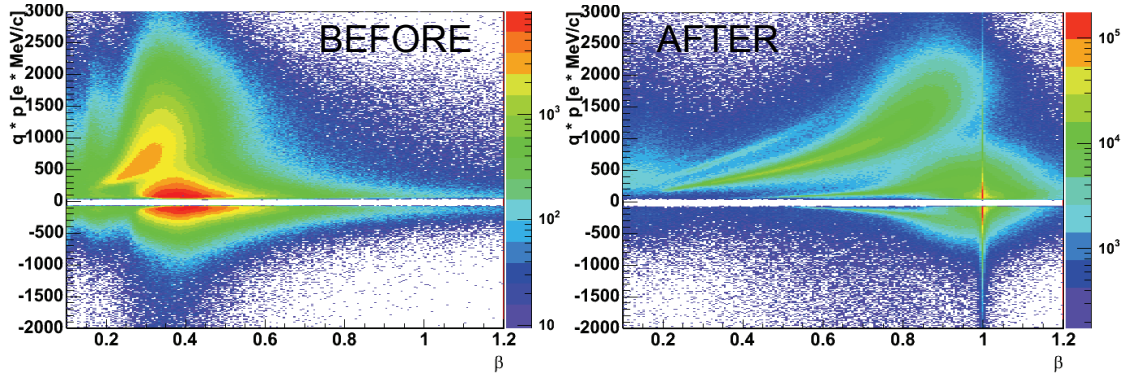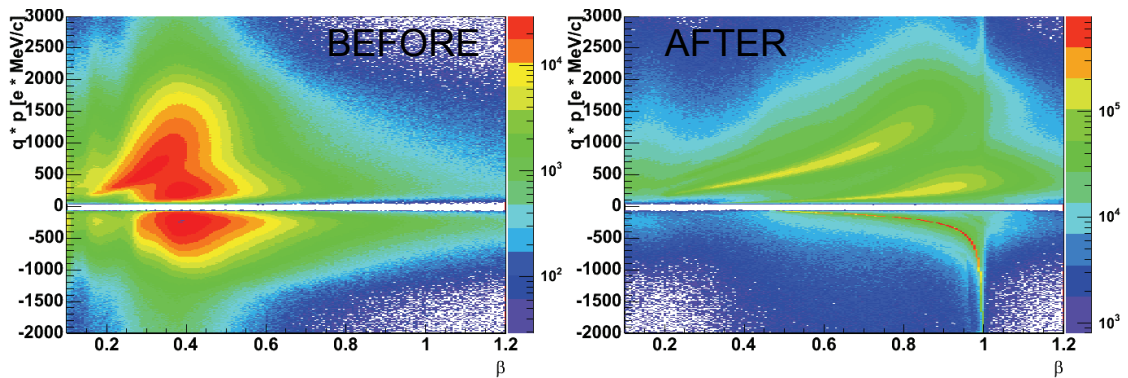

Figure 6.37 – Plots of momentum versus β for January 2004 data before and after start time reconstruction, for cases of negative pion identification.
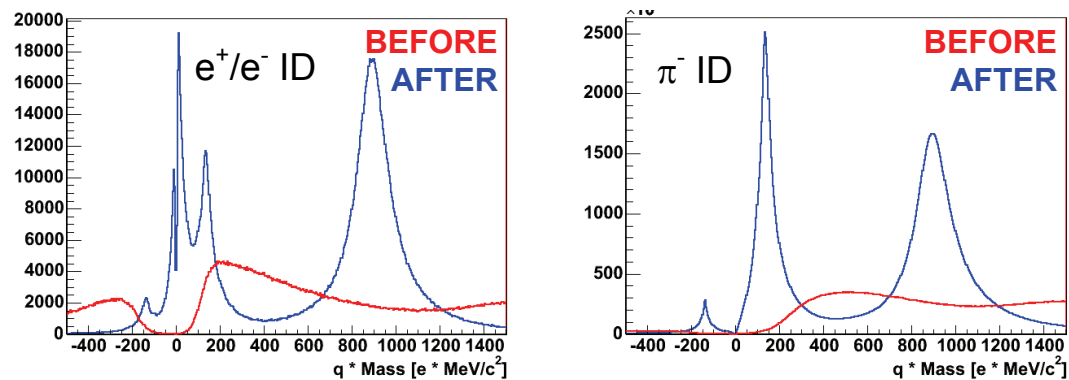

Figure 6.38 – Comparison between single particle mass distributions before and after start time reconstruction, for January 2004 data.

6.5.5 Start time reconstruction summary

In Table 6-3 all the results of start time reconstruction are presented for both simulation and September 2003 data (for January 2004 we do not have a reference time to use), in terms of time residuals between reconstructed and measured time of flight values Δtof, resolution $\sigma_{\Delta tof}$ and efficiency ε as defined in the text (number of identified tracks inside a 5 σ time window divided by the total number of identified tracks).

The impossibility of using a START detector during the experiment worsens the time of flight measurement, because of the already shown motivations. The time calibration procedure becomes much difficult and it has to use dilepton pairs (so a larger data sample than when START is used); the effect is visible in the worse time resolution values obtained for TOF and TOFINO detectors as compared to the September 2003 data (neglecting the contribution from the START detector).

A procedure of time reconstruction was developed and tested in simulation and in experimental data acquired with the START time. Its validity was demonstrated and it was applied also on the January 2004 data, when the START detector was really missing. The obtained momentum versus β plots after time recalculation, which is the main tool to perform particle identification for the HADES spectrometer, shows a good separation between protons and pions.

So we can state that the algorithm fulfills its goals, and it can be used to perform exclusive analysis of decay channels, where the identification of almost all the particles in the final state is required.

Data	ID	System	Δtof [ps]	$\sigma_{\Delta tof}$ [ps]	ε [%]
SIM	e^+e^-	TOF	31	162	99.8
		TOFINO	126	489	98.1
	π^+	TOF	32	192	85.1
		TOFINO	95	506	96.9
SEP03	e^+e^-	TOF	51	316	98.9
		TOFINO	-78	527	95.6
	π^+	TOF	-45	347	90.0
		TOFINO	-153	527	97.2

Table 6-3 – Summary table of results from start time reconstruction, for simulation and September 2003 data.

7 EXCLUSIVE η RECONSTRUCTION

In this chapter the procedure to identify the η meson decays will be presented. The study of the η meson is of particular interest for several reasons. The inclusive η cross section is well known in the vicinity of the production threshold, but at higher energy the experimental values have large errors and they can be significantly improved (see paragraph 2.5).

The η production cross section can be measured both through the hadronic ($\eta \to \pi^+\pi^-\pi^0$) and the dielectron ($\eta \to e^+e^-\gamma$) Dalitz decays, whose branching ratios are known. This fact allows to use the pp→ppη channel as a calibration reaction for the dielectron identification of the spectrometer, in order to normalize the dielectron yields in the heavy ions experiments. Moreover an accurate measurement of the η Dalitz decay could help improving our evaluation of the electromagnetic form factor of the meson.

7.1 Particle identification

In order to perform an exclusive reconstruction we need to identify all the charged particles in the exit channel.

We are interested in reconstructing the η hadronic decay into three pions $pp\eta \to pp\pi^+\pi^-\pi^0$, and the electromagnetic Dalitz decay $pp\eta \to ppe^+e^-\gamma$; thus we need to identify in an event two protons and two pions for the hadronic decay, two protons and a lepton pair in the electromagnetic case.

The lepton identification can be performed by using the correlation of the track with the RICH detector: if the particle provides a signal in the RICH which can be identified as a ring, we can assume that the selected particle is an electron or a positron according to its charge (from the trajectory deflection inside the magnetic field region).

The hadron identification is usually done by a correlated measurement of momentum and velocity of the particles, but in order to use this kind of algorithm we need a correct time of flight measurement. After the start time reconstruction method, explained in chapter 6, we have reliable values of particle velocity which can be used for this purpose.

In the analysis of this chapter only the Runge Kutta tracking algorithm will be used for angle and momentum reconstruction, because of its improved performances respect to Spline algorithm.

For the η hadronic decay we need to identify two protons and two pions. The left side of Figure 7.1 shows the momentum times polarity versus β distribution in experimental data, for events where the start time was reconstructed from a negative pion. We do not need to analyse events which contain leptons, so we can take them out of our sample.

The hadron identification is performed by a graphical cut on the two dimensional distribution. The selection is quite broad in order not to lose efficiency at this stage of the analysis; by imposing constraints from the kinematics of the desired reactions we will be able to remove wrongly identified tracks.

For the η electromagnetic decay we need to identify two protons and a lepton pair. The right side of Figure 7.1 shows the same momentum versus β plot, but this time for events where the start time was reconstructed from an identified lepton.
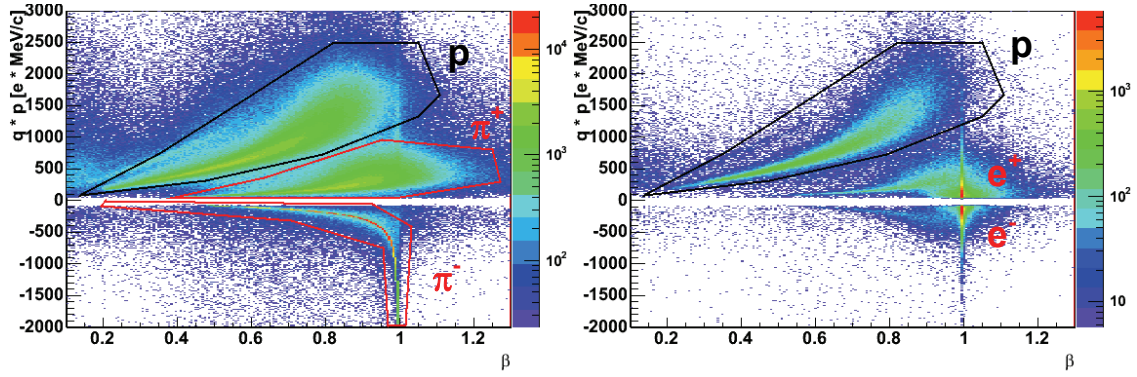
Figure 7.1 – Momentum times polarity versus β distributions for the January 2004 experimental data, in cases where the start time is reconstructed by an identified π⁻ (left plot) and by an identified lepton (right plot). The graphical selections for hadron identification are indicated.

In this case we only need to identify the proton region by the same graphical selection used for the hadronic decay.

In order not to lose statistics the lepton identification was performed by using only RICH correlation, without imposing conditions on the ring quality (minimum bias) and without detecting electromagnetic showers in the Shower detector. Even in this case the misidentified tracks will be removed by further conditions on the kinematics of the event.

For exclusive η reconstruction in experimental data only events with the M4smart[1] 1st level trigger selection were analysed (about 265 millions).

The event reduction after applying several conditions is shown in Figure 7.2, in comparison for experimental and simulation data samples. The numbers can also be read in Table 7-1.

The first condition consists on a selection of events which contain at least three positive and one negative charged particles [(+)>2 && (-)>0]; we can see that this condition strongly reduces the statistics for both the simulation and experimental data samples.

From these numbers we can see that the surviving events after this selection are about 3.2% of the total events for experimental data, while about 1.9 % in simulation. This reflects the fact that in experiment we are much more dominated by secondary particles which are not present in simulation; these tracks are fully reconstructed by the tracking system and increase the number of events inside the selections.

Selection	Explanation	simulation	experiment
M4smart	Trigger selection	155,132,559	263,067,265
(+)>2 && (-)>0	3 positive 1 negative particles	3,005,423	8,335,245
tofrec !=0	Start time reconstruction	2,866,133	7,785,520
p > 1	Two identified protons	2,009,247	5,386,906
pi+ pi-	Two protons and two pions	1,709,904	3,858,643
e+ e-	Two proton and a lepton pair	38,624	115,311

Table 7-1 – Table of event reduction after different kind of selections.

[1] M4smart condition means: at least four particles in META detector, at least two particles in TOFINO detector, and two META opposite sectors hit.

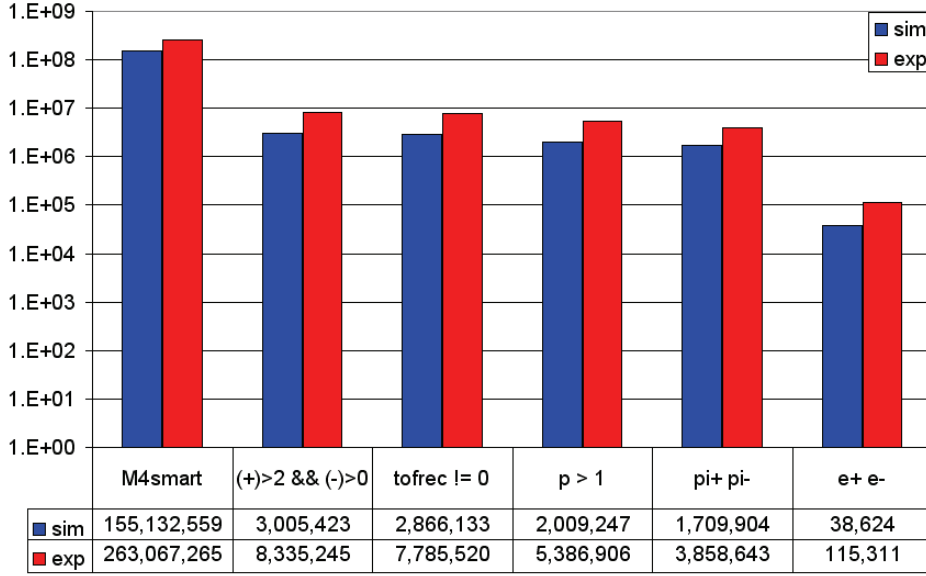|	M4smart	(+)>2 && (-)>0	tofrec != 0	p > 1	pi+ pi-	e+ e-
sim	155,132,559	3,005,423	2,866,133	2,009,247	1,709,904	38,624
exp	263,067,265	8,335,245	7,785,520	5,386,906	3,858,643	115,311

Figure 7.2 – Event reduction after applying several conditions in order to perform exclusive η meson reconstruction, for both simulation and experimental data samples (see the text and Table 7-1).

On a second step we need to impose that the start time is reconstructed [tofrec != 0], in order to perform particle identification by using momentum and velocities. We can see that the event reduction by requiring time reconstruction is minimal, thus meaning that the global efficiency of the start time reconstruction algorithm is quite high.

By using the reconstructed start time we can apply the graphical selection to identify particles. First we select events with at least two protons[2] [p > 1]; then we can search events which contain at least one π^+ and one π^- [pi+ pi-] for hadronic decay, or one electron and one positron [e+ e-] for electromagnetic decay. In the latter case we can see a strong reduction in number of events, considered the low branching ratio for dilepton production.

After we have identified all the four charged particles the event is not yet fully reconstructed, because we are still missing one particle: a neutral pion in the hadronic decay, and a photon in the electromagnetic decay. The missing particle can be found by means of a missing mass analysis.

In order to calculate the missing mass of the system we need to know energy and momentum values of the particles in the initial state and in the exit channel.

The initial state of the reaction is defined by the 4-momentum of the projectile plus the 4-momentum of the target ($E_{ini} = E_{proj} + m_{target}$, $\vec{p}_{ini} = \vec{p}_{proj}$), thus it is substantially fixed by the beam energy. Momenta for the outgoing particles $\vec{p}_{out}$ are provided by the tracking system, while the energy is calculated by $E_{out} = \sqrt{p_{out}^2 + m^2}$, where the mass m is the value assumed from the particle identification.

Thus we can express the missing mass (squared) by the formula:

$$M^2 = \left(E_{ini} - \sum_i E_{out}^i \right)^2 - \left(\vec{p}_{ini} - \sum_i \vec{p}_{out}^i \right)^2 \qquad \textbf{(Eq. 7-1)}$$

---

[2] Physically we cannot have more than two protons in the event, but experimentally we have proton multiplicities even larger than two due to particle misidentification.

where the sum is extended over the detected particles in the exit channel, the two outgoing protons in the case of the missing η or the four particles ppπ$^+$π$^-$ - ppe$^+$e$^-$ respectively for the missing pion or photon.

In the following paragraphs the exclusive reconstruction procedure will be shown separately for hadronic and electromagnetic decays.

7.2   η *hadronic decay*

In this chapter the procedure to identify η mesons decaying into hadrons will be explained.

Using the momentum versus velocity plot of Figure 7.1 (left side) it is possible to identify the particles and to select 4-prong events where two protons, a negative pion and a positive pion are detected; by looking at the missing mass distribution it is then possible to select events with the hadronic decay of the η meson.

The reaction of interest is pp→ppη→ppπ$^+$π$^-$π^0. If we plot the missing mass distribution of the four-particle final state we should observe a peak in the region of the missing neutral pion; moreover, by plotting the missing mass of the two protons of the final state, the peak of the missing η meson should appear.

The analysis will be shown separately for simulation and for experimental data.

7.2.1 *Simulation*

Figure 7.3 shows the *pp* squared missing mass (y axis) versus *ppπ$^+$π$^-$* squared missing mass (x axis), for the simulation data sample.
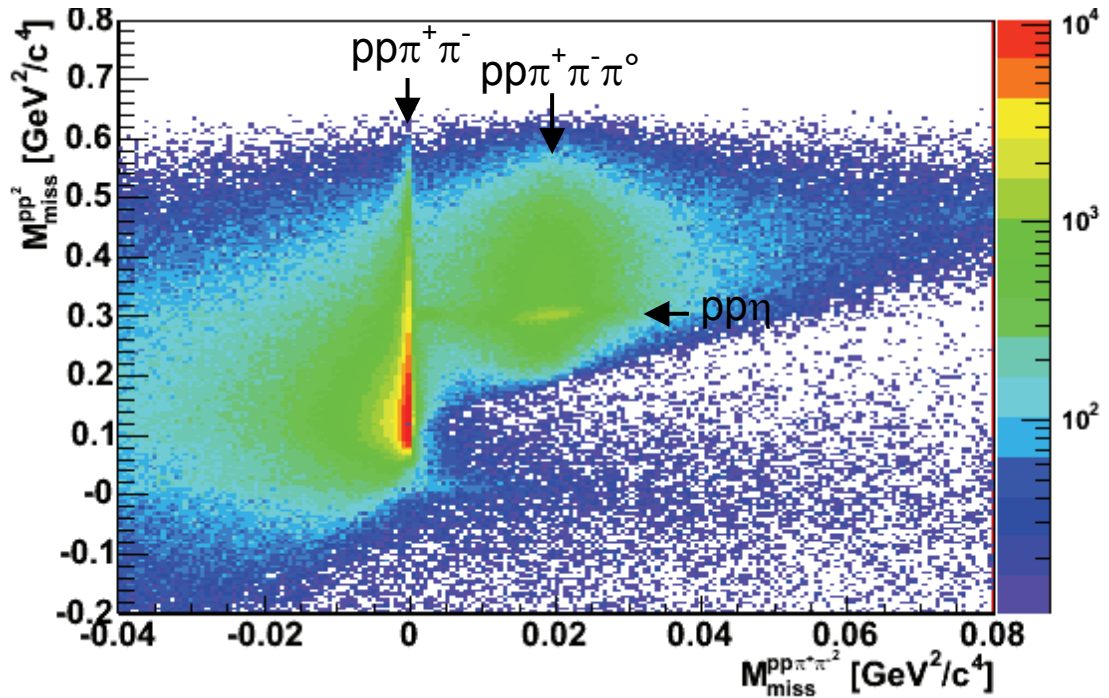

Figure 7.3 – Missing mass plot for four detected particles (two protons, two pions), in simulation. All the visible reaction channels are indicated in the plot.

The simulation is not so close to the experiment, due to an imperfect handling of the detector alignment in the experimental data and to some effects not yet considered in simulation (see chapter 5 for the details), but it provides important hints on what we should expect and what we find in real data.

Looking at the plot one observes that the main part of the distribution stays around the zero value of the four-particles missing mass; this corresponds to the $pp{\to}pp\pi^+\pi^-$ channel fully reconstructed (no missing particles).

In the positive region of the x axis there is a prominent bump, corresponding to events where the π^0 is missing. In this region the η meson appears as a peak in the two-proton missing mass, in form of a horizontal trace in the plot.

In order to identify η mesons the first step is to find events with a missing π^0. If we look at the $pp\pi^+\pi^-$ missing mass distribution of Figure 7.4, in a mass range between 30 MeV/c^2 and 350 MeV/c^2 in order to cut out the strong contribution coming from the $pp{\to}pp\pi^+\pi^-$ channel (peaked at zero), we can see that the missing π° peak is quite evident.

The background contamination is quite low. In order to find the peak position and an estimate of the 4 particles mass resolution we can fit the distribution with a gaussian function (in red) for the main peak, plus a polynomial function (in green) to fit the background; the resulting function is shown in black.

We can see that the correspondence between the fit function and the measured distribution it is not optimal, but it allows to obtain a rough estimate.

The fit result shows that the peak position is centred at 139 MeV/c^2 with a width of 19 MeV/c^2, close to the effective π° mass of 135 MeV/c^2 (within the error bars). From the width we can estimate the resolution for the invariant mass measurement made using four particles ($pp\pi^+\pi^-$); the obtained value is 13.7%.

By imposing a cut around the peak region we can select events with the missing π°, and then we can look at the distribution of the two-proton missing mass.

The selected range of four-particle missing mass is between 50 MeV/c^2 and 250 MeV/c^2. The cut is quite broad in order not to lose missing π° events; the efficiency of the cut is estimated close to 100% for our analysed reaction, so we do not have a strong reduction of η signals from this selection.
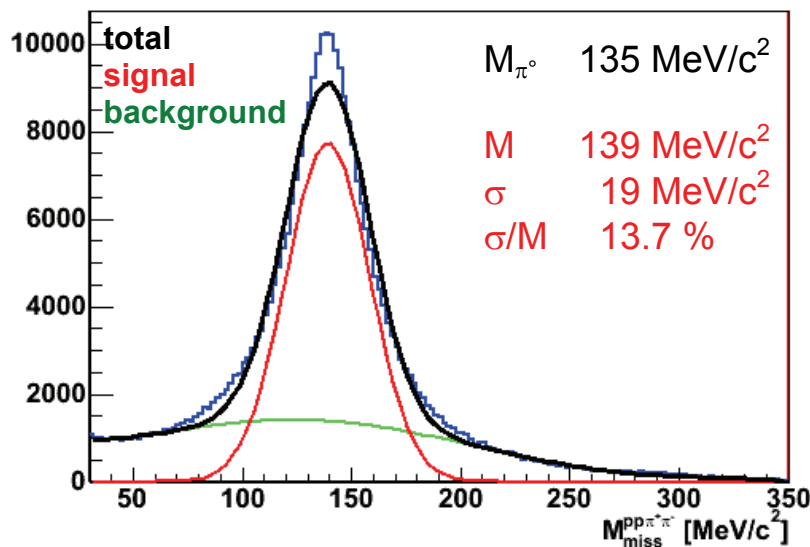

Figure 7.4 – Simulation plot of $pp\pi^+\pi^-$ missing mass distribution between 30 MeV/c^2 and 350 MeV/c^2, in order to discard the contribution from the $pp{\to}pp\pi^+\pi^-$ channel. The missing π° peak is prominent.
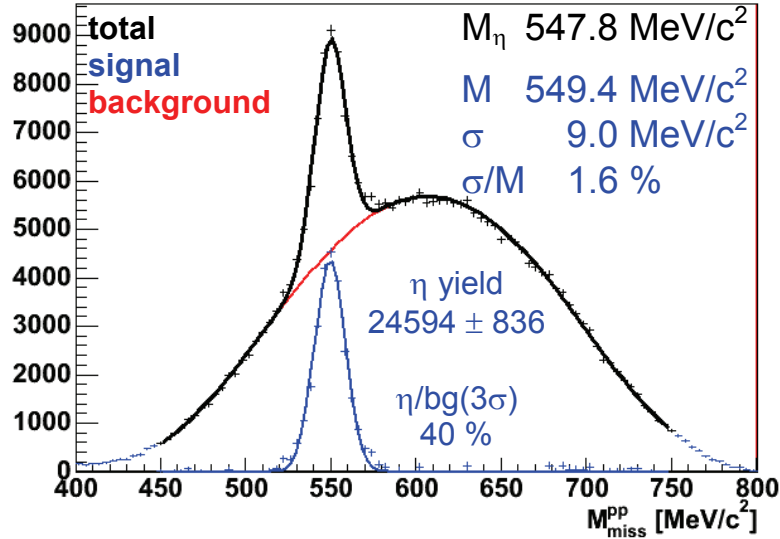
Figure 7.5 – Proton-proton missing mass distribution for simulation data, after the selection on 4 particle missing mass in the range [50 MeV/c², 250 MeV/c²]. Results from a fit with a gaussian (η signal) plus a polynomial (background) functions are reported, as well as total yield and signal/background (bg) ratio in a 3σ mass window around the η peak.

Figure 7.5 shows the proton-proton missing mass distribution, after the missing π° selection (black dots). The error bars in the plot come from statistical error.

The spectrum is composed of the physical background, coming from $pp\pi^+\pi^-\pi^0$ non-resonating channel, plus the well defined peak of the missing η meson.

The distribution can be fitted in order to estimate the peak position, the mass width and the η meson yield. The function (black line) used for the fit was a gaussian for the signal (blue line) plus a polynomial to fit the background (red line).

In this case we see a good agreement between the fit function and the measured distribution. The blue dots represent the estimated η signal, thus the measured distribution less the background fit function.

The peak is located at 549.4 MeV/c², i.e. at the theoretical position (m$_\eta$=547.8 MeV/c²); the width of the gaussian function is 9.0 MeV/c², which corresponds to a two-particle invariant mass resolution of 1.6%.

By integrating the signal fit function over a mass range between 500 MeV/c² and 600 MeV/c², reasonably broad with respect to the estimated peak in order not to lose η signal events, we obtain a yield of 24594 ± 836 η mesons[3] for the full simulation sample.

It is possible to estimate the signal over background ratio in the η meson mass range. The calculation was done over a 3σ mass window around the η peak; an η yield of 24527 was obtained (close to the value obtained by integrating over the [500,600] MeV/c² mass range), while 60756 counts were estimated as the background yield. By dividing these two numbers we obtain about 40% as signal to background ratio.

We can therefore state that in simulation it is possible to identify the η meson by using this missing mass technique.

---

[3] The errors are computed by propagating parameter errors coming from the signal's gaussian fit inside the integral function.

But now we want to apply the same procedure in experimental data, which are affected by a worse momentum resolution, and thus we should expect a worsening in terms of resolution and signal to background ratio.
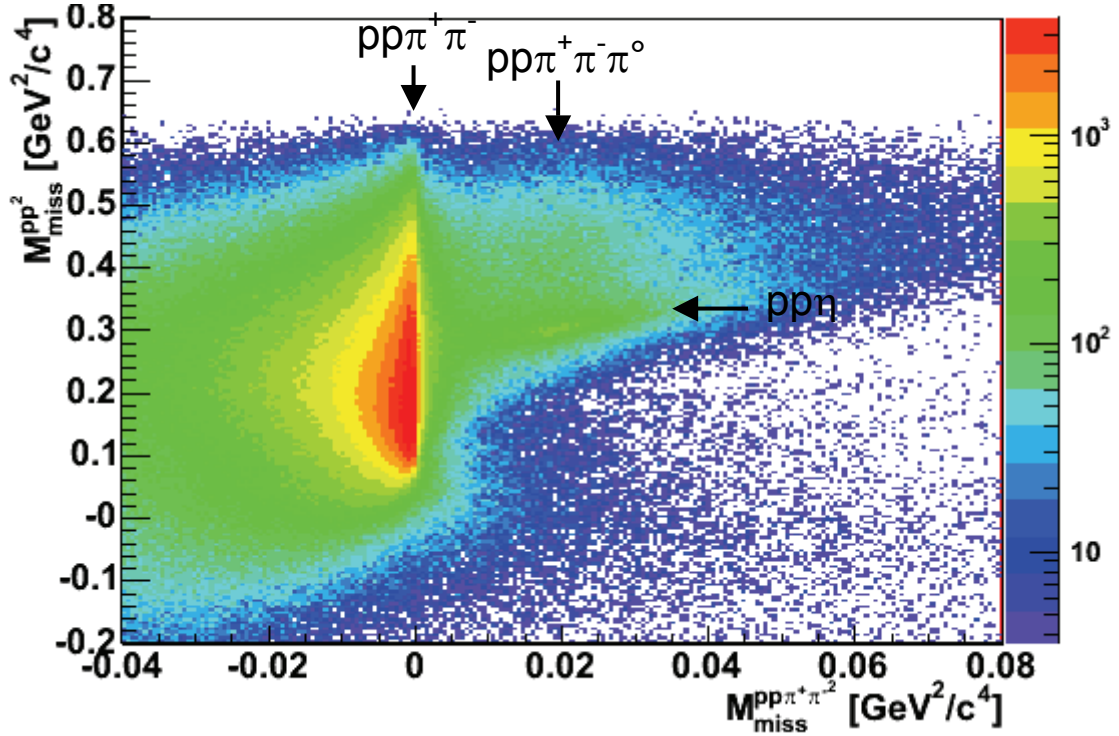
7.2.2 Experimental data

Figure 7.6 – Missing mass plot for four detected particles (ppπ$^+$π$^-$), in experimental data. All the visible reaction channels are indicated.

Figure 7.6 shows the two-dimensional missing mass plot for the January 2004 experimental data sample.

We can see the worse momentum resolution compared to the simulation data (see chapter 5 for differences between momentum resolution in simulation and in experiment); the distributions are broader and the separation between the ppπ$^+$π$^-$ channel and the ppπ$^+$π$^-$π° channel is not so well defined as in the simulation case (see Figure 7.3). Nevertheless the ppη channel is still evident in the plot as well as the missing π°, so the exclusive η reconstruction procedure can be performed also in the experimental data.

First of all only downscaled events (LVL1) were used for the data sample; not downscaled events (LVL2) contain at least a lepton pair and we are not interested in analysing them. In this way, if we calculate the η yield in downscaled events, by multiplying this number times the average downscaling factor we get an estimate of the total number of η meson events (via hadronic decay) which passed the 1st level trigger selection (see paragraph 4.6.1).

After selecting downscaled events, we can plot the ppπ$^+$π$^-$ missing mass distribution as shown in Figure 7.7. In order to reduce possible sources of background events, an additional condition was put in the proton-proton missing mass, by selecting a range between 400 MeV/c^2 and 800 MeV/c^2.
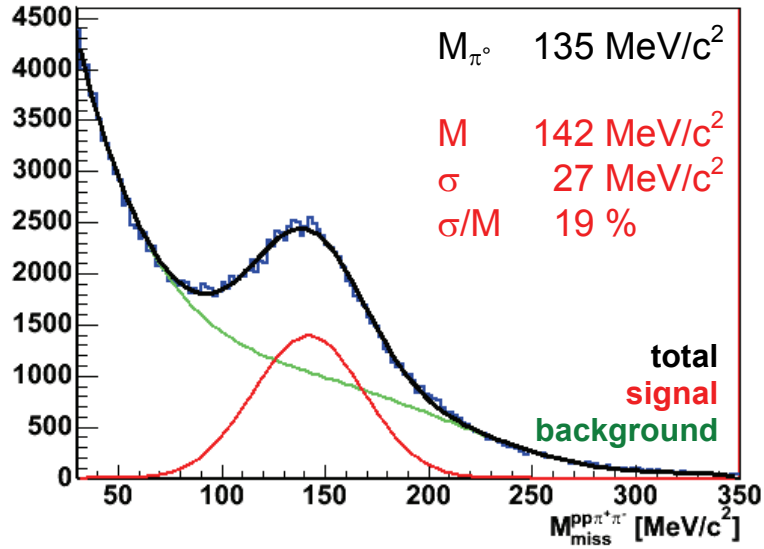
Figure 7.7 – $pp\pi^+\pi^-$ experimental missing mass distribution, after a selection on pp missing mass between 400 MeV/c^2 and 800 MeV/c^2. The background from the $pp\pi^+\pi^-$ channel is higher than in the simulation case, but the missing π° peak is still visible. The distribution was fitted (black line) with the sum of a gaussian function (red line) for the π°, and a polynomial (green line) for the background.

In experimental data we can see that the contribution from $pp\pi^+\pi^-$ channel is much higher, mainly due to the worse momentum resolution; however the missing π° peak is visible and can be selected.

The experimental distribution was fitted (black line) as in the simulation data, with the sum of a gaussian (red line) for the π° signal plus a polynomial function (green line) for the background.

By looking at the fit results, the π° mass peak is centred at 142 MeV/c^2 with a width of 27 MeV/c^2, which corresponds to 19% as invariant mass resolution.

The peak is close to the π° mass value within error bars; the resolution is broader than in simulation, as we expect from the different momentum resolution.

In order to select events with a missing π°, the same 4 particle missing mass selection applied in simulation was used, thus a mass range between 50 MeV/c^2 and 250 MeV/c^2, which corresponds to about a 3.7 σ selection around the π° peak. If we assume that the π° follows a gaussian distribution, we should not lose π° signal events by applying this mass selection (below 0.1%).

The obtained pp missing mass distribution is reported in Figure 7.8. The shape is similar to what obtained in simulation, the η peak is visible but broader, while the background in the low mass region of the distribution is higher, mainly due to the higher contamination from $pp\pi^+\pi^-$ decay channel. The error bars are given by statistical errors.

The distribution was fitted (black line) with a gaussian function for the η peak (blue line) plus a polynomial function for the background (red line). The black dots represent the experimental distribution, while the blue dots correspond to the distribution less the background fit function. We can see that the obtained function fits well the experimental distribution, even if there is a small discrepancy in the higher mass tail of the η signal peak.

The η peak is centred at 554.1 MeV/c^2 with a width of 19.7 MeV/c^2; the obtained missing mass resolution is 3.5%, which is enough to distinguish the η peak.
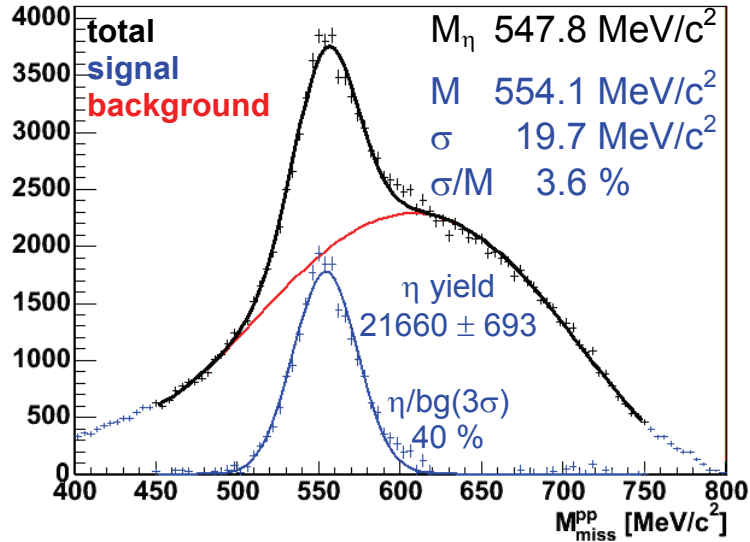
Figure 7.8 – Proton-proton missing mass distribution for experimental data, after the selection on four particle missing mass [50 MeV/c², 250 MeV/c²]. The fit function (black line) is the sum of a gaussian (η signal) plus a polynomial (background) function. Fit results, η yield and signal/background (bg) ratio are reported.

By integrating the signal fit function between 500 MeV/c² and 600 MeV/c² (about 3.6 σ selection, so by assuming an η meson gaussian distribution the signal reduction should be lower than 0.1%), we obtain 21670 ± 693 η signals.

The signal over background ratio was estimated by calculating the signal and the background yield in a 3σ missing mass region around the η signal peak. We obtain 21883 η signal events (almost the same of the [500,600] MeV/c² selection) and 55270 background events; by dividing these two numbers we can estimate a signal/background ratio of about 40%, similar to what obtained in simulation.

To conclude the hadron decay channel analysis we can calculate the total number of η hadronic decays which passed the 1st level trigger selection. All the obtained numbers were calculated only for the downscaled data sample; by multiplying the total yield by the average downscaling factor 2.2 (see paragraph 4.6.2), we obtain a total of 47674 ± 1525 η hadronic decays, without any acceptance corrections.

We can rightfully state that the exclusive reconstruction of the η hadronic decay is possible by means of the HADES spectrometer.

The obtained values of resolution and signal/background ratio can be improved by applying a refinement method, the kinematic refit.

7.2.3 Kinematic refit

The kinematic refit is a procedure to improve the tracking parameters of the particles which concur in a physical reaction, by imposing kinematic constraints.

Let us assume to have a set of parameters provided by the tracking system, which for a particle can be expressed by momentum p, polar and azimuthal angles θ and ϕ. We can express this set of tracking parameters as[4]:

---

[4] We use as track parameter $1/p$ instead of p because it follows a gaussian distribution, a mandatory condition for the kinematic refit procedure

$$\alpha_i = \left(1/p, \theta, \phi\right)^T \qquad\qquad \textbf{(Eq. 7-2)}$$

In our case α_i are the tracking parameters of the four particles needed for the exclusive η reconstruction.

In order to reconstruct the η meson a condition can be imposed on the missing mass of the four particles, which should corresponds to the mass of a π° meson.

A kinematic refit procedure varies the α tracking parameters of all the particles (3 parameters for each of the four particles, so in total 12 parameters) until the best values $\widetilde{\alpha}$ are found which satisfy the imposed constraint.

The constraint is imposed by using the Lagrange multiplier method. In mathematical form, this procedure requires the minimization of the functional F:

$$F = \left(\vec{\alpha} - \vec{\widetilde{\alpha}}\right)W^{-1}\left(\vec{\alpha} - \vec{\widetilde{\alpha}}\right)^T + \lambda^T H(\widetilde{\alpha}) \qquad\qquad \textbf{(Eq. 7-3)}$$

where W is the error matrix, λ is the Lagrange multiplier and H is the physical constraint on the four particles missing mass[5].

In order to perform the kinematic refit we need to know the error values of the W matrix. The errors on angular variables such as θ and ϕ are given by the propagation of errors from the time fits in the drift chambers; these values were multiplied by two in order to take into account a worse angular resolution coming from the small misalignment. The errors on the momentum reconstruction were set sectorwise by using the values obtained in the elastic scattering analysis of chapter 5, separately for simulation and for experimental data.

The analysis procedure for the kinematic refit remains the same as explained before; the four particle missing mass selection between 50 MeV/c^2 and 250 MeV/c^2 is done on the original mass value; the refitted one cannot be used because it is affected by the imposed kinematic constraint.

In Figure 7.9 the comparison between the pp missing mass distribution before and after applying the kinematic refit is shown, for simulation and for experimental data.

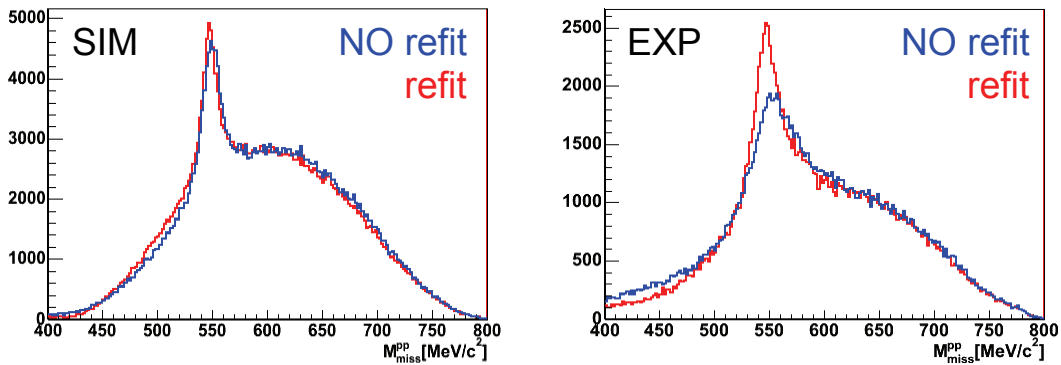**Figure 7.9** – Proton-proton missing mass distributions for simulation (left) and experimental data (right). It is possible to see the comparison between the distribution with and without kinematic refit.

---

[5] If we want to impose not one but n physical constraints, λ and H become $\lambda = \left(\lambda_1, \lambda_2, ..., \lambda_n\right)^T, H = \left(H_1, H_2, ..., H_n\right)$.
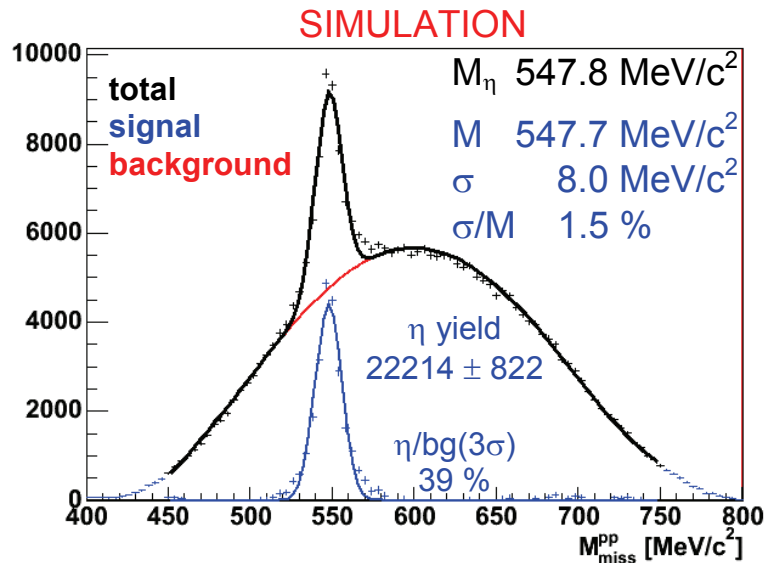
Figure 7.10 – Pp missing mass distribution for simulation, after the kinematic refit.

In simulation it seems that there is no strong improvement in the distribution. The background changes a bit its shape and the η peaks becomes a little narrower. But if we look at the experimental distribution, the kinematic refit improves a lot the missing mass distribution, the η peak is narrower and we have more counts around the peak region.

Now the usual fit procedure can be applied to the pp missing mass distributions, in order to estimate the new values of the peak position, of the mass width and of the signal to background ratio.

Figure 7.10 shows the distribution for simulation data. The peak is centred at 547.7 MeV/c², it is closer to the correct value and the width decreases by 1 MeV/c², moving at 8 MeV/c² which corresponds to a mass resolution of 1.5%.

Under the signal peak in the [500,600] MeV/c² mass range we obtain an η yield of 22214 ± 822, while the new signal to background ratio in a 3σ mass window is 39%.
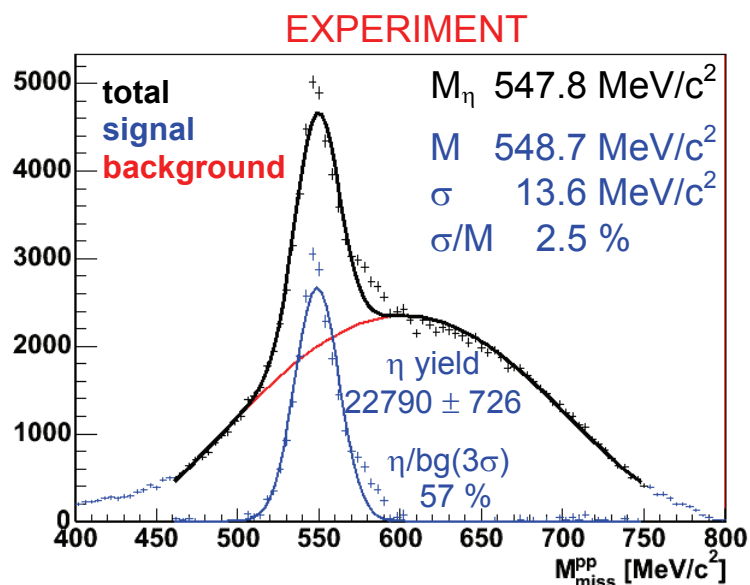

Figure 7.11 – pp missing mass distribution for experimental data, after kinematic refit.

We can state that the improvement is minimal and only in terms of mass resolution. The number of counted η mesons is a bit lower than the old value (even if within the error bars), and the signal/background ratio dropped by one percent. The reason of these reductions can be found by looking at the background subtracted mass distribution (blue dots) and the signal fit function in the plots. After applying the kinematic refit the signal peak is not well fitted by the gaussian in the tail regions, and even at the peak centroid; we can easily see that the fit is underestimating the correct number of η mesons, and then the obtained numbers reflect this feature.

Figure 7.11 shows the experimental distribution after the kinematic refit. Here the improvement is well visible. After the refit the η peak is at 548.7 MeV/c^2, much closer to the theoretical value, while the mass width decreases from 19.7 MeV/c^2 (3.6%) to 13.6 MeV/c^2 (2.5%).

This improvement in the mass resolution affects also the η yield. In the mass region between 500 MeV/c^2 and 600 MeV/c^2 we count 22790 ± 726 η signal events, and the signal/background ratio is now 57% in a 3σ mass region around the η peak. This means that, in the experimental data, by means of a kinematic refit the η signal becomes higher than the background events, as we can easily see from the distribution. Moreover the little higher number of η mesons reconstructed after the kinematic refit shows that the procedure is able to recover events which were rejected by simply using Runge Kutta tracking algorithm, moving them in the correct position under the peak.

In order to evaluate the number of η signal events which passes the 1st level trigger selection, we must multiply the yield by the average downscaling factor 2.2.

In this case we obtain as total number of η events a yield of 50138 ± 1597, which will have to be compared to the numbers obtained from the electromagnetic decay.

Coming back to the signal fit, here we can see problems in the gaussian fit of the signal distribution (blue dots), which become more pronounced toward the higher mass tail and at the peak position. In spite of the good results obtained in the hadronic exclusive reconstruction, this problem remains open for a more refined analysis.

Table 7-2 shows a summary of all the results obtained for the exclusive reconstruction of η meson hadronic decay, for simulation and experimental data, before and after applying a kinematic refit.

		Mass [MeV/c^2]	σ [MeV/c^2]	σ/M [%]	η yield	η/bg [%]
SIM	NO refit	549.4	9.0	1.6	24594±836	40
	refit	547.7	8.0	1.5	22214±822	39
EXP	NO refit	554.1	19.7	3.6	21660±694	40
	refit	548.7	13.6	2.5	22790±726	57

Table 7-2 – Summary of the results for the exclusive reconstruction of the η hadronic decay.

7.3 *η electromagnetic decay*

In this chapter the procedure to perform the exclusive reconstruction of the electromagnetic decay of η mesons will be explained.

The particle identification via the momentum versus velocity plot of Figure 7.1 (right side) is used only for protons; electron and positron are identified by requiring the correlation of their tracks with a recognized pair of rings in the RICH detector.

After the particle identification, the same procedure applied for the hadronic decay will be followed for the electromagnetic case, that is looking at missing mass distributions and searching for missing particles.

The reaction of interest is pp→ppη→ppe$^+$e$^-$γ. If we plot the missing mass distribution of the 4-particle final state we should observe a peak centred at zero, corresponding to the missing photon; moreover, by plotting the missing mass of the two proton final state, we should search the missing η meson peak.

The analysis will be shown separately for simulation and for experimental data, and the kinematic refit will also be used to improve the results.

7.3.1 Simulation

In Figure 7.12 we can see the pp squared missing mass (y axis) versus ppe$^+$e$^-$ squared missing mass (x axis) distribution, for the simulation data sample.
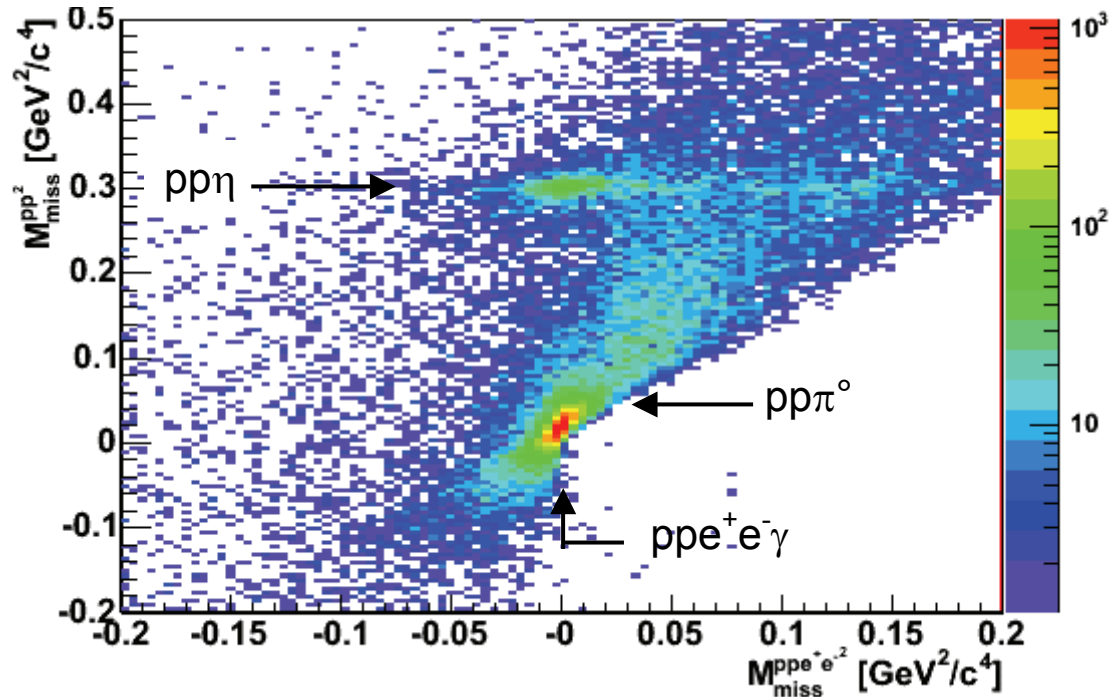

Figure 7.12 – Missing mass plot for four detected particles (two protons, two leptons), in simulation. All the visible reaction channels are indicated in the plot.

In the plot most of the counts are placed at ppe$^+$e$^-$ missing mass values close to zero, which are related to the missing photon; from the statistics we have in the data sample the number of direct decay processes pp→ppe$^+$e$^-$ is almost negligible. The low pp missing mass region is mainly dominated by ppπ° reactions, while the η meson region is well separated and visible at higher mass values.

First of all we must select events where a photon is missing. This can be done by plotting ppe$^+$e$^-$ missing mass distribution.

In order to reduce the contribution from background reactions, a selection on proton-proton squared invariant mass close to the η bump was used, between 0.27

GeV^2/c^4 and 0.33 GeV^2/c^4; in this way the position of the missing γ peak and its width can be evaluated.

In Figure 7.13 the ppe$^+$e$^-$ missing mass (squared) distribution is shown, after this selection; the missing γ peak is well visible over the background. The distribution was fitted by a polynomial function for the background (red line) plus a gaussian for the main peak (blue line); the fit results are shown in the plot.
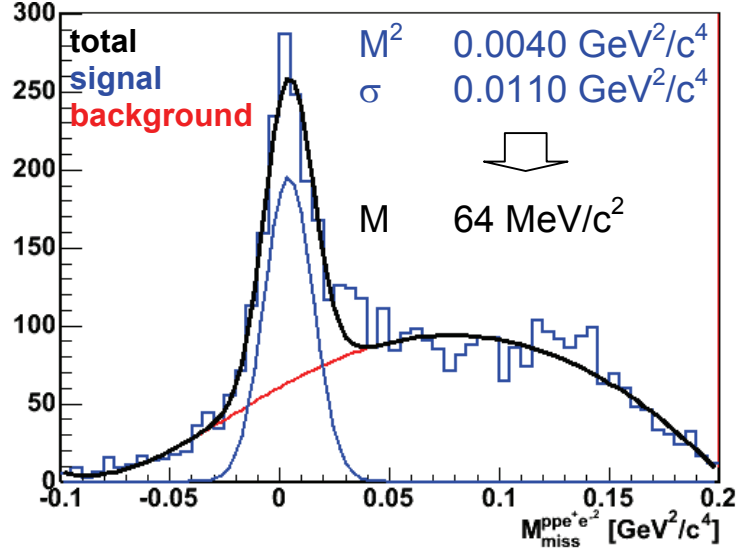

Figure 7.13 – ppe$^+$e$^-$ missing mass squared distribution close to the η bump, for simulation data ($0.27\,GeV^2\big/c^4 < M_{miss}^{pp}{}^{2} < 0.33\,GeV^2\big/c^4$).

From the square root of the peak position we can evaluate the corresponding value of missing mass. We can see that the peak is not centred at zero but at a little higher mass value, about 65 MeV/c^2.

We can compare the obtained distribution with the one in the region of missing π°, so imposing a selection on the two protons missing mass (squared) below 0.2 GeV^2/c^4.

Figure 7.14 shows the distribution so obtained, with the results of the same fit, gaussian (in red) for the γ signal and polynomial (in blue) for the background. Even though the gaussian fit does not reproduce the tails, the peak position is correctly found. It is centred around 20 MeV/c^2, closer to zero than in the η case and even narrower.

This means that, in the case of the η decay channel, the momentum resolution of the four particles is worse than for the π° channel, and there are systematic deviations which move the missing γ peak at positive mass values. We will see that this effect is more pronounced in the experimental data, where we know that the momentum resolution was worse than in simulation.

In order to study the η electromagnetic channel, and also to evaluate the background contribution, we can plot the proton-proton missing mass (of course without the selection used before) by applying a 3σ selection over the ppe$^+$e$^-$ missing mass with the fit values shown in Figure 7.13.

Figure 7.15 shows the obtained missing mass distribution. The η and π° peaks are prominent and the background is kept low. In order to find the meson parameters the distribution was fitted over the whole mass range, by using a combination of two gaussian functions, one for the η (blue) and one for he π° (red) peaks, plus a polynomial background (green).
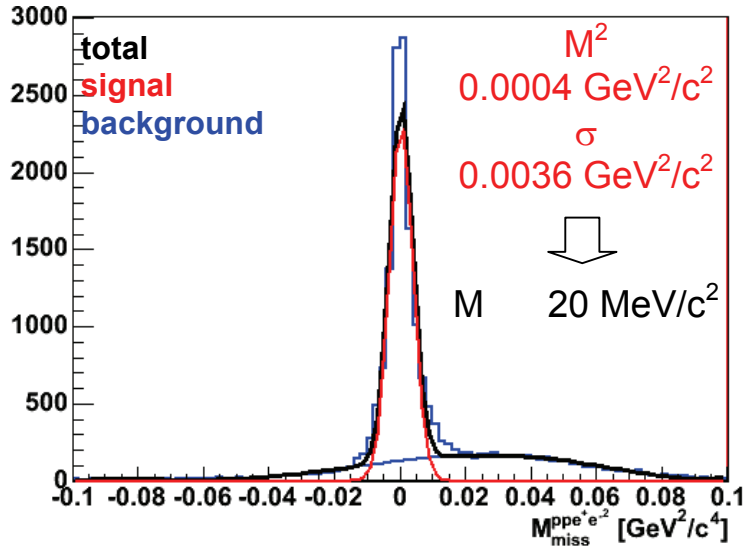
Figure 7.14 – ppe$^+$e$^-$ missing mass squared distribution in the missing $\pi°$ region, for simulation data ($M_{miss}^{pp}{}^2 < 0.2\,GeV^2/c^4$).
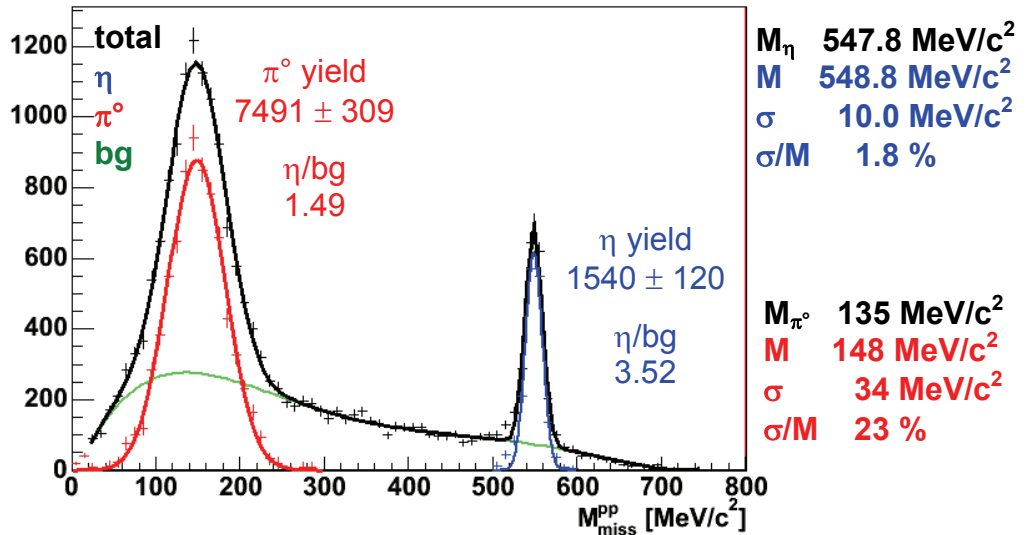

Figure 7.15 – Proton-proton missing mass for simulation data, after a 3σ selection over missing γ mass.

      The background is not easy to evaluate in the low mass region, below the $\pi°$ peak, because at mass values below 50 MeV/c^2 the distribution drops down due to the fact we are evaluating the square root of a number ($M_{miss}^{pp}{}^2$)[6], which can also have negative values (which are rejected in order to perform the computation). Thus we can state that the background evaluation can be misleading in the $\pi°$ region, and so even the $\pi°$ yield.

      Nevertheless the fit function (black line) fits well the distribution. The η meson is peaked at 548.8 MeV/c^2 with a width of 10.0 MeV/c^2, that is at the correct position; the

---

[6] As an example if we have a distribution constant in x, the distribution over $\sqrt{x}$ will decrease toward zero values, because of the $x > 0$ condition that we impose to calculate the square root.

mass resolution so obtained is 1.8%. By integrating the fit function less the background we can estimate, in a 3σ mass range around the peak, 1540 ± 120 η events, with a signal over background ratio of η/bg ~ 3.52.

About the missing π° meson, we can see that its position is at 148 MeV/c² (width 34 MeV/c²), distant from the correct position of 135 MeV/c². This effect is mainly due to the proton momentum loss while crossing the materials around the target region.

In general the particle momentum is reconstructed from the trajectory deviation inside the magnetic field region; effects of energy loss in air and inside MDC chambers are negligible. But before reaching the MDC chambers and the field region, after the particle is emitted inside the target it must cross all the materials placed around that region, mainly the RICH detector. In this region the particle loses energy and momentum, according to its original momentum and its mass.

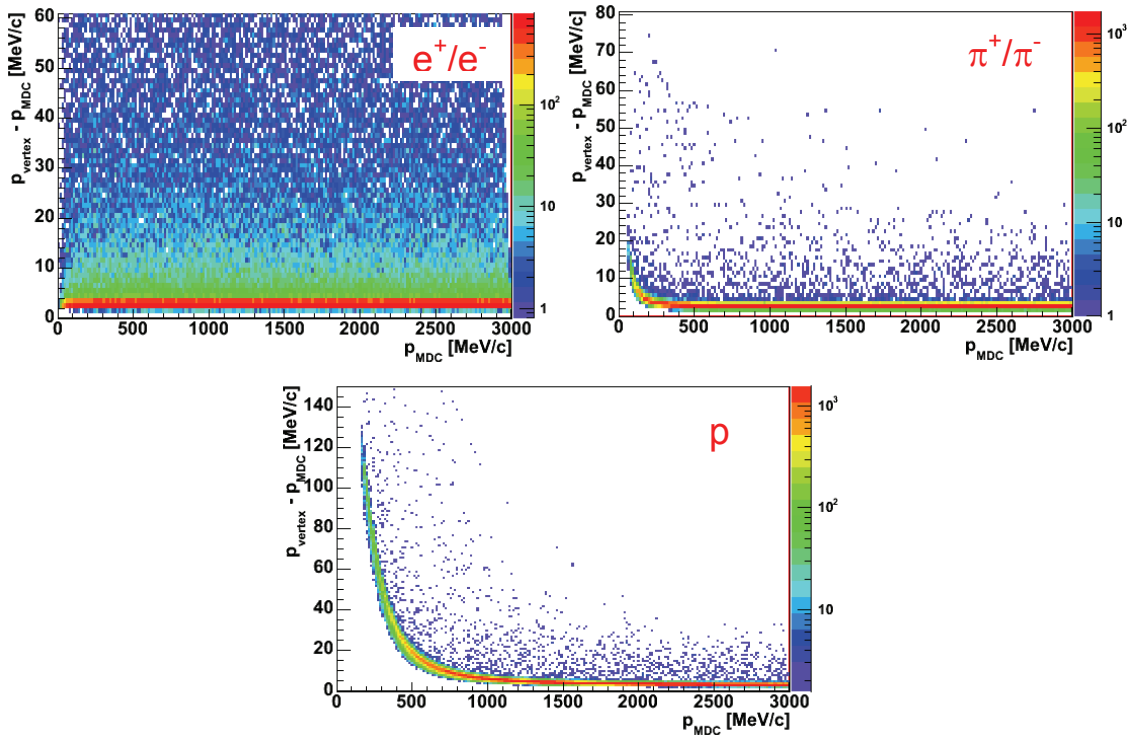**Figure 7.16** - Difference between the proton momentum evaluated at the reaction vertex and in the first layer of MDC1, as a function of the momentum in MDC. Plots were made by using HGEANT simulation, for different kinds of particles.
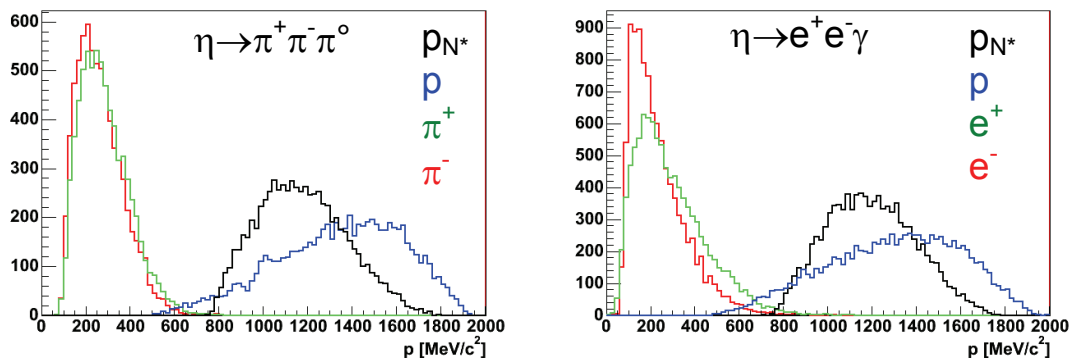

Figure 7.17 – Momentum distribution for final state particles coming from η meson decays, hadronic (on the left) and electromagnetic (on the right) ones, tracked inside HADES acceptance.

By means of the HGEANT simulation it is possible to evaluate the particle momentum at each point of its trajectory. In Figure 7.16 the difference between the particle momentum when emitted at the vertex and when they cross the first layer of MDC1 (i.e. the momentum loss) are plotted as a function of the MDC momentum value (i.e. the reconstructed one), for electrons/positrons, pions and for protons.

While for leptons the momentum loss is negligible, and the same is also for pions up to 100 MeV/c^2, the effect of momentum loss for protons becomes stronger for reconstructed momentum values below 500 MeV/c^2.

The proton momentum loss does not play a role in elastic scattering analysis, because the proton pair acceptance covers the momentum region above 800 MeV/c^2, and it can be ignored in η decay, where protons have at least 500 MeV/c^2 (see Figure 7.17).

In the $\pi°$ decay this effect becomes important. We can select protons coming from ppe^+e^- events, with pp missing mass below 400 MeV/c^2. In the left plot of Figure 7.18 we can see the difference between the reconstructed and the *real* (from simulation) momentum of protons, plotted as a function of the correct one. The effect at momentum values lower that 500 MeV/c^2 is visible, it makes the reconstructed momentum underestimated and widens the missing $\pi°$ mass peak.

On the right plot of Figure 7.18 we can see the same plot but this time using momentum values from the kinematic refit. By applying the refit procedure the discrepancy is somehow recovered.
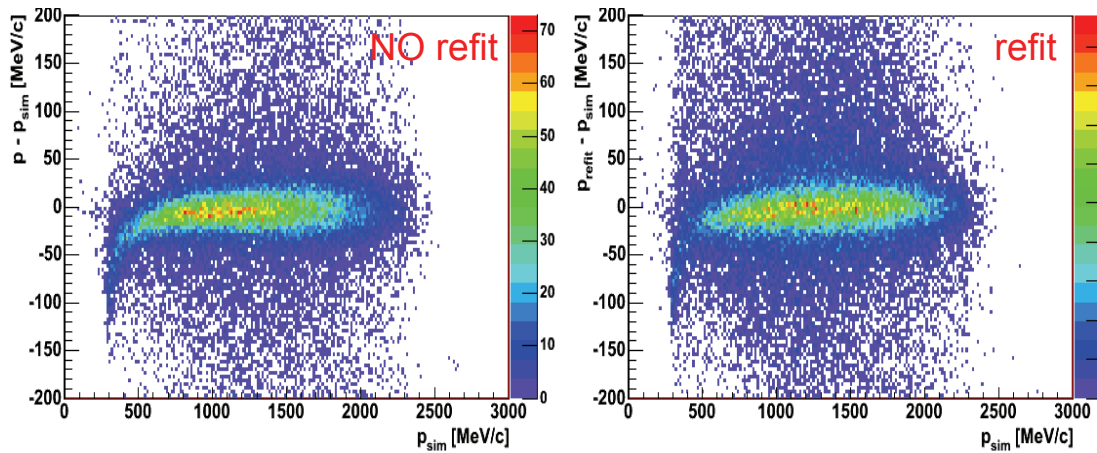
Figure 7.18 – Difference between the reconstructed momentum value and the real one (from simulation) for protons, plotted as a function of the real momentum. On the left plot the distribution is made using Runge Kutta momentum; on the right after the kinematic refit. The deviation at low momenta is partially recovered by the refit procedure.

Figure 7.19 shows the comparison between the pp missing mass distribution without kinematic refit and after applying the procedure. The η peak seems almost unchanged, while the $\pi°$ peak is now narrower and centred at lower mass values, much closer to the correct position.

In Figure 7.20 we can look at the distribution with only the kinematic refit missing mass values. The distribution was fitted by the combination of two gaussian functions for the meson peaks plus a polynomial background.

The η meson peak is centred at 546.0 MeV/c^2 (548.8 MeV/c^2 before the refit) and with a width of 10.6 MeV/c^2 (against 10.0 MeV/c^2 before). The η yield at 3σ is 1453 ± 116, and the signal/background ratio is 3.08 (previously 3.52). From the comparison

between the obtained values before and after the kinematic refit we can state that the η meson values become a little worse than before, but the difference is minimal.

For the π° peak the centre is closer to the correct place, now at 137 MeV/c², while the width from 34 MeV/c² (23%) becomes 21 MeV/c² (15%). The π° yield is now 8242 ± 290 in a 3σ mass region, and the signal/background ratio is 2.36 (to be compared to the old 1.49 factor).

The kinematic refit improved a lot the distribution, even if only in the π° region. In the experimental data we will see that the effect becomes important also for the η meson.
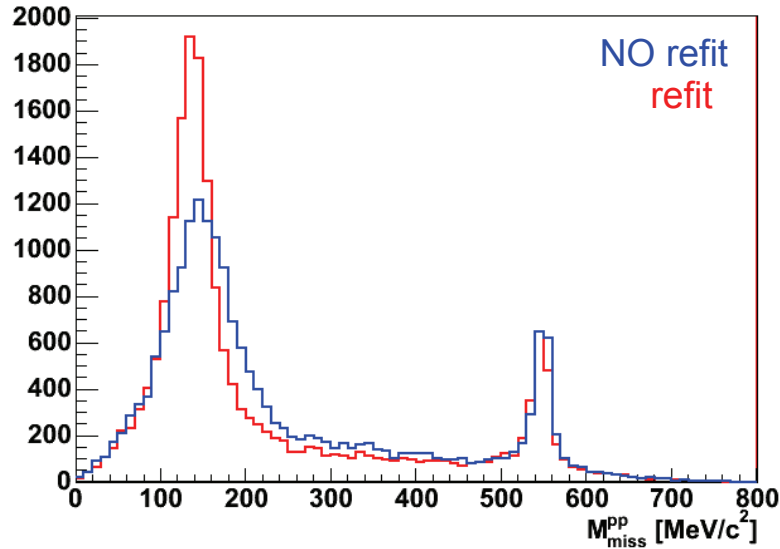
Figure 7.19 – Comparison between pp missing mass distribution before (blue) and after (red) kinematic refit procedure. While the η peak is almost unaffected, the π° peak has improved in terms of centre position and width.

Figure 7.20 – Proton-proton missing mass distribution after kinematic refit.

Once we are able to select the pp→ppη reactions, we must understand which kind of lepton pairs we have in our data sample. By means of our missing mass selections we are able to distinguish events containing pp→ppη, η→e⁺e⁻γ decay channels; while it

could seem obvious to state that we are selecting η Dalitz decays, we must consider that an e⁺e⁻ pair can come even from a conversion process.

Real photons can interact with the materials of the spectrometer (or even with air) and produce conversion pairs γ→e⁺e⁻. The η meson can decay into two gamma rays η→γγ (branching ratio 39.4%), and one of them (even both) can produce a conversion pair; in this case the ppe⁺e⁻ missing mass will be centred at zero (we miss a photon) and the pp missing mass distribution will give us the η meson value. Thus from a missing mass analysis we cannot separate these two different processes. This is the reason why there are not so many papers on the η form factor by using η→e⁺e⁻ Dalitz decay.
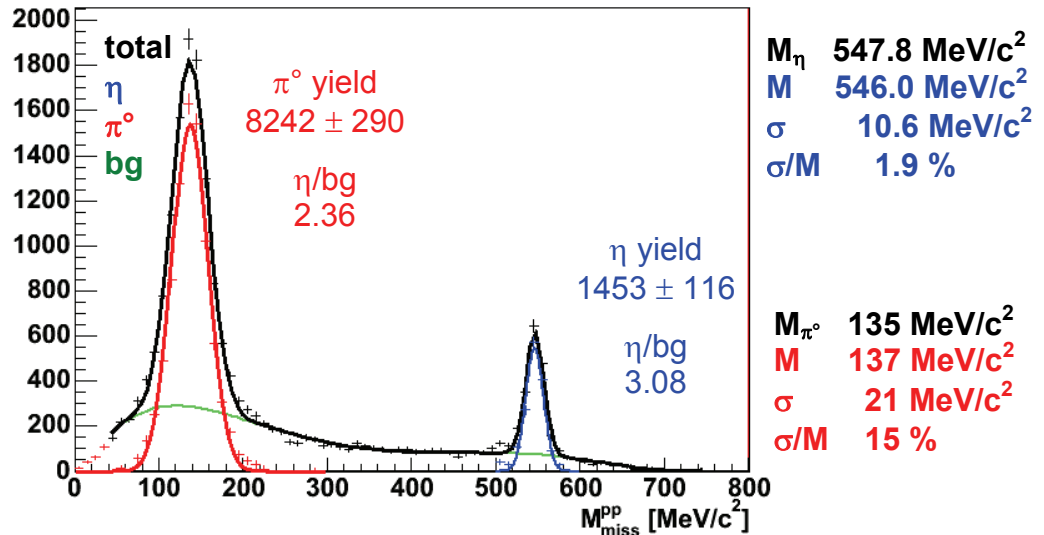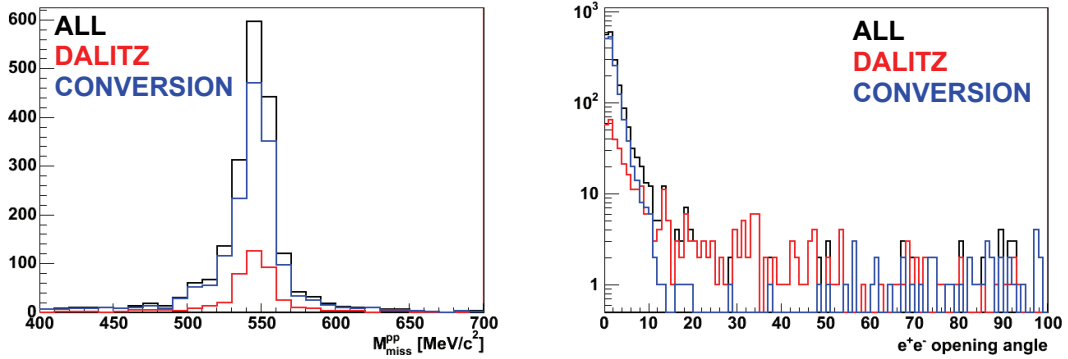

Figure 7.21 – pp missing mass distribution for η decays (on the left), by separating the contribution of the Dalitz decay (in red) from conversion processes (in blue). On the right the e⁺e⁻ opening angle distribution.

In order to understand the contamination we can check by simulation which processes produced the outgoing electrons/positrons. In the left plot of Figure 7.21 the pp missing mass is showed only for η decays, separately for η Dalitz and γ conversion decays. We can see that most of our counts come from conversion processes.

In general the leptons coming from conversion pairs have a small opening angle. The right plot of Figure 7.21 shows the opening angle distribution for dilepton pairs, separately for each sources. We can see that conversion pairs have opening angles lower than 10°; a reduced contribution at higher angles is still present, coming from combinatorial background (leptons coming from different photons).

In general in C+C experiments a selection on opening angle $\alpha > 9°$ is used to reject most of the conversion pairs. Table 7-3 shows the number of η decays coming from different processes, as evaluated by simulation (no 3σ missing mass selections). We can see that without any selections the yield is dominated by conversion pairs, only 20% of the data sample is constituted by Dalitz decays.

The opening angle selection cuts away most of the conversion pairs, only 5% survive after the selection. By applying the 9° opening angle cut, 37% of Dalitz decays survive, but there is still a 34% of conversion processes in the data. This means that in the next future, in order to evaluate correctly the contribution from conversion and to isolate the Dalitz decays, a much deeper analysis is needed on the selection criteria.

Moreover, the conversion processes strongly depend on our knowledge about the detector materials, which are set in HGEANT software. Thus simulation numbers can differ considerably from what really happens in the experiment: in no way we can reliably extrapolate the conversion contribution from the simulation to the experiment.

Table 7-4 shows the summary about the all the values obtained for the exclusive reconstruction of the η electromagnetic decay channels in simulation; values for π° are also shown. We can see that by applying also the 9° opening angle cut the number of

reconstructed η meson goes down to 161 ± 41. The η peak becomes a little broader (12.3 MeV/c^2), mainly because of the lower statistics and therefore larger errors in the fit.

By checking the π° yield we can see a reduction of about 6% as compared to the numbers before the angle cut, while the reduction for η is 11%. We must consider that π° has a lower mass and then the corresponding average opening angle of the outgoing lepton pair is narrower than for η; thus with the opening angle selection we are cutting more π° than η signals.

The same analysis now will be performed with the experimental data.

	No cut	α > 9°	Reduction
ALL	2044	234	11 %
DALITZ	418	155	37 %
CONVERSION	1626	79	5 %
DALITZ / ALL	20 %	66 %	

Table 7-3 – Number of η decays coming from different processes, with and without a selection in opening angle. The reduction is calculated dividing the number of events with α>9° by the number of events without the angular selection.

		Mass [MeV/c^2]	σ [MeV/c^2]	σ/M	yield	η/bg
η	NO refit	548.8	10.0	1.8	1540 ± 120	3.52
	refit	546.0	10.7	2.0	1453 ± 116	3.08
	α>9°	544.5	12.3	2.3	161 ± 41	4.03
π°	NO refit	148.2	34.1	23.0	7491 ± 309	1.49
	refit	136.8	21.5	15.7	8242 ± 290	2.36
	α>9°	132.1	21.8	16.5	557 ± 81	2.68

Table 7-4 - Summary of the results from the exclusive reconstruction of η electromagnetic decay in simulation data. The π° values are also shown.

7.3.2 Experimental data

In Figure 7.22 the two-dimensional missing mass plot is shown. We can see that the background is higher than in simulation, as we should expect, but nevertheless the η meson bump is visible and it can be separated from the other sources.

A proton-proton missing mass range was selected between 0.27 GeV^2/c^4 and 0.33 GeV^2/c^4, like with the simulation data, in order to focus on the η peak region and to evaluate the four particle ppe$^+$e$^-$ missing mass, as shown in Figure 7.23.

It is evident that the background is much higher than in the simulation, but the missing γ peak is visible. The experimental distribution was fitted by a gaussian function for the photon peak (in blue) plus a polynomial function for the background

(in red). It has to be underlined that the main peak is not centred at zero, as we should expect, but is shifted toward positive values and much more than in the simulation.

We can calculate that the centroid position of the missing γ corresponds to a missing mass value of 91 MeV/c², therefore it is shifted toward higher mass values even more than in simulation data. In the next future this effect will have to be investigated with a much deeper analysis of the tracking code.
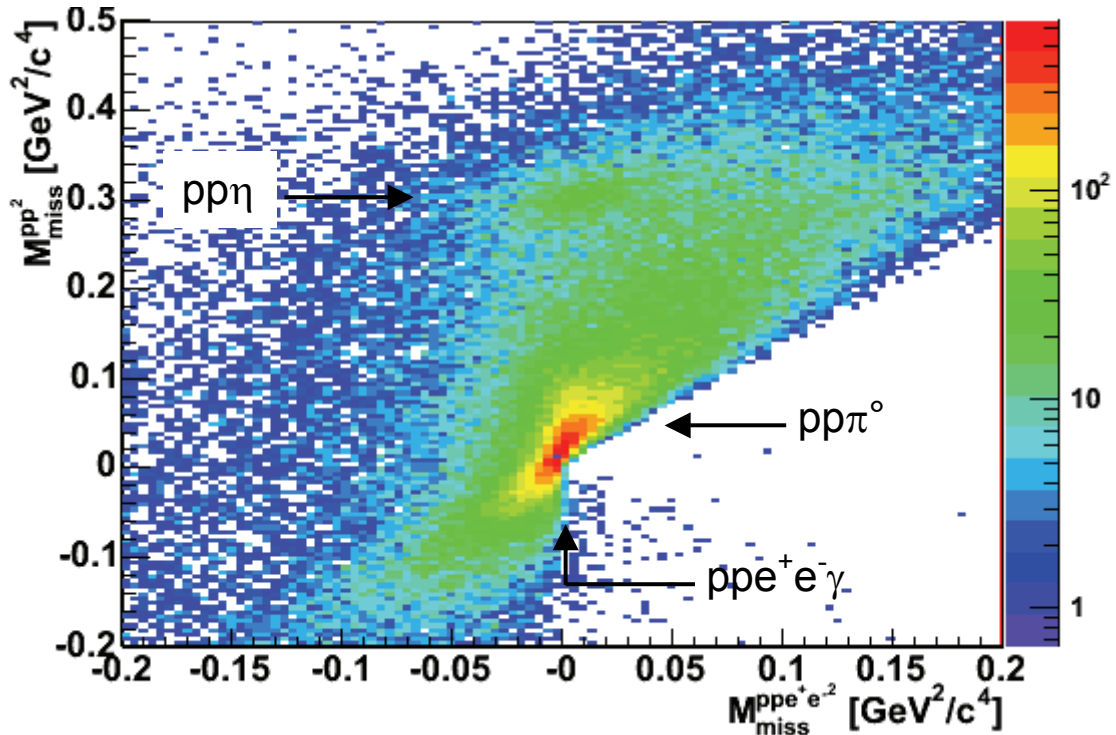
Figure 7.22 – Missing mass plot for four detected particles (ppe⁺e⁻) in experimental data. All the visible reaction channels are indicated in the plot.
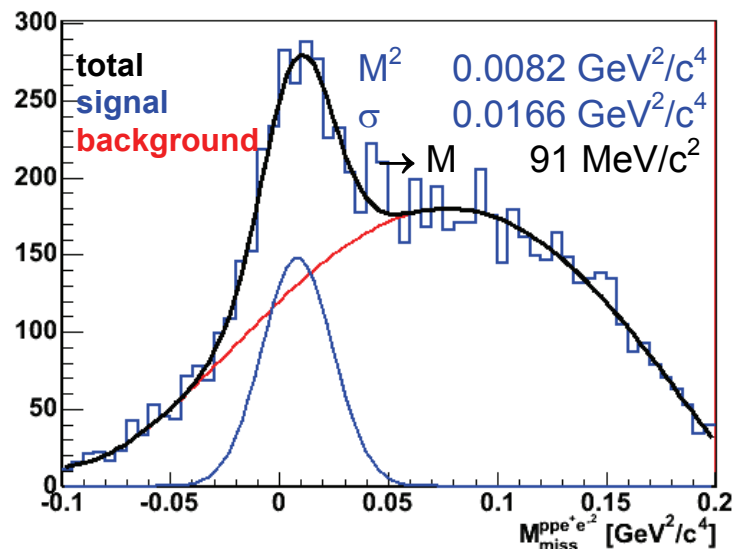
Figure 7.23 – ppe⁺e⁻ missing mass (squared) distribution for experimental data, after the selection $0.27\,GeV^2/c^4 < M_{miss}^{pp}{}^2 < 0.33\,GeV^2/c^4$ (η peak).
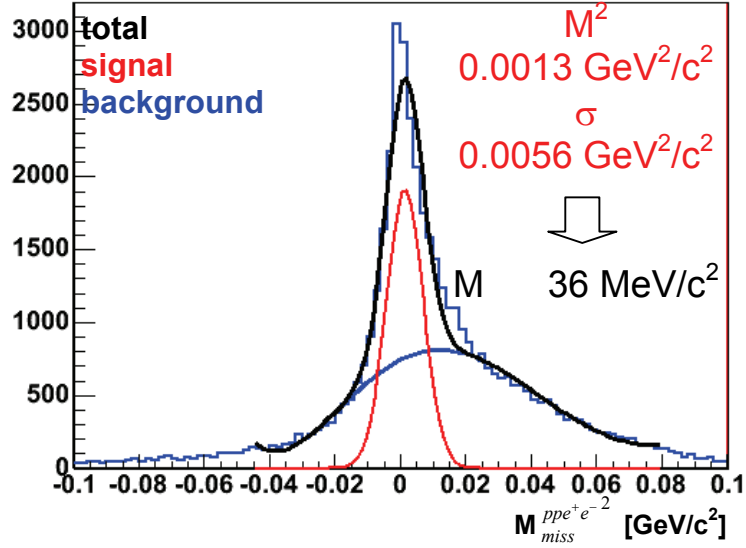
Figure 7.24 – ppe⁺e⁻ missing mass squared distribution in the missing π° region, for experimental data ($M_{miss}^{pp}{}^2 < 0.2 GeV^2/c^4$).

If we look at the ppe⁺e⁻ missing mass distribution in the region of the missing π° ($M_{miss}^{pp}{}^2 < 0.2 GeV^2/c^4$), we can see that the displacement (36 MeV/c²) is reduced with respect to the η meson region.

By applying the same procedure as used in simulation, we can make a 3σ selection over the four particle missing mass around the missing γ, using the fit parameters from the distribution in Figure 7.23.

The missing π° peak is totally dissolved by a low resolution momentum reconstruction, probably due to the proton momentum loss, nevertheless the η meson peak is still well defined.
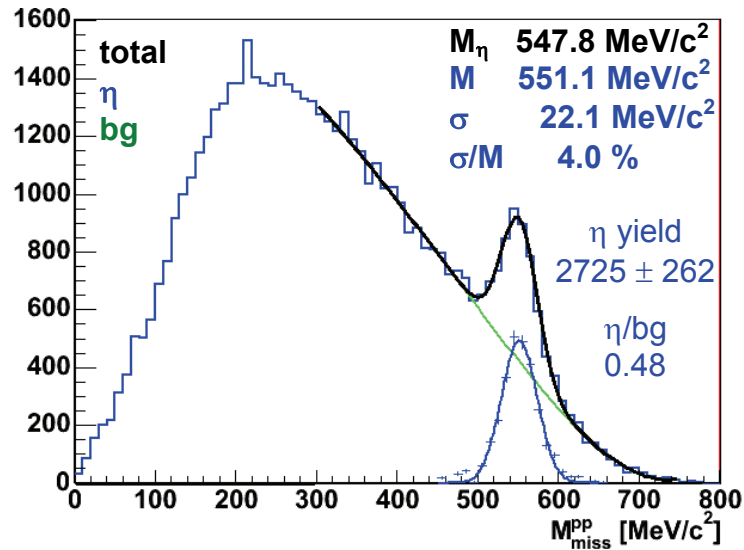
Figure 7.25 – Proton-proton missing mass distribution for experimental data, by applying a 3σ cut on the ppe⁺e⁻ missing mass around the γ peak. The π° peak is completely melted by a low resolution momentum reconstruction.

The experimental distribution was fitted by a polynomial background (green line) plus a gaussian function (in blue) for the peak.

The peak is centred at 551.1 MeV/c^2 with a width of 22.1 MeV/c^2. The achieved mass resolution of 4% is comparable with the one obtained via the hadronic decay (3.6%). The η yield inside a 3σ pp missing mass range is 2725 ± 262, with a signal/background ratio of 0.48.

The distribution is improved by the kinematical refit procedure, as shown in Figure 7.26. The refit is able to move the proton momenta toward the correct values, the peak of the missing π° is now clearly visible and the η peak is now better resolved.
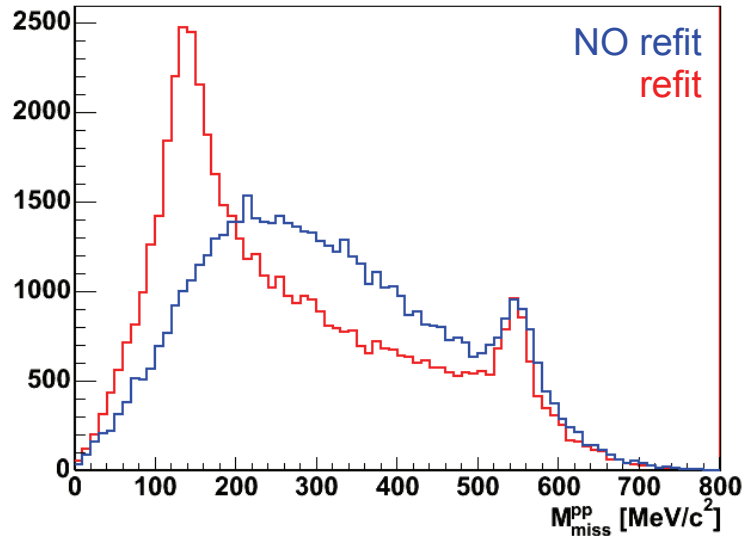

Figure 7.26 – Comparison between pp missing mass distribution with (red) and without (blue) kinematic refit. After the refit procedure the missing π° is clearly visible.

Figure 7.27 shows the kinematical refit distribution, now fitted also in the π° region. The η meson peak is now centred at 546.0 MeV/c^2, and the width is reduced to 17.8 MeV/c^2 (against the previous 22 MeV/c^2 value). The mass resolution corresponds to 3.3 % (previously it was 4.0%), which is a bit higher than the 2.5% for the hadronic decay, but still consistent with the elastic scattering analysis. The reason of this discrepancy mainly depends on the different proton kinematics, and it will need a more accurate study for a refined analysis.

Nevertheless the achieved missing mass resolution is in agreement with the value obtained via the elastic scattering analysis for the proton-proton invariant mass (see table 5-5), where for experimental data we evaluated 2.8 % for the sector pair 1-4, 2.3% for sectors 2-5, and 5.9% for the 3MDC sector pair 3-6. When reconstructing the η channel we combine the momentum measurement of four charged particles which hit different sectors; therefore our final mass resolution is averaged over the resolution of all the involved sectors. It is evident that the low resolution of sector 3 worsens the overall average mass resolution value.

The same fit procedure can be repeated for all the trigger combinations which were used during the data acquisition, such as downscaled first level triggered events (**Ds**), second level triggered events (**LVL2**), downscaled events with a positive 2nd level trigger decision (**LVL2Ds**), and by applying a condition on the e$^+$e$^-$ opening angle α >9°.

Table 7-5 shows a summary of all the values obtained by fitting experimental distributions, for both η and π° mesons.
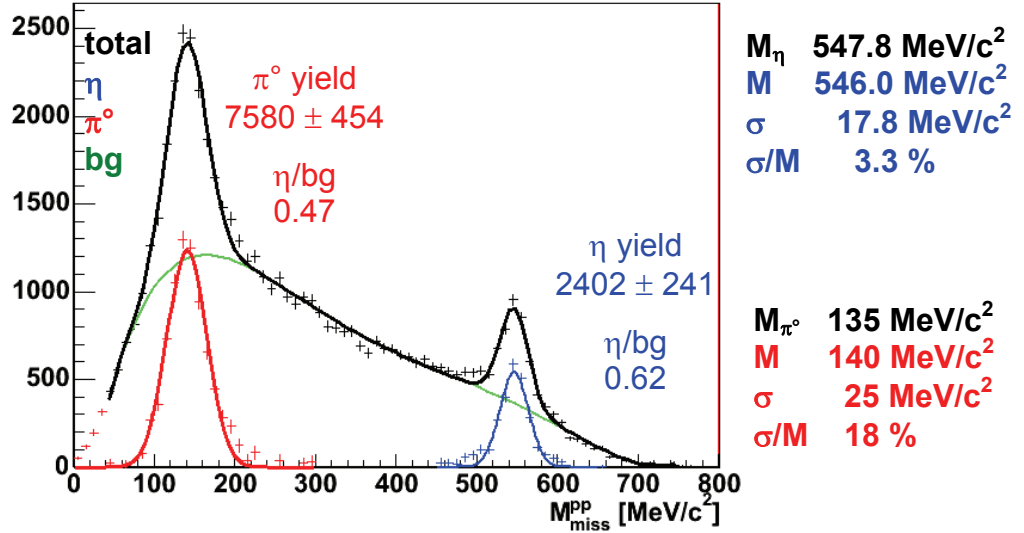
Figure 7.27 – Proton-proton missing mass distribution after kinematic refit, for experimental data.

		Mass [MeV/c²]	σ [MeV/c²]	σ/M	yield	η/bg
	NO refit	551.1	22.1	4.0	2752 ± 262	0.48
	Refit	546.0	17.8	3.3	2402 ± 241	0.62
	Ds	545.5	18.0	3.3	1220 ± 176	0.60
	LVL2	546.4	17.4	3.2	2175 ± 224	0.62
η	LVL2Ds	545.8	19.0	3.5	1053 ± 163	0.58
	α>9°	543.3	23.7	4.4	303 ± 72	0.80
	α>9° Ds	546.5	24.2	4.4	164 ± 51	0.90
	α>9° LVL2	544.0	23.8	4.4	295 ± 70	0.81
	α>9° LVL2Ds	548.2	25.2	4.6	160 ± 23	0.91
	NO refit	-	-	-	-	-
	Refit	140.2	24.6	17.6	7580 ± 454	0.47
	Ds	140.5	24.3	17.3	3997 ± 343	0.48
	LVL2	140.3	24.6	17.5	6898 ± 433	0.47
π°	LVL2Ds	141.0	26.0	18.4	3530 ± 320	0.49
	α>9°	132.6	22.9	17.3	644 ± 104	0.79
	α>9° Ds	136.6	26.9	20.4	381 ± 78	0.94
	α>9° LVL2	131.9	22.3	16.9	583 ± 97	0.76
	α>9° LVL2Ds	135.5	27.7	20.4	323 ± 73	0.82

Table 7-5 – Summary of the results from exclusive reconstruction of η electromagnetic decay in experimental data.

We can see that peak centroids and width values are stable according to different trigger selections. By applying the opening angle cut the statistics of the η meson drops down, therefore the worse resolution values and error bars are connected to a higher

uncertainty coming from the peak fit. But we have to notice that the values do not change so much, showing that the full analysis is consistent.

An open question about the spectrometer setup is the efficiency of the 2nd level trigger, in order to understand how many dilepton events we lose by using the lepton trigger for the data acquisition.

For this kind of analysis we need to use events which are triggered by the downscaling box (see chapter 4), so that they do not depend on the LVL2 decision.

By selecting only downscaled events, we can evaluate how many η mesons are reconstructed in the whole sample (Ds), and in downscaled events which had a positive 2nd level trigger decision (LVL2Ds). By dividing these numbers we obtain an estimate of the efficiency ε_η for η reconstruction:

$$\varepsilon_\eta = \frac{LVL2Ds_\eta}{Ds_\eta} \qquad \textbf{(Eq. 7-4)}$$

The same method can also be applied to evaluate the efficiency ε_{π° for the neutral pion, even if the estimate is less accurate because of the difficulty of background evaluation.

In this way we obtain $\varepsilon_\eta = 0.86 \pm 0.18$, $\varepsilon_{\pi^\circ} = 0.88 \pm 0.11$. The large error bars are related to the error propagation of the parameters coming from the fit. Nevertheless the two obtained values are close to each other and this means that the trigger efficiency estimate is consistent[7].

Hadronic and electromagnetic η decay yields can be evaluated, even if we cannot compare the values to the expectation from the branching ratio values, because at the moment we are not able to isolate the Dalitz decay from the contamination of conversion pairs.

The ratio between hadronic and electromagnetic decay channels can be calculated in simulation by simply dividing the numbers obtained from the η fits, which can be found in Table 7-2 and Table 7-4. In this way we obtain a factor 15.3 ± 1.3 as hadronic/electromagnetic ratio.

In the experiment the same ratio can be calculated with two different methods, by using values from Table 7-2 and Table 7-5.

If we select only downscaled events, we can compare the yields by using the same data sample[8]. By simply dividing downscaled yields we obtain a hadronic to electromagnetic ratio of 18.7 ± 2.9.

Another way consists of using the electromagnetic decays in the 2nd level triggered events. In this case the electromagnetic yield has to be corrected by the trigger efficiency (86 % as previously calculated), while the hadronic channel has to be rescaled to the total number of LVL1 triggered events, therefore it has to be multiplied by the average downscaling factor (2.2). The correct formula is:

$$\frac{\eta_{hadronic}}{\eta_{electromagnetic}} = \frac{\eta_{hadronic}^{Ds} \cdot downscaling}{\eta_{electromagnetic}^{LVL2} / \varepsilon_\eta^{LVL2}} \qquad \textbf{(Eq. 7-5)}$$

---

[7] In general the trigger efficiency depends also on the pair opening angle; with the present fit values, for reconstructed mesons with opening angle larger than 9° the errors are too large to evaluate a reliable efficiency (mainly due to the low number of counts, in particular for η).

[8] Hadronic decays were reconstructed by using only downscaled events.

With this method we obtain a hadronic/electromagnetic factor of 19.8 ± 2.1, which agrees with the value found using downscaling events within the error bars.

At the moment we can state that our experimental ratio is higher than the simulation one. If we consider the electromagnetic channel the one which differs between experiment and simulation, the discrepancy means that in the experiment we are reconstructing only about 80% lepton pairs with respect to the simulation. This is reasonable considering that the RICH efficiency is not yet well understood, and we suspect it has a lower efficiency value than in simulation. Therefore at the moment our electromagnetic sample is contaminated by spurious conversion events, which does not allow us to provide quantitative considerations about normalization factors.

Nevertheless, the two ratios obtained in the experimental data with the two methods agrees, and this means that the evaluated 2nd level trigger efficiency is reasonable; moreover the simulation and experimental ratios are not quite different, thus it is possible to state that the analysis is in a good shape and soon our final normalization factors could be extracted.

7.4 *Exclusive η reconstruction summary*

In this chapter the whole procedure for the η exclusive reconstruction was presented, for both hadronic and electromagnetic decay channels.

The procedure is based first on the selection of events with the interesting four particles in the exit channel (ppπ$^+$π$^-$ for the hadronic decay, ppe$^+$e$^-$ for the electromagnetic decay); in a second stage the four particle missing mass is plotted in order to find the missing particle of the reaction, a neutral pion for η→π$^+$π$^-$π°, a photon for η→e$^+$e$^-$γ; after the missing particle is found, the missing mass for the two outgoing protons is plotted in order to select pp→ppη reactions. By means of a fit procedure the individual contributions to the interesting events and to the background are evaluated, and then the invariant mass resolution and the meson yields can be calculated. A kinematic refit procedure is applied in order to improve the mass resolution, by imposing a kinematic constraint on the reaction of interest.

The hadronic decay channel analysis showed a well defined η peak (signal/background 0.57), centred at the correct position with an invariant mass resolution of 2.5 %. This value is perfectly in agreement with what obtained by the elastic scattering analysis of chapter 5, and it demonstrates the good status of the HADES tracking system and momentum reconstruction. With the fully analysed data sample we are able to reconstruct about 22,000 η hadronic decay events.

By means of the electromagnetic analysis we demonstrated that with the spectrometer we can select exclusively the η decay channel with good performances, achieving an invariant mass resolution of 3.3 % and a signal to background ratio of 0.62. Some problems occur in the π° meson reconstruction without kinematic refit, where the peak spreads away due to the poor resolution; the reason of this effect is well understood and it is connected to the momentum loss of low momenta protons while crossing target and RICH, which is not visible in elastic and η meson reactions. In the near future a momentum dependent correction is foreseen, however at the moment the kinematic refit procedure is able to correct the problem providing a satisfactory π° peak.

Coming back to the electromagnetic channel, we estimated about 2,400 η electromagnetic decays in our experimental data sample. From our simulations we

know that most of these events come from gamma conversion processes, and a limited part is due to true η Dalitz decays. From the simulation we evaluated that the Dalitz channel could be scaled by about a factor 5 in the total yield; by selecting only lepton pairs with opening angle greater than 9° we see that the contribution from conversion processes is reduced but still present, therefore at the moment it is not possible to make any consideration about the η Dalitz decay alone.

The obtained invariant mass resolution values for the hadronic and electromagnetic channels are in agreement with each other, and also with the elastic scattering analysis. The exclusive reconstruction procedures are working and they provide good performances, in order to select the desired channels. Now all the instruments are ready in order to perform physical analysis on the January 2004 data, and in particular on η meson decays.

8 SUMMARY AND CONCLUSIONS

The HADES proton-proton programme is running, with the aim to study the sources of dileptons in an exclusive way.

The first production run was done on January 2004, with *pp* collisions at 2.2GeV. This was the first time the spectrometer ran with the full tracking setup on 4 sectors out of 6, and a mid resolution setup on the remaining two sectors. Thus the potentiality of the spectrometer in a high resolution tracking configuration could be tested and used.

The main goal of the experiment was to collect data with *pp* elastic scattering, for tracking alignment calibration, and to identify the *pp→ppη* reactions through an exclusive reconstruction of the hadronic and the dielectron decay channel. In this work the characterization of the HADES spectrometer was performed.

The analysis work started before the experimental run by studying simulation data, with the aim to optimize the selection trigger for the data acquisition. The enhancement of events containing elastic scattering reactions and η meson decays was mandatory in order to reduce the number of acquired events coming from background reactions. A full characterization of the HADES tracking system was performed, by using elastic events.

The elastic scattering is very important for tracking studies, because of the well known kinematics which constrains the angular variables and the momenta of the outgoing protons; a well focused study can improve the alignment calibration of sub-detectors, in order to achieve the expected values of invariant mass resolution.

The analysis of the tracking software dealt with experimental runs without magnetic field, in order to evaluate the alignment of the inner and outer chambers using straight tracks, and then to reconstruct the reaction vertex and the effective beam position and direction. It was found that in the early part of the beam time the beam was shifted from its nominal position, and hit a narrowing of the beam pipe producing a lot of secondaries from a non-target region. The vertex reconstruction helped in order to evaluate and eliminate this contribution.

The alignment procedure worked well and now there are only weak systematic deviations in the angular reconstruction, as compared to what we expect from the elastic scattering kinematic constraints; the alignment of the outer segment of sector 3 needs an improvement, because the reduced number of operational wire layers and the absence of the related MDC4 chamber did not allow to correctly evaluate the angles.

Afterwards the runs with magnetic field were analysed, in order to test the momentum reconstruction by using two high resolution methods, the Spline and the Runge Kutta algorithms. By means of elastic proton pairs analysis the momentum and invariant mass resolution of each sector was evaluated. At the end the Runge Kutta algorithm provided better performances, by improving the angular reconstruction with respect to what obtained directly from the drift chambers, and achieving a momentum resolution of about 4.5% for the three sectors equipped with four MDC chambers (2, 4, 5); 6% for sector 1 where four chambers were operational but some wire layers were missing; 7% for sector 6 which was equipped with only three MDC chambers; and finally 17% for sector 3, equipped with only three MDC chambers and lacked several wire layers. In this case the trajectory evaluation in the region after the magnetic field had a poor resolution due to the insufficient number of points measured   in space and available for the fit procedure. The overall invariant mass resolution for elastic pairs was about 2.3 – 2.8 % for 4MDC sectors, and 6 % for the 3MDC sector pair.

By performing a systematic study all the problems found were understood, such as the different resolution for each different sector. The obtained values are larger than the expectation from the simulation ($\approx$ 1% invariant mass resolution). This effect can be due to the found misalignment of the beam line, which affects the reconstruction of the angular variables. Moreover, there are some hints that the beam was even tilted with respect to the z axis, and this strongly affects the angular and the momentum reconstruction. Some studies are still going on, in order to evaluate the beam position day by day.

A full characterization of the time of flight system was presented, explaining the calibration procedure and the achieved time and position resolution.

For the January 2004 experiment it was decided not to use a START detector, because of the high number of secondary particles it produced by the interaction of the beam. Thus the time measurement was started event by event by the fastest particle which produced a signal in a scintillator rod of TOF. This feature made the time calibration much difficult, and a new algorithm had to be developed in order to reconstruct the start time of the reaction.

The algorithm relies on using an independent method to identify one particle of the event. The first kind of identification comes from RICH Cherenkov detector, which can select electron/positron tracks; if a lepton candidate is not found, we can try to find in the event a negative charged track (from the deviation of the trajectory inside the magnetic field) and assume it is a negative pion, as among the possible reaction channels the only negative particles can be electrons or negative pions.

From the assumed mass and the measured momentum it is possible to calculate the time-of-flight of the particle, and so the offset to the real start time of the reaction. Finally, we can recalculate the time-of-flight of the other particles belonging to the same event using the reaction time.

The method and the achieved values of time resolution and efficiency were presented, as calculated in simulation data as well as deduced from the September 2003 data, a commissioning run at lower beam intensity when the use of the START detector was possible. A good separation between protons and pions was achieved, therefore it was possible to use the reconstructed time of flight for particle identification, in particular for η meson exclusive reconstruction.

The η production cross sections can be measured both through the hadronic ($\eta \rightarrow \pi^+\pi^-\pi^0$) and the dielectron ($\eta \rightarrow e^+e^-\gamma$) Dalitz decays, whose branching ratios are known. This fact allows to use the pp$\rightarrow$ppη channel as a calibration reaction for the dielectron identification of the spectrometer, in order to normalize the dielectron yields in the heavy ion collision experiments.

The exclusive reconstruction procedure was presented, both for hadronic and electromagnetic decay channel, for simulation and experimental data. After selecting events which contain the desired identified particles in the exit channel, i.e. a proton pair plus a $\pi^+\pi^-$ pair for hadronic or an e^+e^- pair for electromagnetic decay, by exploiting the missing mass technique it is possible to select the η decay channel, to fit the distributions and to evaluate the missing mass resolution and yields. In order to improve the results a kinematic refit procedure was implemented.

The reconstruction of both hadronic and electromagnetic decays is possible with the current setup and resolution. The achieved values of invariant mass resolution are in agreement with what obtained by analysing elastic pairs, and an improvement could come by including momentum corrections from energy loss, even if they should not affect the η mass region but only the π^0 one.

In the electromagnetic channel it is not easy to separate the contribution from Dalitz decay from the background coming from the photon conversion process; a

selection on opening angle can reduce the number of conversion processes in the analysed sample, but it is not enough to completely suppress this contribution, and moreover it strongly reduces the number of remaining Dalitz decays. This analysis needs a more detailed study in the near future, in order to provide the final normalization factor for the dilepton invariant mass distribution from heavy ion collision experiments. The future analysis could include the vertex reconstruction of the dilepton pairs, in order to suppress the contribution of e^+e^- coming from the region outside the target, which can only come from gamma conversion. Moreover, acceptance and efficiency corrections are needed.

In conclusion, the HADES spectrometer is operational also for elementary collisions; in April 2006 an experimental run is foreseen to study p+p collisions at 3.5 GeV, in order to study the production of vector mesons such as ρ and ω, as a reference point for heavy ions experiments.

The high resolution tracking system works properly; there are still some small effects on misalignment, in particular connected to the beam quality, but they are under control and in the near future will be improved. With the imminent installation of the last two MDC4 drift chambers the spectrometer will exploit the full resolution mode in all the sectors: at the moment the poor resolution of the sectors with three MDC affect the missing mass resolution in 4 particles exclusive reconstruction.

The spectrometer can work even without a START detector, in particular in p+p collisions, and it proved capable of providing a good proton/pion identification and separation by means of the algorithm shown.

The exclusive reconstruction procedures are tested and operational, and η meson decays were identified and selected.

We can state that the HADES results are well promising; all the analysis tools are now tested and fully operational, therefore the e+e- production study can now proceed in view of some hopefully outstanding physical results.
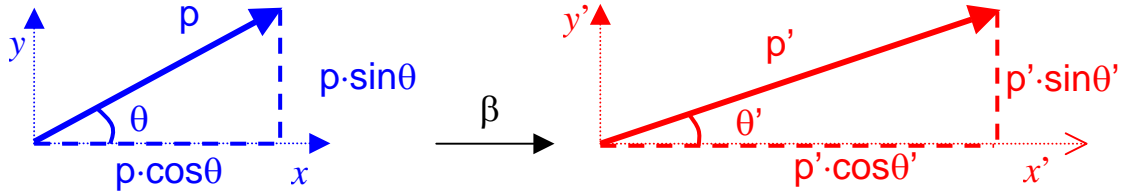
Appendix A - ELASTIC SCATTERING CALCULATIONS

Figure A.1 – Scheme of the Lorentz transformation between two coordinate systems (x, y) and (x', y'), where the second is in motion with respect to the first one at velocity β.

Let us consider the motion of a particle with momentum p and polar angle θ in the (x, y) coordinate system. We can express the transversal and parallel momentum components with respect to the x axis respectively as $p \cdot sin\theta$ and $p \cdot cos\theta$, as shown in the left side of Figure A.1.

If we consider a second coordinate system (x', y'), which moves at constant velocity $\beta = v/c$ respect to the first coordinate system, in relativistic kinematics we can express the momentum coordinates in the new frame as a function of the old coordinates, by using Lorentz transformations:

$$p' \cos \theta' = \gamma \left(p \cos \theta - \beta E \right) \qquad \text{(Eq. A-1)}$$

$$p' \sin \theta' = p \sin \theta \qquad \text{(Eq. A-2)}$$

where E is the total energy of the particle in the original frame and γ is the Lorentz factor $\gamma = \sqrt{1 - \beta^2}$ (we assume in the notation $c \equiv 1$).

The same equations can be used if we have the particle momentum in the centre of mass system (cm) and we want to transform it into the laboratory coordinate system (lab). In this case the laboratory system moves at velocity $-\beta_{cm}$, and we obtain:

$$p_{lab} \cos \theta_{lab} = \gamma_{cm} \left(p_{cm} \cos \theta_{cm} + \beta_{cm} E_{cm} \right) \qquad \text{(Eq. A-3)}$$

$$p_{lab} \sin \theta_{lab} = p_{cm} \sin \theta_{cm} \qquad \text{(Eq. A-4)}$$

By dividing the equation A-4 by the A-3 we obtain:

$$\tan\theta_{lab} = \frac{\sin\theta_{lab}}{\cos\theta_{lab}} = \frac{\sin\theta_{cm}}{\gamma_{cm}\left(\cos\theta_{cm} + \beta_{cm}\dfrac{E_{cm}}{p_{cm}}\right)} \qquad \textbf{(Eq. A-5)}$$

If we consider the identity $\beta = p/E$, at last we have:

$$\tan\theta_{lab} = \frac{\sin\theta_{cm}}{\gamma_{cm}(\cos\theta_{cm}+1)} \qquad \textbf{(Eq. A-6)}$$

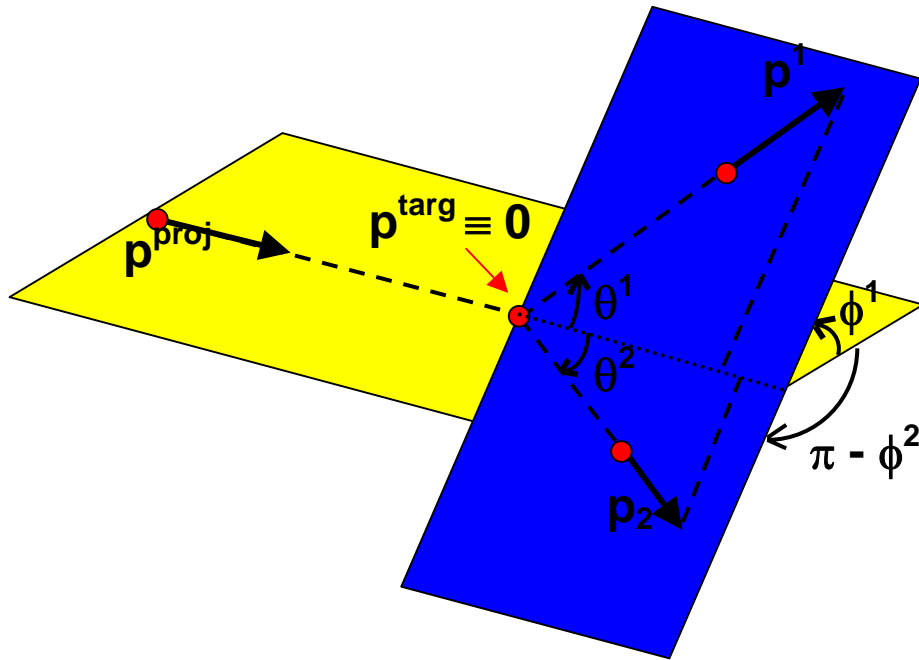We can use this relation in the case of elastic scattering (Figure A.2).

Figure A.2 – Three-dimensional sketch of an elastic scattering collision in the laboratory frame.

In the elastic scattering the two outgoing particles lay on the same reaction plane ($|\phi_1 - \phi_2| = 180°$).

Moreover in the centre of mass coordinate system they are emitted in opposite directions, i.e. at polar angles θ_{cm} and $\pi - \theta_{cm}$ (see the right plot of Figure A.3). Following these considerations we can write the two tangents of the polar angles as:

$$\tan\theta^1 = \frac{\sin\theta_{cm}}{\gamma_{cm}(\cos\theta_{cm}+1)} \qquad \textbf{(Eq. A-7)}$$

$$\tan\theta^2 = \frac{\sin(\pi-\theta_{cm})}{\gamma_{cm}(\cos(\pi-\theta_{cm})+1)} = \frac{\sin\theta_{cm}}{\gamma_{cm}(1-\cos\theta_{cm})} \qquad \textbf{(Eq. A-8)}$$

By multiplying equation A-7 by A-8 we finally obtain:

$$\tan\theta^1 \cdot \tan\theta^2 = \frac{\sin^2\theta_{cm}}{\gamma_{cm}^2\left(1-\cos^2\theta_{cm}\right)} = \frac{1}{\gamma_{cm}^2} \qquad \textbf{(Eq. A-9)}$$

This is the relativistic condition which relates the polar emission angles of the two outgoing particles in an elastic scattering process.
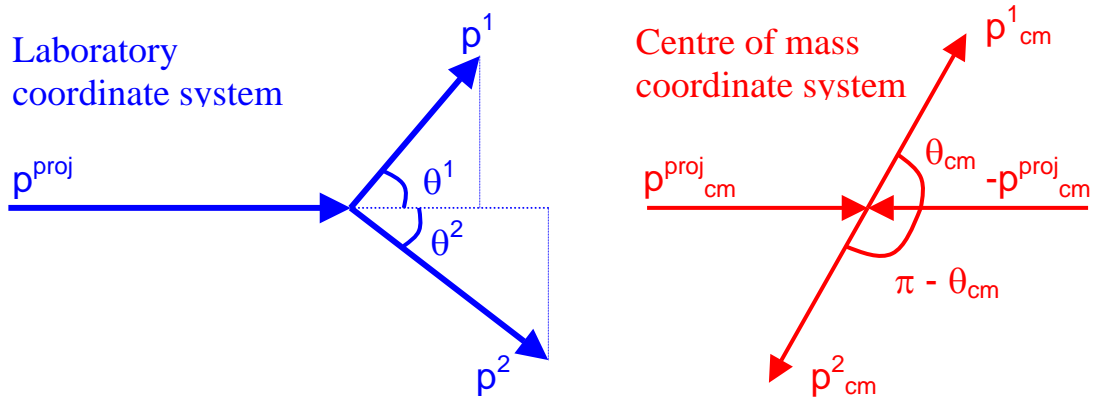

Figure A.3 – Scheme of an elastic scattering reaction, in the laboratory coordinate system (on the left) and in the centre of mass (on the right).

By using momentum conservation in the laboratory coordinate system it is possible to find the relation between the momentum of the outgoing protons and the emission angles.

If we consider the right plot of Figure A.3, the parallel and transversal components of the total momentum respect to the beam axis must remain unchanged before (the hitting projectile proton plus the target proton at rest frame) and after the collision (the two outgoing protons).

We can write these conditions as:

$$p^1\sin\theta^1 - p^2\sin\theta^2 = 0 \qquad \textbf{(Eq. A-10)}$$

$$p^1\cos\theta^1 + p^2\cos\theta^2 = p^{proj} \qquad \textbf{(Eq. A-11)}$$

where p^{proj} is the momentum of the projectile in the laboratory frame.

From the equation A-10 we can evaluate the momentum of the particle 2 as:

$$p^2 = p^1\frac{\sin\theta^1}{\sin\theta^2} \qquad \textbf{(Eq. A-12)}$$

and substitute this formula into the A-11, and we obtain:

$$p^1 \cos\theta^1 + p^1 \frac{\sin\theta^1}{\tan\theta^2} = p^{proj} \qquad\qquad \textbf{(Eq. A-13)}$$

If we use the A-9 the previous equation becomes:

$$p^1 \cos\theta^1 + p^1 \gamma_{cm}^2 \sin\theta^1 \tan\theta^1 = p^{proj} \qquad\qquad \textbf{(Eq. A-14)}$$

We can easily see that the variables of the second particle are not present anymore in the equation, so the relation A-14 is valid for both protons. We can write it as:

$$p = \frac{p^{proj}}{\cos\theta + \gamma_{cm}^2 \sin\theta \tan\theta} \qquad\qquad \textbf{(Eq. A-15)}$$

In this way, by knowing the polar emission angle of a proton coming from an elastic scattering reaction, we can estimate its momentum and compare this value to the one reconstructed by the tracking algorithms.

BIBLIOGRAPHY

[Aga98]:   G. Agakichiev *et al.* :
"Systematic study of low-mass electron pair production in p-Be and p-Au collisions at 450 GeV/c²"
Eur. Phys. J. **C 4** (1998) 231-247

[Ago98]:   C.Agodi *et al.*:
"The Time Of Flight Wall for the HADES Spectrometer"
IEEE Trans. Nucl. Sci. **45** n. 3 (1998) 665

[Ago02]:   C.Agodi *et al.*:
"The HADES Time Of Flight wall"
Nucl. Instr. Meth. **A 492** (2002) 14-25

[Alv04]:   H. Alvarez Pol *et al.*:
"A large area timing RPC prototipe for ion collisions in the HADES spectrometer"
Nucl. Instr. Meth. **A 535** (2004) 277-282

[Bal01]:   P. Balestra *et al.*:
"ϕ and ω meson production in pp reactions at p_{lab} = 3.67 GeV/c"
Phys. Rev. **C 63** (2001) 024004

[Bal04]:   Balanda *et al.*:
"The HADES Pre-Shower detector"
Nucl. Instr. Meth. **A 531** (2004) 445-458

[Bar85]:   L.M.Barkov *et al.*:
"Electromagnetic pion form factor in the timelike region"
Nucl.Phys. **B 256** (1985) 365

[Ber98]:   E.Berdermann *et al.*:
"Diamond Detectors for Heavy Ion Measurements"
Proceedings of "XXXVI Intern. Winter Meeting on Nucl. Phys.", Bormio 1998

[Bra98]:   E.L.Bratkovskaya *et al.*:
"Dilepton production and m_T-scaling at BEVALAC/SIS energies"
Nucl. Phys. **A 634** (1998) 168-189

[Bro91]:   G.E.Brown, M.Rho:
"Scaling effective Lagrangians in a dense medium"
Phys. Rev. Lett. **66** (1991) 2720

[Bre99]:   T. Bretz:
"*Magnetfeldeigenschaften del Spektrometers HADES*"
PhD thesis, Technische Universität München (1999)

[Cas99]:   W.Cassing, E.L.Bratkovskaya
"*Hadronic and electromagnetic probes of hot and dense nuclear matter*"
Phys. Rep. **308** (1999) 65-233

[Che37]:   P.A. Cherenkov:
"*Visible radiation produced by electrons moving in a medium with velocities exceeding that of a light*"
Phys. Rev. **52** (1937) 378

[Dlh80]:   R.I. Djhelyadin *et al.*:
"*Investigation of the electromagnetic structure of the η meson in the decay $\eta \rightarrow \mu^+ \bar{\mu} \gamma$*"
Phys. Lett. **B 94** (1980) 548-550

[Dre98]:   A. Dress:
"*Electromagnetic radiation probing hot and dense nuclear matter*"
Nucl. Phys. **A 630** (1998) 449c-460c

[Ern98]:   C. Ernst *et al.*:
"*Intermediate mass excess of dilepton production in heavy ion collisions at relativistic energies*"
Phys. Rev. **C 58** (1998) 447-456

[Fäs03]:   A. Fässler *et al.*:
"*Dilepton production in proton–proton collisions at BEVALAC energies*"
J. Phys. **G 29** (2003) 603-456

[Gea3]:   GEANT 3
CERN Program Library Long Writeup W5013

[Had94]:   HADES collaboration:
"*HADES: A proposal for High-Acceptance Di-Electron Spectrometer*"
Proposal, GSI Darmstadt (1994)

[Hol05]:   R. Holzmann *for the HADES collaboration*:
"*Di-electron mass spectrum in 2 AGeV $^{12}C+^{12}C$ measured with HADES*"
Quark Matter 2005 presentation, Budapest, August 4-9

[Jan75]:   M. R. Jane *et al.* :
"*A measurement of the electromagnetic form factor of the eta meson an of branching ratio for the eta Dalitz decay*"
Phys. Lett. **B 59** (1975) 103-105
Phys. Lett. **B 73** (1978) 503 (erratum)

[Kag00]:   M. A. Kagarlis:
"*Pluto^{++} A Monte Carlo simulation tool for hadronic physics*"
GSI report 3, July 2000

[Kli90]:   S.Klimt *et al.*:
"*Chiral phase transition in th SU(3) Nambu and Jona-Lasinio model*"
Phys. Letters **B** 249 (1990) 386

[Kli96]:   F.Klingl, N.Kaiser, W.Weise:
"*Effective Lagrangian approach to vector mesons, their structure and decays*"
Z.Phys. **A 356** (1996) 193-206

[Kli97]:   F. Klingl, N. Kaiser, W. Weise:
"*Current correlation functions, QCD sum rules and vector mesons in baryonic matter*"
Nucl. Phys. **A 624** (1997) 527

[Koc95]:   V. Kock:
"*Introduction to Chiral Symmetry*"
LBNL-Report 39463 (1996)

[Mos03]:   U. Mosel *et al.* :
"*Role of baryonic resonances in the dilepton emission in nucleon-nucleon collisions*"
Phys. Rec. **C 67** (2003) 065202

[Mün04]:   C. Müntz *et al.*:
"*The HADES tracking system*"
Nucl. Instr. Meth. **A 535** (2004) 242-246

[PDG04]:   Particle Data Group:
"*Review of particle physics*"
Phys. Lett. **B 592** (2004)

[Por97]:   R.J. Porter *et al.*:
"*Dielectron Cross Section Measurements in Nucleus-Nucleus Reactions at 1.0A GeV*"
Phys. Rev. Letters **79** (1997) 1229

[Pre02]:   W.H. Press
"*Numerical Recipes in C++*"
Cambride University press

[Rap00]:   R. Rapp, J. Wambach:
"*Chiral simmetry restoration and dileptons in relativistic heavy ion collissions*"
Adv. Nucl. Phys. **25** (2000) 1

[Sak69]:   J.J.Sakurai:
"Currents and Mesons"
The University of Chicago Press (1969)

[San00]:   M.Sanchez:
"Kick Plan (Beamtime Edition)"
Internal Paper, GSI, 22/12/2000

[Sch96]:   R.Shicker *et al.*:
"Acceptance and simulation studies for the dielectron spectrometer HADES at GSI"
Nucl. Instr. Meth. **A 380** (1996) 586-596

[Tei96]:   S. Teis *et al.* :
"Pion-production in heavy-ion collisions at SIS energies"
arXiv nucl-th/9609009

[Tlu04]:   P. Tlusty *et al.*:
"Hadron production in C+C at 2 A GeV measured by the HADES experiment"
Proceedings on XLII International Winter Meeting on Nuclear Physics, Ricerca scientifica ed Educazione Permanente, Univ. Milano Vol. 123 (2004) 171-179

[Toi03]:   A. Toia *et al.*:
"A highly selective dilepton trigger based on ring recognition"
Nucl. Instr. Meth. **A 502** (2003) 270-274

[Tra00]:   M. Traxler *et al.*:
"The 2nd level trigger system of the HADES detector"
IEE Trans. Nucl. Sci. **47** (2000) 376-380

[Wil98]:   W. K. Wilson *et al.* :
"Inclusive dielectron cross sections in p+p and p+d interactions at beam energies from 1.04 to 4.88 GeV"
Phys. Rev. **C 57** (1998) 1865-1878

[Zei99]:   K.Zeitelhack *et al.*:
"The HADES RICH detector"
Nucl. Instr. Meth. **A 433** (1999) 438